

Technische Universität München  
Lehrstuhl für Biomolekulare NMR Spektroskopie

**Structural characterization of the membrane mimetic interactions of the  
FATC domains of the protein kinase 'target of rapamycin' and related kinases**

Lisa A. M. Sommer

Vollständiger Abdruck der von der Fakultät für Chemie der Technischen Universität  
München zur Erlangung des akademischen Grades eines

**Doktors der Naturwissenschaften**

genehmigten Dissertation.

Vorsitzender:

Univ.-Prof. Dr. Stephan A. Sieber

Prüfer der Dissertation:

1. Priv.-Doz. Dr. Sonja A. Dames
2. Univ.-Prof. Dr. Aymelt Itzen

Die Dissertation wurde am 03.09.2013 bei der Technischen Universität München  
eingereicht und durch die Fakultät für Chemie am 26.09.2013 angenommen.



Structural characterization of the membrane mimetic  
interactions of the FATC domains of the protein kinase  
'target of rapamycin' and related kinases

Lisa A. M. Sommer

August 2013

Γνωθι σαυτόν

Chilon von Sparta (~555 v.Chr.)

# Abstract

The FATC domain is shared by all members of the family of phosphatidylinositol-3 kinase-related kinases (PIKKs), which control cellular signaling pathways in response to stress and nutrients. It has been shown that the FATC domain plays an important role for the regulation of each PIKK. NMR and (oriented) CD spectroscopy as well as MD simulations were combined to further examine the immersion depth and orientation of the membrane-immersed wild type FATC domain of the 'target of rapamycin' (TOR). The influence of single amino acids on the binding behavior was studied based on a set of mutants. Based on NMR and CD interaction studies the FATC domains of ATM, ATR, DNA-PKcs, SMG-1, and TRRAP may also function as membrane anchors. This may allow a specific and localized signaling output.

# Zusammenfassung

Die Familienmitglieder der Phosphatidylinositol-3 Kinase-verwandten Kinasen (PIKKs), die zelluläre Signalwege in Abhängigkeit von Stress und Nährstoffen kontrollieren, haben die FATC Domäne gemeinsam. Es wurde gezeigt, dass die FATC Domäne eine wichtige Rolle für die Regulierung der PIKKs spielt. NMR und (orientierte) CD Spektroskopie sowie MD Simulationen wurden kombiniert, um die Eintauchtiefe und Orientierung der in Membranen eingetauchten Wildtyp FATC Domäne des "Targets of rapamycin" (TOR) zu untersuchen. Der Einfluss einzelner Aminosäuren auf das Bindungsverhalten wurde anhand eines Sets von Mutanten analysiert. Basierend auf NMR- und CD-Interaktionsstudien könnten die FATC Domänen von ATM, ATR, SMG-1 und TRRAP auch als Membrananker fungieren. Das würde eine spezifische und lokalisierte Signalantwort ermöglichen.

# Contents

<b>1</b>	<b>Biological background</b>	<b>1</b>
1.1	PIKKs . . . . .	1
1.2	TOR . . . . .	2
1.3	DNA-PKcs . . . . .	5
1.4	ATM, ATR, SMG-1 and TRRAP . . . . .	5
1.5	Aim of this thesis . . . . .	7
<b>2</b>	<b>Theory</b>	<b>9</b>
2.1	NMR . . . . .	9
2.1.1	The NMR phenomenon . . . . .	9
2.1.2	Relaxation . . . . .	12
2.1.3	NOE . . . . .	13
2.2	Experimental NMR methods . . . . .	14
2.2.1	Protein NMR . . . . .	14
2.2.2	Chemical shift index . . . . .	14
2.2.3	$^{15}\text{N}$ - $T_1$ , $-T_2$ , $\{^1H\}$ - $^{15}\text{N}$ NOE . . . . .	14
2.2.4	INEPT . . . . .	15
2.2.5	HSQC/HMQC . . . . .	16
2.2.6	NOESY . . . . .	18
2.2.7	HNCA . . . . .	19
2.2.8	HCCH-TOCSY and CCONH-TOCSY . . . . .	21
2.2.9	PGF diffusion measurement . . . . .	23
2.2.10	PRE . . . . .	24
2.3	CD and oriented CD . . . . .	25
2.3.1	CD . . . . .	25
2.3.2	OCD . . . . .	26

<b>3</b>	<b>Materials and Methods</b>	<b>29</b>
3.1	Buffer solutions . . . . .	29
3.2	Cell growth media . . . . .	29
3.3	Expression and purification . . . . .	29
3.4	Membrane mimetics . . . . .	33
3.5	NMR sample preparation . . . . .	33
3.5.1	GB1xa . . . . .	33
3.5.2	DNA-PKcs, ATM, SMG-1, ATR, and TRRAP . . . . .	35
3.5.3	TOR . . . . .	35
3.6	Sample preparation (O)CD . . . . .	36
3.7	CD spectroscopy . . . . .	36
3.8	OCD spectroscopy . . . . .	37
3.9	NMR spectroscopy . . . . .	38
3.10	MD simulations . . . . .	39
<b>4</b>	<b>Results</b>	<b>41</b>
4.1	NMR detection of GB1 fusion proteins . . . . .	41
4.1.1	Spectral appearance of the GB1 tag in the presence of membrane mimetics . . . . .	41
4.1.2	Detection of y1fatc membrane association using GB1 fusions . . . . .	41
4.1.3	Summary and discussion . . . . .	44
4.2	PIKK FATC domains as membrane anchor . . . . .	45
4.2.1	Characteristic features of the amino acid sequences . . . . .	45
4.2.2	Structural characterization of the FATC domain of DNA-PKcs and its interactions with membrane mimetics . . . . .	46
4.2.2.1	NMR interaction studies with membrane mimetics . . . . .	46
4.2.2.2	Secondary structure analysis . . . . .	51
4.2.2.3	Analysis of $^{15}\text{N}$ relaxation data . . . . .	52
4.2.3	NMR and CD characterization of the FATC domains of ATM, SMG-1, TRRAP, and ATR . . . . .	55
4.2.3.1	Membrane mimetic interaction studies . . . . .	55
4.2.3.2	Secondary structure analysis . . . . .	59
4.2.3.3	Analysis of membrane interactions by $^{15}\text{N}$ relaxation and NMR diffusion measurement . . . . .	61
4.2.4	Summary and discussion . . . . .	63
4.3	TOR FATC membrane immersion properties . . . . .	65
4.3.1	Membrane interaction studies with y1fatc and mutant proteins . . . . .	65



---

4.3.1.1	Membrane studies with DPC micelles . . . . .	65
4.3.1.2	Membrane studies with bicelles or liposomes . . . . .	71
4.3.2	NMR experiments with spin labeled micelles . . . . .	76
4.3.3	MD simulations of spin labeled micelles . . . . .	79
4.3.4	Oriented CD spectroscopy of bilayer immersed protein . . . . .	81
4.3.5	Summary and discussion . . . . .	84
<b>5</b>	<b>Conclusion and Outlook</b>	<b>87</b>
	<b>Bibliography</b>	<b>90</b>
<b>A</b>	<b>Appendix</b>	<b>101</b>
A.1	Sequences and parameters . . . . .	101
A.1.1	Primer sequences for site-directed mutagenesis . . . . .	101
A.1.2	Protein sequences . . . . .	101
A.1.3	Protein parameters . . . . .	101
A.2	Protocols . . . . .	108
A.2.1	SDS-PAGE . . . . .	108
A.2.2	RP-HPLC . . . . .	108
A.3	Alignments . . . . .	109
A.4	Secondary structure analysis . . . . .	109
A.5	Membrane immersion model . . . . .	109

# List of Figures

1.1	Domain organization of PIKKs and sequence conservation of their FATC domains	2
1.2	TOR signaling	3
1.3	Sequence conservation of the FATC domain of TOR	4
1.4	Sequence conservation of DNA-PKcs, ATM, ATR, SMG-1, and TRRAP FATC	6
2.1	Energy level diagram and bulk magnetization vector	11
2.2	Relaxation pathways	13
2.3	Pulse sequence of INEPT	15
2.4	Pulse sequence of HSQC	16
2.5	Pulse sequence of SOFAST-HMQC	17
2.6	Correlations in HSQC and NOESY	17
2.7	Pulse sequence and coherence level diagram for 2D NOESY experiment	18
2.8	Pulse sequence for 3D $^1\text{H}$ - $^{15}\text{N}$ NOESY-HSQC experiment	19
2.9	Pulse sequence for HNCA experiment	20
2.10	Correlations in HNCA and HCCH-TOCSY	21
2.11	Pulse sequence of the HCCH-TOCSY experiment	22
2.12	Pulse sequence of the CCONH experiment	22
2.13	Pulse sequences of two PFG-NMR experiments	23
2.14	PRE types	24
2.15	Energy transitions and CD spectra	26
2.16	Schematic OCD spectrum	27
3.1	Chemical structures of lipids and spin labeled fatty acids	34
3.2	Cross-sectional view of the OCD cell	38
4.1	Monitoring of protein membrane mimetic interactions of GB1 fusion proteins	42
4.2	Analysis of the interactions of GB1xa with different membrane mimetics	43
4.3	Distribution of hydrophobicity and charges in the PIKK FATC domains	45

4.4	Membrane interactions of DNA-PKcs FATC with micelles . . . . .	46
4.5	Chemical shift differences of DPC and DicotPA:DOPA titration . . . . .	47
4.6	Interaction of the FATC domain of the fusion protein of DNA-PKcs . . . . .	49
4.7	Assignment of DNA-PKcs FATC and gb1xa . . . . .	50
4.8	CD spectrum of hdnapkfadc . . . . .	51
4.9	$^3J_{HNH\alpha}$ coupling constants of DNA-PKcs FATC . . . . .	51
4.10	$^{13}C^\alpha$ chemical shift analysis of DNA-PKcs FATC . . . . .	52
4.11	Backbone dynamics of the fusion protein of DNA-PKcs FATC . . . . .	53
4.12	Backbone dynamics of DNA-PKcs FATC . . . . .	54
4.13	NMR analysis of the interaction of ATM FATC . . . . .	56
4.14	Interactions of ATM, SMG-1, and TRRAP FATC . . . . .	57
4.15	Membrane association of ATR FATC with DPC micelles . . . . .	58
4.16	$^1H^\alpha$ secondary shifts of ATM FATC . . . . .	59
4.17	$^3J_{HNH\alpha}$ coupling constants of ATM FATC . . . . .	60
4.18	Secondary structure analysis of ATM, SMG-1, and TRRAP FATC . . . . .	60
4.19	Backbone dynamics of ATM FATC . . . . .	61
4.20	Membrane association of TOT FATC wild type and Y2463E/W2466E . . . . .	66
4.21	Association of TOR FATC with DPC micelles . . . . .	67
4.22	Membrane association of untagged mutants of TOR FATC with DPC micelles . .	69
4.23	CD spectra of TOR FATC wild type and mutants . . . . .	71
4.24	Membrane association of tagged mutants of TOR FATC with DPC micelles . . .	72
4.25	Membrane association of mutants of TOR FATC with DMPC/DihpPC bicelles .	73
4.26	Membrane association of mutants of TOR FATC with DMPC liposomes . . . . .	75
4.27	Characterization of TOR FATC using spin labeled DPC micelles . . . . .	77
4.28	Chemical shift analysis of oxidized and reduced micelle-bound TOR FATC . . . .	79
4.29	MD simulation of the spin labeled DPC micelle . . . . .	80
4.30	CD spectra of oxidized and reduced TOR FATC . . . . .	81
4.31	OCD spectra of oxidized and reduced TOR FATC . . . . .	82
4.32	Refined model of the membrane immersion of oxidized and reduced TOR FATC .	83
A.1	The vector pET-21(+) vector . . . . .	102
A.2	RP-HPLC protocol . . . . .	108
A.3	Sequence conservation of the FATC domains . . . . .	110

# List of Tables

2.1	Properties of selected nuclei . . . . .	10
2.2	Protein NMR experiments. . . . .	14
3.1	Buffer compositions . . . . .	30
3.2	PCR sample composition and parameters . . . . .	30
4.1	NOE values of free ATM FATC . . . . .	62
4.2	NOE values of micelle-bound ATM FATC . . . . .	62
4.3	Diffusion measurements of SMG-1 and TRRAP FATCs . . . . .	63
4.4	Membrane association studies with TOR FATC wild type and mutant proteins. . . . .	67
A.1	Mutant versions of y1fatc and the corresponding primers (I) . . . . .	103
A.2	Mutant versions of y1fatc and the corresponding primers (II) . . . . .	104
A.3	Protein sequences . . . . .	105
A.4	Protein sequences PIKKs. . . . .	106
A.5	Protein parameters . . . . .	107
A.6	Secondary structure analysis by CONTIN and CDSSTR . . . . .	111

# Nomenclature

(m)TOR	(mammalian) Target of rapamycin (also known as FRAP, RAFT, RAPT)
ATM	Ataxia telangiectasia mutated
ATR	Ataxia and telangiectasia rad3-related
CD	Circular dichroism
CMC	Critical micelle concentration
CONTIN, CDSSTR	Analysis programs used for secondary structure determination
cryo-EM	Cryo-electron microscopy
dd	double distilled
DihepPC	1,2-Diheptanoyl-sn-glycero-3-phosphocholine
DMPC	1,2-Dimyristoyl-sn-glycero-3-phosphocholine
DNA-PK(cs)	DNA-dependent protein kinase (catalytic subunit)
DOPA	1,2-Dioleoyl-sn-glycero-3-phosphate
DPC	Dodecylphosphocholine
ds	double stranded
FATC	FAT ATM TRRAP C-terminal
FRAP	FKBP-rapamycin-associated protein
GB1	B1 domain of streptococcal protein G
gb1xa/ent	GB1 tag followed by thrombin and factor Xa or enterokinase site
HMQC	Heteronuclear multiple quantum correlation
HSQC	Hetero single quantum coherence
IgG	Immunoglobulin G
INEPT	Insensitive nuclei enhanced by polarization transfer
IPTG	Isopropyl- $\beta$ -D-thiogalactopyranosid
MQ coherence	Multiple quantum coherence

NOESY	Nuclear overhauser effect spectroscopy
NRMSD	Normalized root mean square deviation
OCD	Oriented circular dichroism
P/L	Peptide-lipid-ratio
pET-21(+)	pET <i>E.coli</i> T7 expression vector
PIKK	Phosphatidylinositol-3 kinase-related kinases
PRE	Paramagnetic relaxation enhancement
RAPT	Rapamycin target protein
RH	Relative humidity
RP-HPLC	Reversed phase high pressure liquid chromatography
S/N	Signal to noise ratio
SDS PAGE	Sodium dodecylsulfate polyacrylamide gelelectrophoresis
SMG-1	Suppressor of morphogenesis in genitalia-1
SOFAST-HMQC	Band-selective optimized flip angle short transient - HMQC
SQ coherence	Single quantum coherence
TCEP	Tris-(2-carboxyethyl)-phosphine hydrochloride
TFA	Trifluoroacetic acid
TOCSY	Total correlation spectroscopy
TRRAP	Transformation/transcription domain-associated protein
NMR	Nuclear magnetic resonance
$\delta$	chemical shift (cs), in ppm
<i>A</i>	ampere, SI base unit for the physical quantity of electric current <i>I</i>
<i>kg</i>	kilogram, SI base unit for the physical quantity of mass <i>m</i>
<i>K</i>	Kelvin, SI base unit for the physical quantity of thermodynamic temperature <i>T</i> (293.15 K = 20 °C)
<i>mol</i>	mol, SI base unit for the physical quantity of amount of substance <i>n</i>
<i>m</i>	meter, SI base unit for the physical quantity of length <i>l</i>
<i>ppm</i>	parts per million, a commonly used pseudo unit to describe dimensionless quantities (parts-per notation)
<i>s</i>	second, SI base unit for the physical quantity of time <i>t</i>
<i>T</i>	Tesla, SI derived unit of magnetic field strength or magnetic flux density
<i>u, Da</i>	atomic mass unit ( <i>u</i> ) or dalton ( <i>Da</i> ), 1u equals to one-twelfth of the mass of an atom of carbon ( <sup>12</sup> C) with a value of approximately 1.66 x 10 <sup>-27</sup> kg

# Chapter 1

## Biological background

### 1.1 Phosphatidylinositol-3 kinase-related kinases (PIKKs)

Phosphatidylinositol-3 kinase-related kinases (PIKKs) comprise a family of serine/threonine kinases, which are conserved in evolution and generally possess protein kinase activity. PIKKs have sequence similarity to phosphatidylinositol-3 kinases (PI3Ks), which are in contrast lipid kinases [1]. The members of this family, six known in human beings (TOR, DNA-PKcs, ATM, ATR, SMG-1, TRRAP), and thus regulate various cellular signaling pathways in response to different stresses and nutrient availability [2, 3].

The target of rapamycin (TOR) is the best studied family member and regulates cell growth in response to nutrient and energy supply, as well as to stress conditions [4, 5]. Ataxia-telangiectasia mutated (ATM), ataxia- and Rad3-related (ATR), and DNA-dependent protein kinase catalytic subunit (DNA-PKcs) are involved in the DNA damage response. In particular, DNA-PKcs and ATM respond to DNA double-strand breaks, while ATR respond to DNA replication blocks [6, 7]. Suppressor of morphogenesis in genitalia-1 (SMG-1) plays a role in the nonsense-mediated mRNA decay [2]. Finally, Transformation/transcription domain-associated protein (TRRAP) serves as a scaffold for several histone acetyltransferase complexes and thereby regulates gene transcription [8, 9]. TRRAP is the only member that does not possess kinase activity, but nevertheless has a high sequence similarity with the other PIKKs [8, 2].

All PIKK family members exhibit a similar domain organization illustrated in Fig. 1.1a. The total length of the amino acid sequences varies from about 2500 to 4500 residues [10], however all possess the kinase domain as defining element, whose activity is regulated by the FAT C-terminal (FATC) domain and the PIKK regulatory domain (PRD) [2, 3]. The PRD domain varies in length and sequence composition for different PIKKs [11]. The kinase domain is N-terminally flanked by the FRAP-ATM-FATC (FAT) domain [12]. The FAT domain as well as the preceding N-terminal region are composed of  $\alpha$ -helical repeat motifs mediating protein-protein interactions [13, 14]. The N-terminal HEAT repeat region (so called, because the corresponding repeats are found in Huntingtin, Elongation factor 3,  $\alpha$ -regulatory subunit of protein phosphatase 2A and TOR1) has only low sequence homology when comparing different PIKKs. The very C-terminus of PIKKs corresponds to the FATC domain, which is highly evolutionarily conserved among each family member and consists of about 35 residues (Fig. 1.1b) [1, 12]. The FATC domain occurs in all PIKKs in combination with the FAT domain.

Because of the high degree of conservation, the FATC domain can be substituted among certain PIKK family members while still maintaining kinase function. For example, the FATC domain of ATM can be replaced by DNA-PKcs, ATR, and TRRAP FATC and functionality is retained [15, 2]. However, if ATR or TOR FATC is replaced by ATM FATC, then function is lost [11, 16].

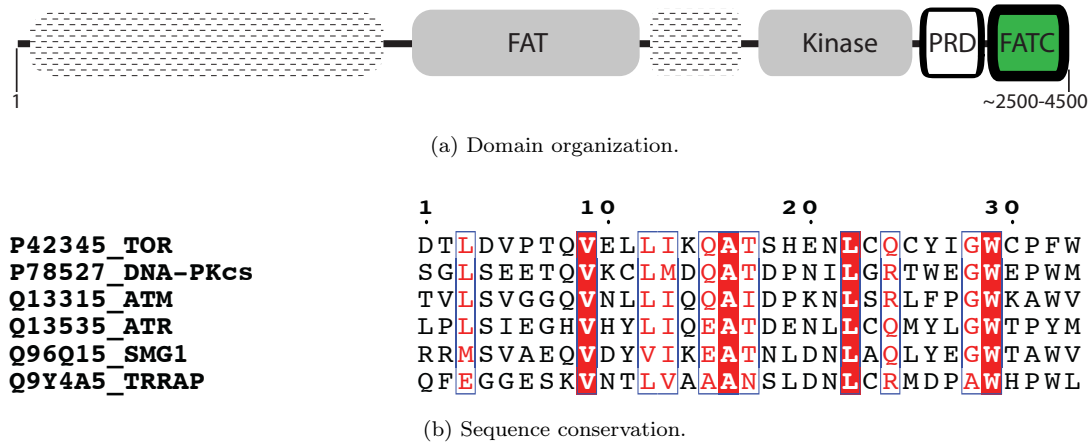


Figure 1.1: Domain organization of PIKKs (a) and sequence conservation of their FATC domains (b). All PIKKs share kinase, FAT, PRD and FATC domain (green). Besides this all contain additional functional regions of variable size that are indicated by the round-cornered patterned rectangles (a). Sequence alignment of the FATC domains of different human PIKKs (b). Sequence alignments were generated using ESPript 2.2 [17].

## 1.2 Target of rapamycin (TOR)

In the 1970s, a bacterial strain called *Streptomyces hygroscopicus*, which produced an antifungal antibiotic, was isolated from a soil sample from Rapa Nui (Easter Island) [18]. This metabolite was found to be a macrocyclic lactone and named rapamycin after the place of discovery. In the following years, several studies showed that rapamycin possesses immunosuppressive properties and inhibits proliferation of mammalian cells [19, 20]. The 'target of rapamycin' (TOR) was first discovered by genetic screening tests while searching for rapamycin resistant proteins in *Saccharomyces cerevisiae* (yeast), which identified TOR1 and TOR2 [21]. It was shown that rapamycin toxicity is mediated by forming an inhibitory complex with the peptidyl-prolyl isomerase FKBP12 (FK506-binding protein of 12 kDa), which binds to a region of TOR termed FRB (FKB12 rapamycin binding) [21, 22, 23]. Mammalian TOR (mTOR) was identified and cloned independently by using an FKBP12-rapamycin affinity purification [24, 25, 26]. Numerous studies over the past years confirmed the importance of TOR signaling in growth and metabolism in response to nutrients and growth factors [4, 27, 28, 29]. Until today, every eukaryote genome examined (such as plants, insects, worms, flies, and mammals) contains at least one TOR gene [30].

The PIKK TOR is a conserved 280 kDa protein kinase involved in the control of cell growth in response to a variety of factors such as nutrients, growth factors, the cellular energy state of the cells and stress such as osmotic stress or hypoxia [5, 31, 4]. TOR is a well known regulator of metabolism and lifespan in organisms with a key role in connecting metabolic stress, aging and cardiovascular diseases [32, 33]. Dysregulation of TOR signaling effects many physiological



functions resulting in neurodegenerative, cognitive, and metabolic diseases (obesity, diabetes) and cancer [33, 34, 35, 36, 37, 38, 39]. Genetic studies of worms, flies and mice have shown that TOR is indispensable for the embryonic development [40, 41, 42, 43]. Further studies have illustrated the role of TOR in neuronal and memory development by stimulating protein synthesis [44, 45, 46] and its function as circadian pacemaker [47].

The mTOR signaling network consists of two major branches, whereby each is regulated by specific TOR complexes (mTORC1 and mTORC2) [48, 49, 50, 51]. Both complexes react differently to the TOR specific inhibitor complex composed of the macrolide rapamycin and the protein FKBP12. TORC1 is sensitive to rapamycin-FKBP12 and regulates temporal aspects of cell growths (mass/size of cells). In contrast, TORC2 is insensitive to rapamycin-FKBP12 and controls spatial aspects of cell growth, such as reorganization of the actin cytoskeleton [52, 4]. Only long term treatment with rapamycin results in dissociation and thereby inhibition of TORC2 activity [53]. Processes mediated by TOR include translation, ribosome synthesis, amino acid transport, transcription of genes, autophagy, and actin organization [29]. An general view of the various pathways is illustrated in Fig. 1.2.

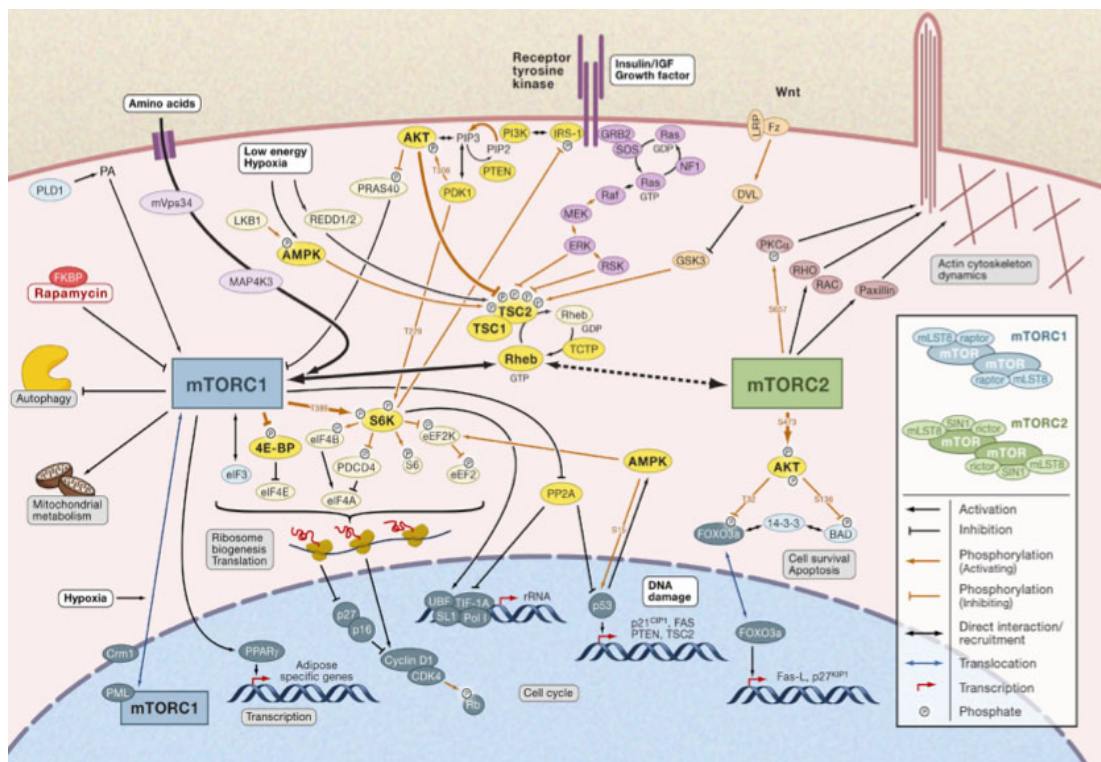


Figure 1.2: The mTOR signaling network consists of two major pathways regulated by mTORC1 or mTORC2 [54].

TOR has been localized at specific plasma membrane regions, at the membranes of lysosomes, the ER, the Golgi and mitochondria, associated with ribosomes and in the nucleus [55, 56, 57, 58, 59, 60, 61, 62, 63]. For what is known, the localization appears to depend on the exact composition of the TOR complexes as well as on the cell type and signaling state and is probably mediated by a whole network of interactions involving protein-protein as well as protein-lipid interactions [64, 65].

In comparison to the numerous studies dealing with the characterization of TOR on the biochemical and cellular level, there is only sparse structural data available. In 1966, a crystal structure of the ternary complex of human FKBP12, rapamycin, and the FRB domain of human TOR (resolution of 2.7 Å) has been solved revealing that rapamycin is sandwiched between the two proteins occupying simultaneously hydrophobic binding pockets in each [23]. Some years later, this structure has been refined (with an optimized resolution of 2.2 Å) [66] and the intermolecular interactions have been characterized using fluorescence polarization and NMR spectroscopy [67]. For the very C-terminal domain, the FATC domain, the structure in solution and bound to membrane mimetics has been characterized suggesting furthermore redox-sensitivity for FATC [68, 69]. For budding yeast TOR1 and a TOR-KOG1 complex an electron microscopy structure has been reconstructed in three dimensions, but only with low resolution (25 Å) [70], as well as a three-dimensional structure of the fully assembled human mTORC1 by cryo-electron microscopy, which revealed that mTORC1 is an obligate dimer with an overall rhomboid shape and a central cavity [71]. Moreover, two models have been built dealing with the catalytic region of TOR and predicting the number and location of structural repeats in the TOR protein [72, 73]. Recently, a crystal structure (3.2 Å) of a mTOR-mLST8 complex containing the FAT, FRB, kinase and FATC domains and the structures of this complex bound to an ATP transition state analogue and ATP-competitive inhibitors, respectively, was presented. The structure reveals an intrinsically active kinase controlled by restricted access [74].

The domain organization of TOR comprises beside the introduced FAT, kinase and FATC domain, the FKBP12-rapamycin-binding (FRB) domain in the C-terminal region, containing the binding site for the TOR inhibitor complex rapamycin-FKBP12. The FATC domain was shown to be indispensable for TOR function [2, 16]. The highly conserved part of the TOR FATC domain consists of 33 amino acids and is rich in hydrophobic and aromatic residues (see Fig. 1.3).

	1	10	20	30																													
<b>P35169_S.cerevisiae1</b>	NE	L	V	P	E	O	V	D	K	L	I	Q	Q	A	T	S	I	E	R	L	C	Q	H	Y	I	G	W	C	P	F	W		
<b>P32600_S.cerevisiae2</b>	ND	L	V	P	E	O	V	D	K	L	I	Q	Q	A	T	S	V	E	N	L	C	Q	H	Y	I	G	W	C	P	F	W		
<b>P42345_H.sapiens</b>	D	T	L	V	P	T	O	V	E	L	L	I	K	Q	A	T	S	H	E	N	L	C	Q	C	Y	I	G	W	C	P	F	W	
<b>H9ENS2_M.mulatta</b>	D	T	L	V	P	T	O	V	E	L	L	I	K	Q	A	T	S	H	E	N	L	C	Q	C	Y	I	G	W	C	P	F	W	
<b>Q9JLN9_M.musculus</b>	D	T	L	V	P	T	O	V	E	L	L	I	K	Q	A	T	S	H	E	N	L	C	Q	C	Y	I	G	W	C	P	F	W	
<b>P42346_R.norvegicus</b>	D	T	L	V	P	T	O	V	E	L	L	I	K	Q	A	T	S	H	E	N	L	C	Q	C	Y	I	G	W	C	P	F	W	
<b>Q9VK45_D.melanogaster</b>	K	S	V	N	E	Q	S	O	V	E	L	L	I	Q	Q	A	T	N	N	E	N	L	C	Q	C	Y	I	G	W	C	P	F	W
<b>Q95Q95_C.elegans</b>	E	P	L	Q	V	T	E	O	L	A	M	L	T	E	Q	A	T	S	P	L	N	L	C	Q	S	Y	I	G	W	C	P	F	W
<b>Q86Q65_D.discoideum</b>	E	T	L	V	P	E	O	V	Q	K	L	I	D	Q	A	T	S	H	E	N	L	C	L	S	Y	V	G	W	C	P	F	W	
<b>Q9FR53_A.thaliana</b>	H	G	L	S	V	K	V	Q	V	Q	K	L	I	N	Q	A	T	S	H	E	N	L	C	Q	N	Y	V	G	W	C	P	F	W

Figure 1.3: Sequence conservation of the FATC domain of TOR illustrated by alignments of the respective sequences from different organisms. Sequence alignments were generated using ESPript 2.2 [17].

An initial NMR structural characterization of the FATC domain of yeast TOR1 (y1fatc) has been shown that the oxidized form consists of an  $\alpha$ -helix that is followed by a hydrophobic disulfide-bonded loop, whose reduction causes an increased flexibility of the C-terminal half. The determined redox potential of the single disulfide bond and additional mutagenesis studies (Cys to Ser) in yeast indicate further that the intracellular redox potential can affect the cellular amount of the TOR protein via the FATC domain [68]. In line with this, it has been shown that TORC1 formation and signaling is redox-sensitive [75, 76, 77].

### 1.3 DNA-dependent protein kinase catalytic subunit (DNA-PKcs)

Exogenous or endogenous influences, such as reactive oxygen species or radiation, can cause DNA double-strand breaks, which can lead to genomic instability, cell death, and increased risk of cancer [78]. There are two distinct pathways for DNA double-strand break repair: Homologous recombination and nonhomologous end joining depending on the state of cell cycle. Nonhomologous end joining is thought to be the predominant pathway in higher eukaryotes and is based on the recognition of DNA termini by the heterodimer Ku protein [79]. The DNA-bound Ku complex recruits and activates a variety of different proteins required for the end joining including DNA-dependent protein kinase catalytic subunit (DNA-PKcs), a member of the aforementioned PIKKs. The recruitment of DNA-PKcs to the double-strand breaks stimulates the kinase activity and causes phosphorylation of various substrates in order to facilitate repair. The heterodimeric Ku protein and the ~470 kDa DNA-dependent protein kinase catalytic subunit are part of a 615 kDa holoenzyme called DNA-dependent protein kinase (DNA-PK) [80]. Loss of either DNA-PKcs or Ku causes increased sensitivity to radiation and incomplete repair of the DNA double-strand breaks [81, 82].

DNA-PKcs has a regulatory role in the repair of DNA strand breaks and shares some phosphorylation targets and activities with ATM [83]. Besides DNA repair, DNA-PKcs is involved in processes around the inflammatory response via NF- $\kappa$ B (nuclear factor kappa-light-chain enhancer) [84] and plays an important role in metabolic gene regulation and the regulation of the homeostasis of cell proliferation [85]. Furthermore, DNA-PKcs has been suggested to play a role in the signaling response to ionizing radiation, which involves phosphorylation of lipid raft proteins [86, 87]. Recently, it has further been shown that treatment of HT-29 cells with cis-9, trans-11-conjugated linoleic acid, substances that can alter the properties of membranes, followed by X-radiation showed delayed double-strand break repair, which correspond with insufficient DNA-PKcs activation [88].

Up to date, several cryo-EM and crystal structures of DNA-PKcs alone or in complex with the Ku70/Ku80 complex have been published [89, 90, 91, 92]. However the localization of different functional domains is due to the low resolution not easily possible. Nevertheless, a comparison of the EM structures of DNA-PKcs alone and in complex with Ku70/Ku80 indicate conformational changes for the FAT and FATC domains [93]. Studies in a mouse model, where the C-terminus of DNA-PKcs is truncated, illustrate that the FATC domain of DNA-PKcs is indispensable for its kinase activity [94, 15, 2]. The sequence conservation of the FATC domain of DNA-PKcs is shown in Fig. 1.4a. As the one of TOR, its C-terminal half is rich in hydrophobic aromatic and aliphatic residues.

### 1.4 The PIKK family members ATM, ATR, SMG-1 and TRRAP

The PIKK family members ATM and ATR are beside DNA-PKcs important for the DNA damage response and signaling in the presence of DNA damages. Both phosphorylate proteins that regulate processes such as DNA repair, cell cycle progression, cellular senescence and apoptosis [2, 6, 95]. DNA repair by ATM is activated the same way as for DNA-PKcs, by the presence of DNA double-strand breaks, whereas ATR responds to a much broader spectrum of DNA damages. This includes double-strand breaks and many types of DNA damage that interfere with DNA replication, such as single stranded DNA gaps or more general to DNA replication blocks and UV-light treatment [95, 7]. Inactive homodimer ATM is recruited to

	1	10	20	30				
P78527_human	S	G	LSEETQVK	LMDQATDPN	ILGR	TW	EGWEPWM	
Q8WN21_horse	S	D	LSEEAQVK	LIDQATDPN	ILGR	TL	VGWEPWM	
Q8WN22_dog	N	G	LSEEAQVK	LIDQATDPN	ILGR	WI	GWEPWM	
P97313_mouse	S	G	LSEETQVK	LVDQATDPN	ILGR	TW	EGWEPWM	
Q8QGX4_chicken	D	R	LSEETQVRC	LIDQATDPN	LGRV	WE	EGWEPWM	
Q9DEI1_frog	D	G	LTEETQVQC	LIDQATDPN	LGRV	WK	GWEPWI	
Q7Q293_fly	G	T	ISTELOT	EMLL	LEMAIDSRL	LGIT	YSGWYPWF	
D0N2S7_oomycete	A	E	LSSLTQAQE	L	LAMATAPDL	LGR	TFOGWM	PWL
Q4LBF0_paramecium	Q	T	LSVIOQVDC	L	IDLATDPN	ILGRA	WK	GWAPFI
Q54UC0_dyctiostelium	V	C	SSVKEQI	DC	LIDQSTDPN	ILSRA	WV	GWNGAL

(a) DNA-PKcs

	1	10	20	30					
Q13315_human	T	V	LSVGGQVNL	L	LIQQA	TDPKNLSR	LF	P	GWKAWV
B3VMJ2_dog	T	V	LSVGGQVNL	L	LIQQA	MDPKNLSR	LF	P	GWKAWV
Q6PQD5_pig	T	V	LSVGGQVNF	L	LIQQA	MDPKNLSK	LF	S	GWKAWV
Q62388_mouse	T	V	LSVGGQVNL	L	LIQQA	MDPKNLSR	LF	P	GWKAWV
D4ACL8_rat	T	V	LSVGGQVNL	L	LIQQA	MDPKNLSR	LF	P	GWKAWV
Q59IS5_zebrafish	T	V	LSVGGQVNL	L	LIQQA	MDPKNLSR	LF	P	GWQAWV
H2MBY9_japanesericefish	A	V	LSVGGQVNL	L	LIQQA	MDPKNLSR	LF	S	GWQAWV

(b) ATM FATC.

	1	10	20	30								
Q13535_human	L	P	LSIEGHVHYLI	Q	EATDEN	LLC	Q	MYLGW	T	P	Y	M
E2QXA4_dog	L	P	LSIEGHVHYLI	Q	EATDEN	LLC	Q	MYLGW	T	P	Y	M
F1SKG2_pig	L	P	LSIEGHVHYLI	Q	EATDEN	LLC	Q	MYLGW	T	P	Y	M
Q9JKK8_mouse	L	P	LSIEGHVHYLI	Q	EATDEN	LLC	Q	MYLGW	T	P	Y	M
D3Z822_rat	L	P	LSIEGHVHYLI	Q	EATDEN	LLC	Q	MYLGW	T	P	Y	M
F1R6S9_zebrafish	L	P	LSIEGHVHYLI	Q	EATD	DNLLC	M	MYLGW	G	P	Y	L
H2M9Q9_japanesericefish	L	P	LSIEGHVHYLI	Q	EATDE	KLLC	Q	MYLGW	G	P	Y	L

(c) ATR FATC.

	1	10	20	30																													
Q96Q15_human	R	R	M	S	V	A	E	Q	V	D	Y	V	I	K	E	A	T	N	L	D	N	L	A	Q	L	Y	E	G	W	T	A	W	V
F1PBU5_dog	R	R	M	S	V	A	E	Q	V	D	Y	V	I	K	E	A	T	N	L	D	N	L	A	Q	L	Y	E	G	W	T	A	W	V
F1MBL6_pig	R	R	M	S	V	A	E	Q	V	D	Y	V	I	K	E	A	T	N	L	D	N	L	A	Q	L	Y	E	G	W	T	A	W	V
Q8BXX6_mouse	R	R	M	S	V	A	E	Q	V	D	Y	V	I	K	E	A	T	N	L	D	N	L	A	Q	L	Y	E	G	W	T	A	W	V
G3IKE4_chinesehmaster	R	R	M	S	V	A	E	Q	V	D	Y	V	I	K	E	A	T	N	L	D	N	L	A	Q	L	Y	E	G	W	T	A	W	V
C5J7W8_zebrafish	R	R	M	S	V	T	E	Q	V	D	Y	V	I	K	E	A	T	N	V	D	N	L	A	Q	L	Y	E	G	W	T	A	W	V
K1QQ53_oyster	K	R	F	S	V	A	E	Q	V	E	F	V	I	K	E	A	R	N	L	D	N	L	S	V	L	Y	E	G	W	T	P	W	V

(d) SMG-1 FATC.

	1	10	20	30																													
Q9Y4A5_human	Q	F	E	G	G	E	S	K	V	N	T	L	V	A	A	A	N	S	L	D	N	L	C	R	M	D	P	A	W	H	P	W	L
E2RJS8_dog	Q	F	E	G	G	E	S	K	V	N	T	L	V	A	A	A	N	S	L	D	N	L	C	R	M	D	P	A	W	H	P	W	L
E1BKJ5_pig	Q	F	E	G	G	E	S	K	V	N	T	L	V	A	A	A	N	S	L	D	N	L	C	R	M	D	P	A	W	H	P	W	L
E9PWT1_mouse	Q	F	D	G	G	E	S	K	V	N	T	L	V	A	A	A	N	S	L	D	N	L	C	R	M	D	P	A	W	H	P	W	L
D3ZGS2_rat	Q	F	D	G	G	E	S	K	V	N	T	L	V	A	A	A	N	S	L	D	N	L	C	R	M	D	P	A	W	H	P	W	L
H2V1S0_fugu	Q	F	E	G	G	E	S	K	V	N	T	L	V	A	A	A	N	S	L	D	N	L	C	R	M	D	P	A	W	H	P	W	L
C5NN12_japanesericefish	Q	F	E	G	G	E	S	K	V	N	T	L	V	A	A	A	N	S	L	D	N	L	C	R	M	D	P	A	W	H	P	W	L

(e) TRRAP FATC.

Figure 1.4: Sequence conservation of the FATC domains of DNA-PKcs (a) ATM (b), ATR (c), SMG-1 (d), and TRRAP (e) illustrated by alignments of the respective sequences from different organisms. Sequence alignments were generated using ESPrnt 2.2 [17].

DNA double-strand breaks by a multisubunit complex. The association of ATM and this complex at the DNA results in autophosphorylation, which converts the inactive dimer in the active monomer [96]. Furthermore, ATM plays a role in the oxidative stress response and is part of the redox-sensing system by linking genome stability and carbon metabolism [6, 97]. Beside the localization in the nucleus, it was also found at cytoplasmic vesicles [98]. For CKIP-1, a protein involved in muscle differentiation and the regulation of the actin cytoskeleton, it has been shown that the recruitment of ATM to the plasma membrane is mediated by the C-terminal region (the kinase domain and the FATC domain) [99]. ATR has a crucial role in stabilizing the genome during DNA replication and is also essential for cell survival [100]. Based on the known putative substrates, ATR may be involved in a broad spectrum of cellular processes that go well beyond DNA replication and repair [95].

The PIKK SMG-1 is besides the regulation of nonsense-mediated mRNA decay involved in cell survival during TNF $\alpha$ -induced stress, the genotoxic cell response, oxidative stress resistance [101, 102, 103], and acts as a negative regulator of HIF-1 $\alpha$  (hypoxia-inducible factor-1 $\alpha$ ) [104].

The PIKK TRRAP is supposed to be a central regulator in cellular processes (cell cycle progression, checkpoint control) through recruitment of histone acetyltransferase complexes [105]. Downregulation of TRRAP may be a critical step guiding transcriptional reprogramming and differentiation of embryonic stem cells (ESC), since failure to downregulation prevents differentiation of ESC [106]. Fig. 1.4 shows the FATC domains of ATM, ATR, SMG-1, and TRRAP, which are highly evolutionarily conserved among each family member and shown to play an important role for the regulation of their function [2, 15, 102, 107, 108] (see appendix Fig. A.3 for further details). All are similarly rich in aromatic and aliphatic hydrophobic residues.

## 1.5 Aim of this thesis

Early, it was recognized that PIKKs share a unique conserved C-terminal domain, the FATC domain, that plays an important role in the regulation of their function [1, 12]. This was confirmed for several family members based on mutagenesis studies [102, 16, 107, 15]. Moreover, the FATC domains of some PIKKs appear to be functionally equivalent, at least with respect to some interactions [2]. Although, it has been shown that some FATC domains mediate protein-protein interactions [15, 108, 109], the question remained as to whether there is a further more general common property of the FATC domains that influences PIKK function. For TOR, which is localized at different cellular membranes and the nucleus [55, 56, 57, 60], NMR binding studies with different membrane mimetics have shown that the FATC domain acts as a membrane anchor [69]. For PIKKs involved in DNA repair, such as ATM, ATR and DNA-PKcs, a predominant localization in the nucleus is expected, however for ATM and DNA-PKcs additional functions as well as membrane localization have already been suggested in several publications [85, 86, 6, 97]. The PIKK SMG-1 is supposed to have a further function in the oxidative stress response and lifespan regulation and a subpopulation of hSMG-1 molecules is found to be localized to mitochondria [101, 103].

An analysis of the FATC domains of the known PIKKs shows that they are rather hydrophobic and particularly rich in aromatic residues (Fig. 1.1b) and thus may also interact with lipids and membranes as shown for TOR FATC. To confirm this assumption, the membrane association of the five other FATC domains with different membrane mimetics was studied by means of NMR, CD and PFG-diffusion measurement. Moreover, the structure of the FATC domain of DNA-PKcs and ATM was investigated more precisely based on multi-dimensional NMR structural and relaxation data.

Another aim of this thesis is to provide a better understanding of the membrane association of the TOR FATC domain. Based on earlier NMR binding studies, the FATC domain can interact with different membrane mimetics, such as differently composed neutral and negatively charged micelles and neutral bicelles [69]. The three-dimensional structures of the micelle-immersed oxidized and reduced forms of *y1fatc* are similar to that of the free oxidized state, whereby the  $\alpha$ -helix of the micelle-immersed states extends more to the C-terminus and is slightly distorted around residue A2453, which is presumably at the interface between the micelle and the solvent [69]. Although not restricted by a disulfide bond, the C-terminus of the reduced micelle-immersed state folds also back to the  $\alpha$ -helix. Based on an estimate for the dissociation constant ( $K_d$ ) from the NMR diffusion data, the oxidized form has a slightly higher affinity for dodecylphosphocholine (DPC) micelles than the reduced form [69]. A model of the membrane-binding of *y1fatc* suggests that the C-terminal hydrophobic bulb-like region of the FATC membrane anchor of both is embedded in the micelle making contact to the hydrophobic fatty acid tails, while a rim of charged residues can interact with the positively and negatively charged parts of the headgroups [69]. First mutagenesis data targeted the two tryptophans W2466 and W2470, since tryptophans play often an important role for the interaction between membranes and proteins. However, replacement of one or both tryptophans by alanine did not abrogate the interaction with DPC micelles, suggesting that the other hydrophobic aromatic and aliphatic residues in the membrane anchor contribute also significantly to the affinity for membrane mimetics [69].

For a better understanding of the influence of single residues in the *y1fatc* membrane anchor on the interaction with different membrane mimetics, a set of mutants was studied by means of NMR spectroscopy. Furthermore, the immersion depth was analyzed in more detail based on interaction studies with spin labeled micelles and complementary MD simulations. The tilt angle of the single  $\alpha$ -helix with respect to the bilayer was estimated from OCD measurements.

## Chapter 2

# Theory - Physical basics of the applied methods

This chapter illustrates some basic ideas and selected concepts of modern nuclear magnetic resonance (NMR) spectroscopy, which were used for the work described in this thesis. For a more comprehensive understanding of the physical principles of NMR, the reader is referred to the literature [110, 111, 112, 113].

### 2.1 Nuclear magnetic resonance (NMR)

#### 2.1.1 The NMR phenomenon

The basis of nuclear magnetic resonance is the reorientation of nuclear spins in an applied magnetic field  $B_0$ . Based on the composition of neutrons and protons, nuclei may have an intrinsic angular momentum  $\vec{I}$ , known as spin, depending on their spin quantum number  $I$  ( $I = 0, \frac{1}{2}, 1, \frac{3}{2}, 2, \dots$ ). Nuclei commonly used in biomolecular NMR spectroscopy are  $^1\text{H}$ ,  $^{13}\text{C}$ ,  $^{15}\text{N}$ ,  $^{19}\text{F}$ ,  $^{31}\text{P}$  (with  $I = \frac{1}{2}$ ) and  $^2\text{H}$ ,  $^{14}\text{N}$  (with  $I = 1$ ), respectively. The magnitude of the spin angular momentum is given according to:

$$|\vec{I}^2| = \hbar^2 [I(I+1)] \quad (2.1)$$

with  $\hbar = \frac{h}{2\pi}$  and  $h$  being Planck's constant. In the presence of a magnetic field, a nuclear spin has  $2I + 1$  possible energy levels. By convention, the  $z$  component of  $\vec{I}$  is quantized as:

$$I_z = \hbar m \quad (2.2)$$

described by the magnetic quantum number,  $m = \{-I, -I+1, \dots, I-1, I\}$ . The angular momentum of a spin  $I = \frac{1}{2}$  such as in  $^1\text{H}$  and  $^{13}\text{C}$  can thus occupy two permitted orientations ( $I_z = +\frac{1}{2}\hbar, -\frac{1}{2}\hbar$ ), which are termed the  $\alpha$ - and  $\beta$ -state; where  $\alpha$  is 'spin up' ( $m = +\frac{1}{2}$ ) and  $\beta$  is 'spin down' ( $m = -\frac{1}{2}$ ). In the absence of an external field, these states have the same energy (degenerate) and  $\vec{I}$  does not have a preferred orientation.

The magnetic moment  $\mu$  is collinear with  $\vec{I}$  and is given by:

$$\vec{\mu} = \gamma \vec{I}; \quad \mu_z = \gamma I_z = \gamma \hbar m \quad (2.3)$$

where  $\gamma$  is the gyromagnetic ratio, a characteristic constant for a given nucleus. Tab. 2.1 summarizes relevant nuclei and their properties.

Table 2.1: Properties of selected nuclei.

nuclei	spin	natural abundance [%]	$\gamma [\text{rad s}^{-1} T^{-1}] (\times 10^7)$
$^1\text{H}$	$\frac{1}{2}$	99.98	26.75
$^2\text{H}$	1	0.02	4.11
$^{13}\text{C}$	$\frac{1}{2}$	1.11	6.73
$^{14}\text{N}$	1	99.63	1.93
$^{15}\text{N}$	$\frac{1}{2}$	0.37	-2.71
$^{19}\text{F}$	$\frac{1}{2}$	100.00	25.18
$^{31}\text{P}$	$\frac{1}{2}$	100.00	10.84

The spin states in the presence of an external magnetic field  $\vec{B}$ , which is per definition directed along the  $z$  axis ( $\vec{B}_0$ ), possess energy, which emerge by the interaction between  $\vec{B}_0$  and the magnetic moment  $\mu_z$  (projection of  $\mu$  onto  $\vec{B}_0$ ), and is described by:

$$E = -\gamma I_z \vec{B}_0 = -m \hbar \gamma \vec{B}_0 \quad (2.4)$$

The stronger the magnetic field and the larger  $\gamma$ , the greater the differences  $\Delta E$  between the energy levels (Fig. 2.1a). At equilibrium, the energy states  $\alpha$  and  $\beta$  are unequally populated (with the lower one being more probable) and the population ratio is given by the Boltzmann equation:

$$\frac{N_\beta}{N_\alpha} = e^{-\Delta E/kT} \quad (2.5)$$

where  $N_\alpha$  and  $N_\beta$  are the populations of the ground ( $\alpha$ ) and excited state ( $\beta$ ),  $T$  is the absolute temperature, and  $k$  is the Boltzmann constant. The population difference between the  $\alpha$ - and  $\beta$ -state is in the order of  $10^5$  for  $^1\text{H}$  spins for  $B_0 = 11.7T$ . The energy difference between these two states (also known as Zeeman states), is according to the selection rule for spin  $\frac{1}{2}$  nuclei  $\Delta m = \pm 1$  and thus the photon energy  $h\nu$  needed for the transition is

$$\Delta E = h\nu = \hbar\omega = \hbar\gamma \vec{B}_0 \quad (2.6)$$

and therefore proportional to  $\mu$  and  $\vec{B}_0$ . Since the population difference is very small, NMR is compared to other techniques such as UV/VIS spectroscopy, a rather insensitive method. This limitation is overcome by the usage of high magnetic field strengths  $\vec{B}_0$  which increase the difference between the ground and the excited state.



Based on these conditions (Eq. 2.6), the required frequency for matching the difference between the spin states  $\Delta E$ , by an appropriate radio frequency pulse (*rf*), is given by:

$$\omega_{rf} = \omega = \frac{\Delta E}{h\nu} = \gamma \vec{B}_0 \quad \text{or} \quad \nu_0 = \frac{\gamma \vec{B}_0}{2\pi} \quad (2.7)$$

with  $\omega_{rf}$  as pulse radio frequency and  $\omega$  as Lamor (nuclear resonance) frequency. Thus, nuclei precess around  $\vec{B}_0$  with their Lamor frequency at thermal equilibrium. Due to the higher population of the  $\alpha$ -state, one expects a net magnetization  $\vec{M}_0$  parallel to the field  $\vec{B}_0$  (Fig. 2.1b). All contributing spins possess components in the  $xy$  plane, which however cancel out.

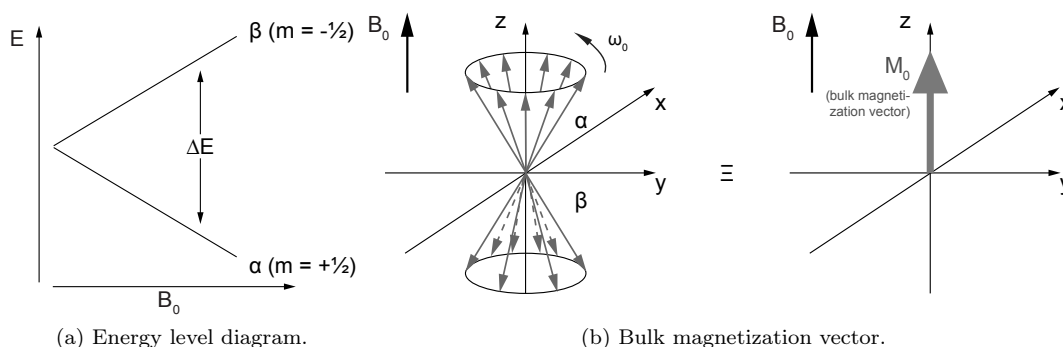


Figure 2.1: NMR energy level diagram and bulk magnetization vector. Schematic illustration of the increase in energy level difference for nuclear spins as the magnetic field is increased. The difference of spin quantum number between the Zeeman states is for spin  $\frac{1}{2}$  nuclei  $\Delta m = \pm 1$  (a). Following an *rf* pulse along  $x$  (or  $y$ ), the bulk magnetization (b) is tilted away from the  $z$  towards the  $xy$  plane and precesses in the  $xy$  plane around the static magnetic field  $\vec{B}_0$  with a Lamor frequency  $\omega_0$ .

The chemical shift is a specific property of a nuclear spin, whose origin is the motion of the surrounding electrons inducing a local magnetic field, defined by:

$$\omega = \gamma(1 - \sigma) \vec{B}_0 \quad (2.8)$$

in which  $\sigma$  is the average isotropic shielding constant. Variations in the local chemical environment cause slight modifications in the resonance frequencies. Since resonance frequencies are directly proportional to  $\vec{B}_0$ , the difference in chemical shift between two resonance signals measured in frequency units scales with  $\vec{B}_0$ . To obtain a field-independent parameter, the resonance frequencies are transformed into chemical shifts, defined as  $\delta$  in *ppm*, using the following equation:

$$\delta = \frac{\Omega - \Omega_{ref}}{\omega_0} \times 10^6 = (\sigma_{ref} - \sigma) \times 10^6 \quad (2.9)$$

in which  $\Omega$  and  $\Omega_{ref}$  are the offset frequencies of the signal of interest and a reference signal (e.g. TSP, DSS) [111, 110, 112].

### 2.1.2 Relaxation

NMR uses an oscillating magnetic field to excite nuclei in an external magnetic field to detect the precession of the magnetization vector. The commonly used pulses  $\frac{\pi}{2}$  (90°) and  $\pi$  (180°) rotate the magnetization from the equilibrium in the  $xy$  plane (transverse plane) and invert the magnetization from  $z$  to  $-z$ , respectively. Equilibrium is hereby the state in which the populations of the energy levels fulfill the Boltzmann distribution and no coherence is present. Immediately after a  $rf$  pulse is switched off, the system tries to return to equilibrium state by a process called relaxation: The spin-lattice or longitudinal relaxation describes the recovery of the populations according to the Boltzmann equation. The spin-spin or transverse relaxation characterizes the decay of spin coherence. The longitudinal and transverse relaxation rate are named  $R_1$  and  $R_2$  and their corresponding time constants are  $T_1$  and  $T_2$ . The following equations describe the return to  $z$  and the dephasing in the  $xy$  plane:

$$M_z(t) = M_0 + e^{-t/T_1} [M_z(0) - M_0] \quad (2.10)$$

$$M_x(t) = M_0 \exp(-t/T_2) \sin(\Omega t) \quad (2.11)$$

$$M_y(t) = M_0 \exp(-t/T_2) \cos(\Omega t) \quad (2.12)$$

The reason for nuclear spin relaxation is the coupling of the spin system to the environment, historically termed the lattice, and the interaction of spins with another. Random motions, especially rotations caused by thermal agitation and collisions modify the local magnetic field around the nuclei. Besides rotational reorientation, internal dynamics of atoms or molecular groups, and paramagnetic species contribute to relaxation. If the 'motion-generated' fluctuating fields around the nucleus contain frequency components fulfilling the resonance condition (Eq. 3.7), transitions are induced. A transition of the spin system from higher energy to lower energy is more probable because the lattice is in equilibrium with a larger populated  $\alpha$ -state. For isotropic rotational diffusion, the probability of a motional fluctuation field providing a particular frequency is described by the spectral density function  $J(\omega)$ , which represents the strength of the fluctuating field:

$$J(\omega) = \frac{2}{5} \frac{\tau_c}{(1 + \omega^2 \tau_c^2)} \quad (2.13)$$

in which the rotational correlation time  $\tau_c$ , is approximately the average time for the molecule to rotate by one radian. It varies due to molecular size, solvent viscosity, and temperature, and is for globular proteins described by Stokes' law according to:

$$\tau_c = \frac{4\pi\eta_w r_H^3}{3kT} \quad \text{with} \quad r_H = \frac{3VM_r}{4\pi N_A} + r_w \quad (2.14)$$

where  $\eta_w$  is the viscosity of the solvent at temperature  $T$ ,  $r_H$  the effective hydrodynamic radius of the protein, and  $k$  is the Boltzmann constant. The hydrodynamic radius itself can be roughly estimated from the molecular mass  $M_R$ , the Avogadro constant  $N_A$ , and the hydration layer radius  $r_w$  (1.6 - 3.2 Å) surrounding the protein. For proteins with molecular weights up to about 30 kDa,  $\tau_c$  is commonly estimated from the ratios of  $^{15}\text{N}$ - $T_1$  and  $T_2$  relaxation rates. Typical correlation times at room temperature in aqueous solutions are in the range of 5 - 20 ns [114].

As a general rule of thumb, the  $\tau_c$  of a monomeric protein in solution in ns is approximately 0.6 times its molecular mass  $M_R$  (in kDa). The linewidth of NMR signals is proportional to  $\tau_c$ , which is proportional to the molecular mass  $M_R$ . Hence, larger molecules have broader lines in the NMR spectrum [111, 110, 112].

### 2.1.3 The nuclear Overhauser effect (NOE)

The nuclear Overhauser effect (NOE) is the change in intensity of an NMR resonance when the transition of another resonance is saturated by a weak *rf* pulse thus eliminating the population difference across the transitions. The basis of the NOE is the coupled relaxation of the longitudinal magnetization of dipolar coupled nuclei ( $I_z$  and  $S_z$ ). Hence, the NOE is a measure of the magnetization transfer from one nucleus to another and is defined by the cross relaxation rate constant  $\sigma$  or the NOE factor  $\eta$ :

$$\eta = \frac{\sigma}{\rho_I} \frac{\gamma_S}{\gamma_I} \quad (2.15)$$

where  $\rho_I$  represents the longitudinal relaxation rate of spin  $I$ .

Figure 2.2 shows the energy levels for a two-spin system with the transitions being frequency labeled. The transition probabilities for transitions between the energy levels ( $\alpha\alpha$ ,  $\alpha\beta$ ,  $\beta\alpha$ ,  $\beta\beta$ ) are denoted by  $W_0$ ,  $W_I$ ,  $W_S$ , and  $W_2$ .  $W_0$  and  $W_2$  are only of relevance if the spins couple.  $W_{1I}$  and  $W_{1S}$  correspond to the longitudinal relaxation rate. For each particular transition the appropriate motional fluctuating field has to provide the Larmor frequency of spin  $I$ ,  $S$  and the sum or difference of spin  $I$  and  $S$ , respectively.

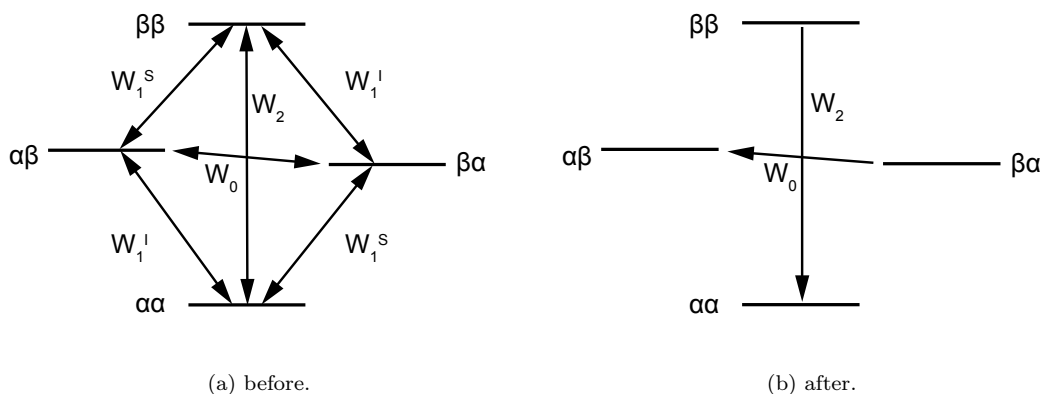


Figure 2.2: Relaxation pathways before (a) and immediately after (b) saturation of the  $S$  transition (adapted from [112]).

The cross-relaxation rate constant is nonzero only if  $W_2 - W_0 \neq 0$ . Therefore the relaxation mechanism has to generate nonzero rate constants for zero-quantum ( $W_0$ ) and double-quantum ( $W_2$ ) transitions to detect NOE. If  $W_0$  is the dominant relaxation pathway, saturating  $S$  decreases the intensity of  $I$  (negative NOE), while if  $W_2$  is the dominant pathway, saturating  $S$  increases the intensity of  $I$  (positive NOE).

## 2.2 Experimental NMR methods

### 2.2.1 Protein NMR

NMR spectroscopy provides three types of information useful for spectral assignments: Through-bond interactions (via scalar coupling), through-space interactions (via dipolar coupling), and the chemical environment (via the chemical shift). Tab. 2.2 summarizes some experiments (including the chemical shift index) that can be used for assignment and structure analysis.

Table 2.2: Protein NMR experiments.

Chemical shift index	secondary structure
Fingerprints	2D $^{15}\text{N}$ HSQC, 2D $^{13}\text{C}$ HSQC
Sequential assignment	3D HNCA ( $^{15}\text{N}$ -edited NOESY)
Side chain assignment	3D HCCH- and CCONH-TOCSY
Distance restraints	$^{15}\text{N}$ - and $^{13}\text{C}$ -edited NOESY
Dynamic information (backbone)	$^{15}\text{N}$ $T_1$ , $-T_2$ , and $\{^1H\}$ - $^{15}\text{N}$ NOE
Stereo specific assignments, dihedral angle information for backbone $\varphi$ and side chain $\chi_1$ *	3D HACAHB-COSY, 3D HNHB, etc.

\* not used in the context of this work.

### 2.2.2 Chemical shift index

Observed chemical shifts in proteins are commonly partitioned into the sum of two components: the random coil chemical shifts,  $\delta_{rc}$ , and the conformation dependent secondary chemical shifts,  $\Delta\delta$ . The random coil chemical shift of a nucleus in an amino acid residue is the chemical shift that is observed in a peptide, which is free to access all sterically allowed regions of its conformational space. The secondary chemical shift contains the contribution from secondary and tertiary structure, which display characteristic patterns for secondary structure elements.

The  $^1\text{H}$  resonances can be categorized on the basis of their chemical shifts: The backbone amide protons,  $^1\text{H}^N$ , resonate between 10.0 and 7.0 ppm, the backbone  $\alpha$  protons,  $^1\text{H}^\alpha$ , between 6.0 and 3.5 ppm, aliphatic side chain protons between 3.5 and 1.0 ppm, and methyl protons resonate at chemical shifts  $<1.5$  ppm. Information on amino acid type can be obtained from the  $^{13}\text{C}$  chemical shift data of e.g. the HNCA combined with side chain experiments (3D HCCH- and CCONH-TOCSY). Random coil chemical shifts of  $^1\text{H}$ ,  $^{13}\text{C}$ , and  $^{15}\text{N}$  for the 20 common amino acids, including the 'nearest-neighbor' effects, can be found in several studies [115, 116].

### 2.2.3 $^{15}\text{N}$ - $T_1$ , $-T_2$ , $\{^1H\}$ - $^{15}\text{N}$ NOE

NMR relaxation experiments such as  $^{15}\text{N}$ - $T_1$ ,  $^{15}\text{N}$ - $T_2$  relaxation times and  $\{^1H\}$ - $^{15}\text{N}$  NOE provide valuable information on reorientational global and local dynamics in the picosecond to nanosecond time scale [117]. For biological macromolecules in solution,  $T_2$  values are in the range of tens of milliseconds and  $T_1$  values are in the order of seconds. The transverse relaxation time  $T_2$  is inversely proportional to the correlation time  $\tau_c$ . The longitudinal relaxation time  $T_1$  increases for short and very long  $\tau_c$  and goes through a minimum at  $\frac{1}{\omega_0}$ .

The value of the  $\{^1H\}$ - $^{15}N$  NOE is determined by measuring two spectra, one with the  $S$  spin saturated for a period of time sufficient to establish the NOE enhancement of the  $I$  spin and the other with the  $S$  spin not saturated. The value depends on  $\gamma$  of the respective nuclei (for  $^{15}N$  negative) and the tumbling of the molecule.

### 2.2.4 Insensitive nuclei enhancement polarization transfer (INEPT)

Most protein experiments start by excitation of  $^1H$  magnetization, because of the high natural abundance of the  $^1H$  nucleus and its great sensitivity due to its large gyromagnetic ratio. After transferring  $^1H$  magnetization to the less sensitive  $X$  nucleus (i.e.  $^{15}N$  or  $^{13}C$ ) and allowing the spins to evolve due to the particular pulse sequence, the magnetization is finally transferred back to  $^1H$  for detection (out-and-back experiment). The transfer is often done by using the insensitive nuclei enhancement polarization transfer (INEPT) (Fig. 2.3).

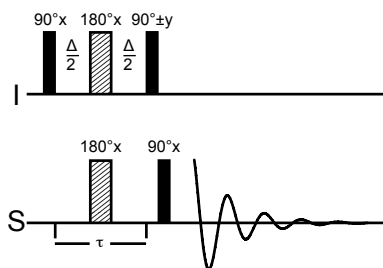


Figure 2.3: Pulse sequence of the INEPT. Filled black rectangles represent  $90^\circ$  pulses and diagonal patterned rectangles represents  $180^\circ$  pulses (adapted from [111]).

Magnetization of nuclei is denoted by different capital letters and the indices (X, Y, Z) indicate the orientation of the magnetization vector. In a Cartesian coordinate system, for a single spin-half, the x-, y- and z components of the magnetization are represented by the spin angular momentum operators  $I_x$ ,  $I_y$ ,  $I_z$  respectively. A vector along the z axis,  $I_z$ , represents polarization (population difference between the  $\alpha$  and  $\beta$  spin states) and a vector within the  $xy$  plane,  $I_x$  and  $I_y$ , represents single-quantum coherence.

Starting from the equilibrium magnetization ( $I_z$ ) the first  $90^\circ$  pulse generates transverse magnetization

$$I_z + S_z \longrightarrow -I_y + S_z \quad (2.16)$$

Evolution during the period of free precession  $\tau$  and the  $180^\circ$  pulses refocusing the chemical shifts cause the following transformation for the spins:

$$-I_y + S_z \xrightarrow{\pi I_x} \xrightarrow{\pi S_x} \xrightarrow{\pi J_{IS}\tau 2I_z S_z} I_y \cos \pi J_{IS}\tau - 2I_x S_z \sin \pi J_{IS}\tau - S_z \quad (2.17)$$

The chemical shift evolution during period  $\tau$  is removed by the  $180^\circ$   $I$  spin pulse and the  $S$  spin label is inverted by the  $180^\circ$   $S$  spin pulse, thereby enabling the precession of the  $I$  spin vector. The following  $90^\circ$  pulse on the  $I$  spin, with alternating phase  $\pm y$ , gives:

$$I_y \cos \pi J_{IS}\tau - 2I_x S_z \sin \pi J_{IS}\tau - S_z \xrightarrow{\pi I_y} I_y \cos \pi J_{IS}\tau \pm 2I_x S_z \sin \pi J_{IS}\tau - S_z \quad (2.18)$$

and the final  $90^\circ$  pulse on the  $S$  spin results in:

$$I_y \cos \pi J_{IS} \tau \pm 2I_z S_z \sin \pi J_{IS} \tau - S_z \xrightarrow{\pi S_x} I_y \cos \pi J_{IS} \tau \mp 2I_z S_y \sin \pi J_{IS} \tau + S_y \quad (2.19)$$

After subtraction of the two experiments with alternating phase, the only term left is:

$$-2I_z S_y \sin \pi J_{IS} \tau \quad (2.20)$$

Setting the delay  $\tau = \frac{1}{2J_{IS}}$  (thereby  $\frac{\Delta}{2} = \frac{1}{4J_{IS}}$ ), then  $\sin \pi J_{IS} \tau = 1$ , and the pure anti-phase term  $-2I_z S_y$  evolves during detection [112]. The chemical shift Hamiltonian of the  $I$  and the  $S$  spin is refocused.

The INEPT and variation of this pulse sequences are a crucial part of one of the most useful and simplest heteronuclear two-dimensional experiment, the  $^1\text{H}$ - $^{15}\text{N}$  HSQC.

### 2.2.5 Hetero Single/Multiple Quantum Coherence (HSQC/HMQC)

Generally, indirect or proton detection is used for heteronuclear correlation NMR experiments in order to increase the sensitivity. In the HSQC experiment (Fig. 2.4, 2.6a) the transferred coherence evolves during an indirect evolution period ( $t_1$ ) as the heteronuclear single quantum coherence (HSQC) [118]. The resulting spectrum is two-dimensional with one axis for  $^1\text{H}$  and the other for a heteronucleus, most often  $^{15}\text{N}$  or  $^{13}\text{C}$ . It provides a fingerprint of the protein, because each amide group or aliphatic carbon represents one single cross peak.

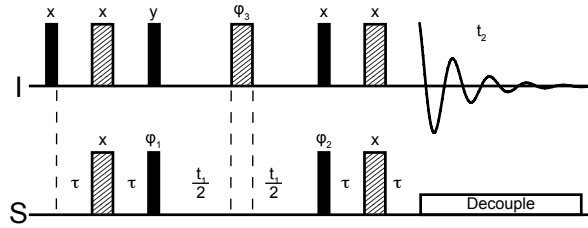


Figure 2.4: Pulse sequence of the HSQC experiment, in which the phase cycling is  $\varphi_1 = x, -x$ ;  $\varphi_2 = 2(x), 2(-x)$ ;  $\varphi_3 = 4(y), 4(-y)$  and the receiver =  $2(x, -x, -x, x)$ . (adapted from [110]).

The HSQC employs two INEPT types transfers, one the one hand to transfer  $I$  spin magnetization into anti-phase  $S$  spin coherence (single quantum, heteronuclear) and on the other hand to transfer the evolved transverse  $S$  spin coherence back to observable  $^1\text{H}$  magnetization for detection. Evolution in terms of product operators is described as follows:

$$I_z \xrightarrow{\frac{\pi}{2} I_x - \tau - \pi I_x, \pi S_x - \tau - \frac{\pi}{2} I_y, \frac{\pi}{2} S_x} -2I_z S_y \quad (\text{after INEPT}) \quad (2.21)$$

$$\xrightarrow{\frac{t_1}{2} - \pi I_x - \frac{t_1}{2}} 2I_z S_y \cos \omega_s t_1 - 2I_z S_x \sin \omega_s t_1 \quad (\text{after } t_1) \quad (2.22)$$

$$\xrightarrow{\frac{\pi}{2} I_x, \frac{\pi}{2} S_x - \tau - \pi I_x, \pi S_x - \tau} -I_x \cos \omega_s t_1 - 2I_y S_x \sin \omega_s t_1 \quad (\text{after reverse INEPT}) \quad (2.23)$$

with the delay  $\tau = \frac{1}{4J_{IS}}$ . The term  $I_y S_x$  is unobservable multiple quantum coherence and is thereby neglected, only the pure absorptive term  $-I_x \cos \omega_s t_1$  is observed. The  $180^\circ I$  pulse in the middle of evolution refocuses the heteronuclear  $J_{IS}$  coupling [110, 112].

The recently introduced SOFAST-HMQC experiment (Fig. 2.5) is an alternative technique for fast acquisition of two-dimensional heteronuclear correlation spectra, which provides the required high sensitivity and enables real-time site-resolved NMR studies on a time scale of seconds. The pulse sequence is optimized for longitudinal relaxation, which allows to use very short interscan delays ( $t_{rec}$ ) and thus fast data acquisition. The advantage of HMQC-type coherence transfer is the use of shape pulses compared to HSQC-based sequences, which reduces signal loss due to  $B_1$  field inhomogeneities and pulse imperfections [119].

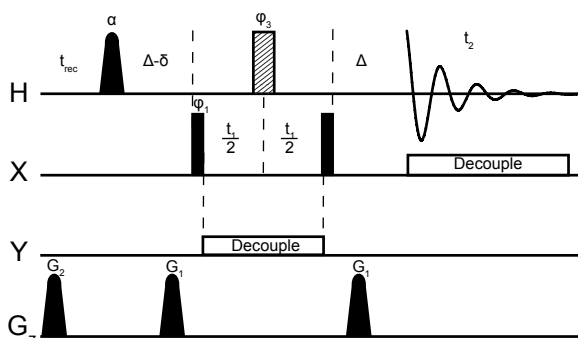


Figure 2.5: Pulse sequence of the SOFAST-HMQC experiment to record  $^1\text{H}$ -X ( $X = ^{15}\text{N}$  or  $^{13}\text{C}$ ) correlation spectra of proteins. Filled black rectangles indicate  $90^\circ$  pulses and diagonal patterned rectangles represents  $180^\circ$  pulses, except for the first  $^1\text{H}$  excitation pulse applied with flip-angle  $\alpha$ . The variable flip-angle pulse has a polychromatic PC9 shape,  $\Delta$  is set to  $\frac{1}{2J_{HX}}$ , the delay  $\delta$  accounts for spin evolution during the PC9 pulse, and  $t_{rec}$  is the recycle delay between scans (adapted from [119]).

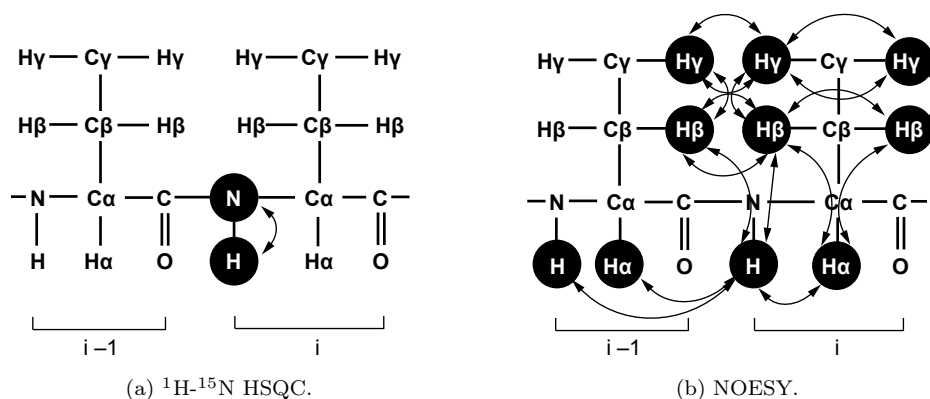


Figure 2.6: Schematic representation of the protein backbone and the correlations that can be observed in an HSQC (a) and NOESY (b). Black shaded circles indicate nuclei for which chemical shift is measured. Magnetization transfer and direction are marked by black lines. The  $^1\text{H}$ - $^{15}\text{N}$  HSQC correlates amide nitrogen with the directly attached proton (a). The NOESY (see subsection 2.2.6 on the next page) correlates nuclei close in space ( $\sim 5 \text{ \AA}$ ) (b).

## 2.2.6 Nuclear Overhauser Enhancement Spectroscopy (NOESY)

The NOESY experiment [120] is mainly performed to obtain distance restraints using the NOE to correlate protons that are close in space (distance smaller than 5 Å). The experiment gives a spectrum in which a cross peak at respective frequency coordinates ( $F_1, F_2$ ) indicates that the spin at  $F_1$  is chemically exchanging with the spin at  $F_2$ . The first  $90^\circ_x$  pulse creates transverse magnetization, and the spins evolve during  $t_1$  according to their chemical shifts. The second  $90^\circ_x$  pulse returns magnetization back to the  $z$  axis (more precise  $-z$ ). During the mixing period  $\tau_m$ , magnetization transfer occurs under the influence of cross relaxation. The transverse components, which are not required, are removed by phase cycling and only magnetization in  $z$  direction remains. Finally, the third  $90^\circ_x$  pulse creates observable magnetization. The cross peaks arise due to internuclear magnetization transfer, while the diagonal peaks emerge from those spins which do not undergo chemical exchange during  $\tau_m$  (Fig. 2.7).

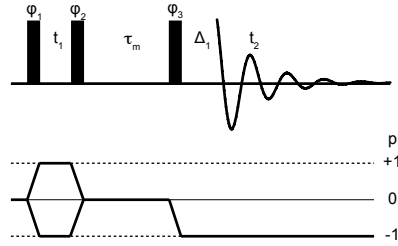


Figure 2.7: Pulse sequence (top) and coherence level diagram (bottom) for the 2D NOESY experiment. The coherence transfer starts at level  $p = 0$ , corresponding to thermal equilibrium, and by acting of an  $rf$  pulse  $p = \pm 1$  is created. During the mixing time  $\tau_m$ , coherence is conserved and finally ends up at  $p = -1$ , where it can be detected.

After the second  $90^\circ_x$  pulse the existing magnetization is described by:

$$I_z \xrightarrow{\frac{\pi}{2} x - t_1 - \frac{\pi}{2} x} [-I_z \cos \omega_I t_1 + I_x \sin \omega_I t_1 - S_z \cos \omega_S t_1 + S_x \sin \omega_S t_1] \cos \pi J_{IS} t_1 \quad (2.24)$$

$$- \left[ 2I_x I_y \cos \omega_I t_1^{(1)} + 2I_y S_x \cos \omega_S t_1^{(2)} + 2I_z I_y \sin \omega_I t_1 + 2I_y I_z \sin \omega_S t_1 \right] \sin \pi J_{IS} t_1$$

The first (1) and second (2) term representing single and double quantum coherence are negligible because they do not lead to observable magnetization. For the NOESY only longitudinal magnetization components during  $\tau_m$  are interesting. The first two pulses are phase cycled by  $90^\circ$  each ( $x, x, y, y, -x, -x, -y, -y$ ). Thereby undesired coherence orders are canceled and only zero quantum (ZQ) coherence remains:

$$(-I_z \cos \omega_I t_1 - S_z \cos \omega_S t_1) \cos \pi J_{IS} t_1 - (I_y S_x - I_x I_y) \times [\cos \omega_I t_1 - \cos \omega_S t_1] \sin \pi J_{IS} t_1 \quad (2.25)$$

After  $\tau_m$ , in which the ZQ term precesses according to the difference in chemical shift of  $I_I$  and  $I_S$ , and the third  $90^\circ$  pulse the resulting evolution is:

$$[I_y \alpha_{II} \cos \omega_I t_1 + S_y \alpha_{SS} \cos \omega_S t_1 + I_{yx} \alpha_{SI} \cos \omega_S t_1 + S_y \alpha_{IS} \cos \omega_I t_1] \times \cos \pi J_{IS} t_1$$

$$+ (I_z S_x - I_x S_z) \cos (\omega_I - \omega_S) \times \tau_m [\cos \omega_S t_1 - \cos \omega_I t_1] \sin \pi J_{IS} t_1 \quad (2.26)$$



The terms represent diagonal peaks proportional to the mixing coefficient  $\alpha_{II}$  and  $\alpha_{SS}$ , and NOE cross peaks proportional to  $\alpha_{SI}$  and  $\alpha_{IS}$  [112, 110]. In Fig. 2.6b, the magnetization transfer between all protons using the NOE experiment is illustratively presented.

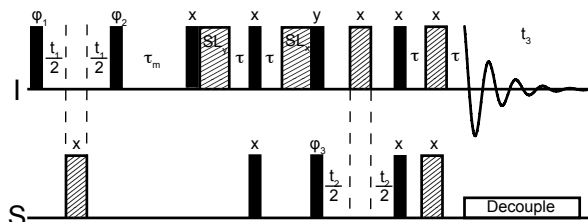


Figure 2.8: Pulse sequence for the 3D  $^1\text{H}$ - $^{15}\text{N}$  NOESY-HSQC experiment. The phase cycling is:  $\varphi_1 = 2(x), 2(-x)$ ;  $\varphi_2 = 4(x), 4(-x)$ ;  $\varphi_3 = x, -x$ ; and receiver =  $x, -x, -x, x, -x, x, x, -x$ . The spin-lock purge pulses (SL) are applied for 1-2 ms (adapted from [110]).

The basic pulse sequence of the NOESY-HSQC ( $I = ^1\text{H}$ , and  $S = ^{15}\text{N}$  or  $^{13}\text{C}$ ) experiment is illustrated in Fig. 2.8. The basic homonuclear NOESY experiment is heteronuclear-edited in the third dimension and resolve cross peaks between the  $^1\text{H}$  spins according to the chemical shift of the heteronuclei bonded directly to the  $^1\text{H}$ . The complete magnetization transfer is described by:

$$I_I \xrightarrow{NOE} I_S \xrightarrow{^1J_{IS}} S \xrightarrow{^1J_{IS}} I \quad (2.27)$$

(t<sub>1</sub>)                      (t<sub>2</sub>)    (t<sub>3</sub>)

### 2.2.7 HNCA

In the HNCA experiment, the amide  $^1\text{H}$  and  $^{15}\text{N}$  chemical shifts of residue  $i$  are correlated with the  $^{13}\text{C}^\alpha$  of residue  $i$  (intraresidue) by  $J_{^{15}\text{N}(i),^{13}\text{C}^\alpha(i)}$  coupling (7 - 11 Hz) and residue  $i-1$  (interresidue) by  $J_{^{15}\text{N}(i),^{13}\text{C}^\alpha(i-1)}$  coupling (9 Hz) [121]. The pulse sequence of the HNCA experiment is illustrated in a simple version in Fig. 2.9.

In the following, I, N, and  $\text{C}^\alpha$  denote the intraresidue  $^1\text{H}$ ,  $^{15}\text{N}$ , and  $^{13}\text{C}^\alpha$  spins, the carbonyl spin of the preceding residue is  $\text{C}'$ . The chemical shifts are denoted as  $\omega_N$  and  $\omega_{\text{C}^\alpha}$  and  $J_{\text{NC}'}$  is the interresidue  $^{15}\text{N}$ - $^{13}\text{CO}$  coupling constant [112, 110]. In the first INEPT step magnetization is transferred to  $^{15}\text{N}$ . During  $t_1$  the magnetization evolves according to the  $^{15}\text{N}$  chemical shift. Evolution due to scalar coupling between  $^{15}\text{N}$  spins and  $^1\text{H}$ ,  $^{13}\text{C}^\alpha$ , and  $^{13}\text{CO}$  is eliminated by the  $180^\circ$  refocusing pulse in the middle of  $t_1$ :

$$I_z \xrightarrow{A} -2I_z N_y \xrightarrow{t_1} 2I_z N_y \cos \omega_N t_1 \cos \pi J_{\text{NC}'} t_1 \quad (2.28)$$

The  $^{15}\text{N}$  magnetization becomes anti-phase with respect to the  $^{13}\text{C}^\alpha$  spins during the delay  $\delta$ , which is set to an integral multiple of  $\frac{1}{J_{\text{NH}}}$  such that the  $^{15}\text{N}$  magnetization remains anti-phase with respect to the coupled protons.

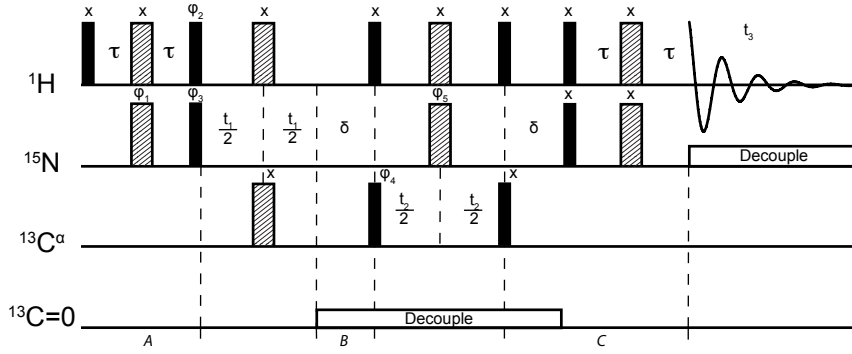


Figure 2.9: Pulse sequence for three-dimensional HNCA experiment. The delay  $\delta$  is adjusted to be an integral of  $\frac{1}{J_{NH}}$  that the  $^{15}\text{N}$  magnetization is antiphase with respect to its coupled protons. The phase cycling is:  $\varphi_1 = x, -x$ ;  $\varphi_2 = y, -y$ ;  $\varphi_3 = x$ ;  $\varphi_4 = 2(x), 2(-x)$ ;  $\varphi_5 = 4(x), 4(y), 4(-x), 4(-y)$ ; receiver =  $2(x, -x, -x, x)$  (adapted from [112]). For further details see text.

Afterwards, the simultaneous application of  $90^\circ$  pulses to both  $^1\text{H}$  and  $^{13}\text{C}^\alpha$  results in three spin coherence ( $^{15}\text{N} - ^1\text{H} - ^{13}\text{C}^\alpha$ ).

$$\begin{aligned}
 &\xrightarrow{B} -4I_y N_x C_y^\alpha \cos \omega_N t_1 \cos \pi J_{NC'} t_1 \\
 &\xrightarrow{t_2} 4I_y N_x C_y^\alpha \cos \omega_N t_1 \cos \pi J_{NC'} t_1 \cos \pi J_{C^\alpha} t_2
 \end{aligned} \tag{2.29}$$

By refocusing of the  $^1\text{H}$  and  $^{15}\text{N}$  chemical shifts through the simultaneous  $180^\circ$  pulses in the middle of  $t_2$ , only  $^{13}\text{C}^\alpha$  chemical shifts evolve during this period. Finally, magnetization is transferred back to observable  $^1\text{H}$  by reversing the described procedure excluding  $t_1$  evolution:

$$\xrightarrow{C} I_x \cos \omega_N t_1 \cos \pi J_{NC'} t_1 \cos \pi J_{C^\alpha} t_2 \tag{2.30}$$

The existence of a significant two-bond coupling  ${}^2J_{NC^\alpha_{(i-1)}}$  between  $^{15}\text{N}(i)$  and the preceding  $^{13}\text{C}^\alpha_{(i-1)}$  spin,  $J_{C^\alpha_{(i-1)}}$ , will cause a signal prior to detection given by:

$$\begin{aligned}
 &I_x \cos \omega_N t_1 \cos \pi J_{NC'} t_1 \times \\
 &\left[ \cos \pi J_{C^\alpha} t_2 \left( \sin \pi J_{NC^\alpha} \delta \cos \pi J_{NC^\alpha_{(i-1)}} \delta \right)^2 + \cos \omega_{C^\alpha_{(i-1)}} t_2 \left( \sin \pi J_{NC^\alpha_{(i-1)}} \delta \cos \pi J_{NC^\alpha} \delta \right)^2 \right]
 \end{aligned} \tag{2.31}$$

For both equations, the detected signal is modulated by  $t_1$  and  $t_2$  resulting in pure absorptive lineshapes and for the HNCA experiment two sets of correlations are obtained: intraresidue  $^{13}\text{C}^\alpha_{(i)} - ^{15}\text{N}_{(i)} - ^1\text{H}_{(i)}$  connectivity via one-bond  ${}^1J_{NC^\alpha}$  coupling and via two-bond  ${}^2J_{NC^\alpha}$  coupling the interresidue  $^{13}\text{C}^\alpha_{(i-1)} - ^{15}\text{N}_{(i-1)} - ^1\text{H}_{(i-1)}$  connectivity, which is illustrated in Fig. 2.10a. One can detect peaks for both  $\text{C}^\alpha_{(i)}$  and  $\text{C}^\alpha_{(i-1)}$  in the spectrum, however the coupling to  $\text{C}^\alpha_{(i)}$  is usually stronger and thus these peaks generally appear with a greater intensity in the spectra.

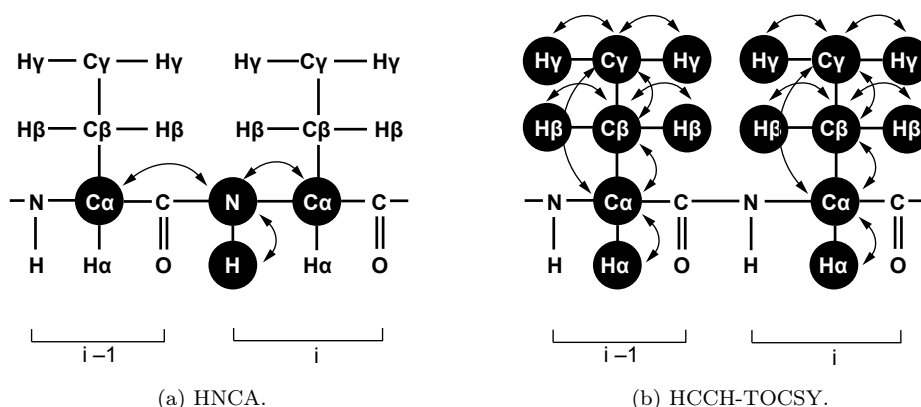
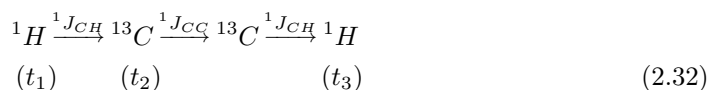


Figure 2.10: Schematic representation of the protein backbone and the correlations that can be observed in an HNCA (a) and HCCH-TOCSY (b) experiment. Black shaded circles indicate nuclei for which chemical shift is measured. Magnetization transfer and direction is marked by black lines. Magnetization is passed from  $^1\text{H}$  to  $^{15}\text{N}$  and then via the  $J_{\text{NC}\alpha}$  coupling to the  $^{13}\text{C}\alpha$  and then back again to  $^{15}\text{N}$  and  $^1\text{H}$  for detection. Chemical shift evolves for  $^1\text{H}$  as well as  $^{15}\text{N}$ , and  $^{13}\text{C}\alpha$ , resulting in a three-dimensional spectrum (a). In the HCCH-TOCSY (see subsection 2.2.8), magnetization is transferred from the side chain hydrogen nuclei to their attached  $^{13}\text{C}$  nuclei, followed by isotropic  $^{13}\text{C}$  mixing and finally transfer back to the side chain hydrogen atoms for detection (b).

## 2.2.8 HCCH-TOCSY and CCONH-TOCSY

The HCCH-TOCSY (total correlation spectroscopy) is used to assign side chain  $^1\text{H}$  and  $^{13}\text{C}$  resonances and make use of the  $^1J_{\text{CH}}$  ( $\sim 140$  Hz) and the  $^1J_{\text{CC}}$  coupling (32 - 40 Hz) by transfer of magnetization along the side chain via:



The transfer is achieved by isotropic mixing of the  $^{13}\text{C}$  spins, which results in both direct and multiple-relayed magnetization transfer along the carbon side chain [122, 123]. The pulse sequence is shown in Fig. 2.11 and the correlations obtained are illustrated in Fig. 2.10b.

After evolution during  $t_1$ ,  $^1\text{H}$  magnetization is transferred to the attached carbon ( $\text{C}_A$ ) via  $^1J_{\text{CH}}$  in an INEPT-type sequence, while the  $180^\circ$  pulse in the middle of  $t_1$  ensures decoupling of  $^1\text{H}$  spins from  $^{13}\text{C}$  spins. During the delay  $2\delta_1$  the  $^{13}\text{C}$  magnetization, originally anti-phase with respect to  $^1\text{H}$ , becomes in-phase, and evolves during  $t_2$  under the influences of  $^{13}\text{C}$  chemical shift.  $^1\text{H}$ - $^{13}\text{C}$  coupling is removed by the  $180^\circ$  pulse on  $^1\text{H}$ , while the  $180^\circ$   $^{13}\text{CO}$  pulse destroys dephasing of  $^{13}\text{C}\alpha$  magnetization. The  $\text{C}_A$  magnetization becomes anti-phase with respect to its  $^{13}\text{C}$  coupling partner  $\text{C}_B$  during  $t_2$ . The short spin lock trim pulse along the  $x$  axis defocus all in-phase  $^{13}\text{C}$  magnetization that is not parallel to the effective field. The subsequent isotropic mixing (DIPSI-3, 20 - 35 ms [124, 125]) transfers the in-phase  $^{13}\text{C}$  magnetization to its neighbors via  $^1J_{\text{CC}}$  coupling. Using a reverse INEPT sequence the  $^{13}\text{C}$  magnetization is finally transferred back to the attached protons and detected in  $t_3$ . This results in a three-dimensional spectrum with an appearance similar to a two-dimensional  $^1\text{H}$ - $^1\text{H}$  TOCSY, but edited by the  $^{13}\text{C}$  chemical

shift in the third dimension at the diagonal where the magnetization originates. Hence, the cross peaks are not symmetric about the diagonal [112, 110].

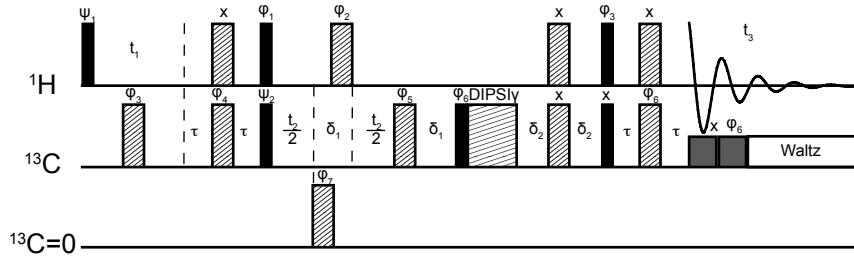


Figure 2.11: Pulse sequence of the HCCH-TOCSY experiment. The phase cycling is:  $\varphi_1 = y, -y$ ;  $\varphi_2 = 4(x), 4(y), 4(-x), 4(-y)$ ;  $\varphi_3 = 8(x), 8(-x)$ ;  $\varphi_4 = 2(x), 2(-x)$ ;  $\varphi_5 = 2(x), 2(y), 2(-x), 2(-y)$ ;  $\varphi_6 = 4(x), 4(-x)$ ;  $\varphi_7 = 8(x)$ ;  $\psi_1 = x; \psi_2 = x$  receiver  $= 2(x, -x, -x, x), 2(-x, x, x, -x)$ . The delay  $\tau = 1.5$  ms, slightly less than  $\frac{1}{4J_{CH}}$ , the delays  $\delta_1, \delta_2$  are set to  $\sim \frac{1}{6J_{CH}} = 1.1$  ms (adapted from [112]).

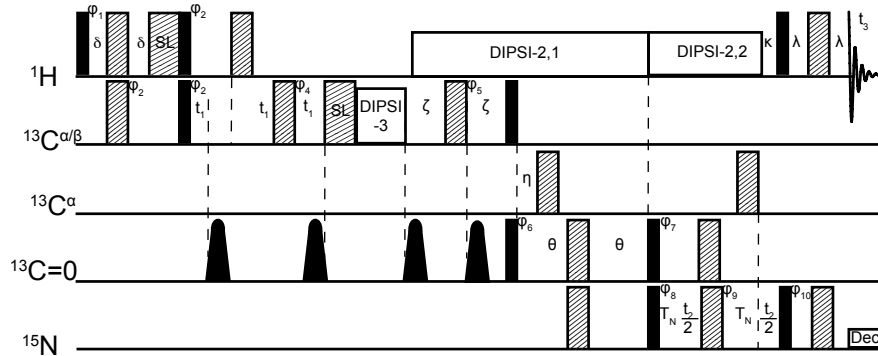


Figure 2.12: Pulse sequence of the CCONH experiment. The phase cycling is:  $\varphi_1 = y$ ;  $\varphi_2 = x, -x$ ;  $\varphi_3 = x$ ;  $\varphi_4 = 8(x), 8(y), 8(-x), 8(-y)$ ;  $\varphi_5 = 4(x), 4(-x)$ ;  $\varphi_6 = 2(x), 2(-x)$ ;  $\varphi_7 = 48.5^\circ$ ;  $\varphi_8 = 4(x), 4(-x)$ ;  $\varphi_9 = 8(x), 8(-x)$ ;  $\varphi_{10} = 16(x), 16(-x)$ ; Acq. =  $P, -P, -P, P, -P, P, P, -P$ , with  $P = (x, -x, -x, x)$ . Quadrature in the  $t_1$  and  $t_2$  domains is obtained by changing the phases  $\varphi_3$  and  $\varphi_8$ , respectively, in the usual States-TPPI manner (adapted from [126]).

The CCONH-TOCSY is another experiment to correlate the  $^1\text{H}$  and  $^{15}\text{N}$  amide resonances of one residue with the  $^{13}\text{C}^\alpha$  and all other  $^1\text{H}$  and  $^{13}\text{C}$  side chain resonances of its preceding residue. In Fig. 2.12 the pulse sequence for the CCONH is illustrated. The complete transfer of magnetization for the CCONH-TOCSY is described by:

$${}^1\text{H} \xrightarrow{{}^1J_{CH}} {}^{13}\text{C} \xrightarrow{{}^1J_{CC}} {}^{13}\text{C} \xrightarrow{{}^1J_{CACQ}} {}^{13}\text{C} \xrightarrow{{}^1J_{NCQ}} {}^{15}\text{N} \xrightarrow{{}^1J_{NH}} {}^1\text{H} \quad (2.33)$$

### 2.2.9 Pulsed field gradient (PFG) diffusion measurements

Diffusion refers to the random translational motion of molecules and determines the encounter of molecules and thus influences the rate of chemical reactions. It depends on several physical parameters such as molecular size and shape, temperature, and viscosity, and can be described by Stokes' law (see eq. 2.14). The measurement of diffusion constants provides information about intermolecular interactions, the shape, and the size of diffusing molecules [127, 128].

Pulsed field gradient NMR spectroscopy can be used to measure diffusion constants and thus gives information about ligand binding affinities. In PFG measurements, molecules are spatially labeled using pulse sequences that incorporate pulsed-field gradients. As the name already indicates, the strength of a gradient pulse varies, mostly linearly, along the sample volume. The gradient pulses enable the determination of the position of nuclei before (gradient encoding) and after (gradient decoding) the diffusion time  $\Delta$  [129]. The measured signal is the integral over the whole sample volume and the NMR signal intensity  $I$  is attenuated depending on the diffusion time  $\Delta$  and the gradient parameters ( $G, \delta$ ) according to

$$I = I_0 \exp \left[ -D (\gamma \delta G^2) \left( \Delta - \frac{\delta}{3} \right) \right] \quad (2.34)$$

where  $I_0$  is the signal intensity in the absence of the applied magnetic field,  $D$  the diffusion coefficient,  $G$  the gradient strength, and  $\delta$  the length of the gradient. The decay rates of the exponential curves are proportional to  $D$ , which can be calculated from the slope.

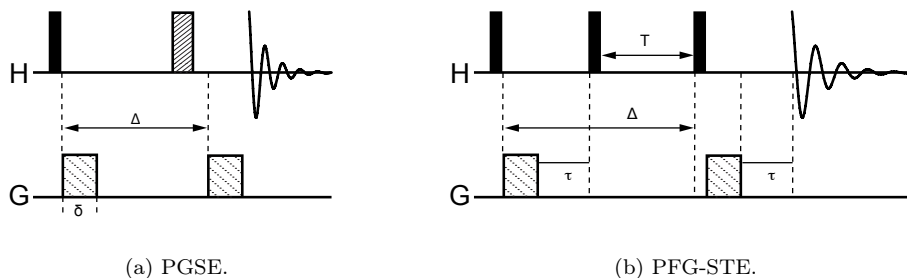


Figure 2.13: Pulse sequences of two PFG-NMR experiments that can be used for diffusion measurement: Pulsed gradient spin echo (PGSE) (a) and Pulsed-field stimulated echo sequence (PFG-STE) (b) (adapted from [130, 131]).

Two standard pulse experiments for diffusion measurement are pulsed gradient spin echo sequence (PGSE) and pulsed-field stimulated echo sequence (PFG-STE) [130, 131], which are shown schematical in Fig. 2.13. For PFG-STE the encoding and decoding periods are separated by  $90^\circ$  pulses, which allow diffusion to occur in the longitudinal direction. Since the time, magnetization is held in the  $xy$  plane (as long as  $T \ll T_1$ ), is short, diffusion is responsible for the measured signal decay, but not  $T_2$ . The last  $90^\circ$  pulse transfers magnetization back in the  $xy$  plane for decoding of the spins [129]. PFG-NMR is a well-established method for the measurement of protein diffusion coefficients to characterize the binding of proteins to membrane mimetics [132, 133]. The binding of the protein to a membrane mimetic results in an increase of its diffusion coefficient since it diffuses now as a larger and more slowly moving complex.

### 2.2.10 Paramagnetic probes and paramagnetic relaxation enhancement (PRE)

Paramagnetic relaxation enhancement (PRE) is a powerful tool to investigate structural aspects of dynamic processes providing long-range distance information up to 35 Å (depending on the paramagnetic ion) compared to NOE restraints, which provide short-range distance information (<6 Å). The PRE arises from dipolar interactions between a nucleus and the unpaired electrons of a paramagnetic center. The resulting PRE displays a  $r^{-6}$  distance dependency. Because the magnetic moment of an unpaired electron is much greater than that of a  $^1\text{H}$  nucleus, a paramagnetic center in solution can cause large effects on a NMR spectrum. In general, the vicinity of a paramagnetic ion or complex can cause shifts and the reduction of the intensities of NMR signals. The relaxation of a spin close to a paramagnetic center (PRE) is described by the Solomon-Bloembergen equation:

$$\frac{1}{T_{1M}} = \frac{2}{15} \left( \frac{\mu_0}{4\pi} \right) \frac{\gamma_I^2 g^2 \mu_B^2 S(S+1)}{r^6} \left( \frac{3\tau_c}{1 + \omega_I^2 \tau_c^2} + \frac{7\tau_c}{1 + \omega_S^2 \tau_c^2} \right) \quad (2.35)$$

where  $\frac{1}{T_{1M}}$  is the paramagnetic dipolar electron-nuclear relaxation,  $\mu_0$  is the permeability of a vacuum,  $g^2 \mu_B S(S+1)$  is the square of the electronic magnetic moment,  $\mu_I^2$  is proportional to the square of the nuclear magnetic moment,  $r$  is the electron-nucleus distance,  $\tau_c$  is the correlation time, and  $\omega_S$  the electronic and  $\omega_I$  the nuclear Larmor frequency. The correlation time  $\tau_c$  depends on the overall rotational correlation time  $\tau_R$ , the electron spin relaxation time of  $S$   $\tau_S$ , and also the chemical exchange lifetime  $\tau_M$ :

$$\tau_c^{-1} = \tau_R^{-1} + \tau_M^{-1} + \tau_S^{-1} \quad (2.36)$$

The PRE can be observed in any paramagnetic system (isotropic and anisotropic), while the two other NMR observables yielding long range information, PCSs (pseudocontact shifts) and RDCs (residual dipolar coupling), can only be detected in anisotropic systems. Nitroxide spin radicals,  $\text{Mn}^{2+}$ ,  $\text{Gd}^{3+}$ ,  $\text{Fe}^{3+}$ ,  $\text{Cu}^{2+}$ , and many other paramagnetic metal ions are used for PRE experiments [134, 111, 135, 136].

In principle there are three kinds of PREs, which are illustrated in Fig. 2.14: intramolecular PREs arising from the paramagnetic group within the same molecule, intermolecular PREs arising from the paramagnetic group located on the interaction partner, and solvent PREs emerging from random collisions between a protein and the solute paramagnetic substance.

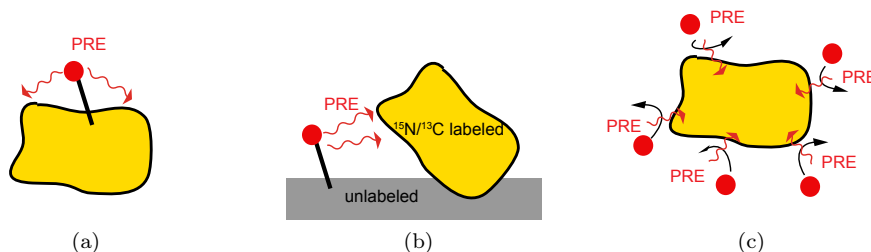


Figure 2.14: Illustration of (a) intramolecular PRE, (b) intermolecular PRE, and (c) PREs arising by a solute paramagnetic substance (adapted from [134]).

Nitroxide spin labels attached to lipids or fatty acid molecules are often used for labeling of membrane mimetics providing information about the local environment at a particular depth in the membrane [137, 138, 139]. Analyzing shifts and/or quenching of NMR signals of for example proteins in the absence and presence of a spin label in the membrane mimetic allows to obtain information about the immersion depth.

## 2.3 CD and oriented CD

### 2.3.1 Circular dichroism (CD)

A variant of absorption spectroscopy used for optically active molecules, meaning asymmetric molecules, is circular dichroism (CD). The optical activity can be seen as the rotation of linearly polarized light by the difference in absorption for the right- and left-handed circularly polarized light, which both obey Lambert-Beer's law:

$$A(\nu) = \varepsilon(\nu)lc \quad (2.37)$$

where  $\varepsilon(\nu)$  is the extinction coefficient in  $[M^{-1}cm^{-1}]$ ,  $c$  the concentration in  $[\frac{mol}{l}]$ , and  $l$  the path length in  $[cm]$ . CD is defined as the difference  $\Delta A$  in extinction coefficients for right-(R) and left-handed (L) circularly polarized light:

$$\Delta A(\lambda) = A_L(\lambda) - A_R(\lambda) = [\varepsilon_L(\lambda) - \varepsilon_R(\lambda)]lc = \Delta\varepsilon lc \quad (2.38)$$

where the subscripts  $L$  and  $R$  denote the handedness of the light. For proteins the mean residue weight ellipticity  $\theta_{MRW}$  is often used to normalize the data with respect to the molecular weight. Linearly polarized light is defined as oscillation of the electric vector in only one plane and can be considered to have two components, respectively, electric vectors ( $E_R$  and  $E_L$ ), which are contra-rotating circularly around the direction of propagation. Circularly polarized light is made by two polarized waves, perpendicular to each others oscillation plane, that are out of phase by  $\frac{\pi}{2}$  after passing a retarder. The sum of these two linearly polarized lights emerging from the the retardation give either an electric vector rotating as a right-handed or left-handed helix [107, 140].

For proteins, the main chromophores are the peptide bond, the aromatic side chains, and some prosthetic groups. The spectral region dominated by the peptide backbone (190 - 260 nm) is of interest and can be used for an estimate of the secondary structure. A negative band at about 222 nm due to the  $n\pi^*$  transition, and a negative and positive band at about 208 and 190 nm due to parallel and perpendicular components of the  $\pi\pi^*$  transition, respectively, are corresponding to an  $\alpha$ -helical secondary structure. The  $\alpha$ -helix content of a protein might be estimated by the magnitude of the negative band around 222 nm. The CD spectrum for a  $\beta$ -strand is represented by a negative band at around 210 - 225 nm and a positive band with a maximum at 190 - 200 nm. A typical random coil spectrum points out a negative band around 200 nm (Fig. 2.15).

The basic principle involved in the analysis of CD spectra and used for the estimation of secondary structure is that the protein CD spectrum can be expressed as combination of CD spectra of individual secondary structure components:  $\alpha$ -helical,  $\beta$ -strand, and random coil [141]. Secondary structure analysis is usually performed based on different sets of reference proteins (15 - 30) having a good representation of  $\alpha$ -helix and  $\beta$ -strand, and mixed proteins ( $\alpha$ -helix and  $\beta$ -strand). For a good analysis, a reference protein set with the largest possible representation

of CD spectral features and secondary structural combinations is required [142]. Three popular CD analysis programs are CONTIN, SELCON3, and CDSSTR, which are recommended to be used in conjunction for a reliable analysis [143].

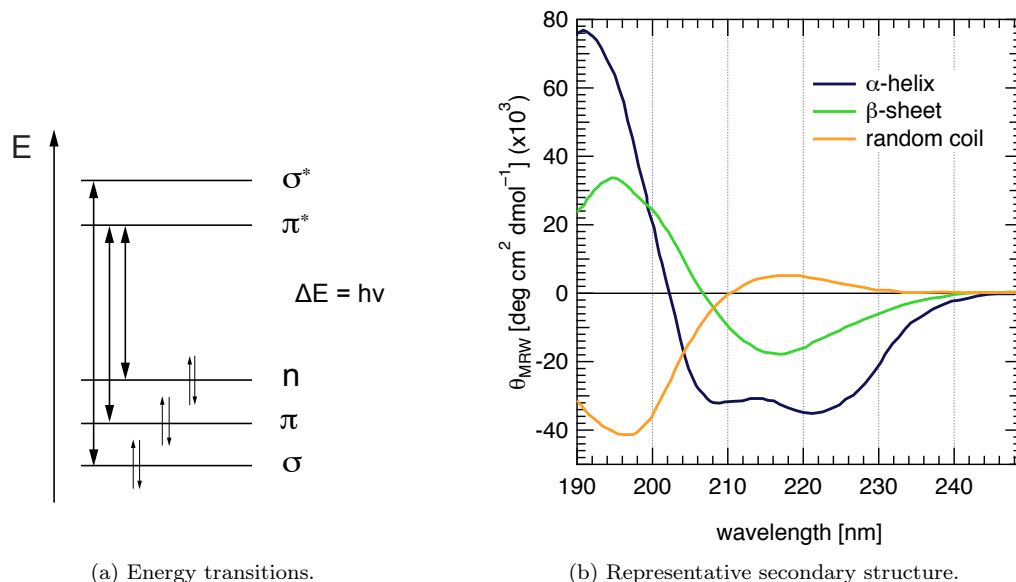


Figure 2.15: Energy transitions (a) and the CD spectra of representative secondary structure:  $\alpha$ -helix,  $\beta$ -sheet, and random coil (b) [144].

### 2.3.2 Oriented circular dichroism (OCD)

Around the 1990s, oriented circular dichroism (OCD) was established for the determination of the orientation of  $\alpha$ -helices embedded in lipid bilayers [145, 146]. OCD is based on Moffitt's theory [147, 148], which predicts that the transition dipole moment of the  $\pi\pi^*$  electronic transitions of the amide chromophores in a helix are polarized parallel or perpendicular to the helix axis. Multilayer samples of short peptides/proteins with a single  $\alpha$ -helix that are reconstituted in lipid bilayers are sandwiched between two fused silica plates. The OCD is obtained by measuring the so oriented sample at different rotation angles with respect to the light vector. To exclude disturbing effects caused by linear polarization and linear birefringence a special sample chamber is used, in which the sample is placed in distilled water and which is allowed to be rotated about its axis [145, 146]. The advantage of this arrangement is that both linear birefringence and linear polarized light are diminished. The OCD spectra are recorded in step of  $45^\circ$  by rotation of the chamber and at each angle three scans are performed as an average.

OCD has a high sensitivity, which enables measurements with very low amounts of peptide/protein sample [149] in a very short time. However, OCD can mainly provide qualitative to semi-quantitative information about the tilt angle of an  $\alpha$ -helix with respect to the membrane normal. Figure 2.16 shows theoretical OCD spectra: A helix oriented parallel to the bilayer normal results in a so called I-spectrum, while a helix oriented perpendicular to the bilayer normal in a so called S-spectrum. Both have a characteristic shape and minima at different wavelength [150]. The tilt angle of an  $\alpha$ -helix with respect to the bilayer can be estimated by analyzing contributions from I- and S-spectra. Additional factors affecting the OCD signal are the content of  $\alpha$ -helical secondary structure, affinities for a membrane mimetic, and aggregation.



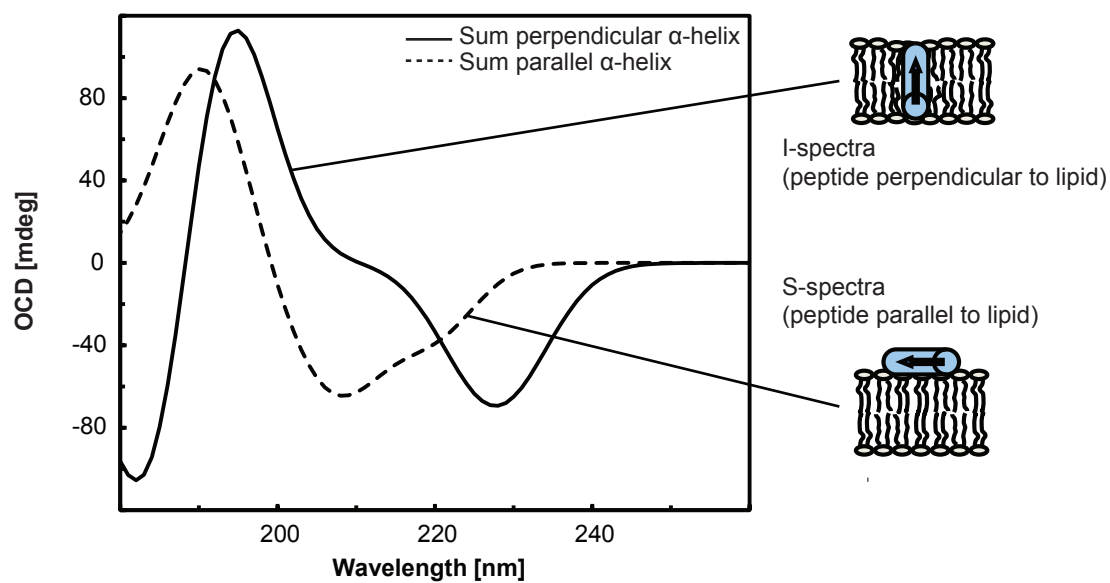


Figure 2.16: Schematic representation of an OCD spectrum with I- and S-spectra and their corresponding bands. The I-state representing a peptide oriented perpendicular to the membrane is depicted by a black line. The S-state representing a parallel aligned peptide is shown by a dashed line.



## Chapter 3

# Materials and Methods

If not indicated otherwise, chemicals and supplementary materials were purchased from Roth (Germany), Serva (Germany), Sigma-Aldrich (Germany), and VWR (Germany). The isotopes,  $^{15}\text{NH}_4\text{Cl}$  and  $^{13}\text{C}$  glucose, and  $\text{D}_2\text{O}$  were bought from Eurisotop (Germany).

### 3.1 Buffer solutions

The used buffers and their respective composition are summarized in Tab. 3.1.

### 3.2 Cell growth media

LB medium, agar plates and antibiotics were prepared as described by Sambrook [151]. For the expression of proteins M9 minimal medium was used, which was composed of 200 mL 5×M9 salts (34 g/L  $\text{Na}_2\text{HPO}_4$ , 15 g/L  $\text{K}_2\text{HPO}_4$ , 2.5 g/L  $\text{NaCl}$ ,  $\text{H}_2\text{O}$ ), 2 mL 1 M  $\text{MgSO}_4$ , 0.1 mL 1 M  $\text{CaCl}_2$ , 10 mL 100×BME vitamins (Sigma), 1 g  $\text{NH}_4\text{Cl}$ , 2 g glucose, 100 mg/L ampicillin, adjusted to 1 L  $\text{H}_2\text{O}$ . Each single component was either autoclaved or sterile filtrated. Uniformly  $^{15}\text{N}$ -labeled protein was prepared in M9 minimal medium containing  $^{15}\text{NH}_4\text{Cl}$  as the sole nitrogen source. Uniformly  $^{15}\text{N}$ - $^{13}\text{C}$ -labeled protein was prepared in M9 minimal medium containing  $^{15}\text{NH}_4\text{Cl}$  and  $^{13}\text{C}$  glucose as the sole nitrogen and carbon source, respectively.

### 3.3 Plasmid cloning, protein expression and purification

Wild type *S. cerevisiae* TOR1 FATC ( $\hat{=}$  y1fatc, residues 2438 - 2470) was cloned into the expression vector GEV2 [152] using the BamHI and XhoI sites and overexpressed in *E. coli* BL21 or Rosetta (DE3) (Novagen, Merck Millipore, United Kingdom) as described in [68]. Mutant versions of y1fatc were obtained by site-directed mutagenesis (QuickChange<sup>®</sup> site-directed mutagenesis protocol [153]) replacing one or more residues by alanine or other amino acids [154]. The used primers are given in the appendix in Tab. A.1 on page 103 and A.2 on page 104 and were designed according the rules described in [153].

The PCR sample composition and the used parameters are listed in Tab. 3.2. The success of the mutagenesis reaction was verified by DNA sequencing (GATC or Eurofins MWG Operon). The prepared mutated y1fatc proteins are shown in the appendix in Tab. A.3 on page 105.

Table 3.1: Buffer compositions.

Buffer	application	composition	pH
Lysis buffer	Cell lysis	2 mM benzamidine, 2 mM EDTA, 50 mM Tris	7.5
TST buffer	Affinity chromatography (IgG)	50 mM Tris, 150 mM NaCl, 0.05 % Tween 20	7.6
(NH <sub>4</sub> )(H <sub>3</sub> CCO <sub>2</sub> H)	Affinity chromatography (IgG)	0.005 M (NH <sub>4</sub> )(H <sub>3</sub> CCO <sub>2</sub> H)	5.0
H <sub>3</sub> CCO <sub>2</sub> H	Affinity chromatography (IgG)	0.5 M H <sub>3</sub> CCO <sub>2</sub> H	3.4
Resuspending buffer	Digest buffer, Resuspension buffer	50 mM Tris, 100 mM NaCl, 2 mM CaCl <sub>2</sub>	8.0
NMR buffer	Standard sample buffer (NMR)	50 mM Tris, 100 mM NaCl	6.5
RP-Buffer A	RP-HPLC buffer A	0.1 % TFA, H <sub>2</sub> O	-
RP-Buffer B	RP-HPLC buffer B	0.1 % TFA, 90% AcN, H <sub>2</sub> O	-

Table 3.2: PCR sample composition and parameters.

(a) Composition.

Component	Volume [ $\mu$ L]
dsDNA template (5 - 50 ng)	0.5 - 1.0
Oligonucleotide primer forward (125 ng)	1.0
Oligonucleotide primer backward (125 ng)	1.0
50 $\times$ dNTP mix (10 mM each)	1.0
50 $\times$ reaction buffer	5.0
ddH <sub>2</sub> O	40.0 - 40.5
<i>Pfu Turbo</i> DNA polymerase (2 - 3 u/ $\mu$ L) (add last)	1.0

(b) Parameters.

Segment	Cycle(s)	Temperature [ $^{\circ}$ C]	Time [ <i>min</i> ]
1	1	95	3
2	18	95	1/2
		55	1
		68	6*
3	1	68	6
		4	$\infty$

\* Based on the length of the template vector of  $\sim$ 5.4 kbp and the *Pfu Turbo* DNA polymerase activity of 1 min/kpb at 68  $^{\circ}$ C.

All proteins were overexpressed in *Escherichia coli* BL21 (DE3) in LB or  $^{15}\text{N}$  M9 minimal medium. The culture was grown until an  $\text{OD}_{600}$  of  $\sim 0.7 - 0.9$  was observed, following induction with 1 mM IPTG for 3 h at 37 °C. The fusion protein consisting of the B1 domain of protein G (GB1), a thrombin and a factor Xa site as well as y1fatc, as wild type or mutated variant, ( $\triangleq$  y1fatc-gb1xa, 99 residues), was mostly expressed soluble. If necessary, the inclusion body fraction was extracted as described [68]. The purification of the fusion proteins followed either the original protocol using ultrasonication for cell lysis [68] or a heat shock protocol [155]. GB1 fusion protein from supernatant after cell lysis was extracted by IgG affinity chromatography as described in the manufacturer's manual (GE Healthcare, Germany [156]). The purified protein was lyophilized. If the GB1 fusion protein was directly used for NMR monitored binding studies [157], the protein was resuspended in NMR buffer, washed several times using ultrafiltration spin columns (Amicon Ultra, MWCO 3000, Merck Millipore, United Kingdom) and concentrated. To obtain pure y1fatc protein, the fusion protein was resuspended in resuspension buffer and overnight digested with Factor Xa (New England Biolabs, Germany). The GB1 tag was subsequently removed by RP-HPLC in an acetonitrile/trifluoroacetic acid system (see Appendix, Fig. A.2 on page 108) and fractions containing pure y1fatc or the mutated version were lyophilized. Lyophilized pure y1fatc was resuspended in NMR buffer as described [68]. The correct molecular weight of the used proteins was confirmed by mass spectrometry.

Residues 4096 - 4128 of human DNA-PKcs (see Appendix, Tab. A.4 on page 106 and Tab. A.5 on page 107) corresponding to its FATC domain (hdnapkfadc) were cloned into GEV2 [152] using the XhoI and BamHI sites [158]. An additional factor Xa cleavage site was introduced by the used PCR primers and another variant with an enterokinase (hdnapkfadc-gb1ent) instead of a factor Xa (hdnapkfadc-gb1xa) cleavage site was prepared by site-directed mutagenesis [158]. The success of the mutagenesis was verified by DNA sequencing. Either variant was overexpressed in *Escherichia coli* BL21 (DE3) (Novagen, Merck Millipore, United Kingdom) in LB or  $^{15}\text{N}$ -, or  $^{15}\text{N}$ - $^{13}\text{C}$  M9 minimal medium at 37 °C. When the  $\text{OD}_{600}$  of the culture was  $\sim 0.7 - 0.9$ , protein expression was induced with 1 mM IPTG for 3 h. Both, the fusion protein consisting of the B1 domain of protein G (GB1, 56 residues), a thrombin and a factor Xa site and hdnapkfadc ( $\triangleq$  hdnapkfadc-gb1xa, 99 residues) or the one with enterokinase instead factor Xa site ( $\triangleq$  hdnapkfadc-gb1ent, 100 residues) were mainly obtained from the soluble fraction after sonication of the cells in lysis buffer. The GB1 fusion proteins were purified using an IgG sepharose column as described in the manufacturer's manual (GE Healthcare, Germany [156]). The purified protein was lyophilized, resuspended in NMR buffer and washed several times with the same buffer using centrifugal filter devices (Amicon Ultra, MWCO 3000, Merck Millipore, United Kingdom). To prevent intermolecular disulfide bond formation by the single cysteine, 10 mM TCEP were added to the final protein stock solution.

As described in the master thesis of Martin Schaad [158], pure  $^{15}\text{N}$ -hdnapkfadc was prepared in the following way: The cell pellet was resuspended in PBS and the cell suspension sonicated. The resulting cell lysate was centrifuged for 30 min at 35000 rpm. The supernatant was transferred to a new tube and incubated for 5 min in an 80 °C water bath [155], followed by incubation for 10 min on ice and centrifugation for 30 min at 17500 rpm. The supernatant was purified using IgG sepharose as described in the manufacturer's manual (GE Healthcare, Germany [156]). Fractions containing hdnapkfadc-gb1ent were pooled and lyophilized, resuspended in 50 mM Tris, 100 mM NaCl, 8 M urea, pH 8.0, dialysed to resuspending buffer and digested with enterokinase (New England Biolabs, Germany). The GB1 tag and undigested fusion protein were removed by RP-HPLC in an acetonitrile/trifluoroacetic acid buffer system. Before the RP-HPLC run, the sample was incubated at room temperature with 10 mM TCEP to remove cellular glutathion from the single cysteine. Fractions containing pure hdnapkfadc were lyophilized, resuspended in 20 mM  $\text{NaP}_i$ , 50 mM NaCl, 10 mM TCEP, pH 6.5 (initial structural characterization) or NMR buffer (NMR titrations) and concentrated.

Mass spectrometry confirmed the correct molecular weight. Because the protease digest with factor Xa was not successful and the one with enterokinase not very efficient, most NMR studies were done using directly the GB1 fusion protein [157].

Residues 3024 - 3056 of human ATM FATC (see Appendix, Tab. A.4 on page 106 and Tab. A.5 on page 107) were cloned into GEV2 [152] using the BamHI and XhoI sites and overexpressed in *E. coli* BL21 (DE3) (Novagen, Merck Millipore, United Kingdom) in LB or  $^{15}\text{N}$  M9 minimal medium. An additional factor Xa or enterokinase protease site was introduced by the used PCR primers or site-directed mutagenesis [158]. Expression was done at 37 °C. Cells were grown to an  $\text{OD}_{600}$  of  $\sim 0.9$  and  $\sim 0.7$ , respectively, and induced with 1 mM IPTG for 3 h. Cells were harvested by centrifugation at 4 °C. The cell pellet was resuspended in 25 mL lysis buffer, thoroughly vortexed, and stored at  $-20$  °C. The fusion protein consisting of the B1 domain of protein G (GB1), a thrombin and an enterokinase or factor Xa site as well as the human ATM FATC domain ( $\hat{=}$  hatmfatc-gblent, 100 residues or hatmfatc-gb1xa, 99 residues in total) was mainly expressed soluble. The fusion protein was extracted by incubating the cell suspension for 5 min at 80 °C. This heating step resulted also in an initial purification since many *E. coli* proteins precipitate under these conditions [155]. Afterwards the cell suspension was cooled on ice for 10 min. Following centrifugation at 4 °C for 30 min at 20000 g, the supernatant containing the fusion protein was further purified by IgG affinity chromatography as described in the manufacturer's manual for IgG sepharose (GE Healthcare, Germany [156]). The purified fusion protein was lyophilized, resuspended in  $\sim 10$  mL NMR buffer, washed two times, and concentrated using a centrifugal filter device (Amicon Ultra, MWCO 3000, Millipore Merck, United Kingdom). Because the digestion of hatmfatc-gb1xa with either factor Xa or thrombin or of hatmfatc-gblent with enterokinase or thrombin was also inefficient, the purified GB1 fusion protein was directly used for the interaction studies with lipids and membrane mimetics [157]. Since hatmfatc-gblent is more stable compared to hatmfatc-gb1xa, it was preferentially used.

The purity and identity of the purified proteins was analyzed by SDS-PAGE (see Appendix, protocol A.1.4) and mass spectrometry. Protein concentrations were determined by UV/VIS measurements.

Chemically synthesized peptides (HPLC purified, purity  $>90\%$ ) corresponding to the FATC domains of human SMG-1 ( $\hat{=}$  hsmg1fatc, see Appendix, Tab. A.4 on page 106 and Tab. A.5 on page 107), human ATR ( $\hat{=}$  hatrfatc, see Appendix, Tab. A.4 on page 106 and Tab. A.5 on page 107), and human TRRAP ( $\hat{=}$  htrrapfatc, see Appendix, Tab. A.4 on page 106 and Tab. A.5 on page 107) were obtained from Thermo Scientific, Germany. 7.3 mg hsmg1fatc peptide were initially dissolved in  $\sim 9$  mL NMR buffer. This peptide solution was concentrated using a centrifugal filter device (Amicon Ultra, MWCO 3000, Millipore Merck, United Kingdom). Since the solution got slightly turbid when the volume was reduced to  $\sim 2.5$  mL, the salt concentration was increased to 300 mM and the pH to 8.0 to improve the solubility of the peptide. This peptide solution was washed twice with 50 mM Tris, 300 mM NaCl, pH 8.0 and finally concentrated to a 1.44 mM stock solution. 5 mg hatrfatc peptide were initially dissolved in  $\sim 2.6$  mL NMR buffer containing 10 mM TCEP. The high turbidity of the solution indicated that this peptide is not very soluble in aqueous buffer. Increasing the pH to 8.0 and heating for 10 min at 42 °C as well as lowering the NaCl concentration to 50 mM by dilution improved the solubility. The resulting peptide solution was concentrated with a centrifugal filter device (Amicon Ultra, MWCO 3000, Millipore Merck, United Kingdom) to obtain a 1.42 mM stock solution. However, due to aggregation problems, it had to be diluted again for the NMR measurements. The final pH for the NMR and CD measurement was 7.7. For htrrapfatc 5 mg peptide were dissolved in NMR buffer to obtain a 1.0 mM stock solution.

### 3.4 Preparation of membrane mimetics

Dodecylphosphocholine (DPC, Fig. 3.1a), 1,2-dioctanoyl-*sn*-glycero-3-phosphate (DioctPA, Fig. 3.1d), and 1,2-dioleoyl-*sn*-glycero-3-phosphate (DOPA, Fig. 3.1e) were purchased from Avanti Polar Lipids, USA. 1,2-Diheptanoyl-*sn*-glycero-3-phosphocholine (DihepPC, Fig. 3.1b) was bought from Avanti Polar Lipids, USA and Affymetrix, USA. 1,2-dimyristoyl-*sn*-glycero-3-phosphocholine (DMPC, Fig. 3.1c) was obtained from Genzyme Pharmaceuticals, Switzerland and Affymetrix, USA. Deuterated  $d_{38}$ -DPC was bought from Cambridge Isotope Laboratories, USA, and 5-doxyyl-stearic acid (5-SASL, Fig. 3.1g ) and 16-doxyyl-stearic acid (16-SASL, Fig. 3.1h) from Sigma Aldrich, Germany.

Generally, lipid stock solutions for the titrations were prepared as follows. A defined amount of lipid from a concentrated stock in chloroform was placed in a glass vial and dried under a stream of nitrogen gas. The dried lipid was then dissolved in buffer or the protein sample, the pH was adjusted to 6.5. Only DihepPC was weighted and then directly dissolved in buffer or the peptide solution (only htrapatc). Micelles form above the critical micelle concentration (CMC), which is 1.1 mM for DPC [159] and 1.4 - 1.8 mM for DihepPC [160, 161].

For the preparation of bicelles consisting of DMPC and DihepPC ( $q = 0.2$ ,  $[DMPC] = 0.04$  M, and  $[DihepPC] = 0.20$  M,  $c_L \sim 12.3$  % w/w, respectively,  $q = 0.3$ ,  $[DMPC] = 0.0625$  M, and  $[DihepPC] = 0.21$  M,  $c_L \sim 14.4$  % w/w) the appropriate amount of a DMPC stock solution in chloroform was placed in a glass vial and dried by nitrogen gas. Bicelles were formed by stepwise addition of the appropriate amount of a DihepPC stock solution in buffer and vigorous vortexing after each step. Last, the protein solution was added and the pH was adjusted to 6.5.

For the preparation of liposomes, an appropriate amount of DMPC in chloroform needed for a 50 mM or 100 mM solution, respectively, was placed in a glass vial and dried under a stream of nitrogen gas. The lipid was resuspended in NMR buffer and dissolved by seven cycles of freezing in liquid nitrogen, incubation in a water bath at 40 °C, and vigorous vortexing. The formation of small unilamellar vesicles (SUVs) was induced by incubation in an ultrasonic bath for about 30 min. Centrifugation for 5 min at maximum speed in a table top centrifuge allowed the separation of the remaining large, uni- and multilamellar vesicles that form a fluffy white precipitate. Only the clear supernatant containing the SUVs was used for the NMR and CD sample preparation. Using the 50 mM stock solution the final sample contained <30 mM DMPC and using the 100 mM stock solution <60 mM. Note that the exact amount of DMPC left after centrifugation of the ultra sonicated liposome mixture is not known.

## 3.5 NMR sample preparation

### 3.5.1 GB1xa

For NMR association studies of gblxa, ylfatc and ylfatc-gblxa fusion proteins and mutant versions the protein concentration was in the range of  $\sim 50 - 150$   $\mu$ M  $^{15}$ N-labeled protein in 50 mM Tris, 100 mM NaCl, 0.02 %  $\text{NaN}_3$  (95 %  $\text{H}_2\text{O}/5$  %  $\text{D}_2\text{O}$ ), pH 6.5. NMR samples in the presence of micelles contained either 50 - 150 mM DPC or 50 mM DihepPC. The bicelles were composed of DMPC/DihepPC bicelles ( $q = 0.2$ ,  $[DMPC] = 0.04$  M, and  $[DihepPC] = 0.20$  M,  $c_L \sim 12.3$ % w/w) and the liposomes were prepared using the 50 mM DMPC stock with an end concentration <30 mM.

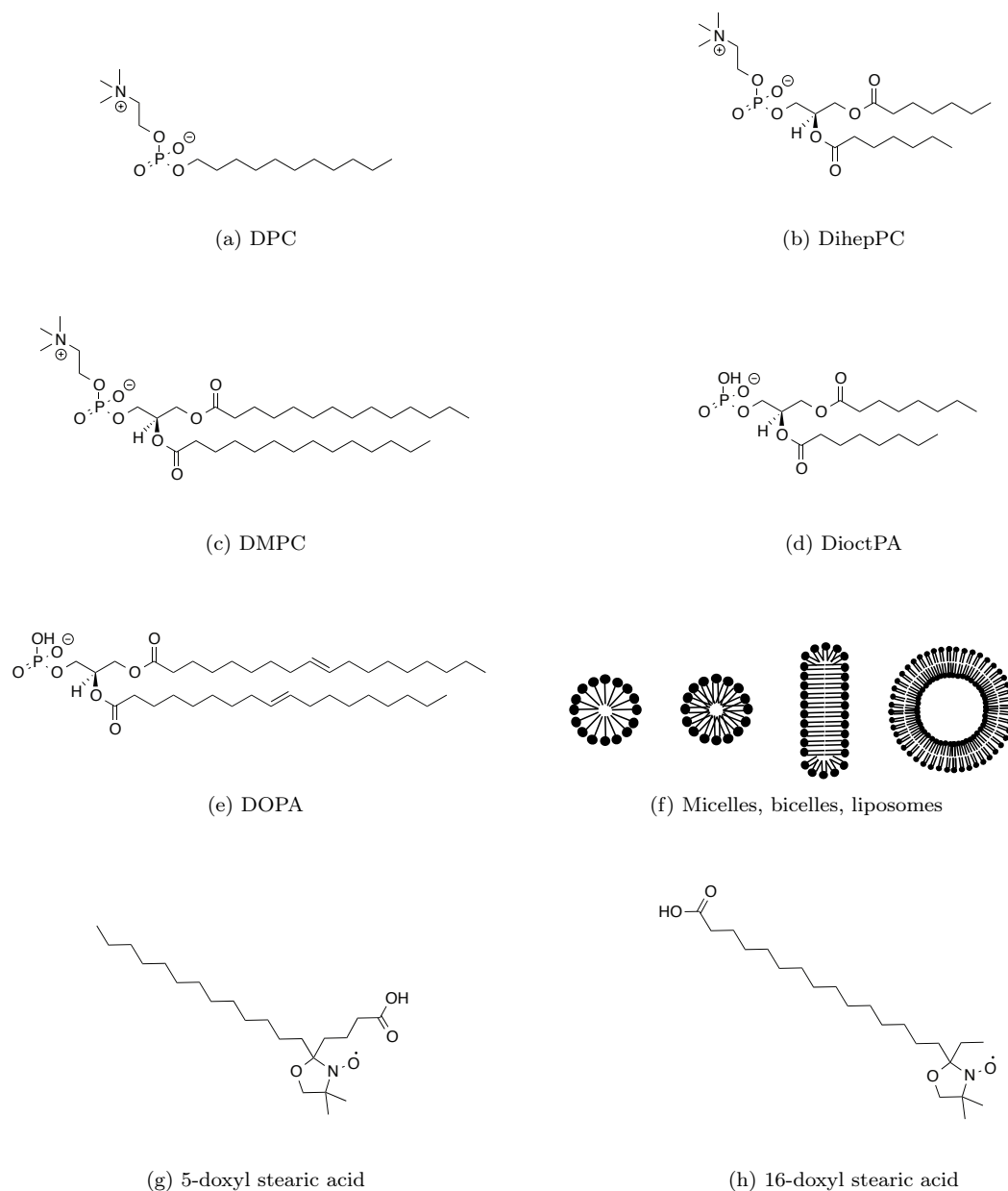


Figure 3.1: Chemical structures of the used lipids and spin labeled fatty acid molecules. Dodecylphosphocholine (DPC) (a), 1,2-Diheptanoyl-*sn*-glycero-3-phosphocholine (DihepPC) (b), 1,2-Dimyristoyl-*sn*-glycero-3-phosphocholine (DMPC) (c), 1,2-Dioctanoyl-*sn*-glycero-3-phosphate (DioctPA) (d), 1,2-Dioleoyl-*sn*-glycero-3-phosphate (DOPA) (e). Schematic representation of membrane mimetics (from left to right): small spherical micelles composed of detergents or lipids with one or two fatty acid lipid chain (e.g. DPC ~19 kDa), more planar bicelles (>250 kDa), and the spherical liposomes of the small unilamellar vesicle type (SUV) (f). 5-doxyyl stearic acid (5-SASL) (g) and 16-doxyyl stearic acid (16-SASL) (h).



### 3.5.2 DNA-PKcs, ATM, SMG-1, ATR, and TRRAP

For the NMR resonance assignment and structural characterization in the absence and presence of micelles, the samples contained  $\sim 0.4$  mM of  $^{15}\text{N}$ - or  $^{15}\text{N}$ - $^{13}\text{C}$ -hdnapkfadc-gblent in 50 mM Tris, 100 mM NaCl, 10 mM TCEP, 0.02 %  $\text{NaN}_3$  (95 %  $\text{H}_2\text{O}/5$  %  $\text{D}_2\text{O}$ ), pH 6.5 with or without 150 mM  $\text{d}_{38}$ -DPC. The sample that was used for the resonance assignment and initial structural characterization of pure hdnapkfadc contained  $\sim 0.4$  mM  $^{15}\text{N}$ -labeled protein in 20 mM NaPi, 50 mM NaCl, 10 mM TCEP, 0.02 %  $\text{NaN}_3$  (95 %  $\text{H}_2\text{O}/5$  %  $\text{D}_2\text{O}$ ), pH 6.5. For the titrations and interaction studies of pure hdnapkfadc or hdnapkfadc-gbl (ent or xa) with different lipids or lipid mixtures, the protein concentration was in the range of  $\sim 65$  - 100  $\mu\text{M}$  in 50 mM Tris, 100 mM NaCl, 0.02 %  $\text{NaN}_3$  (95 %  $\text{H}_2\text{O}/5$  %  $\text{D}_2\text{O}$ ), pH 6.5. The concentration of the DPC stocks in buffer used for the titrations were 50 mM, 250 mM, and 1 M. For the titration with the negatively charged lipid phosphatidic acid (PA) a 4:1 mixture of DioctPA and DOPA was used (in total 50 mM lipid, 40 mM DioctPA, 10 mM DOPA). The bicelles for the sample of  $^{15}\text{N}$ -hdnapkfadc-g1xa were composed of DMPC/DihepPC ( $q = 0.3$ ,  $[\text{DMPC}] = 0.0625$  M, and  $[\text{DihepPC}] = 0.21$  M,  $c_L \sim 14.4$  % w/w).

All hatmfadc-gblent NMR samples contained 50 mM Tris, 100 mM NaCl, 0.02 %  $\text{NaN}_3$  (95 %  $\text{H}_2\text{O}/5$  %  $\text{D}_2\text{O}$ ), pH 6.5. The samples in the absence or presence of 150 mM  $\text{d}_{38}$ -DPC had a concentration of  $\sim 0.46$  mM  $^{15}\text{N}$ -labeled protein and those in the absence or presence of  $< 30$  mM DMPC liposomes  $\sim 0.12$  mM. The sample used for the titration with DPC and those in presence and absence of 50 mM DihepPC micelles or DMPC/DihepPC bicelles ( $q = 0.2$ ,  $[\text{DMPC}] = 0.04$  M, and  $[\text{DihepPC}] = 0.20$  M,  $c_L \sim 12.3$  % w/w) had a concentration of  $\sim 0.2$  mM  $^{15}\text{N}$ -hatmfadc-gblent, respectively. The concentration of the used DPC stocks for the NMR monitored titration of hatmfadc-gblent was 25 mM and 500 mM. For the final titration step (10 to 50 mM DPC), an appropriate amount of DPC in chloroform was dried under a stream of  $\text{N}_2$  gas and dissolved by adding the NMR sample from the second last titration step.

All hsmg1fad peptide NMR samples contained 50 mM Tris, 300 mM NaCl, 0.02 %  $\text{NaN}_3$  (95 %  $\text{H}_2\text{O}/5$  %  $\text{D}_2\text{O}$ ), pH 8.0. The peptide concentration in the samples of the free peptide or in presence of 50 mM  $\text{d}_{38}$ -DPC or 50 mM DihepPC was  $\sim 1$  mM. All hatrfadc peptide NMR samples contained 50 mM Tris, 50 mM NaCl, 0.02 %  $\text{NaN}_3$  (95 %  $\text{H}_2\text{O}/5$  %  $\text{D}_2\text{O}$ ), pH 7.7. The peptide concentration in the samples of the free peptide or in presence of 50 mM  $\text{d}_{38}$ -DPC was  $\sim 0.23$  mM. All htrrapfad peptide NMR samples contained 50 mM Tris, 100 mM NaCl, 0.02 %  $\text{NaN}_3$  (95 %  $\text{H}_2\text{O}/5$  %  $\text{D}_2\text{O}$ ), pH 6.5. The peptide concentration in the samples of the free peptide or in presence of 50 mM  $\text{d}_{38}$ -DPC or 48 mM DihepPC was  $\sim 0.92$  mM.

### 3.5.3 TOR

For NMR membrane interaction studies in the absence and presence of DPC micelles the protein concentrations of y1fad wild type and mutant versions of y1fad were in the range of 20 - 200  $\mu\text{M}$  in 50 mM Tris, 100 mM NaCl, 0.02 %  $\text{NaN}_3$  (95 %  $\text{H}_2\text{O}/5$  %  $\text{D}_2\text{O}$ ), pH 6.5 with or without 50 mM or 100 mM DPC. The concentration of the DihepPC stocks in buffer used for the titration of y1fad wild type were 25 mM, 250 mM, and 0.5 mM. The bicelles for the samples of  $^{15}\text{N}$ -y1fad wild type or mutant versions were composed of DMPC/DihepPC ( $q = 0.2$ ,  $[\text{DMPC}] = 0.04$  M, and  $[\text{DihepPC}] = 0.20$  M,  $c_L \sim 12.3$  % w/w). The liposomes for the samples of  $^{15}\text{N}$ -y1fad wild type or mutant versions were prepared using 50 mM DMPC stock with an end concentration  $< 30$  mM. For PRE experiments with oxidized y1fad, samples containing  $\sim 66$   $\mu\text{M}$  and 50 mM  $\text{d}_{38}$ -DPC were prepared. The concentration of 5- and 16-doxyl stearic acid was increased by stepwise addition of a small amount of a 0.25 mM stock solution in buffer. The procedure was analogous for the reduced form. Reduction of the protein was achieved by addition of 10 mM TCEP.

### 3.6 OCD and reference CD sample preparation

Weighed amounts of the lipid powders were dissolved in 50:50 chloroform/methanol (v/v) to get 7 mM stock solutions. Aliquots of these stock solutions were mixed in a glass vial and thoroughly vortexed to obtain the DMPC/DMPG mixture (1:1 molar ratio). Subsequently, the organic solvents were removed under a gentle stream of nitrogen, followed by overnight vacuum pumping to remove solvent residuals from the respective DMPC or DMPC/DMPG lipid film that had formed in the vial. The lipid films were dispersed by the addition of 600  $\mu\text{L}$  10 mM phosphate buffer (PB) pH 7.0 and homogenized by vigorously vortexing for 10 times one min and by ten freeze-thaw cycles. Afterward, small unilamellar vesicles were formed by sonication of the multilamellar vesicles for four min in a strong ultrasonic bath (UTR 200, Hielscher, Germany). The sonication procedure was repeated three times.

Liposomes for the OCD and corresponding reference CD measurements were prepared as follows. A weighed amount of the protein was dissolved in 10 mM PB resulting in a stock solution with a y1fatc protein concentration of 284  $\mu\text{M}$ . For preparation of the final CD samples aliquots of the protein stock solution were added to aliquots of 10 mM PB or the corresponding liposome solution in 10 mM PB. Reduction of the y1fatc disulfide bond in some of the protein samples was performed by adding a 40-fold molar excess of TCEP-HCl and incubation for  $\sim 2$  h. The final protein concentration in 10 mM PB alone was between 29  $\mu\text{M}$  and 38  $\mu\text{M}$  and in the lipid vesicle samples 14.8  $\mu\text{M}$  and 29.5  $\mu\text{M}$ , respectively, whereas the lipid concentration in the vesicles was held constant at 1.475 mM resulting in peptide-to-lipid (P/L) ratios of 1:100 and 1:50.

To prepare oriented CD (OCD) samples, aliquots of around 140  $\mu\text{l}$  of the corresponding y1fatc SUV solutions were deposited with a pipette as a circular-shaped spot of  $\sim 12$  mm diameter on a quartz glass plate, and the water was evaporated in a gentle stream of air until the sample appeared dry. The amount of deposited lipid was in the range of 0.15 - 0.22  $\mu\text{mole}$ , and the total amount of peptide on the glass plate was 1.5 - 4 nmole with the same P/L ratios of 1:50 or 1:100 that had been adjusted before in the vesicle samples. The circular quartz glass plate with 20 mm diameter (Suprasil QS, Hellma Optik GmbH, Jena, Germany) serves as UV transparent window with the dried sample, which is assembled with a second clean window in the OCD sample cell to form the compartment for hydration and measurement of the sample. Here, the glass-enclosed, air-exposed lipid film was rehydrated for about 15 h at 30  $^{\circ}\text{C}$  and 97 % relative humidity (RH), using a saturated  $\text{K}_2\text{SO}_4$  solution filled into the bottom of the cell. During hydration the lipids spontaneously align as lipid bilayers, which are macroscopically oriented parallel to the glass surface.

### 3.7 CD spectroscopy

All CD spectra were recorded at 298 K on Jasco J-715 or J-720 (Jasco, Germany) spectropolarimeters in the range of 190 - 260 nm using a quartz cuvette with a pathlength of 0.1 cm. Spectra were generally recorded with an acquisition time of 50 nm/min (8 s response time) and five scans. The sample for the CD measurement of pure hdnapkf<sub>atc</sub> was 25  $\mu\text{M}$  in 20 mM  $\text{NaP}_i$ , 50 mM NaCl, 10 mM TCEP, pH 6.5. The peptide concentration of the hsmg1fatc samples was 56.8  $\mu\text{M}$ , the one of the hatrfatc samples 16.4  $\mu\text{M}$ , and the one of the htrrapfatc samples 25.2  $\mu\text{M}$ . The buffer for the peptide samples was the same as for the NMR measurements.

The protein concentration for CD experiments with y1fatc and mutants was approximately 30  $\mu\text{M}$  in 50 mM Tris, 100 mM NaCl, pH 6.5. In the case of the quadruple mutant sample, the determination of the protein concentration was error-prone and could only be estimated.

The DPC samples contained additionally 50 mM DPC. The mean residue weight ellipticity  $\theta_{MRW}$  was derived according to:

$$\theta_{MRW} = \frac{(\theta_m - \theta_{ref}) \times 100}{c \times d \times N_a} \quad (3.1)$$

$$(3.2)$$

where  $\theta_m$  is the ellipticity of the protein sample [*mdeg*],  $\theta_{ref}$  is the ellipticity of the reference sample [*mdeg*],  $c$  denotes the protein concentration [ $\frac{mol}{l}$ ],  $d$  corresponds to the path length of the cuvette [*cm*], and  $N_a$  equals the number of amino acids in the protein sequence (for untagged PIKK FATCs  $N_a = 33$ ).

### 3.8 OCD and corresponding reference CD spectroscopy

CD spectra of the reduced and oxidized protein in phosphate buffer and in DMPC or DMPG/DMPC (1:1) liposomes were recorded on a J-815 spectropolarimeter (JASCO). The samples were measured in a quartz glass cell (Suprasil, Hellma Optik GmbH, Jena, Germany) of 1 mm path length between 260 and 185 nm at 0.1 nm intervals. Spectra were recorded at 25 °C for the protein in PB and at 30 °C for the protein-liposome solutions, i.e. above the phase transition temperature of the lipids, using a water-thermostated rectangular cell holder. Three repeat scans at a scan-rate of 10 nm/min, 8 s response time and 1 nm bandwidth were averaged for each sample and the baseline of the respective protein-free sample, which was subtracted from the sample spectrum. CD spectra were smoothed by the adaptive smoothing method, which is part of the Jasco Spectra Analysis software. Secondary structure analysis was performed using the CONTIN and CDSSTR program with the implemented ridge regression algorithm [162, 163], that is provided by the DICHROWEB server [164, 165]. The quality of the fit between experimental and back-calculated spectrum corresponding to the derived secondary structure element fractions was assessed from the normalized root mean square deviation (NRMSD), with a value <0.1 considered as a good fit [165]. For calculating mean residue ellipticities used for secondary structure estimation, the concentration of the ylfatc protein stock solution was determined based on the UV absorbance of the protein at 280 nm. The absorption spectrum in the range of the aromatic bands was recorded in the range from 340 – 240 nm using a quartz glass half-micro-cuvette with 1 cm optical path length (Hellma, Müllheim, Germany). The blank for the UV absorption measurement was the corresponding 10 mM PB solution. Afterwards, the concentration of the corresponding final peptide solutions for CD measurements in aqueous PB and in the liposomes was calculated from the respective dilution factors.

The set-up (Karlsruhe Institute of Technology, Institute for Biological Interfaces (IBG-2), Germany) used for the OCD measurements is similar to the cell described by Chen [149]. The optical path of the CD spectropolarimeter is parallel to the cylindrical axis of the cell and normal to the quartz glass window with the oriented sample (Fig. 3.2). It consists of an aluminum frame with two ring-shaped cavities and a central bore for taking up the sample holder. Water from a computer-controlled external water bath thermostat with a thermo-electric feedback module was passed through the closed outer cavity of the cell, which allowed to control the temperature of the whole cell over a 5 - 50 °C range with a stability of  $\pm 0.1$  °C. The second cavity around the central bore was filled with a small volume of saturated salt solution for controlling the humidity of the sample.

The sample holder consists of a threaded tube with two quartz glass windows fixed vertically inside at a distance of 6 mm by two brass rings. Halfway between the windows the casing contains holes in a circular arrangement around the tube, so that the vapor from the salt solution

can hydrate the sample without direct contact between the solution and the sample. The space between the two windows is sealed by four O-rings to avoid contact with ambient air. The humidity and temperature within the sample cell is monitored by a capacitive relative humidity and temperature sensor (SHT 75, Sensirion, Switzerland), which is fixed in the immediate vicinity of the sample (within 12 mm) in a gap between the sample holder and the cavity containing the salt solution. The humidity can be measured with an absolute accuracy of  $\pm 1.8$  % RH by the sensor ( $\pm 3\%$  at values  $> 90$  % RH). When using a saturated  $\text{K}_2\text{SO}_4$  salt solution with 96 – 98 % RH, the equilibration of temperature and humidity in the closed OCD cell takes  $\sim 2 - 3$  h. However, to assure proper hydration across the whole depth of the lipid bilayers, all samples were hydrated overnight ( $\sim 15$  h). Sample equilibration was ensured by acquiring OCD spectra over a period of hours [150].

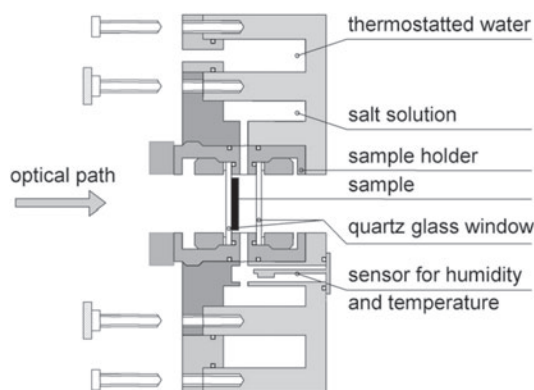


Figure 3.2: Cross-sectional view of the OCD cell (Jochen Bürck, KIT) [150].

The OCD cell is computer controlled and can be integrated in a J-810 spectropolarimeter (Jasco, Germany) as an accessory, attached in such a way that the optical path runs along the cylindrical axis of the cell (normal to the quartz glass window surface carrying the oriented lipid film) and a symmetrical rotation around the beam axis was assured. The temperature was maintained at 30 °C for ylfatc in oriented DMPC or DMPC/DMPG (1:1) bilayers. To reduce possible spectral artifacts caused by linear dichroism (LD) or linear birefringence (LB) due to imperfections in the sample, strain in the quartz glass windows or imperfect alignment of the windows [145, 146], the OCD spectra were recorded in steps of  $45^\circ$  by rotation of the cell [149]. At each angle three scans were recorded as an average, using the same data acquisition parameters as in the conventional CD measurements above, as well as for the baseline of the respective protein-free sample. The eight rotational spectra were subsequently averaged, and the background spectra of lipid bilayers without peptide were subtracted.

### 3.9 NMR spectroscopy

NMR spectra were acquired at 298 K and 318 K on Bruker Avance 500 and 750 MHz spectrometers, the 500 MHz one equipped with a cryogenic probe. The data were processed with NMRPipe [166] and analyzed using NMRView [167]. Assignments for the  $^{13}\text{C}$ ,  $^{15}\text{N}$ , and  $^1\text{H}$  nuclei of hdnapkfadc-gb1ent were based on three-dimensional HNCA, CCONH-TOCSY, HCCH-TOCSY, and  $^{15}\text{N}$ - and  $^{13}\text{C}$ -edited NOESY spectra. Pure, free hdnapkfadc was assigned based on three-dimensional  $^{15}\text{N}$ -edited NOESY and TOCSY spectra, as well as three-dimensional HNHA [168] and HNHB data sets. Information about backbone dynamics was derived from

the measurement of  $^{15}\text{N}$  relaxation experiments, including  $T_1$ ,  $T_2$ , and  $\{^1\text{H}\}$ - $^{15}\text{N}$  NOE at 500 MHz. Assignments for the  $^{15}\text{N}$ , and  $^1\text{H}$  nuclei of micelle immersed hatmfatc-gblent were based on three-dimensional  $^{15}\text{N}$ -edited NOESY and TOCSY as well as HNHA [168] data sets. Information about backbone dynamics was derived from  $\{^1\text{H}\}$ - $^{15}\text{N}$  NOE data at 500 MHz. For the calculation of  $^1\text{H}$ ,  $^{15}\text{N}$ , and  $^{13}\text{C}$  secondary shifts, random coil values from the literature were used [116]. The interaction with membrane mimetics was monitored based on  $^1\text{H}$ - $^{15}\text{N}$  HSQC and one-dimensional  $^1\text{H}$  NMR spectra, and for hatmfatc-gblent also based on  $\{^1\text{H}\}$ - $^{15}\text{N}$  NOE data. For hsmg1fatc and htrrapfatc the  $^1\text{H}$ - $^{15}\text{N}$  HSQC had to be recorded at natural abundance. For hsmg1fatc, in the absence and presence of  $\text{d}_{38}$ -DPC, this was done using the SOFAST-HMQC pulse program [119, 169]. The average chemical shift change for the backbone amide nitrogen and proton for hdnapkfatc due to the presence of DPC micelles or DihepPC/DMPC bicelles was calculated as:

$$\Delta\delta(N, H)_{av} = \left[ (\Delta\delta_{HN})^2 + \left( \frac{\Delta\delta_N}{5} \right)^2 \right]^{0.5} \quad (3.3)$$

For hatrfatc, natural abundance  $^1\text{H}$ - $^{15}\text{N}$  HSQC spectra could not be recorded because the peptide concentration could not be increased sufficiently without suffering from aggregation problems. NMR diffusion measurements for hsmg1fatc and htrrapfatc were measured using the DOSY tool in Bruker Topspin 3.1 as described in the manufacturer's manual [170]. The length of the gradient  $\delta$  and the diffusion time  $\Delta$  was set to 4000 msec/200 msec and 3000 msec/300 msec.

### 3.10 MD simulations

Molecular dynamics simulations were run using GROMACS 4.5 [171, 172]. Four systems were simulated, the oxidized peptide (2kio) and the reduced peptide (2kit) [69] with either the 5- or 16-SASL. The peptide and a spin labeled stearic acid were simulated with a DPC micelle (50 DPCs) and explicit water (ca. 10 000 water molecules). The systems were created with the peptide in bulk water outside of the preformed micelle that contained a single spin labeled stearic acid (5- or 16-SASL). In each simulation, the peptide absorbed quickly onto the interface of the micelle. The Berger force field was used for DPC [173], GROMOS54a7 for the peptide [174], SPC for water [175], and a modified GROMOS force field for the spin labeled stearic acid [176, 177]. Each simulation was run for 500 ns using a 2 - 4 fs time step. Bond lengths were constrained with the LINCS algorithm [178] and water bond lengths and angles were constrained with SETTLE [179]. A temperature of 310 K was maintained using the V-rescale thermostat and a 0.1 ps coupling constant [180]. Isotropic pressure coupling using the Berendsen weak coupling algorithm was used with 1 bar reference pressure,  $4.5 \times 10^{-5} \text{ bar}^{-1}$  compressibility and a 2.5 ps coupling constant [181]. The particle mesh Ewald algorithm (PME) was used for long electrostatic interactions [182, 183]. Lennard-Jones interactions were cut-off at 1.0 nm. Analysis was then performed yielding radial distribution functions, minimum distances between the peptide and micelle members, and peptide stability measurements (RMSD and peptide length). Images were generated with the program VMD [184].



# Chapter 4

## Results

### 4.1 Probing the interaction of peptides and proteins with membrane mimetics using GB1 fusion proteins

#### 4.1.1 Spectral appearance of the GB1 tag in the presence of membrane mimetics

The ability of the GB1 fusion tag to interact with membranes was probed by recording  $^1\text{H}$ - $^{15}\text{N}$  HSQC spectra in the presence and absence of different membrane mimetics. For this purpose, the cleaved off fusion tag from the purification of the free yeast TOR1 FATC domain was used, which consists of GB1 that is C-terminally followed by a linker region containing a thrombin (LVPRGS) [152] and an additional factor Xa site (IEGR) (Fig. 4.1a). This construct is referred to as GB1xa [185]. Figure 4.1b shows a superposition of the  $^1\text{H}$ - $^{15}\text{N}$  HSQC spectra of  $^{15}\text{N}$ -GB1xa in the presence of DPC or DihepPC micelles or DihepPC/DMPC bicelles or DMPC liposomes. Separate plots for each membrane mimetic, in the case of DPC for different concentrations are given in Fig. 4.2a - 4.2d. The majority of residues of GB1xa shows no significant spectral changes. Only in the presence of high concentrations of DPC and DihepPC micelles and DihepPC/DMPC bicelles, very small local shifts can be observed for some residues, which presumably arise from unspecific interactions in the presence of high mM concentrations of the respective lipids. However, these shifts are so small that the overall spectral appearance is maintained (Fig. 4.1b, Fig. 4.2a - 4.2d). A change in the overall appearance was also not the case, when GB1xa is titrated stepwise with DPC in buffer (Fig. 4.2a, see also [186]). Thus, the presence of the GB1 fusion tag is not expected to disturb the detection of membrane association of a linked target protein.

#### 4.1.2 Detection of y1fatc membrane association using GB1 fusions

To test the usefulness of GB1 fusion proteins to probe protein membrane interactions, as a first step spectra of the y1fatc-gb1xa fusion in the absence and presence of DPC micelles and DMPC liposomes were recorded (Fig. 4.1c, for which the spectrum of the free gb1xa was superimposed).

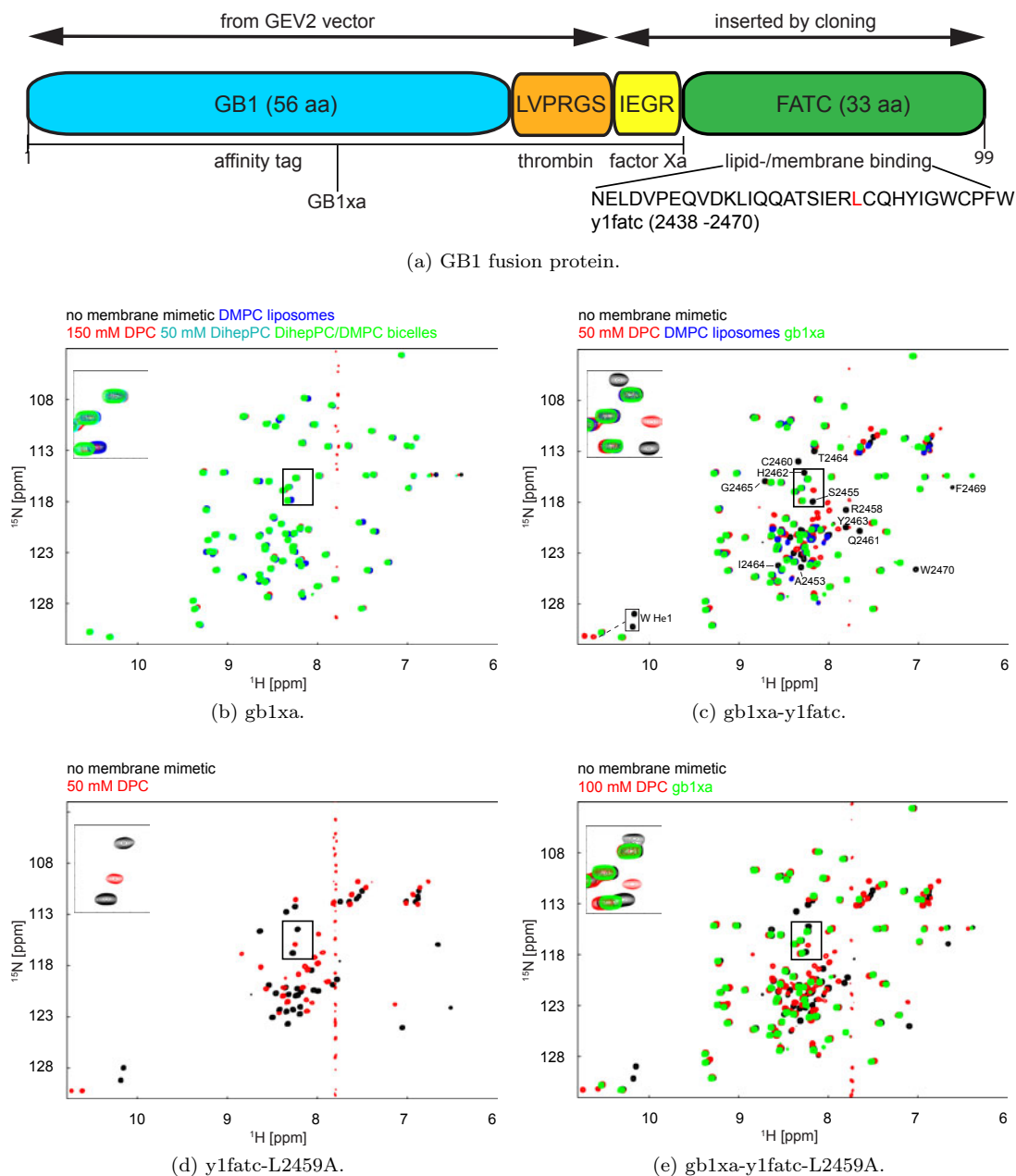


Figure 4.1: Schematic representation of the used GB1 fusion proteins (a) and monitoring of membrane mimetic interactions (b-e). Buildup of the GB1 fusion proteins with the sequence of y1fatc on the bottom right (a). Superposition of the  $^1\text{H}$ - $^{15}\text{N}$  HSQC spectra of gb1xa in the absence and presence of the indicated membrane mimetics (b). Superposition of the  $^1\text{H}$ - $^{15}\text{N}$  HSQC spectra of gb1xa-y1fatc in the absence and presence of DPC micelles or DMPC liposomes. The indicated assignments for well resolved peaks for the free y1fatc part were adapted from the published values (BMRB accession code 6228 [68]) (c). Superposition of the  $^1\text{H}$ - $^{15}\text{N}$  HSQC spectra of y1fatc-L2459A and gb1xa-y1fatc-L2459A in the absence and presence of DPC micelles (d-e). To better identify the signals that belong to y1fatc and that shift upon addition of membrane mimetics, the spectrum of gb1xa was additionally shown on top in green. *Reprinted (adapted) with permission from [157] - Copyright (2012) Protein Science.*



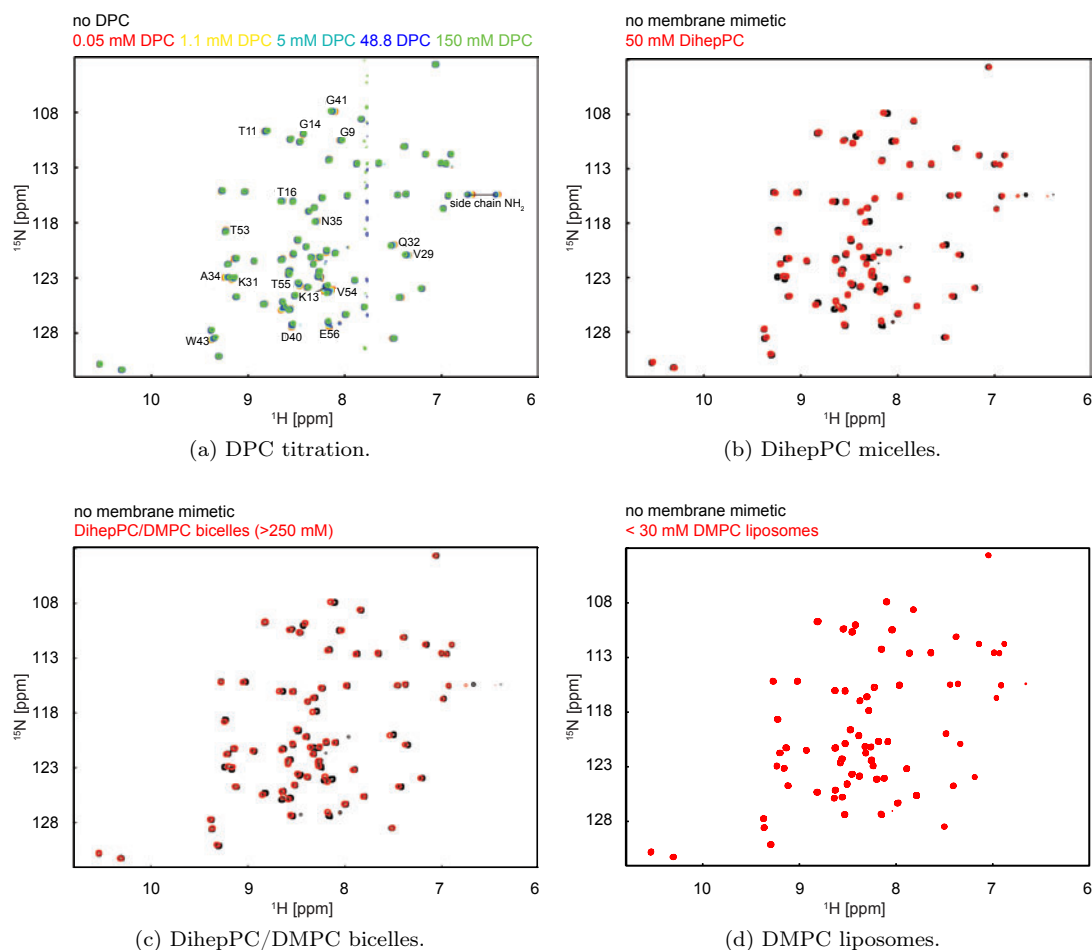


Figure 4.2: Analysis of the interactions of GB1xa with different membrane mimetics. NMR titration of  $^{15}\text{N}$ -gb1xa with DPC (a). The color coding and the respective lipid concentration is indicated at the top of the plot. Micelles are formed above the critical micelle concentration (CMC, 1.1 mM for DPC). The assignments for some peaks showing slight shifts are indicated. Superposition of the  $^1\text{H}$ - $^{15}\text{N}$  HSQC spectra of gb1xa in the absence and presence of 50 mM DihepPC micelles (b). Micelles are formed above the critical micelle concentration (CMC, 1.4 - 1.8 mM for DihepPC). Superposition of the  $^1\text{H}$ - $^{15}\text{N}$  HSQC spectra of gb1xa in the absence and presence DihepPC/DMPC bicelles (>250 mM), and DMPC liposomes (<30 mM) (c-d). Reprinted (adapted) with permission from [157] - Copyright (2012) Protein Science.

As can be seen, only peaks of the FATC part show major chemical shift changes. The observed spectral changes in the presence of DPC are similar compared to what is observed for untagged y1fatc [69]. Using higher DPC concentrations ( $\sim 150$  mM) to drive the association equilibrium towards the bound state and for the oxidized form additionally to higher temperatures (318 K), almost all peaks of the reduced and oxidized micelle immersed state of y1fatc can be made visible [69]. This should similarly be possible using the GB1 fusion protein instead of the untagged one. The resonances of the liposome-bound form are harder to be detected, because SUVs are significantly larger [187] compared to the rather small DPC micelles ( $\sim 19$  kDa) [188]. Thus, association with a liposome broadens the protein signals beyond detection. In this case, higher lipid concentrations or higher temperatures will presumably not solve the problem.

If the resonances of the liposome-bound state shall be made visible, one may consider the use of deuterated protein in combination with transverse relaxation optimized (TROSY) NMR methods [189]. To directly compare the spectral changes obtained with the untagged protein and fused to GB1, the interaction of a mutant of y1fatc was probed, in which L2459 was replaced by alanine and which is referred to as y1fatc-L2459A. Fig. 4.1d and 4.1e show superpositions of the  $^1\text{H}$ - $^{15}\text{N}$  HSQC spectra of y1fatc-L2459A or as fusion to GB1 in the absence and presence of DPC micelles, respectively. The observed spectral changes are similar to those observed for the wild type (Fig. 4.1c) indicating that replacing L2459 in the membrane anchor by alanine does not significantly impair micelle association. For most residues, the chemical shifts of the backbone and side chain amides of GB1 tagged and untagged y1fatc-L2459A in the free and DPC micelle-bound states are very similar. Thus, the presence of GB1 and the linker region appears not to affect the structure of the following FATC region.

The factor Xa (IEGR) and the thrombin site (LVPRGS) have a net charge of 0 and +1, respectively. However, the presence of more strongly charged protease sites, such as an enterokinase (ent) recognition site (DDDDK, net charge -3) may slightly lower the affinity for membrane mimetics, especially if they contain negatively charged lipids such as phosphoinositides (PIPs) or phosphatidic acid (PA). Hence, the interaction of the FATC domain of DNA-PKcs fused to either gb1xa or gb1ent with DPC and liposomes was probed, which however reveals no difference in the association behavior either (see section 4.2).

### 4.1.3 Summary and discussion

The purification schemes of recombinant proteins follow very often the strategy to express proteins as tagged fusion proteins. Besides the use of polyhistidine (His), glutathione-S-transferase (GST), and maltose-binding protein (MBP) fusion proteins for structural, biochemical, and functional analysis [190, 191], also fusions to the B1 domain of streptococcal protein G (GB1) are utilized. Commonly, the advantage of using fusion proteins is the high level of expression, the enhanced solubility and stability of the target protein, and the accelerated purification of the target protein [192]. For these reasons, the usage of fusion proteins for the production of high amount of protein with sufficient purity is widely distributed in NMR spectroscopy and X-ray crystallography [155]. The first purification step for GB1 fusion proteins using IgG affinity chromatography is simple and very efficient regarding the yield, however the following cleavage is laborious, not always complete and might result in digest of the target protein. Furthermore, the digest implies an additional purification step such as RP-HPLC to separate the target protein from the tag.

Since the digest and the necessary further purification step are time consuming, expensive, and requiring optimization of digest and purification conditions, the idea of this study was to develop a method, which enables fast and efficient monitoring of membrane interactions. The focus was on the FATC domain of the serine/threonine kinase TOR and the role of single residues regarding the association behavior to membrane mimetic particles. The data reveal that the GB1 domain, the cleaved off fusion tag of the FATC domain of yeast TOR1, shows no significant spectral changes with any tested lipid or membrane mimetic in the NMR experiments. Only for high mM concentrations of the applied lipids small local shifts for some residues can be observed, emerging presumably from unspecific interactions. However, the overall spectral appearance is maintained. The following comparison of the association of the wild type or a mutant protein of the FATC domain of yeast TOR1 (L2459A, leucine to alanine), tagged or untagged, with different membrane mimetics shows, that the GB1 fusion tag does not impair the detection of membrane association of the FATC domain. Thus, differences in the spectral appearance, observed in the absence and presence of a particular membrane mimetic using GB1 fusion proteins, correspond to the target protein (here y1fatc or y1fatc-L2459A).

Because of the linker region, GB1 and the attached target protein tumble rather independently. This and the small size of the GB1 tag allows the use of GB1 fusion proteins, at least for small to mid-size target proteins, to record NMR data for the chemical shift assignment and the structural characterization of the free and micelle-bound states [157]. As a consequence, several mutants could be investigated very fast and cost-efficient.

## 4.2 Membrane mimetic interactions of the FATC domains of different PIKKs

### 4.2.1 Characteristic features of the amino acid sequences

The alignment of the FATC domains of different human PIKKs (Fig. 4.3) illustrates that the C-terminal halves of DNA-PKcs, ATM, ATR, SMG-1, and TRRAP (shown are the well-conserved 33 residues) are rich in hydrophobic aromatic and aliphatic residues, similar to the FATC domain of TOR, which has been shown to interact with membrane mimetics [69]. For many of these hydrophobic residues a positive free energy contribution for the transfer of a model peptide from a lipid bilayer to water has been shown [193]. All share a conserved tryptophan at position 29 that is preceded by a small residue (mostly G, only for TRRAP with A). In addition, all contain at least another tryptophan and/or one or more tyrosine residues. Tryptophan rich peptides have been shown to have a high affinity for membrane mimetics and are often found at the interface between the apolar interior and the polar aqueous environment, based on an analysis of the membrane regions of several proteins [194]. Tyrosine with its side chain hydroxyl group may favor a similar location if present in a membrane-binding region.

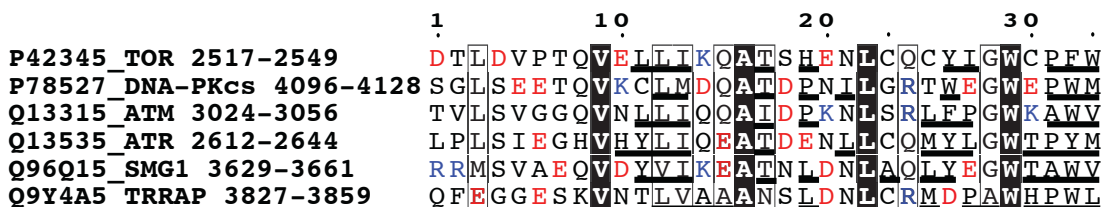


Figure 4.3: Distribution of hydrophobic and charged residues in the FATC domains of different human PIKKs. Hydrophobic aliphatic and aromatic residues are underlined. Negatively charged residues are colored red, whereas positively charged ones are shown in blue. *Reprinted (adapted) with permission from [10] - Copyright (2013) JBC.*

The amino acid sequence alignments of the FATC domains of DNA-PKcs, ATM, ATR, SMG-1, and TRRAP from different organisms are shown in Fig. 1.4. As can be seen the FATC domain of each PIKK has been evolutionarily highly conserved, especially among higher eukaryotes. More variation can be seen if lower eukaryotes and/or plants are included (see appendix, Fig. A.3). However, there is again a very high degree of sequence conservation if all plant or insect or other subgroups of species are considered, suggesting that the exact composition may be important for the regulation of the function and possibly a specific localization pattern. Based on these observations, all FATC domains were studied regarding their respective binding behavior to membrane mimetics and DNA-PKcs and ATM were structurally characterized in particular.

## 4.2.2 Structural characterization of the FATC domain of DNA-PKcs and its interactions with membrane mimetics

### 4.2.2.1 NMR interaction studies with membrane mimetics

The C-terminal six residues of the human FATC domain of DNA-PKcs (human: GWEPWM, Fig. 4.3) exhibit similarity to the predicted lipid binding motif of the human FATC domain of TOR (human: GWCPFW) [69]. To estimate the ability of the FATC domain of DNA-PKcs to interact with lipids or membrane mimetic particles,  $^1\text{H}$ - $^{15}\text{N}$  HSQC spectra of the pure FATC in the presence of increasing concentrations of DPC were acquired (Fig. 4.4a).

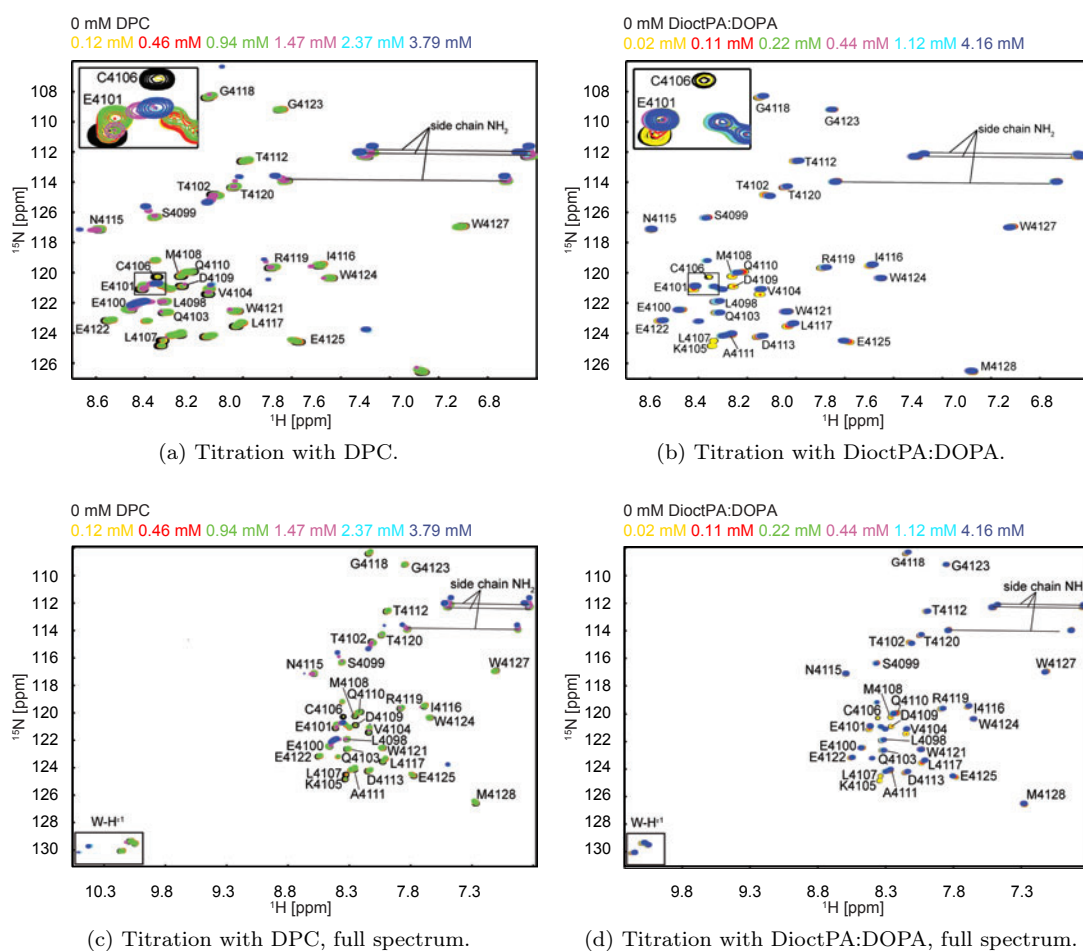


Figure 4.4: Membrane interactions of the FATC domain of DNA-PKcs with different micelles.  $^1\text{H}$ - $^{15}\text{N}$  HSQC spectra of hdnapkfatc in the presence of increasing amounts of DPC or a 4:1 mixture of DiocTPA:DOPA, respectively. The insert in the upper left corner shows an enlarged view of the region highlighted by a black square (a,b). Full  $^1\text{H}$ - $^{15}\text{N}$  HSQC spectra of hdnapkfatc in the presence of increasing amounts of DPC or a 4:1 mixture of DiocTPA:DOPA (c,d). The lipid concentrations with the respective color coding are indicated above each plot. *Reprinted (adapted) with permission from [10] - Copyright (2013) JBC.*

Up to a concentration of 0.94 mM DPC no significant spectral changes can be observed. However, at the next titration point corresponding to 1.47 mM DPC, which is just above the CMC

of DPC (1.1 mM), several resonances disappear or shift significantly. At 3.79 mM only few resonances in the N-terminal region and around residues 4115 - 4120 are still well visible. Fig. 4.5 illustrates the spectral changes as a function of the hdnapkfatc sequence. As expected based on previous lipid binding studies with the FATC domain of TOR [69], several resonances in the tryptophan-rich C-terminus (W4121 - M4128) show strong chemical shifts or disappear in the presence of 3.79 mM DPC. Consistent with this, the side chain amide protons of the three tryptophans show also strong chemical shift changes (Fig. 4.4c). In addition, several residues in the central region from C4106 to D4113 that contains several charged as well as hydrophobic, but no aromatic residues, reveal also medium to strong spectral changes. The side chain amides in this region (Q4103, Q4111, and N4115) show weak chemical shift changes. Since cellular membranes contain several lipids with negatively charged headgroups, the interaction of hdnapkfatc with a 4:1 mixture of the short chain lipid DioctPA (C8) and the long chain lipid DOPA (C18) was further analyzed (Fig. 4.4b). Significant spectral changes are already visible at the second titration point (0.11 mM total lipid). In the literature no values can be found for the CMC of DioctPA and DOPA. The CMC for DioctPA is expected to be in the same order as the one for dioctanoyl-phosphocholine (DioctPC, CMC 0.27 mM) and the one for 1,2-dioctanoyl-phosphoglycerol (DioctPG, CMC 1.21 mM) and the one for DOPA in the range of CMCs for dipalmitoyl-phosphocholine (CMC 0.46 mM) and dimyristoyl-phosphoglycerol (DMPG, CMC 0.011 mM)<sup>1</sup>. A mixture of DioctPA and DOPA is expected to form micelles at lower lipid concentrations than DioctPA alone, because the CMC of DOPA is much smaller compared to that for DioctPA due to the longer fatty acid chain (C18 versus C8). Thus, the CMC of the mixture is expected to be below  $\sim 0.1$  mM and hdnapkfatc may as observed for DPC only interact with membrane mimetic particles but not with single lipids.

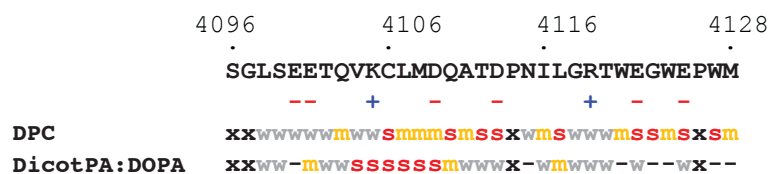


Figure 4.5: Summary of the chemical shift differences observed in the NMR titrations (Fig. 4.4). In all cases spectral changes were observed around the estimated CMC. Residues that disappeared just above the CMC are marked with a *red s*. Residues that disappeared or shifted significantly above the CMC are colored with an *orange m*, and those that disappeared or shifted at higher lipid concentrations are labeled with a *grey w*. Residues that were not significantly affected by the addition of lipid are marked with '-', while 'x' represents amino acids that show no  $^1\text{H}$ - $^{15}\text{N}$  HSQC peak. *Reprinted (adapted) with permission from [10] - Copyright (2013) JBC.*

In line with the presence of several negatively charged amino acids in the sequence (Fig. 4.5), the observed spectral changes are overall smaller than with the neutral DPC. This can be explained by electrostatic repulsion between the negative charges in the PA headgroup and the side chains of the present aspartates and glutamates (Fig. 4.5). In contrast to DPC, the strongest chemical shift changes with DicotPA:DOPA occur around the positively charged residue K4105. The backbone amide resonances of V4104 to Q4110 disappear or show significant chemical shift changes (Fig. 4.4b, 4.5), whereas the C-terminal tryptophan-rich region that contains two negatively charged glutamates show only very weak to no changes for the backbone resonances as well as for the side chain amides of the three tryptophans (Fig. 4.4b, 4.4d, and 4.5).

<sup>1</sup>All CMC values are found at the website of Avanti Polar Lipids ([www.avantilipids.com](http://www.avantilipids.com)) [195].

Since the yield of hdnapkfatc following the protease digest of the GB1 fusion protein was very low, the GB1 fusion protein with an additional enterokinase recognition site (hdnapkfadc-gb1ent) was used for further lipid binding experiments and structural characterization of the micelle-immersed state, based on results of section 4.1. To ensure that the presence of the GB1 tag does not influence the affinity of the interaction with DPC micelles,  $^{15}\text{N}$ -hdnapkfadc-gb1ent was titrated with DPC (Fig. 4.6a) similar as done for the pure FATC domain (Fig. 4.4a). However, the final DPC concentration was significantly higher ( $\sim 60$  mM) to shift the equilibrium more to the micelle immersed state. As for the pure FATC domain (Fig. 4.4a), several peaks of hdnapkfatc-gb1ent start to shift at  $\sim 1.5$  mM (Fig. 4.6a), which is just above the CMC of DPC (1.1 mM). Until  $\sim 10$  mM there are still significant shifts. Between  $\sim 10 - 60$  mM only small further shifts occur. Since the enterokinase cleavage site contains four negatively charged aspartates and only one positively charged lysine (DDDDK), a titration of the fusion protein variant containing an overall neutral factor Xa site (IEGR) was done using  $^{15}\text{N}$ -hdnapkfadc-gb1xa with DPC as shown in Fig. 4.6b. Overall the same resonances show about the same strength and direction of chemical shift changes as observed for  $^{15}\text{N}$ -hdnapkfadc-gb1ent (Fig. 4.6a) and for untagged hdnapkfatc (Fig. 4.4a). This indicates that neither the GB1 tag nor the enterokinase or factor Xa site have a significant influence on the affinity for DPC micelles.

The structural characterization of the micelle-immersed state was done using a higher protein concentration ( $\sim 0.4$  mM) and a DPC concentration of 150 mM to ensure that the equilibrium is shifted to the micelle-associated state. A superposition of the respective  $^1\text{H}$ - $^{15}\text{N}$  HSQC spectrum with that of the free protein at about the same concentration is given in Fig. 4.6c. To better discriminate the FATC peaks from that of the GB1 tag, a spectrum of the latter is shown on top. The assignments for the FATC part in presence and absence of DPC micelles are indicated. Assignments for the full fusion protein including the GB1 tag are given in Fig. 4.7. Compared to the spectrum at  $\sim 60$  mM DPC, the spectral appearance of the micelle-immersed form is about the same. DPC forms rather small spherical micelles ( $54 \times 351.5$  Da =  $\sim 19$  kDa) with a high curvature [196, 188]. Moreover, DPC has only one fatty acid tail (Fig. 3.1a) and thus resembles more a lysolipid influencing the packing mode of the fatty acid chains in the micelle. To evaluate the influence of the curvature and the packing density of the membrane mimetic on the interaction with hdnapkfatc, additional NMR interaction studies with neutral bicelles and liposomes were performed (Fig. 4.6d, 4.6e).

In bicelles, the rather planar bilayer is formed by a long chain lipid, whereas the rim is formed by a short chain lipid or a bile acid (Fig. 3.1b, 3.1c) [197]. Moreover, bicelles are significantly larger ( $>250$  kDa) [197] than e.g. DPC micelles ( $\sim 19$  kDa) [188]. Figure 4.6d shows a superposition of the  $^1\text{H}$ - $^{15}\text{N}$  HSQC spectra of hdnapkfatc-gb1ent in the absence and presence of bicelles composed of DMPC and DihepPC, which both share the neutral phosphocholine headgroup with DPC (Fig. 3.1a). As observed with DPC micelles (Fig. 4.6c) the GB1 tag shows also no significant changes in the presence of bicelles (Fig. 4.6d).

Liposomes are very large spherical particles that are composed of one or more bilayers. To analyze the interaction of hdnapkfatc with liposomes, small unilamellar vesicles (SUVs) composed of DMPC were used (Fig. 3.1c). In contrast to DPC micelles or DMPC/DihepPC bicelles, the presence of liposomes induces no significant spectral changes (Fig. 4.6e). Using SUVs that were prepared starting from a higher concentrated DMPC suspension does not change the result (Fig. 4.6f). It has to be noted that the final lipid concentration in the liposome samples is remarkably lower ( $<30$  mM or 60 mM) than in the bicelle sample ( $\sim 270$  mM). However, the fact that hdnapkfatc shows significant chemical shift changes in the presence of small concentrations of DPC or even negatively charged lipids as well as DMPC/DihepPC bicelles, but not with DMPC SUVs may rather be explained based on the different curvature and fatty acid chain packing properties (Fig. 3.1f). Although bicelles have a rather planar bilayer area, they have a rather curved rim region, which may show a curvature comparable to that of micelles.

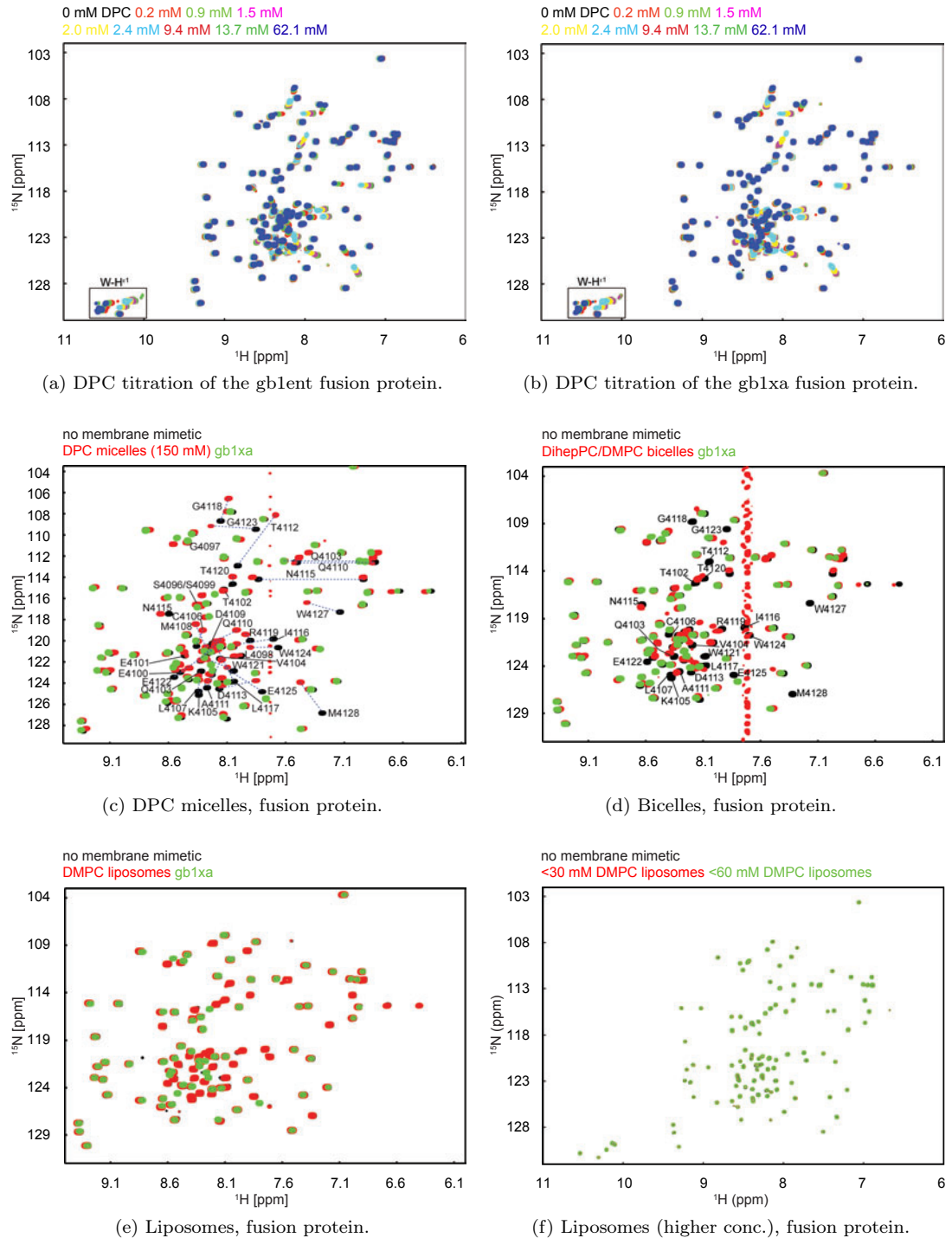
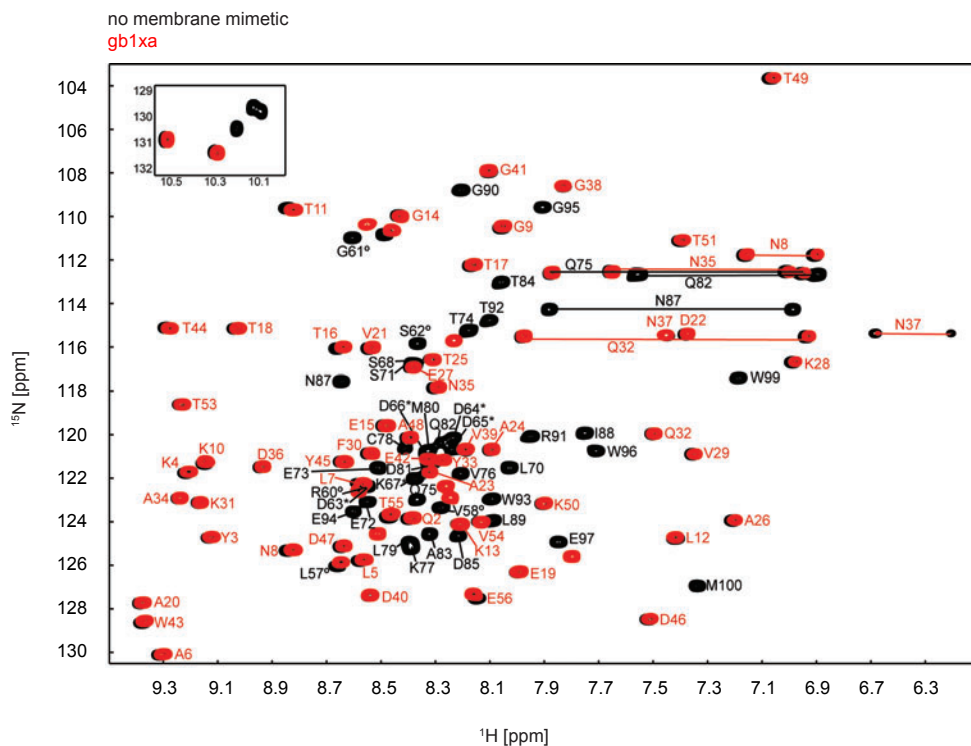
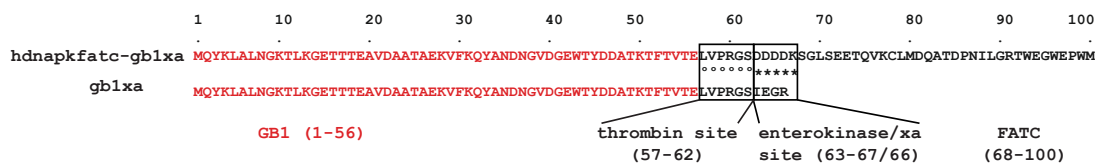


Figure 4.6: Interaction of the human FATC domain of DNA-PKcs with different membrane mimetics. Superposition of the  $^1\text{H}$ - $^{15}\text{N}$  HSQC spectra of hdnapkfatc-gb1ent and hdnapkfatc-gb1xa in the presence of increasing amounts of DPC, respectively. The used DPC concentrations and the respective color coding are indicated at the top of each plot (a,b). Superposition of the  $^1\text{H}$ - $^{15}\text{N}$  HSQC spectra of hdnapkfatc-gb1ent in the absence and presence of DPC micelles and DihepPC/DMPC bicelles ( $\sim 270$  mM) (c,d) or DMPC liposomes ( $< 30$  mM DMPC and/or  $< 60$  mM DMPC), respectively (e,f). To better discriminate the peaks corresponding to the FATC part, the spectrum of the gb1xa is shown on top. Reprinted (adapted) with permission from [10] - Copyright (2013) JBC.



(a) Superposition of the  $^1\text{H}$ - $^{15}\text{N}$  HSQC spectra of hdnapkfatc and gb1xa.

(b) Amino acid sequence of the fusion protein of DNA-PKcs FATC domain and gb1xa.

Figure 4.7: Assignment of the DNA-PKcs FATC domain (a) and GB1 tag (b). Superposition of the  $^1\text{H}$ - $^{15}\text{N}$  HSQC spectra of free hdnapkfatc-gb1ent (black) and gb1xa (red). The assignments that were derived based on the NMR spectra for hdnapkfatc-gb1ent are indicated by the one letter amino acid code and the sequence position. The small insert shows the spectral region containing the resonances for the tryptophan side chain amide protons (a). The 56 residues of the GB1 domain are colored in red, the linking thrombin-enterokinase or thrombin-factor Xa sites and the C-terminal 33 residues of the human DNA-PKcs FATC domain (4096-4128, full length) in black. Residues corresponding to the thrombin cleavage site are additionally labeled with a black circle and these corresponding to the enterokinase cleavage site with a black asterisk (b). Reprinted (adapted) with permission from [10] - Copyright (2013) JBC.



## 4.2.2.2 Secondary structure analysis

The structure of hdnapkfatc was initially characterized using untagged  $^{15}\text{N}$ -labeled protein. Based on the CD spectrum (Fig. 4.8) and the observed  $^3J_{\text{HNH}\alpha}$  coupling constants (Fig. 4.9), the free protein is rather unstructured.

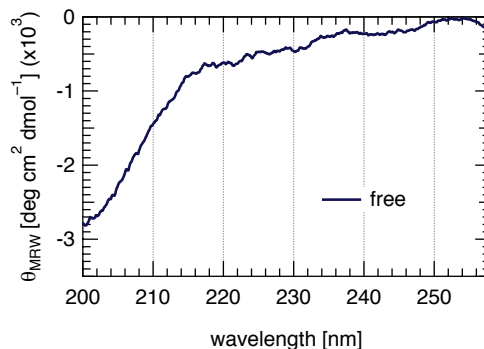


Figure 4.8: The CD spectrum of hdnapkfatc shows a minimum around 200 nm typical for a unstructured protein and only a very weak minimum at 222 nm that usually together with a second minimum at 208 nm indicates the presence of  $\alpha$ -helical secondary structure. *Adapted with permission from [10]- Copyright (2013) JBC.*

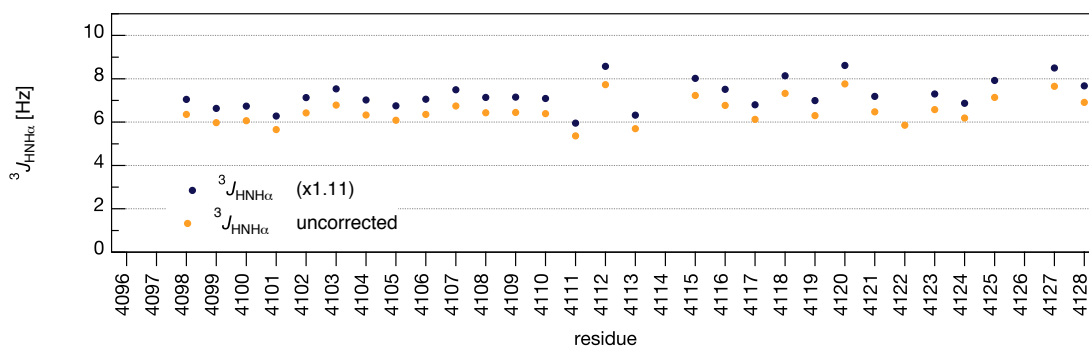


Figure 4.9:  $^3J_{\text{HNH}\alpha}$  coupling constants of the human DNA-PKcs FATC domain. The coupling constants were derived from a 3D HNHA spectrum (*orange*: uncorrected, *blue*: corrected by 11% as suggested in the literature [168]). Values below about 6 - 6.5 Hz are typically observed in  $\alpha$ -helical regions, whereas values above about 8 - 8.5 Hz are characteristic for residues in  $\beta$ -sheets. Values in the range of about 6.5 - 8 Hz are typical for protein regions undergoing conformational exchange. *Adapted with permission from [10] - Copyright (2013) JBC.*

A comparison of the assigned  $^1\text{H}^\alpha$  chemical shift values with the respective random coil values indicates for the majority of the residues only a small tendency to populate  $\alpha$ -helical secondary structure. This is confirmed by the analysis of  $^{13}\text{C}^\alpha$  secondary shifts of the FATC part of free hdnapkfatc-gb1ent (Fig. 4.10, blue bars). The interaction with DPC micelles strongly increases the content of  $\alpha$ -helical secondary structure (Fig. 4.10, orange bars). Based on the shown  $^{13}\text{C}^\alpha$  and the  $^1\text{H}^\alpha$  secondary shifts (data not shown), the FATC part of micelle-immersed hdnapkfatc-gb1ent contains roughly two  $\alpha$ -helical stretches that are disturbed around residues T4112 - D4113 preceding P4114 and finish around T4120. The presence of helical secondary structure in the micelle-immersed state is further confirmed by the observation of helix-typical NOE correlations (data not shown). The C-terminal tryptophan-rich region contains residues

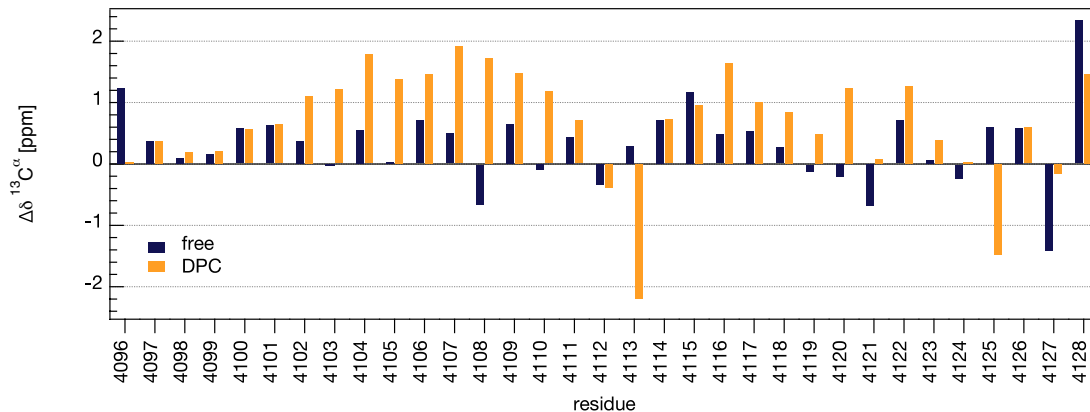


Figure 4.10:  $^{13}\text{C}^\alpha$  shift analysis of the human DNA-PKcs FATC domain. Estimation of the secondary structure content of free and micelle-bound hdnapkfatc based on its  $^{13}\text{C}^\alpha$  secondary shifts. The data were measured using hdnapkfatc-gblent. The difference between the measured  $^{13}\text{C}^\alpha$  chemical shift and the random coil value for the respective amino acid was plotted as a function of the amino acid sequence (*blue*: free, *orange*: micelle immerse state). Values significantly higher than the random coil value indicate the presence of  $\alpha$ -helical and those significantly lower of  $\beta$ -sheet secondary structure. Adapted with permission from [10] - Copyright (2013) JBC.

that have  $^{13}\text{C}^\alpha$  secondary shifts that are typical for either  $\alpha$ -helix or  $\beta$ -sheet. This has similarly been observed for the  $^{13}\text{C}^\alpha$  secondary shifts of the corresponding region of the TOR FATC domain [69]. Thus, this region may as observed for the free oxidized as well as the oxidized and reduced micelle-immersed states of the TOR FATC domain [68, 69], fold back onto the preceding helical region. This folding back or loop formation may be facilitated by the glycine at position 4123. This glycine is not only conserved in the FATC domain of DNA-PKcs and TOR (Fig. 4.3), but also in the ones of other PIKKs (see subsection 4.2.3).

#### 4.2.2.3 Analysis of $^{15}\text{N}$ relaxation data

The backbone dynamics of free and micelle-immersed hdnapkfatc-gblent were studied by  $^{15}\text{N}$  relaxation experiments. The presence of the GB1 tag makes the analysis of the relaxation data for the FATC part difficult since exchange effects arising from motions of the two proteins with respect to each other may have to be considered. Based on the presented relaxation data for the whole fusion protein in the absence and presence of DPC micelles (Fig. 4.11), the FATC and the GB1 part tumble rather independently in both states and the thrombin and enterokinase sites act as flexible linker. The average  $^{15}\text{N}$ - $T_1$ ,  $^{15}\text{N}$ - $T_2$  and  $\{^1\text{H}\}$ - $^{15}\text{N}$  NOE values for the GB1 tag (residues 1-56) are  $479 \pm 35$  ms,  $73 \pm 11$  ms, and  $0.66 \pm 0.07$  for the free protein and  $496 \pm 40$  ms,  $64 \pm 11$  ms, and  $0.65 \pm 0.08$  for the micelle associated fusion protein, respectively. The  $^{15}\text{N}$ - $T_1$  and the  $\{^1\text{H}\}$ - $^{15}\text{N}$  NOE values are in the range reported for the isolated GB1 domain [198]. The  $^{15}\text{N}$ - $T_2$  values for the GB1 tag, especially in the absence of micelles, are significantly lower than expected for a completely unhindered isotropic reorientation of a 6 kDa protein. Using a model system based on GB1 domains connected by different linker regions, it has been shown that each domain exhibits different rotational diffusion and alignment properties even if the linker was 18 residues long [199]. In the absence of micelles the FATC domain is to a big extent in an unstructured, flexible form which may further result in an additional viscous drag. A similar effect has been observed for the N-terminal domain of Formin C that contains a large unstructured loop [200].

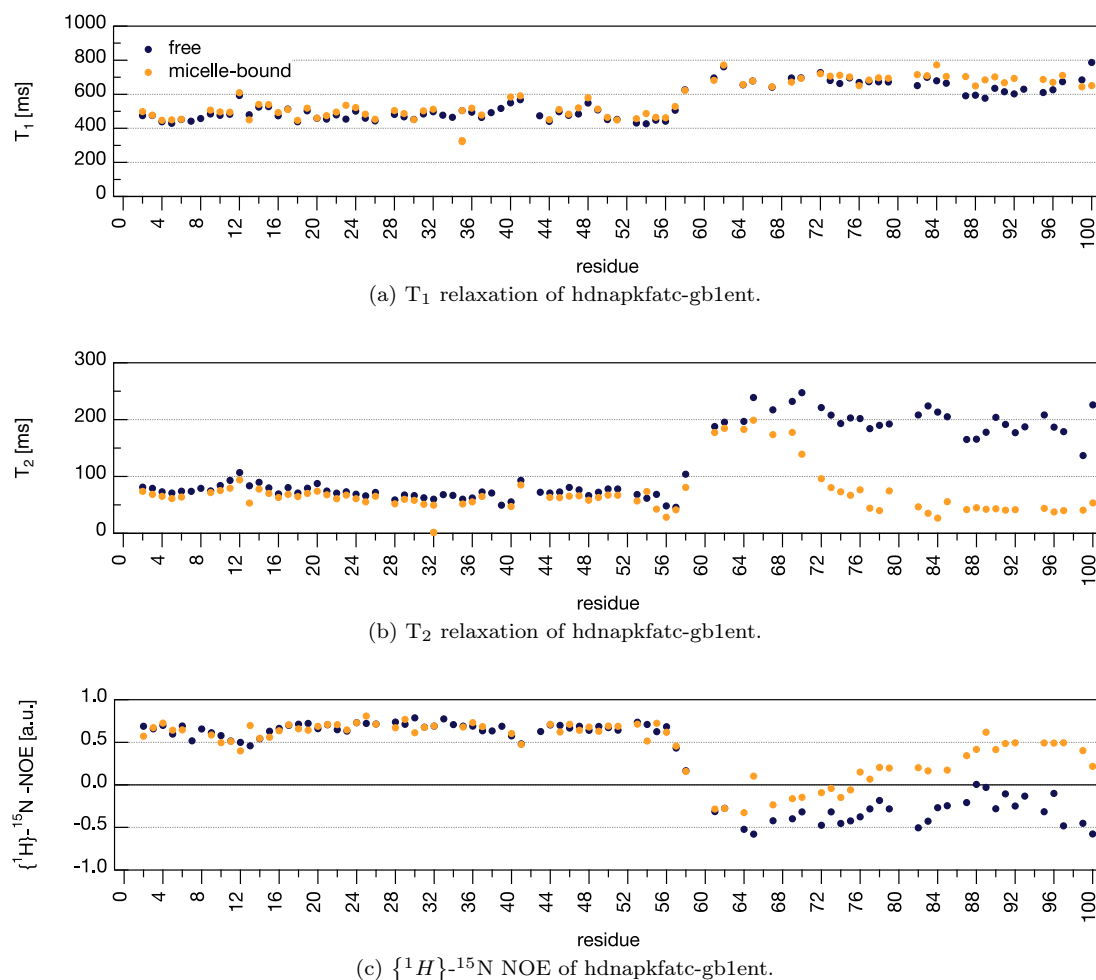


Figure 4.11: Backbone dynamics of the free and micelle-immersed DNA-PKcs FATC domain.  $^{15}N\text{-}T_1$  (a) and  $^{15}N\text{-}T_2$  (b) relaxation times and  $\{^1H\}\text{-}^{15}N$  NOE values (c) of hdnapkfatc-gblent were plotted as a function of the sequence. The free form is displayed by *blue* and that of the micelle-immersed form by *orange* points. *Adapted with permission from [10] - Copyright (2013) JBC.*

The  $^{15}N\text{-}T_1$ ,  $^{15}N\text{-}T_2$  and  $\{^1H\}\text{-}^{15}N$  NOE data for the FATC part of the free and micelle-immersed fusion protein are shown in Fig. 4.12. The average  $^{15}N\text{-}T_1$ ,  $^{15}N\text{-}T_2$  and  $\{^1H\}\text{-}^{15}N$  NOE values for residues 4108 - 4128 of the FATC part of the fusion protein are  $645 \pm 51$  ms,  $191 \pm 23$  ms, and  $-0.27 \pm 0.17$  for the free and  $689 \pm 31$  ms,  $42 \pm 6$  ms, and  $0.34 \pm 0.18$  for the micelle associated form, respectively. The association of hdnapkfatc-gblent with DPC micelles results only in a small increase of the average  $T_1$  value. Overall, a stronger increase of the  $T_1$  values would be expected upon interaction with the  $\sim 19$  kDa DPC micelles [188]. Unstructured proteins or protein regions show higher  $T_1$  values than the respective folded state, which has for example been shown for an SH3 domain [201]. Thus, a smaller increase of  $T_1$  than expected, can at least in part be accounted for by the fact that the FATC domain in the free state is rather unstructured and flexible and becomes significantly structured only upon interacting with micelles. Therefore, the increase in  $T_1$  due to an increase in the molecular weight upon complex formation is partially compensated by the FATC domain becoming more structured.

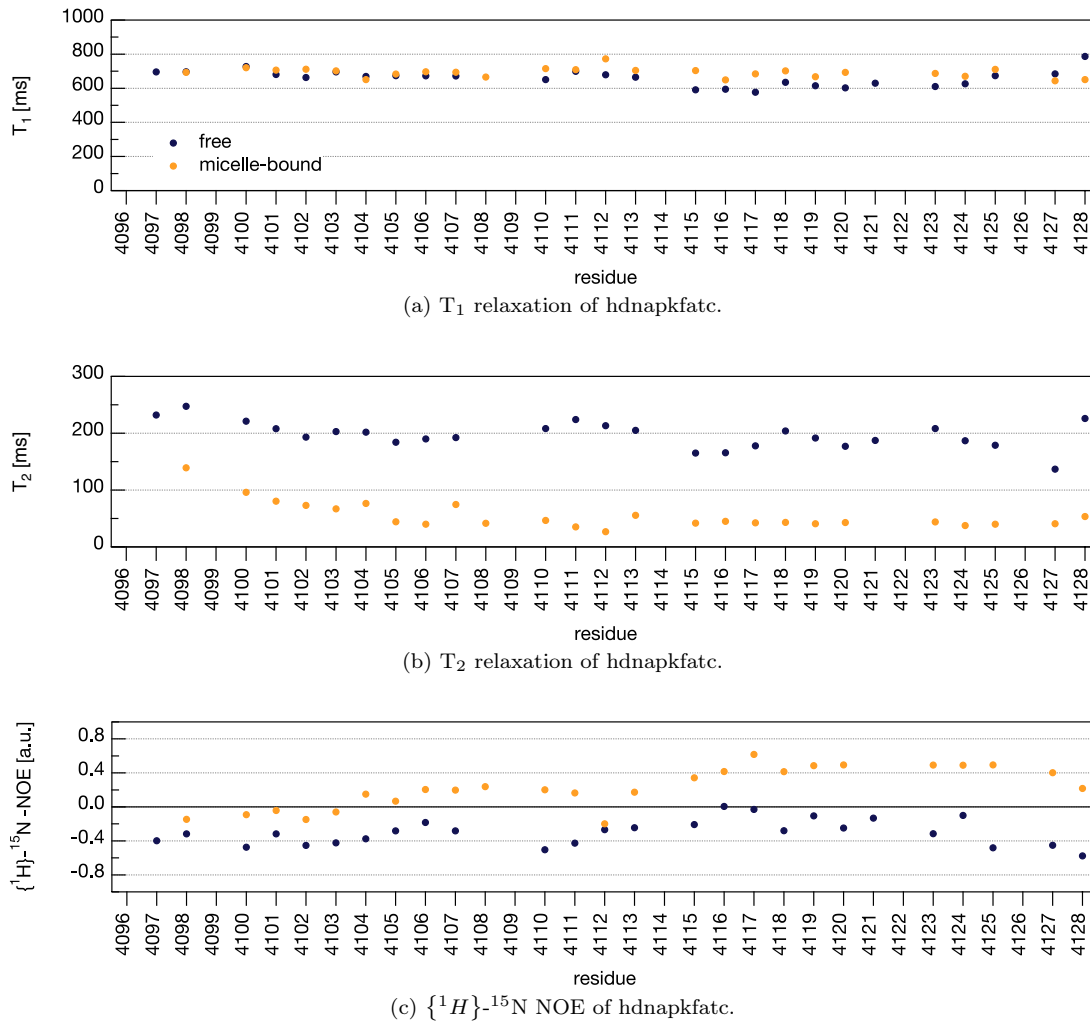


Figure 4.12: Backbone dynamics of the free and micelle-immersed DNA-PKcs FATC domain. (a)  $^{15}N$ - $T_1$  and (b)  $^{15}N$ - $T_2$  relaxation times and (c)  $\{^1H\}$ - $^{15}N$ -NOE values (c) were plotted as a function of the sequence. The data for the free form is shown in *blue* and that of the micelle-immersed form as *orange* points. The data was determined by measurement of  $^{15}N$ -hdnapkfadc-gblent. Adapted with permission from [10] - Copyright (2013) JBC.

Another factor influencing the  $^{15}N$  relaxation parameters may be the time scale of the exchange between the free and the micelle-immersed state. The  $T_2$  times of most residues decrease strongly from about  $\sim 190$  ms in the free form to  $\sim 40$  ms in micelle-immersed state. This confirms that the FATC part interacts with the DPC micelles. Overall the  $T_2$  values of the bound state are in the range expected for a  $\sim 23$  - 30 kDa complex ( $\sim 19$  kDa DPC micelle,  $\sim 4$  - 11 kDa protein) [69, 188]. The increase in the  $\{^1H\}$ - $^{15}N$  NOE values for most of the FATC domain confirms that it binds to the DPC micelles and is consistent with a more structured state, indicated by the observed secondary chemical shifts (Fig. 4.10).

### 4.2.3 NMR and CD characterization of the FATC domains of ATM, SMG-1, TRRAP, and ATR

#### 4.2.3.1 Membrane mimetic interaction studies

In order to find out if membrane binding is a general property of the FATC domain of all PIKKs, the interaction of the FATC domains of ATM, ATR, SMG-1 and TRRAP with different membrane mimetics was also probed by specific NMR interaction studies. The interaction of the FATC domain of human ATM (hatmfatc) with different membrane mimetics was analyzed in more detail using, as for the FATC domain of DNA-PKcs, the procedure described in chapter 4.1 [157]. Fig. 4.13 shows the superpositions of the  $^1\text{H}$ - $^{15}\text{N}$  HSQC spectra of hatmfatc-gblent in the absence and presence of either DPC or DihepPC micelles or DMPC/DihepPC bicelles or DMPC liposomes (Fig. 4.13a - 4.13d).

With all four tested membrane mimetics a major change of the spectral appearance of the FATC peaks is observed. Addition of 150 mM DPC or 50 mM DihepPC or DMPC/DihepPC bicelles ( $\sim 270$  mM) results in the disappearance of many resonances characteristic for the free form and the appearance of new peaks for the membrane-associated state. As for the other analyzed FATC domains, spectral shifts can be seen for many backbone amide groups as well as for the side chain amides of the two tryptophans and those of some glutamines and asparagines, respectively. The titration of hatmfatc-gblent with increasing amounts of DPC is shown in Fig. 4.14a. In the presence of 0.1 mM DPC, no significant spectral changes are seen. At 1.1 mM DPC, which corresponds to the CMC of DPC, some peaks of the FATC part get weaker and/or show small shifts. Increasing the DPC concentration to 5 mM results in further shifts. The spectra at  $\sim 10$  and  $\sim 49$  mM DPC are about the same as at 5 mM. This indicates that hatmfatc interacts only with the membrane mimetic micelles and not with single DPC molecules. If DMPC liposomes are added ( $< 30$  mM DMPC), the peaks disappear or are not visible due to the significantly larger size of SUVs compared to bicelles and micelles, which results in a significant line broadening for the liposome associated hatmfatc-gblent. In addition, the total lipid concentration in the sample with SUVs is much lower ( $\ll 30$  mM DMPC). Therefore, the equilibrium is not as much shifted to the bound form. Finally, the affinity for liposomes may be lower as for micelles or bicelles due to differences in the surface curvature and packing density.

A superposition of the natural abundance  $^1\text{H}$ - $^{15}\text{N}$  SOFAST-HMQC spectra of a 33 residue peptide corresponding to the FATC domain of human SMG-1 (hsmg1fatc) in the absence and presence of 50 mM  $d_{38}$ -DPC is shown in Fig. 4.14c. Since the CMC of DPC is 1.1 mM [159], DPC should be mostly present in membrane mimetic micelles (Fig. 3.1f). The peak pattern in the two spectra is clearly different, indicating an interaction of hsmg1fatc with the membrane mimetic micelles, which results in a change of the chemical environment for all detectable peaks. In addition, the interaction of hsmg1fatc with also neutral DihepPC micelles was analyzed by recording natural abundance  $^1\text{H}$ - $^{15}\text{N}$  HSQC spectra (Fig. 4.14d). Also in this case, the spectral appearance changes significantly if 50 mM DihepPC (CMC 1.4 - 1.8 mM) are present [160, 161]. Thus, hsmg1fatc appears also to interact with DihepPC micelles. With both types of micelles all detectable backbone amides are found at new positions, which is accompanied by an overall increase in the dispersion of the signals. The latter indicates that the peptide may become more structured upon interacting with micelles. Strong shifts are also observed for the side chain amide  $\text{H}\varepsilon 1$  protons of both tryptophans that are characterized by proton chemical shifts around 10 - 11 ppm (Fig. 4.14c, 4.14d). The intensity of these peaks is negative because of spectral folding in the  $^{15}\text{N}$  dimension. Finally, smaller shifts are visible for the side chain amide protons of glutamines and asparagines ( $^1\text{H} \sim 6.5 - 7.5$  ppm,  $^{15}\text{N} \sim 111 - 114$  ppm).

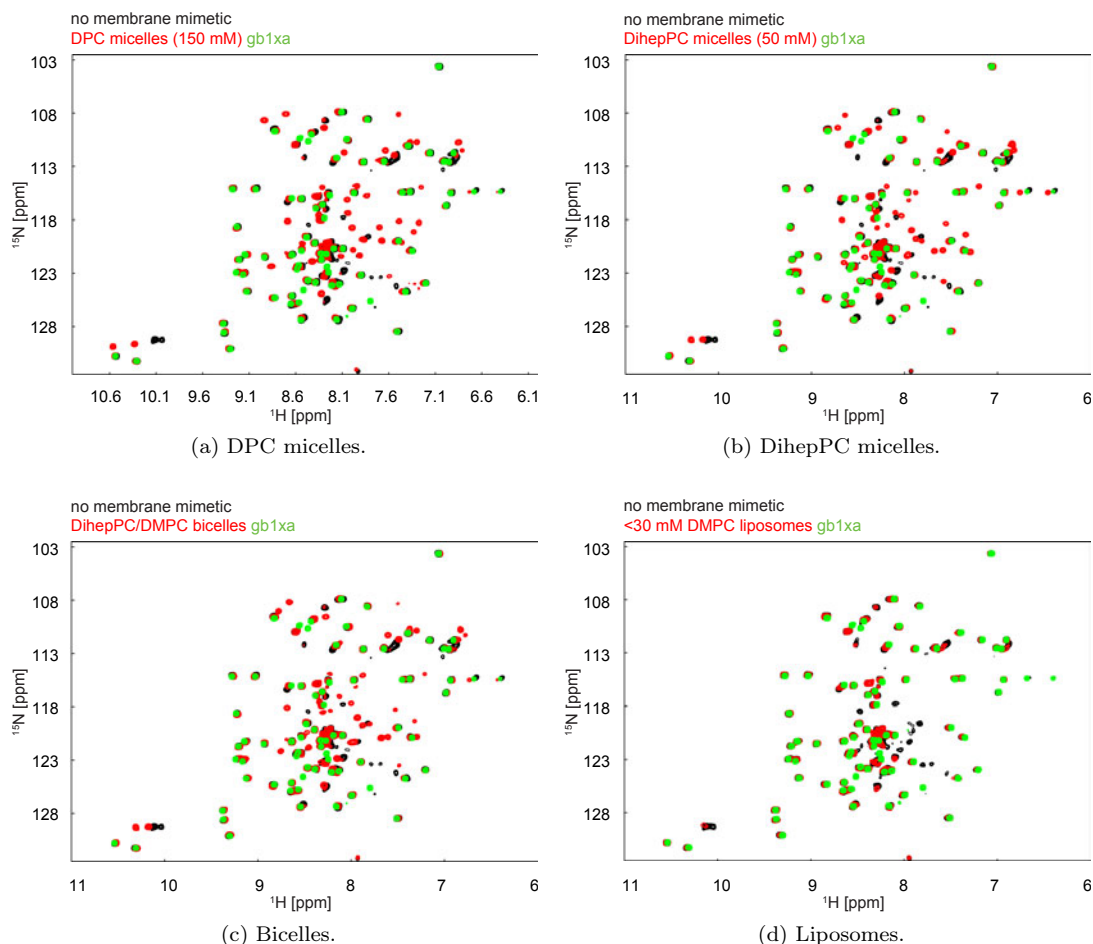


Figure 4.13: NMR analysis of the interaction of the human ATM FATC domain. Superpositions of the  $^1\text{H}$ - $^{15}\text{N}$  HSQC spectra of hatmfatc-gb1ent in the absence and presence of either DPC or DihepPC micelles, or DihepPC/DMPC bicelles or DMPC liposomes (a-d). The spectrum of the free form is always shown in *black* and the one with the respective membrane mimetic in *red*. To better identify the signals of the ATM FATC part, the spectrum of gb1xa is additionally plotted in *green* on top. *Reprinted (adapted) with permission from [10] - Copyright (2013) JBC.*

The fact that the number of backbone amide resonances is smaller than expected based on the number of residues in the sequences can be explained by following reasons. First, the sensitivity of a  $^1\text{H}$ - $^{15}\text{N}$  HSQC/HMQC spectrum recorded at natural abundance is significantly lower than one recorded of a  $^{15}\text{N}$ -enriched sample and consequently weaker resonances may not be detected. Second, some resonances may be very broad and thus weak because of motional averaging and/or exchange between the free and the micelle-immersed state.

The interaction of the FATC domain of human TRRAP (htrrapfatc) with membrane mimetics was also analyzed by recording  $^1\text{H}$ - $^{15}\text{N}$  HSQC spectra in the absence and presence of either DPC or DihepPC micelles at natural abundance (Fig. 4.14b). Also in this case, the spectral appearance changes significantly for almost all detectable resonances. In the case of DPC, the number of detectable peaks as well as their dispersion increases, indicating that htrrapfatc becomes more structured upon interacting with DPC micelles.

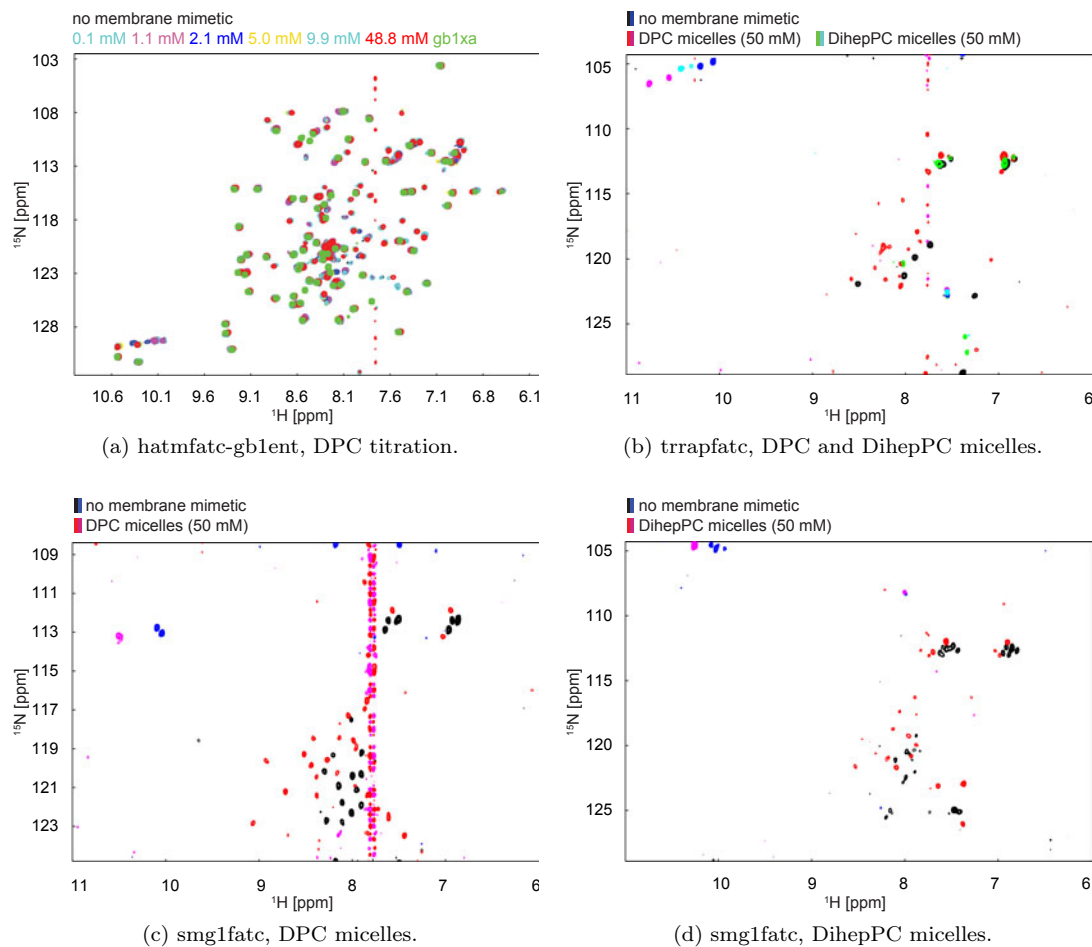


Figure 4.14: Membrane interactions of the FATC domains of human ATM, SMG-1, and TRRAP. Superposition of the  $^1\text{H}$ - $^{15}\text{N}$  HSQC spectra of hatmfatc-gb1ent in the presence of increasing amounts of DPC (a). The color coding and the respective DPC concentrations are given at the top of the spectrum. To better discriminate the peaks corresponding to the FATC part, the spectrum of gb1xa is shown in green on top. Superpositions of the  $^1\text{H}$ - $^{15}\text{N}$  HSQC spectra of hsmg1fatc and htrrapfatc in the absence and presence of either DPC or DihepPC micelles (50 mM each time). Positive peaks are colored in *black*, *red* and *green*, negative in *blue*, *magenta* and *cyan* (b-d). Reprinted (adapted) with permission from [10] - Copyright (2013) JBC.

Both DPC and DihepPC micelles induce significant shifts of the tryptophan side chain H $\epsilon$ 1 protons, albeit the effect is stronger with DPC than with DihepPC. Shifts for the side chain amide protons of glutamine and asparagines are only seen in the presence of DPC micelles. This and the overall smaller shifts for the two tryptophan side chain protons as well as the smaller number of peaks in the presence of DihepPC micelles, suggest that a higher concentration of DihepPC may be needed to induce spectral changes of similar strength as observed with DPC micelles. The reason can be either a lower affinity for DihepPC compared to DPC micelles or because the number of DihepPC micelles at a concentration of 50 mM is lower than the one of DPC micelles at the same concentration [161, 188].

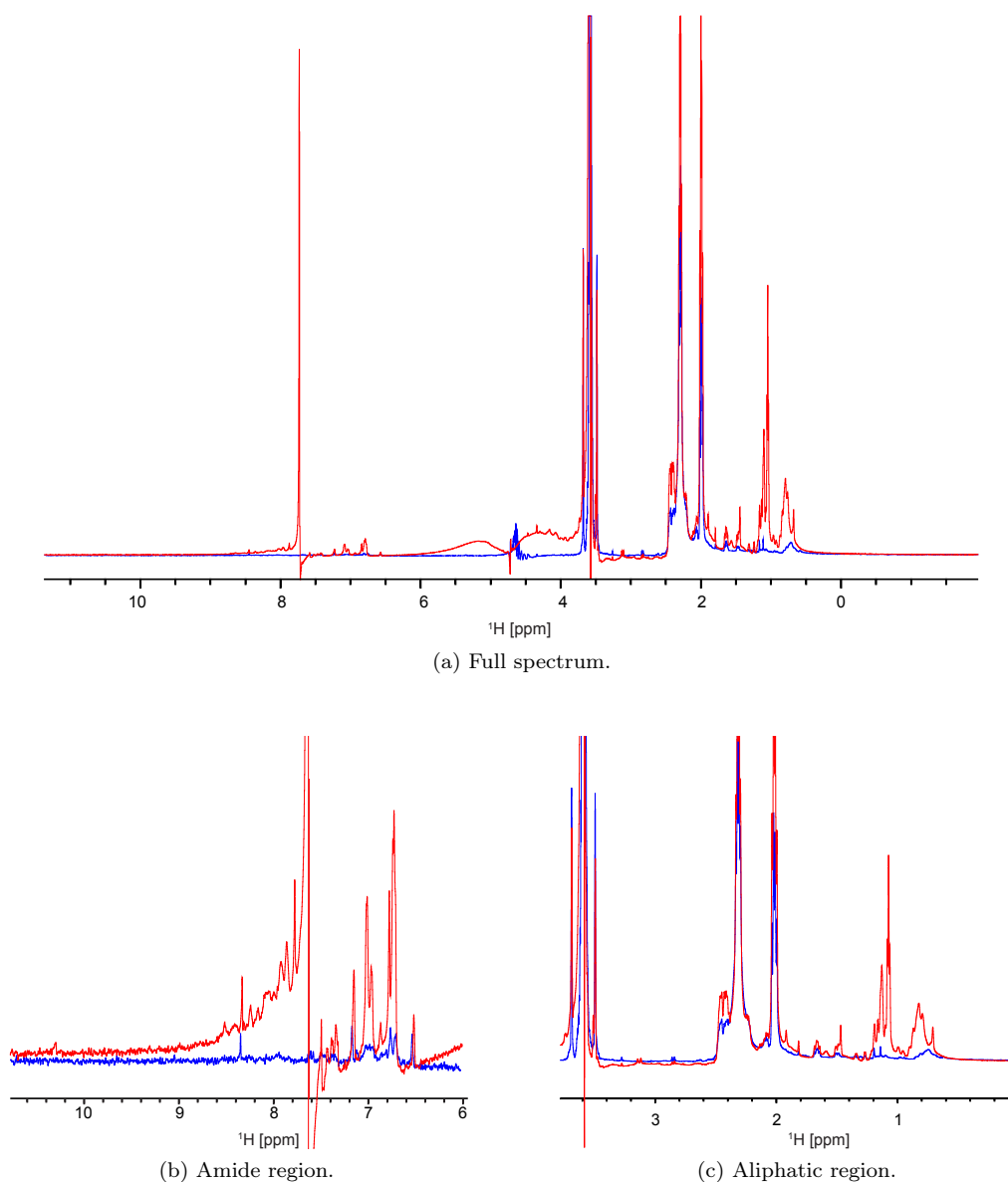


Figure 4.15: Association of hatrfatc with DPC micelles monitored by 1D  $^1\text{H}$  NMR spectra. The spectrum of the free form is shown in *blue*, the one in presence of 50 mM  $\text{d}_{38}$ -DPC in *red*. The top panel shows the full spectrum (a), the bottom left one only the amide region (b), and the bottom right one the aliphatic region (c). In the amide region (b) almost all signals arise from the protein, except the the strong signal at about 7.6 ppm, which is presumably from chloroform or another substance present in the DPC stock. *Adapted with permission from [10] - Copyright (2013) JBC.*

The interaction of a peptide corresponding to the FATC domain of human ATR (hatrfatc) with DPC micelles could only be monitored based on one-dimensional  $^1\text{H}$  NMR spectra (Fig. 4.15a). Overall the spectral appearance of the 1D  $^1\text{H}$  NMR spectrum changes dramatically in the presence of 50 mM  $\text{d}_{38}$ -DPC. Looking only at the amide region (Fig. 4.15b), the number of



resonances as well as their intensity and dispersion increases in the presence of micelles. This includes the appearance of a small signal for the side chain amide proton of the single tryptophan ( $\sim 10.4$  ppm). An increase of the signal intensity is also evident for the aliphatic region (Fig. 4.15c). However, in this chemical shift range signals from the buffer (Tris, TCEP) and residual signals from  $d_{38}$ -DPC disturb the interpretation. Overall the data suggest that hatrfatc interacts with DPC micelles and thereby may become more structured.

#### 4.2.3.2 Secondary structure analysis

Also for the FATC domains of ATM, SMG-1, TRRAP, and ATR, the signal dispersion in the NMR spectra increased upon addition of a membrane mimetic (Fig. 4.13, Fig. 4.14), which indicates that the respective protein also have become more structured resulting in a more diverse chemical environment for the different micelle-immersed residues. An analysis of the  $^1H^\alpha$  secondary shifts and the  $^3J_{H^NH^\alpha}$  values (Fig. 4.16, 4.17) reveals helical secondary structure in hatmfatc. The data indicate the presence of two helical stretches in about the same regions as for DNA-PKcs (Fig. 4.10, 4.16). Moreover, residues 3051 - 3054 at the C-terminal hatmfatc may form another short helix or helical turn (Fig. 4.16), because it has not a proline at the third last position (3054) as DNA-PKcs (P4126), but at position 3050.

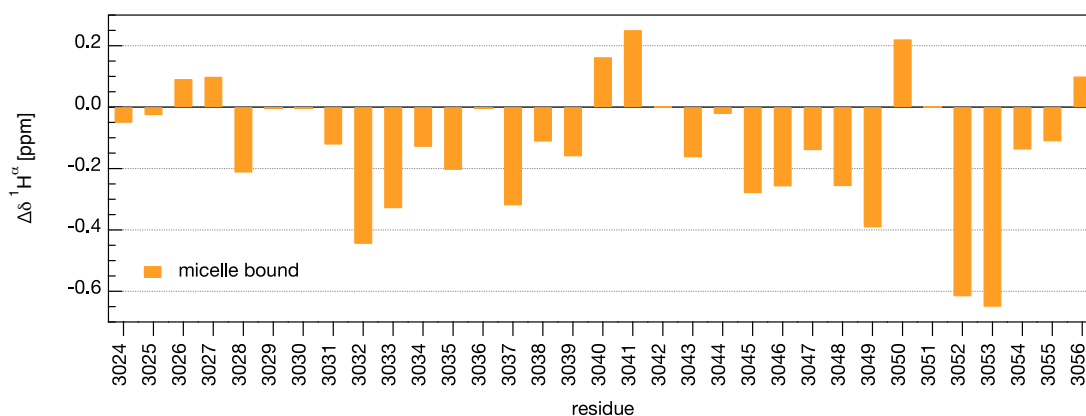


Figure 4.16: Analysis of  $^1H^\alpha$  secondary shifts of the micelle-bound human ATM FATC domain. The secondary structure content of micelle-immersed hatmfatc was estimated based on its  $^1H^\alpha$  secondary shifts. The difference between the measured  $^1H^\alpha$  chemical shift and the random coil value for the respective amino acid [115] was plotted as a function of the amino acid sequence (micelle-bound hatmfatc-gblent in the presence of 150 mM DPC). Values significantly lower than the random coil value indicate the presence of  $\alpha$ -helical and those significantly higher of  $\beta$ -sheet secondary structure. Adapted with permission from [10] - Copyright (2013) JBC.

The change in the secondary structure content of hsmg1fatc, htrapfatc and hatrfatc was monitored by circular dichroism spectroscopy (Fig. 4.18). The hsmg1fatc peptide shows a spectrum characteristic of an unfolded protein in the free form (Fig. 4.18a). In the presence of 50 mM DPC the absolute signal intensity increases and the minimum shifts from about 205 to 208 nm. In addition a second minimum becomes visible at about 222 nm. Minima at 208 and 222 nm are typically observed for proteins containing a significant amount of  $\alpha$ -helical secondary structure. The higher absolute mean residue ellipticity at 208 compared to 222 nm can be explained by the presence of a remaining short unstructured stretch.

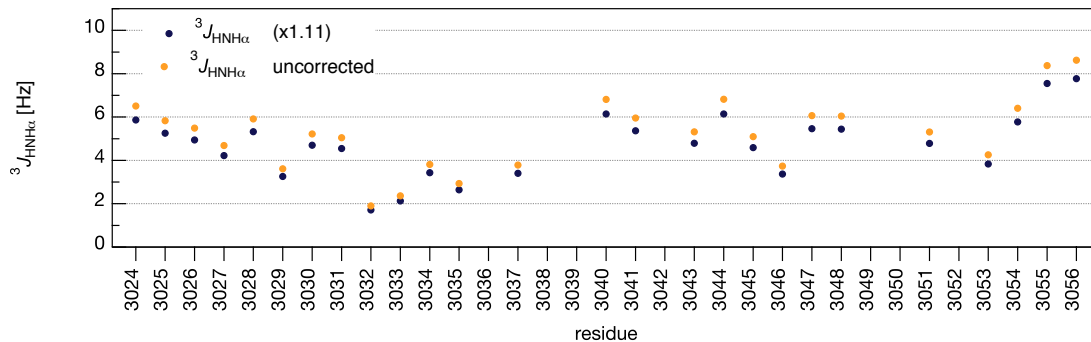


Figure 4.17: Analysis of  $^3J_{HNH\alpha}$  coupling constants of the micelle-bound human ATM FATC domain.  $^3J_{HNH\alpha}$  coupling constants were derived from a 3D HNHA spectrum (*orange*: uncorrected, *blue*: corrected by 11% as suggested in the literature [168]). Values below about 6 - 6.5 Hz are typically observed in  $\alpha$ -helical regions, whereas values above about 8 - 8.5 Hz are characteristic for residues in  $\beta$ -sheets. Values in the range of about 6.5 - 8 Hz are typical for protein regions undergoing conformational exchange. *Adapted with permission from [10] - Copyright (2013) JBC.*

The spectrum of free htrrapfatc is also typical for an unfolded protein with a minimum around 200 nm, whereas the spectrum in the presence of DPC micelles show minima at about 208 and 222 nm that indicate the presence of  $\alpha$ -helical secondary structure (Fig. 4.18b). The presence of DihepPC micelles results also in significant spectral change and a minimum at about 208 nm, however the minimum at 222 nm is not well resolved. Thus, the amount of helical secondary structure in the DihepPC micelle-immersed state is expected to be lower than in the DPC micelle-immersed one. This is consistent with the fact that fewer NMR signals are visible for the DihepPC micelle-associated form than for the DPC micelle-associated one (Fig. 4.14b).

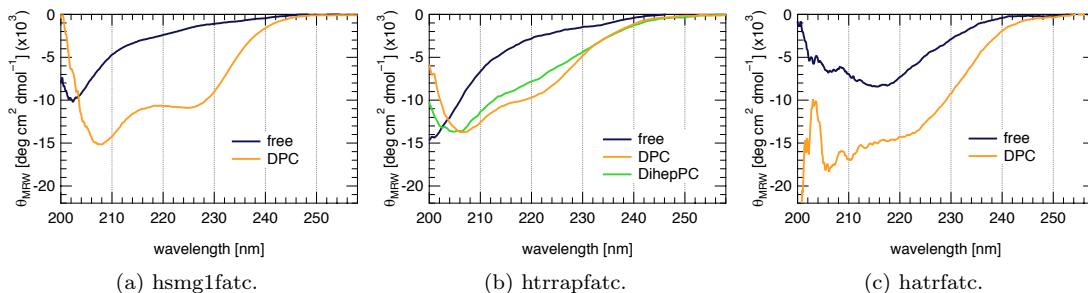


Figure 4.18: Analysis of secondary structure changes of the FATC domains of human SMG-1 (a), TRRAP (b), and ATR (c) upon interaction with membrane mimetics. Superposition of CD spectra of the hsmg1fatc (left), htrrapfatc (middle), and hatrfatc (right) in the free form (*blue*) and in the presence of 50 mM DPC (*orange*) and for htrrapfatc additionally with 50 mM DihepPC micelles (*green*). *Adapted with permission from [10] - Copyright (2013) JBC.*

The spectrum of the free form of hatrfatc shows a minimum at 215 nm, which is typically observed for proteins containing  $\beta$ -sheet structure (Fig. 4.18c). This  $\beta$ -sheet typical appearance may be related to the observation that the free hatrfatc peptide has a tendency to aggregate. Addition of 50 mM DPC results in a change of the spectral shape, which is characterized by the appearance of minima at about 208 and 222 nm that are typical for  $\alpha$ -helical secondary structure. Due to the bad spectral quality, the two minima can however not be as clearly

detected as for SMG-1 and TRRAP. The quality of the CD spectra of hatrfatc is lower because smaller protein concentrations had to be used, as the protein had to be diluted to lower the TCEP concentration to reduce too strong distortions from its presence at higher concentrations.

#### 4.2.3.3 Analysis of membrane interactions by $^{15}\text{N}$ relaxation and NMR diffusion measurement

For hatrfatc-gb1ent the association with membrane mimetics was further confirmed by  $\{^1\text{H}\}$ - $^{15}\text{N}$  NOE data (Fig. 4.19).

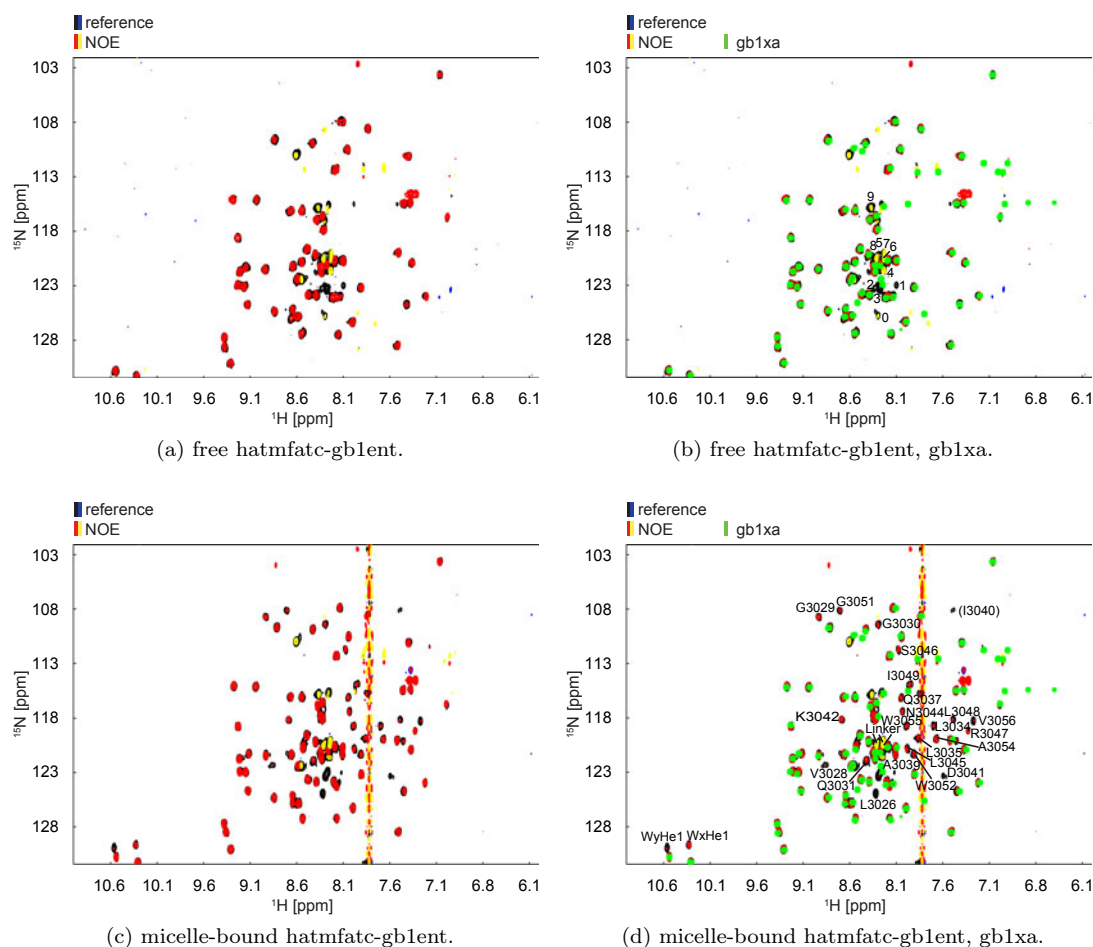


Figure 4.19: Analysis of changes in the backbone dynamics of hatrfatc-gb1ent upon interaction with DPC micelles based on  $\{^1\text{H}\}$ - $^{15}\text{N}$  NOE data. Superposition of spectra of free and micelle-bound hatrfatc-gb1ent without (reference) and with NOE effect (a-d). For both the spectrum of gb1xa (in green) is additionally shown on top to identify the peaks corresponding to the FATC part (b,d). Positive peaks are colored in black and red, negative in blue and yellow. For some residues the assignment by the one-letter amino acid code and the sequence position is indicated and the corresponding NOE value have been determined (Tab. 4.1, 4.2). *Reprinted (adapted) with permission from [10] - Copyright (2013) JBC.*

Already the fact that several of the backbone resonances of the free FATC domain of human ATM appear not to be visible in the  $^1\text{H}$ - $^{15}\text{N}$  HSQC spectra (Fig. 4.13), indicates increased backbone dynamics, presumably due to motional averaging, which may broaden some of the signals beyond detection. Since the sequential assignment of the free state is hampered by the lack of several  $^1\text{H}$ - $^{15}\text{N}$  correlations, the  $\{^1\text{H}\}$ - $^{15}\text{N}$  NOE data for free hatmfatc-gb1ent is only qualitatively interpreted making use of the fact that the signals of the GB1 tag can be differentiated from the ones of the FATC domain based on spectral superpositions (Fig. 4.19b, 4.19d). As indicated by the presence of zero to negative intensity peaks in the spectrum with NOE effect of the free form, most of the FATC part must be rather flexible (Tab. 4.1). For the well-resolved peaks visible for the linker and the FATC part, the NOE values range between  $-0.6 - 0.2$ . In contrast, in the presence of DPC micelles most of the peaks for the FATC part are visible and show a positive intensity, thus also indicating positive NOE values (Tab. 4.2). The NOE values for residues V3028 to V3056 range between  $\sim 0.3 - 0.75$ . This confirms that the ATM FATC domain interacts with DPC micelles. Considering the range of NOE values typically observed for structured and flexible regions of protein or protein complexes of similar size ( $\sim 5 - 25$  kDa) [69, 200, 201], most of the micelle-immersed ATM FATC domain appears rather well-structured with NOE values  $> 0.5$ .

Table 4.1: NOE values of free hatmfatc-gb1ent. *Adapted with permission from [10] - Copyright (2013) JBC.*

peak	NOE value	peak	NOE value	peak	NOE value
0	$-0.56 \pm 0.05$	4	$-0.89 \pm 0.03$	7	$-0.55 \pm 0.02$
1	$-0.45 \pm 0.06$	5	$0.19 \pm 0.06$	8	$-0.44 \pm 0.01$
2	$-0.09 \pm 0.07$	6	$-0.34 \pm 0.01$	9	$-0.30 \pm 0.02$
3	$0.12 \pm 0.02$				

Table 4.2: NOE values of micelle-bound hatmfatc-gb1ent. *Adapted with permission from [10] - Copyright (2013) JBC.*

residue	NOE value	residue	NOE value	residue	NOE value
L3026	$0.11 \pm 0.02$	A3039	$0.64 \pm 0.03$	F3049	$0.48 \pm 0.04$
V3028	$0.55 \pm 0.06$	D3041	$0.32 \pm 0.06$	G3051	$0.64 \pm 0.05$
G3029	$0.61 \pm 0.04$	K3043	$0.54 \pm 0.03$	W3052	$0.72 \pm 0.03$
G3030	$0.57 \pm 0.03$	N3044	$0.56 \pm 0.04$	A3054	$0.56 \pm 0.02$
Q3031	$0.54 \pm 0.03$	L3045	$0.57 \pm 0.04$	W3055	$0.48 \pm 0.03$
L3034	$0.60 \pm 0.05$	S3046	$0.52 \pm 0.03$	V3056	$0.29 \pm 0.03$
L3035	$0.59 \pm 0.04$	R3047	$0.73 \pm 0.05$	WxH $\epsilon$ 1	$0.44 \pm 0.02$
Q3037	$0.68 \pm 0.04$	L3048	$0.42 \pm 0.05$	WyH $\epsilon$ 1	$0.11 \pm 0.01$
linker	$-0.27 \pm 0.01$	linker	$-0.42 \pm 0.01$	linker	$-0.29 \pm 0.01$

Since the FATC domains of SMG-1 and TRRAP are not  $^{15}\text{N}$ -labeled,  $^{15}\text{N}$  relaxation data can not be recorded. Instead, diffusion constants are obtained for both proteins (Tab. 4.3), since the NMR samples of *hsmg1fatc* and *htrrapfatc* have rather high protein concentrations ( $\sim 1$  mM). The diffusion constants of the free forms are  $\sim 1.7 - 1.8 \times 10^{-10} \text{ m}^2\text{s}^{-1}$ . Addition of deuterated DPC micelles lowers the diffusion constant significantly to  $\sim 1.0 - 1.1 \times 10^{-10} \text{ m}^2\text{s}^{-1}$  for *hsmg1fatc* and  $\sim 0.9 - 1.0 \times 10^{-10} \text{ m}^2\text{s}^{-1}$  for *htrrapfatc* (Tab. 4.3). This is in the range expected for a complex of  $\sim 23$  kDa arising from the association of a  $\sim 4$  kDa peptide with a  $\sim 19$  kDa DPC micelle and using only a DPC concentration of 50 mM. The diffusion constant for the reduced and oxidized TOR FATC domain in the presence of 30 mM DPC, which corresponds to a partially micelle-bound situation, is  $1.32$  and  $1.13 \times 10^{-10} \text{ m}^2\text{s}^{-1}$  and in the presence of 170 mM DPC, which corresponds to the bound state,  $0.59$  and  $0.72 \times 10^{-10} \text{ m}^2\text{s}^{-1}$  [69]. The diffusion constant of the DPC micelle alone at 170 mM is  $1.10 \times 10^{-10} \text{ m}^2\text{s}^{-1}$  [69]. Thus the diffusion data confirm the association of the SMG-1 and TRRAP FATC domains with membrane mimetic DPC micelles. Diffusion measurements in the presence of DihepPC were hampered by the huge signal from the undeuterated lipid, which impair the reliable detection and analysis of the peptide signals.

Table 4.3: Diffusion measurements of SMG-1 and TRRAP FATC domains. *Adapted with permission from [10] - Copyright (2013) JBC.*

protein	free		50 mM $\text{d}_{38}$ -DPC	
	cs [ppm]	D ( $\times 10^{-10}$ ) [ $\text{m}^2\text{s}^{-1}$ ]	cs [ppm]	D ( $\times 10^{-10}$ ) [ $\text{m}^2\text{s}^{-1}$ ]
<i>hsmg1fatc</i>	1.124	1.76	1.861	1.12
	0.832	1.76	1.490	1.03
	0.784	1.78	0.901	1.09
<i>htrrapfatc</i>	1.940	1.87	1.489	0.95
	1.311	1.69	0.873	0.95
	0.843	1.72	0.740	0.92
	0.778	1.77	-	-

#### 4.2.4 Summary and discussion

It has been shown that the six known members of the PIKK family regulating a number of cellular signaling pathways, share the conserved FATC domain that plays an important role for the regulation of their function [1, 12], which is furthermore confirmed in mutagenesis studies [102, 16, 107, 15, 108]. Although it has been shown that some FATC domains mediate protein-protein interactions [15, 108, 109], the question remained whether there is further a more general common property of the FATC domain that influences PIKK function. Sequence alignments of the FATC domain of all PIKKs show that they share characteristic features in their amino acid sequence. Based on the presented NMR and CD data for the FATC domains of human DNA-PKcs, ATM, ATR, SMG-1, and TRRAP combined with the earlier published data for TOR, the ability to interact with membrane mimetics and thus a potential role for the mediation or regulation of interactions at cellular membranes may be one function that is common to all PIKK FATC domains.

NMR membrane binding studies suggest that the FATC domains of DNA-PKcs, ATM, SMG-1, TRRAP, and ATR have the ability to interact with membrane mimetics. Differences in the distribution of hydrophobic and charged side chains in the respective FATC domains may thus result in different preferences for specific membrane properties such as surface charge and curvature or the packing density of the lipid acyl chains as well as the presence of cholesterol or certain proteins. The analysis of the studies of the respective PIKK FATC domains with different membrane mimetics shows that spectral changes occurred only above the respective CMC and thereby the FATC domains appear not to recognize specific lipid headgroups and/or interact with single lipids but only with membrane mimetic structures such as micelles, bicelles, or liposomes. These results are in line with earlier data presented for the TOR FATC domain [69].

The interaction study of DNA-PKcs FATC with a negatively charged mixed phosphatidic acid membrane mimetic induced strong changes in a region harboring a positively charged lysine, which is in contrast to the results for the FATC domain of TOR showing similar changes for all tested lipids [69]. It is supposed that the differences in the amino acid sequences of DNA-PKcs and TOR FATC regarding the charge of amino acids cause varying binding behavior, such as the weakened interaction between the lipid and the C-terminal region of DNA-PKcs due to electrostatic repulsion. The FATC domain of DNA-PKcs interacts with neutral micelles and bicelles, but has no apparent affinity for neutral DMPC SUVs, which is further in contrast to the results for the FATC domains of TOR as well as ATM, which both interact with DMPC liposomes. The observation that the FATC domain of DNA-PKcs has no significant affinity for liposomes indicates that its interactions with membrane regions may be more sensitive to the surface curvature and lipid packing than the those of TOR and ATM.

The analysis of CD,  $^3J_{HNH\alpha}$  coupling constants,  $^{13}\text{C}^\alpha$  and  $^{15}\text{N}$  relaxation data show that free DNA-PKcs FATC is rather unstructured. A comparison of  $^{15}\text{N}$  relaxations and chemical shifts of the free and micelle-bound FATC domain of DNA-PKcs confirm the association with micelles and are consistent with a more structured state and reduced backbone dynamics. The CD data for the FATC domains of SMG-1 and TRRAP, and the  $\{^1\text{H}\}$ - $^{15}\text{N}$  NOE data in the case of ATM, also reveal that the respective FATC domains are rather unstructured and flexible. The interaction with micelles causes an increase in  $\alpha$ -helical secondary structure content, which is visible for all tested FATC domains in the CD, NMR diffusion measurements, or  $\{^1\text{H}\}$ - $^{15}\text{N}$  NOE data. In contrast, the oxidized form of the TOR FATC domain is rather well structured, consisting of an  $\alpha$ -helix and a disulfide-bonded loop [68]. Upon addition of DPC micelles the population of  $\alpha$ -helical secondary structure significantly increases in the respective FATC domain. Folding upon binding to membrane mimetics, corresponding to higher population of  $\alpha$ -helical secondary structure in the presence of a membrane mimetic, has also been observed for other small proteins such as the 30-residue long glucagon-like peptide 1 targeting G protein-coupled receptor [202]. Therefore, the observed formation and/or stabilization of  $\alpha$ -helical structure may enable the interaction of the respective PIKK with specific membrane proteins.

Based on the  $^{13}\text{C}^\alpha$  secondary shifts the  $\alpha$ -helical structure of DNA-PKcs FATC in the presence of DPC micelles is distorted at the alanine (A4111), which was also observed for TOR FATC. The respective structures of the oxidized and reduced micelle-immersed states of the TOR FATC domain show a distortion of the  $\alpha$ -helix around A2453, which is not present in the free form and which has been suggested to arise, because this alanine is at the interface between the solvent and micelle [69]. The C-terminal region may further fold back onto the preceding region, presumably facilitated by a conserved glycine, which is shared by the FATC domains of all PIKKs, but TRRAP having an also rather small alanine at the equivalent position. Secondary structure analysis for the FATC domain of ATM reveals that the helical regions are interrupted after A3039 and P3050/G3051. Thus, alanine and glycine may play a role for the formation of similar membrane-bound structures and/or for the positioning in the membrane, as already proposed for the TOR FATC domain [69].

Summarizing, this study shows that the ability to interact with membrane mimetics appears to be a general property of the PIKK FATC domains. Differences in the distribution of hydrophobic and charged side chains in the respective FATC domains may thus result in different preferences for specific membrane properties such as surface charge and curvature or the packing density of the lipid acyl chains as well as the presence of cholesterol or certain proteins. This is expected to result in different binding specificities for different cellular membranes or membrane regions, which would be consistent with the different localization patterns and localized specific activities of the various PIKKs in cells.

### 4.3 Detailed characterization of the membrane interactions of the TOR FATC domain

#### 4.3.1 Membrane interaction studies with y1fatc and mutant proteins

Recent data have shown that y1fatc can interact with different membrane mimetic particles. Based on the structures of oxidized and reduced y1fatc immersed in DPC micelles and the binding surface determined from the DPC titration of oxidized y1fatc [69], an initial model for the membrane immersion was proposed. To define the membrane association properties in more detail, additional structural studies were performed. Fig. 4.20a and 4.20c show superpositions of the  $^1\text{H}$ - $^{15}\text{N}$  HSQC spectra of y1fatc in the absence and presence of either DPC micelles or DihepPC/DMPC bicelles used as a reference for the following studies. Due to the interaction with the rather small DPC micelles (19 kDa [188, 196]) or DihepPC/DMPC bicelles (>250 kDa [197]), several peaks of y1fatc shift to new positions, as already described [69].

Since liposomes are considered to be a better mimetic for natural membranes as micelles as well as bicelles, the interaction of y1fatc with neutral DMPC liposomes of the small unilamellar vesicle (SUV) type was also analyzed. In the presence of liposomes at a DMPC concentration below 30 mM (Fig. 4.20e) several peaks of y1fatc disappear in the respective  $^1\text{H}$ - $^{15}\text{N}$  HSQC spectra. This indicates that y1fatc also interacts with the very large DMPC liposomes resulting in broadening of most of its resonances beyond detection. Furthermore, the interaction with micelles composed of a neutral diacyllipid (DihepPC, Fig. 4.21a) was studied completing the already existing data of neutral micelles composed of phosphocholine headgroups and micelles with negatively charged diacyllipid headgroups [69]. The overall spectral changes are similar as with DPC micelles and bicelles in which the rim is formed by DihepPC. Accordingly, most resonances of y1fatc show also different chemical shifts in the presence of DihepPC micelles compared to the free state. Since y1fatc can interact with neutral and negatively charged micelles, bicelles, and liposomes (Fig. 4.20a, 4.20c, 4.20e, and 4.21a) its interaction with membrane mimetics appears not to be very sensitive to specific membrane properties such surface charge and curvature or the packing of the fatty acid tail, which has already been proposed earlier [69].

##### 4.3.1.1 Membrane studies with DPC micelles

Tryptophans are known to play an important role for the membrane interactions of proteins [194, 203]. Thus, the effect of replacing one or both tryptophans by alanine (y1fatc W2466A and W2466A/W2470A) on the interaction with DPC micelles was initially analyzed. However, neither mutant showed a significantly reduced affinity for DPC micelles [69]. This suggests that the other aromatic and aliphatic residues in the y1fatc membrane anchor (Fig. 1.3) significantly contribute to the binding affinity.

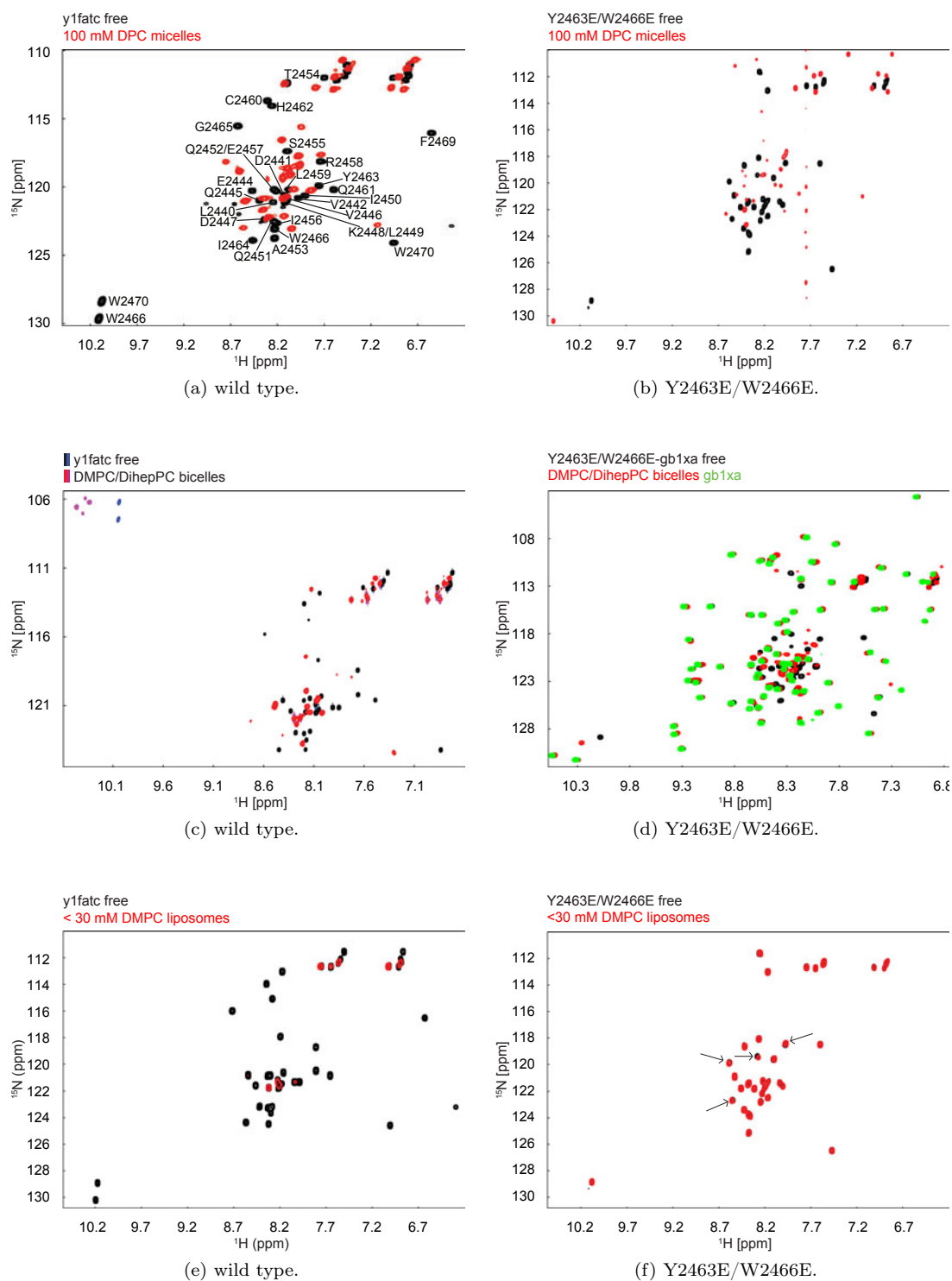


Figure 4.20: Comparison of the membrane association of y1fatc wild type with the mutant Y2463E/W2466E. Superposition of the  $^1\text{H}$ - $^{15}\text{N}$  HSQC spectra of y1fatc and Y2463E/W2466E with 50 mM DPC micelles, DMPC/DihepPC bicelles (<250 mM), and DMPC liposomes (<30 mM) (a-f). Residues marked with *black* arrows show small chemical shift changes upon binding to DMPC liposomes (f).



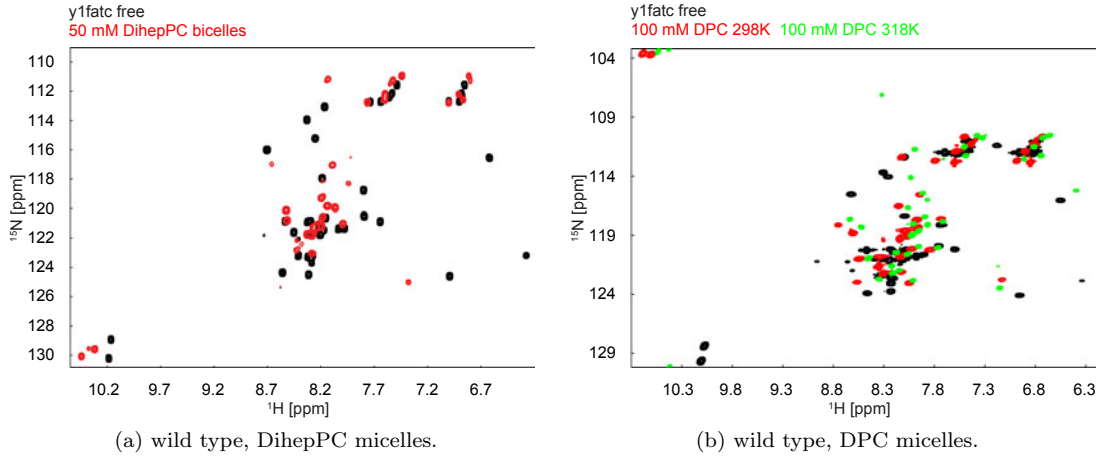


Figure 4.21: Association of y1fatc with DPC (a) and DihepPC micelles (b). Superposition of the  $^1\text{H}$ - $^{15}\text{N}$  HSQC spectra of y1fatc with 50 mM DihepPC micelles (a) and 100 mM DPC micelles at 298 and 318 K (b).

Table 4.4: Membrane association studies with TOR FATC wild type and mutant proteins. Mutants that were affected by the respective membrane mimetic are marked with '+', while '-' represents mutants that were not affected. Lipid binding studies with DihepPC/DMPC bicelles and/or DMPC liposomes were not performed (n.p.) for all mutants.

y1fatc protein	gb1xa	micelles	bicelles	SUVs
wild type	yes/no	+	+	+
L2459A	no	+	n.p.	n.p.
H2462A	no	+	n.p.	n.p.
Y2463A	yes/no	+	+	~ -
F2469A	no	+	n.p.	n.p.
W2466A	no	+	n.p.	n.p.
W2466A/W2470A	no	+	n.p.	n.p.
Y2463A/I2464A/W2466A/W2470A	no	+	n.p.	n.p.
Y2463E/W2466E	yes/no	+	+	~ -
Y2463D/I2464D/W2466A	yes	+	+	-
Y2463D/I2464D/W2466E/W2470R	yes	+	+	-
H2462R/Y2463D/I2464D/W2466A/F2469D	yes	+	+	-
G2465S/W2466S	yes	+	+	-
H2462R/Y2463D/I2464D/G2465S/W2466S/F2469D	yes	+	+	-
L2459E/H2462R/Y2463D/I2464D/G2465S/W2466A/F2469D	yes	+	n.p.	-
L2459S/H2462R/Y2463D/I2464D/W2466E/F2469D	yes	+	n.p.	-

To better understand the role of single residues for the interaction with membrane mimetics and to find a mutant that is not able to interact with membrane mimetics anymore, an ensemble of 13 additional y1fatc mutant proteins (see Appendix, Tab. A.3 on page 105) was analyzed regarding interactions with DPC micelles, DihepPC/DMPC bicelles and DMPC liposomes (Fig. 4.20, 4.22, 4.24, 4.25, and 4.26). In Tab. 4.4 an overview of all experiments performed with the respective y1fatc mutant is presented.

First, y1fatc single mutant proteins were prepared by replacing each time one hydrophobic residue in the membrane anchor by alanine (L2459A, H2462A, Y2463A, and F2469A). The superpositions of the  $^1\text{H}$ - $^{15}\text{N}$  HSQC spectra in the absence and presence of a high concentration of DPC micelles are shown in Fig. 4.22. As the W2466A mutant, all newly prepared single mutants show strong spectral changes and a spectrum different from the free form with well-dispersed peaks. Thus all can still interact with DPC micelles. At 298 K oxidized micelle-immersed wild type y1fatc reveals fewer peaks than expected based on the number of residues in the sequence, because several of the peaks of the membrane anchor are not visible. They become only visible if the temperature is raised to 318 K, which reduces the affinity of the interaction with micelles (Fig. 4.21b, [69]). Based on a comparison of the number of peaks visible for the respective micelle-immersed states at 298 and 318 K with the wild type (Fig. 4.20a and 4.21b), single replacements by alanine have no significant effect on the affinity. At 318 K all mutants show as the wild type an increase of the number of peaks, which appears only somewhat less for the mutant Y2463A. However, the spectral appearance of H2462A and Y2463A (Fig. 4.22b and 4.22c) reveals a greater conformational heterogeneity compared to the well-structured free and micelle-immersed wild type protein [68, 69]. Several peaks appear as some kind of doublet, which can be seen looking at the number of resonances in the region around 10 ppm, where in case of a single conformation (or very fast dynamics) only two cross peaks should be visible for the side chain amide groups of the two tryptophans. Hence, residues H2462 and Y2463 may play a role for the backbone flexibility or packing in the disulfide bonded loop in the free and or micelle-immersed state. Moreover, they may influence the rate of cis/trans polymerization of P2468 or alter the interactions with the surrounding micellar environment.

Because the replacement of one (L2456A, H2462A, Y2463A, F2469A, W2466A) or two residues (W2466A/W2470A) does not significantly reduce the interaction with DPC micelles, additional mutants were prepared in which more residues were replaced by alanine or in which some residues were replaced by a polar or even a charged residue (see Appendix, Tab. A.3). The quadruple y1fatc mutant Y2463A/I2464A/W2466A/W2470A shows as the single or double alanine mutants strong spectral changes in the presence of DPC micelles (Fig. 4.22e). However, in this case the number and intensity of the micelle-immersed peaks does not significantly increase at higher temperature, indicating slightly decreased affinity compared to the oxidized micelle-immersed wild type. Similarly, replacement of two hydrophobic residues by negatively charged amino acid as in the y1fatc mutants Y2463E/W2466E or Y2463D/I2463D/W2466A (Fig. 4.20b and 4.22f) appears only to slightly reduce the affinity for DPC micelles.

Additionally, the change in the secondary structure content of several mutants was monitored by circular dichroism spectroscopy (Fig. 4.23). The replacement of one residue shows a spectrum of a partially  $\alpha$ -helical protein in the free form (Fig. 4.23b, 4.23c, 4.23d, and 4.23g) represented by the minimum at about 208 nm. In the presence of 50 mM DPC the absolute signal intensity increases and a second minimum becomes visible at about 222 nm. These minima are typically observed for proteins containing a significant amount of  $\alpha$ -helical secondary structure. The CD spectra of L2456A and H2462A mutants are similar compared to that of the wild type (Fig. 4.23a), whereas the replacement of Y2463 and F2469 mutants appears to result in spectra with less  $\alpha$ -helical secondary structure content. The spectra of the quadruple mutant and both negatively charged mutants in the free form appear all to have a bigger contribution from an unfolded protein.

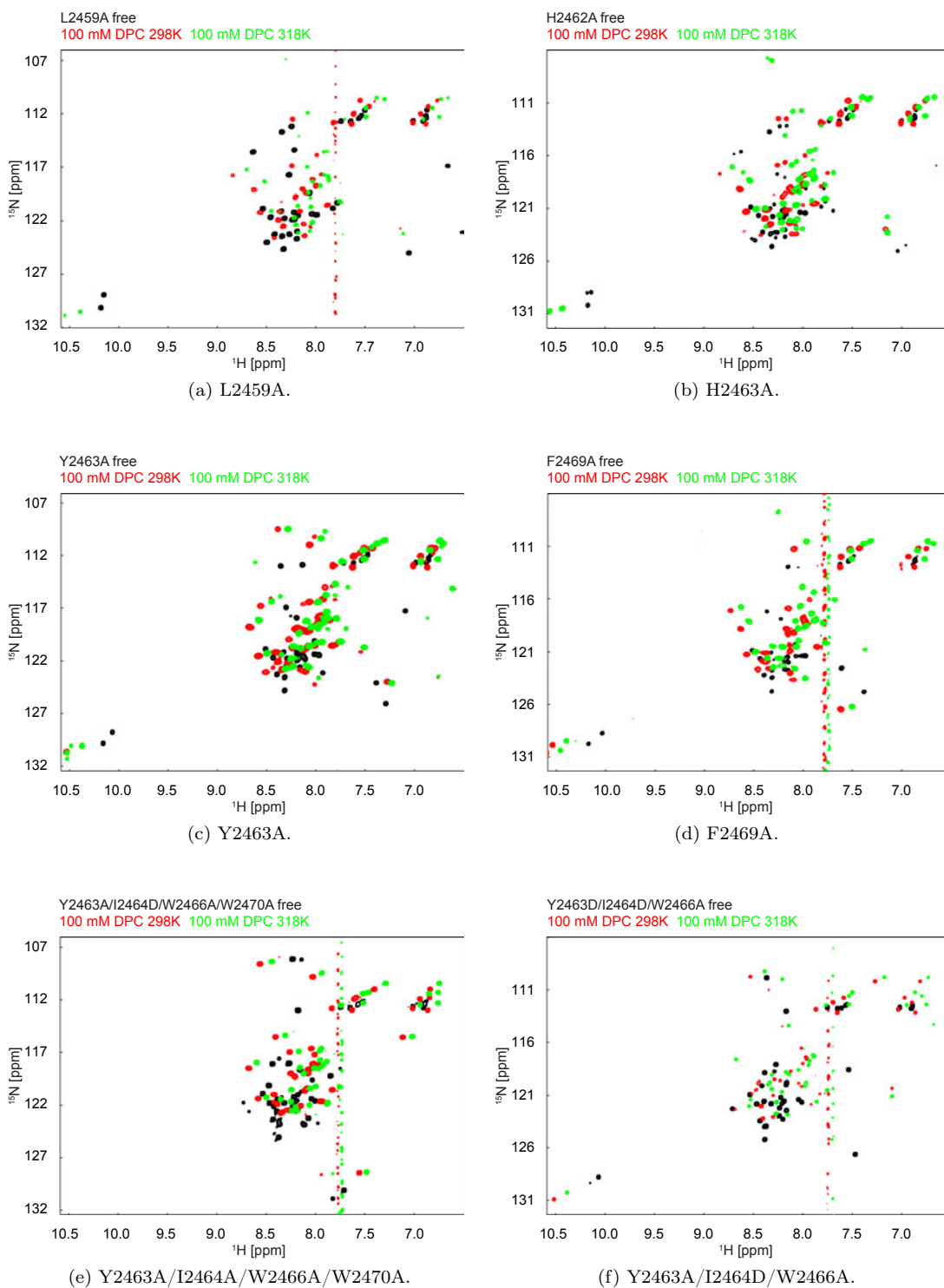
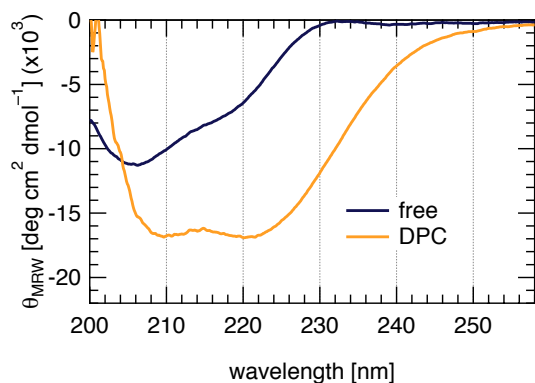
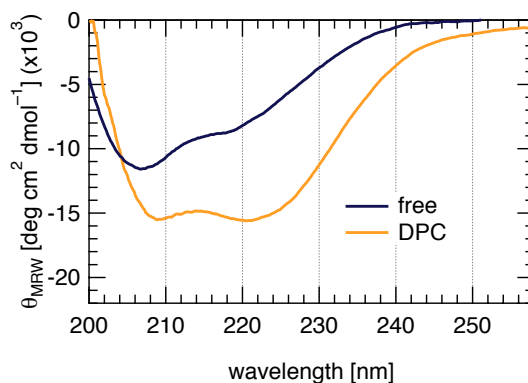


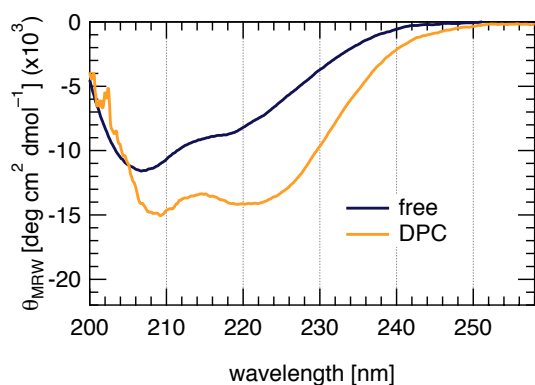
Figure 4.22: Membrane association of untagged mutant proteins of  $\gamma$ 1fatc with DPC micelles (a-f). Superposition of the  $^1\text{H}$ - $^{15}\text{N}$  HSQC spectra of L2459A, H2463A, Y2463A, F2469A, Y2463A/I2464A/W2466A/W2470A, and Y2463A/I2464D/W2466A respectively, with 100 mM DPC micelles at 298 and 318 K.



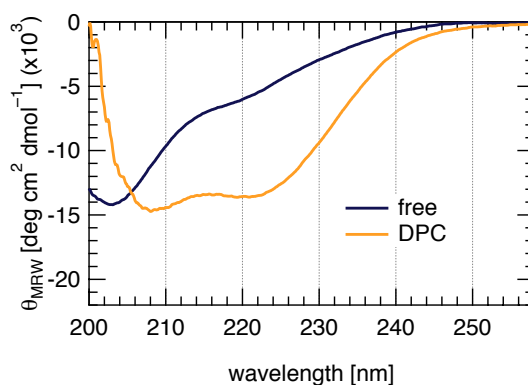
(a) wild type.



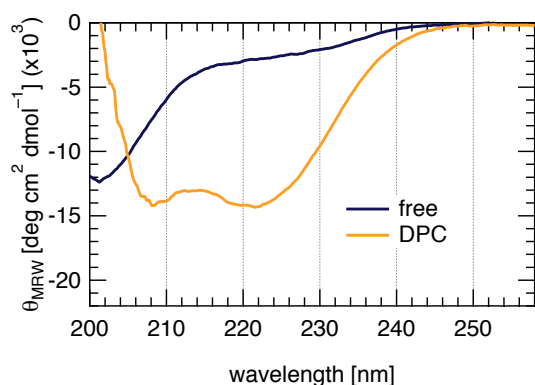
(b) L2459A.



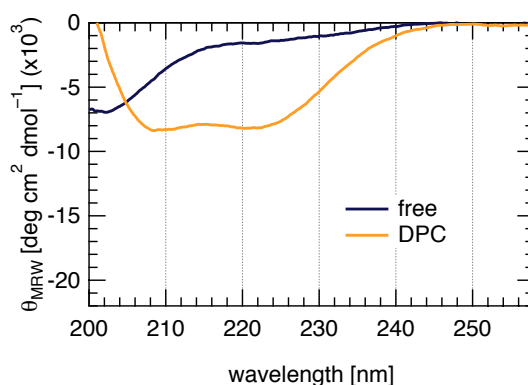
(c) H2463A.



(d) Y2463A.



(e) Y2463E/W2466E.



(f) Y2463A/I2464D/W2466A.

continued on next page

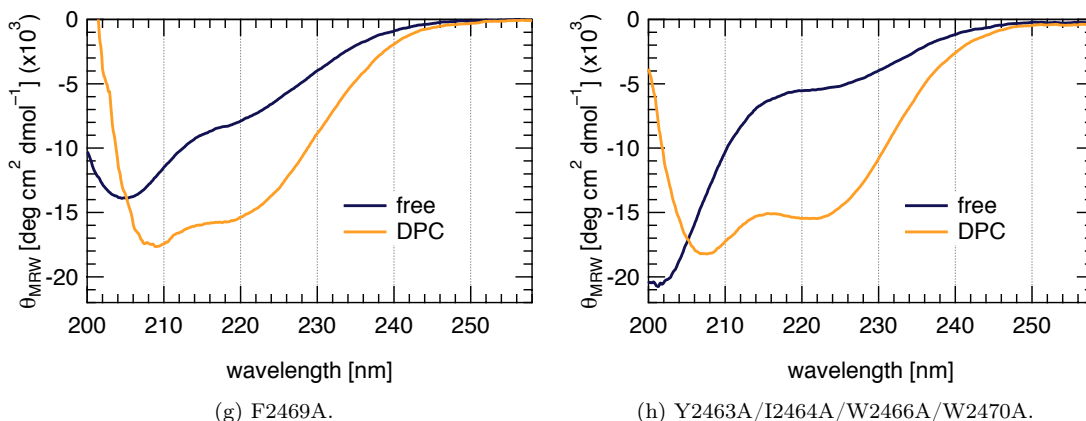


Figure 4.23: CD spectra of y1fatc and mutant proteins in the absence and presence of DPC micelles (a-h). CD spectra of the wild type, L2459A, H2463A, Y2463A, F2469A, Y2463A/I2464A/W2466A/W2470A, Y2463E/W2466E, and Y2463A/I2464D/W2466A respectively. The free form is marked in *blue*, the micelle-bound in *orange*.

However, in the presence of DPC micelles they still show a significant  $\alpha$ -helical secondary structure characterized by the two characteristic minima (Fig. 4.23h, 4.23e, and 4.23f). In the case of the y1fatc quadruple mutant,  $\theta_{MRW}$  is only approximately determined, because the protein concentration can not be accurately measured by UV/VIS. Overall, the CD data can only be used for a qualitatively analysis.

Therefore, further mutants were designed with either more drastic replacements of hydrophobic residues by polar or charged ones. For the following NMR interaction studies of additional y1fatc mutant proteins, the GB1 fusion protein was used based on the results illustrated in Chapter 4.1 [157]. As reference the superposition  $^1\text{H}$ - $^{15}\text{N}$  HSQC spectra of the wild y1fatc as fusion protein (y1fatc-gb1xa) is used (Fig. 4.1c). Replacement of up to seven hydrophobic residues with mostly polar or charged residues does not abrogate the interaction with membranes (Fig. 4.24). Finally, y1fatc mutants were prepared in which G2465, that is suggested to facilitate the formation of the disulfide bond, was replaced by serine (y1fatc G2465S/W2466S and H2462R/Y2463D/I2464D/G2465S/W2466S/F2469A). The idea was that this mutant may not as easily form the bulb-like structure determined for the oxidized as well as reduced micelle-immersed state [69]. However, also these two mutants are still able to interact with membrane mimetic DPC micelles (Fig. 4.24).

In conclusion, all tested y1fatc mutant proteins can still interact with DPC micelles. Thus, the remaining hydrophobic residues are still able to make interactions with the hydrophobic interior of DPC micelles, whereas the present polar or charged residues presumably mediate interactions with the positive and negative charges of the DPC headgroup.

#### 4.3.1.2 Membrane studies with bicelles or liposomes

Because DPC micelles are rather small spherical particles with a high curvature and DPC is also used as detergent, the association of various y1fatc mutant protein was analyzed with DihepPC/DMPC bicelles that have a planar region consisting of a lipid bilayer. The superpositions of the  $^1\text{H}$ - $^{15}\text{N}$  HSQC spectra of several y1fatc mutant proteins in the free form and with DMPC/DihepPC bicelles ( $\sim 270$  mM) are shown in Fig. 4.20d and 4.25.

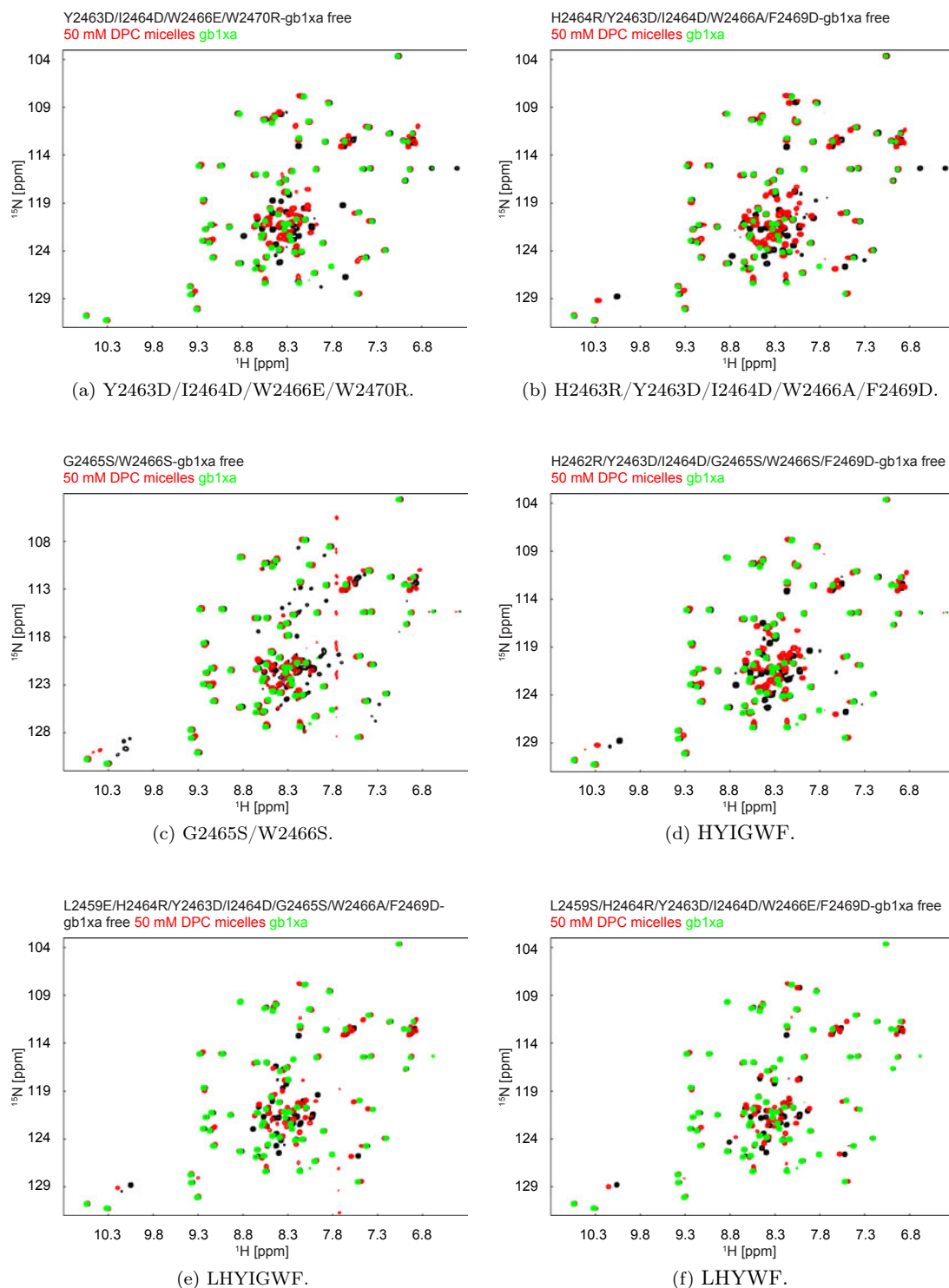


Figure 4.24: Membrane association of tagged mutant proteins of *y1fatc* with DPC micelles (a-f). Superposition of the  $^1\text{H}$ - $^{15}\text{N}$  HSQC spectra of tagged mutant proteins with 50 mM DPC micelles at 298 K. H2462R/Y2463D/I2464D/G2465S/W2466S/F2469D (HYIGWF), L2459E/H2462R/Y2463D/I2464D/G2465S/W2466A/F2469D (LHYIGWF), L2459S/H2462R/Y2463D/I2464D/W2466E/F2469D (LHYIWF).

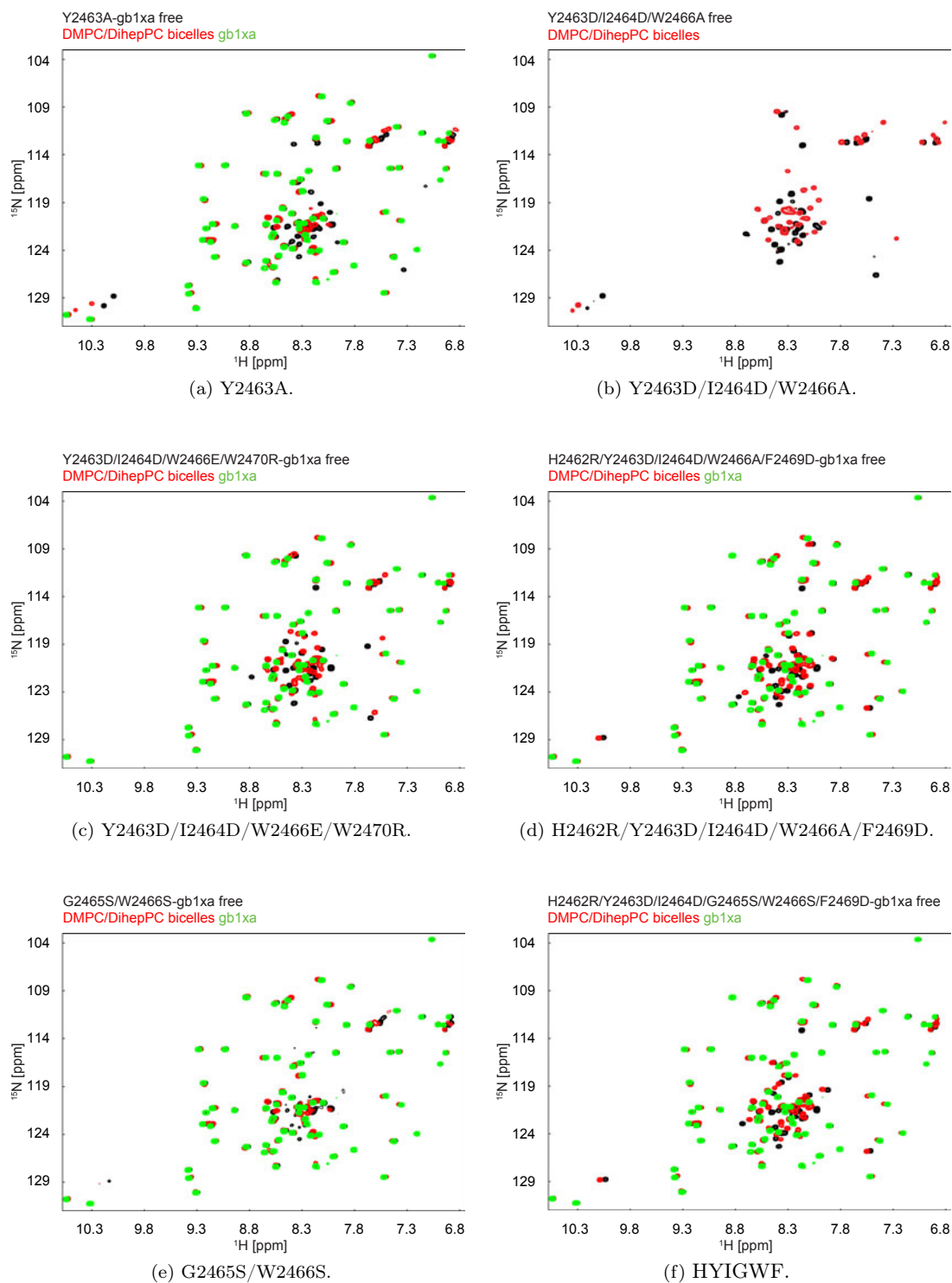
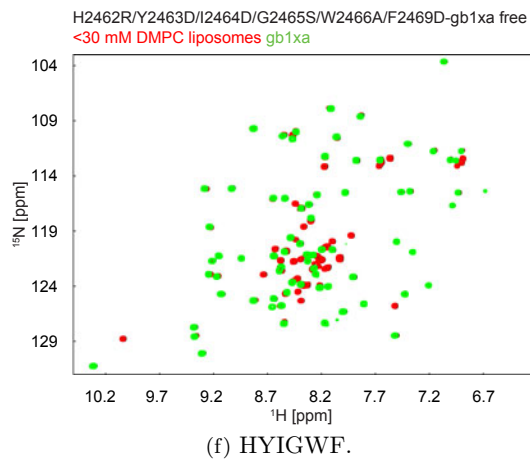
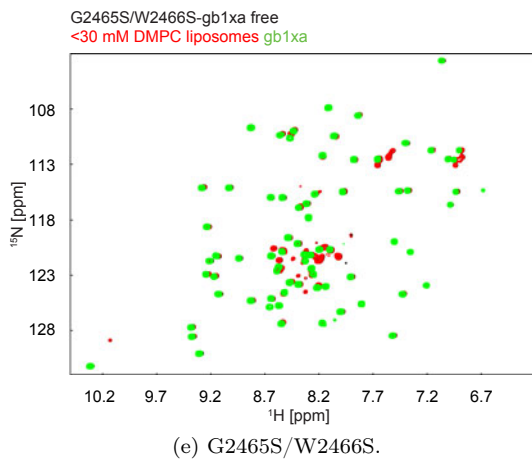
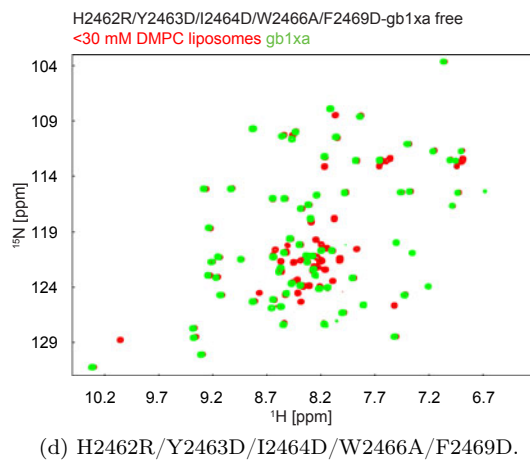
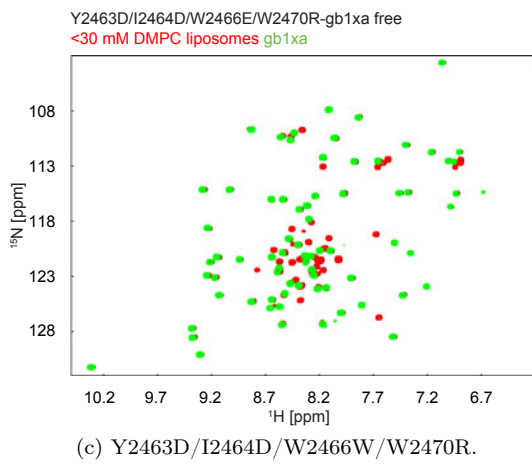
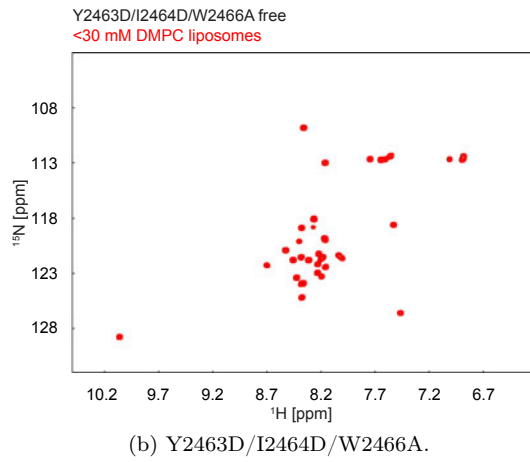
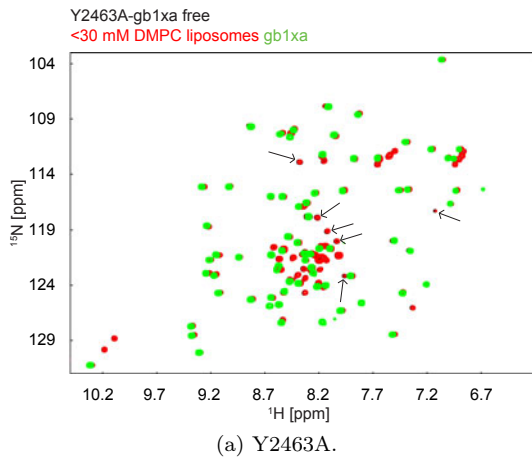


Figure 4.25: Membrane association of mutant proteins of  $\gamma 1\text{fatc}$  with DMPC/DihepPC bicelles (a-f). Superposition of the  $^1\text{H}$ - $^{15}\text{N}$  HSQC spectra of untagged and tagged mutant proteins with DMPC/DihepPC (>250 mM). H2462R/Y2463D/I2464D/G2465S/W2466S/F2469D (HYIGWF).



continued on next page



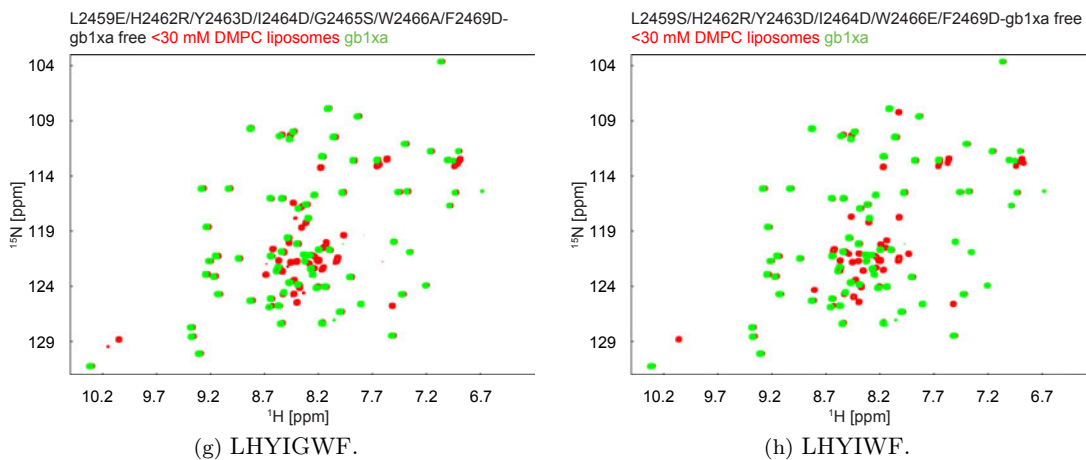


Figure 4.26: Membrane association of mutant proteins of *y1fatc* with DMPC liposomes (a-h). Superposition of the  $^1\text{H}$ - $^{15}\text{N}$  HSQC spectra of untagged and tagged mutant proteins with  $<30$  mM DMPC liposomes. Residues marked with *black* arrows show small chemical shift changes upon binding to DMPC liposomes (a). H2462R/Y2463D/I2464D/G2465S/W2466S/F2469D (HYIGWF), L2459E/H2462R/Y2463D/I2464D/G2465S/W2466A/F2469D (LHYIGWF), L2459S/H2462R/Y2463D/I2464D/W2466E/F2469D (LHYIWF).

However, even a *y1fatc* mutant with six residues of the membrane anchor replaced by polar or charged residues shows still significant spectral changes in the presence of the high concentrations of bicelles indicating a significant affinity of all *y1fatc* mutants for bicelles (Tab. 4.4).

Finally, the affinity for liposomes better resembling natural membranes was probed, since all tested *y1fatc* mutants can still interact with rather high concentrations of DPC micelles or DihepPC/DMPC bicelles. The liposomes were prepared from lower lipid concentrations with a final concentration of  $<30$  mM in the sample. Oxidized wild type *y1fatc* interacts with DMPC liposomes resulting in the disappearance of the majority of its resonance (Fig. 4.20e). Replacement of two aromatic residues by glutamate (Y2463E, W2466E) significantly reduces the interaction with liposomes. Accordingly, only very minor spectral changes can be seen comparing the  $^1\text{H}$ - $^{15}\text{N}$  HSQC spectra in the absence and presence of liposomes (Fig. 4.20f). Even replacement of only one aromatic residue by alanine (Y2463A), here as fusion protein Y2463A-gb1xa, results in similar minor spectral changes upon addition of liposomes (Fig. 4.26a). Consistent with this, mutation of three or more residues cause no spectral changes at all (Fig. 4.26).

In summary, the NMR interaction studies of *y1fatc* with different membrane mimetics show that at least in case of the TOR FATC domain high concentrations of micelles and bicelles appear not to be suitable to find rather moderate mutations that abrogate membrane interactions. Only the use of liposomes (DMPC SUVs) at low concentrations results in clearly different binding behavior of the mutant proteins compared to the wild type and demonstrates that the replacement of one or two residues is probably sufficient to abrogate the binding of the TOR FATC domain to cellular membranes.

### 4.3.2 NMR experiments with spin labeled micelles

For the membrane immersion of the oxidized and reduced TOR FATC domain an initial model was derived using the respective calculated structures and the micelle binding surface from the titration of oxidized  $\gamma$ 1fatc with DPC [69]. Based on this model several hydrophobic residues in the C-terminal region (I2456 - W2470) may penetrate the micelle and interact with the hydrophobic interior, whereas a rim of charged residues (E2457, R2458, C-terminal carboxyl group) may interact with charges in the lipid headgroups [69]. For a more detailed determination of the immersion depth,  $^1\text{H}$ - $^{15}\text{N}$  HSQC spectra of oxidized or reduced  $\gamma$ 1fatc in the presence of micelles (50 mM DPC) and increasing concentrations of either 5- or 16-SASL (1 to at maximum 4 mM) were recorded and the respective spectral changes analyzed. The CMC value determined for 5-SASL (Fig. 3.1g) is 3.5  $\mu\text{M}$  [204] and this for 16-SASL (Fig. 3.1h) presumably in the same range, therefore both spin labels are expected to incorporate into DPC micelles. Nitroxide radicals are supposed to significantly enhance the transverse relaxation of the neighboring nuclei due to their large electronic relaxation time constants, whereas the pseudocontact shifts are negligible [205]. Thus, residues embedded in the micelle are supposed to reveal significant paramagnetic relaxation. In addition, they may show changes of their chemical shifts due to changes in the chemical environment compared to pure DPC micelles. Both effects are depending on the distance to micelle embedded 5- or 16-SASL, respectively. The immersion depth of the doxyl spin label in the micelle depends on its position along the stearic acid acyl chain. Whereas for 5-SASL the doxyl group is at the C5 position and thus approximately in the center of the C18 fatty acid chain, for 16-SASL it is close to the terminus and further away from the carboxyl group (Fig. 3.1g, 3.1h).

In the presence of 1 mM 5-SASL, the  $^1\text{H}$ - $^{15}\text{N}$  HSQC spectra of micelle-bound oxidized  $\gamma$ 1fatc show significant shifts for several residues, which become stronger upon increase of the concentration to 2 mM (Fig. 4.27c). Consistent with the previously established model for membrane immersion, several residues in the bulb-like C-terminal loop (G2465 - W2470) reveal the strongest shifts, whereas residues that are expected to be closer to the micellar surface smaller shifts (Fig. 4.28a, 4.28c, blue bars). At higher 5-SASL concentrations, up to 4 mM (Fig. 4.27b), the signals of the membrane anchor shift further. The change of the signal intensity due to paramagnetic relaxation enhancement reveals a rather moderate decrease being similar for all residues at 1 mM 5-SASL (data not shown). Increasing the 5-SASL concentrations, the reduction of signal intensity becomes gradually more different as a function of the sequence, but does not simply correlate with the observed chemical shift changes (Fig. 4.28a, 4.28c). As expected several residues from the bulb-like hydrophobic region (I2456, G2465, F2469, W2470) show a strong reduction of their signal intensity. Nevertheless, the intensity of N-terminal residues (L2440 - V2442) that are expected to be exposed to the solvent, is also significantly reduced. The reason might be the proximity to the doxyl group, additional dynamic effects of the protein itself, the movement of the protein and the spin label in the micelle as well as the on- and off-rate for micelle association.

This indicates that the change in the chemical shifts appears more sensitive to the immersion depth of the respective residues than the reduction in intensity for a peripheral membrane associated protein. Using concentrations of 1 to 2 mM 16-SASL, the induced chemical shift and intensity changes are overall stronger as observed for 5-SASL (Fig. 4.27d). As with 5-SASL, several residues of the C-terminal region (G2465 - W2470) show the strongest chemical shift changes in the presence of 2 mM 16-SASL. However, most residues N-terminal of the hydrophobic bulb (K2448 - Q2452) that are expected to reside at the micelle water interface or at the micelle surface reveal also significant chemical shift changes (Fig. 4.28a, 4.28c). The reduction in signal intensity is also strongest in the C-terminal region G2465 - W2470 (data not shown). However, it is rather strong along the whole sequence and appears as with 5-SASL not only to depend on the immersion depth of the respective residues.

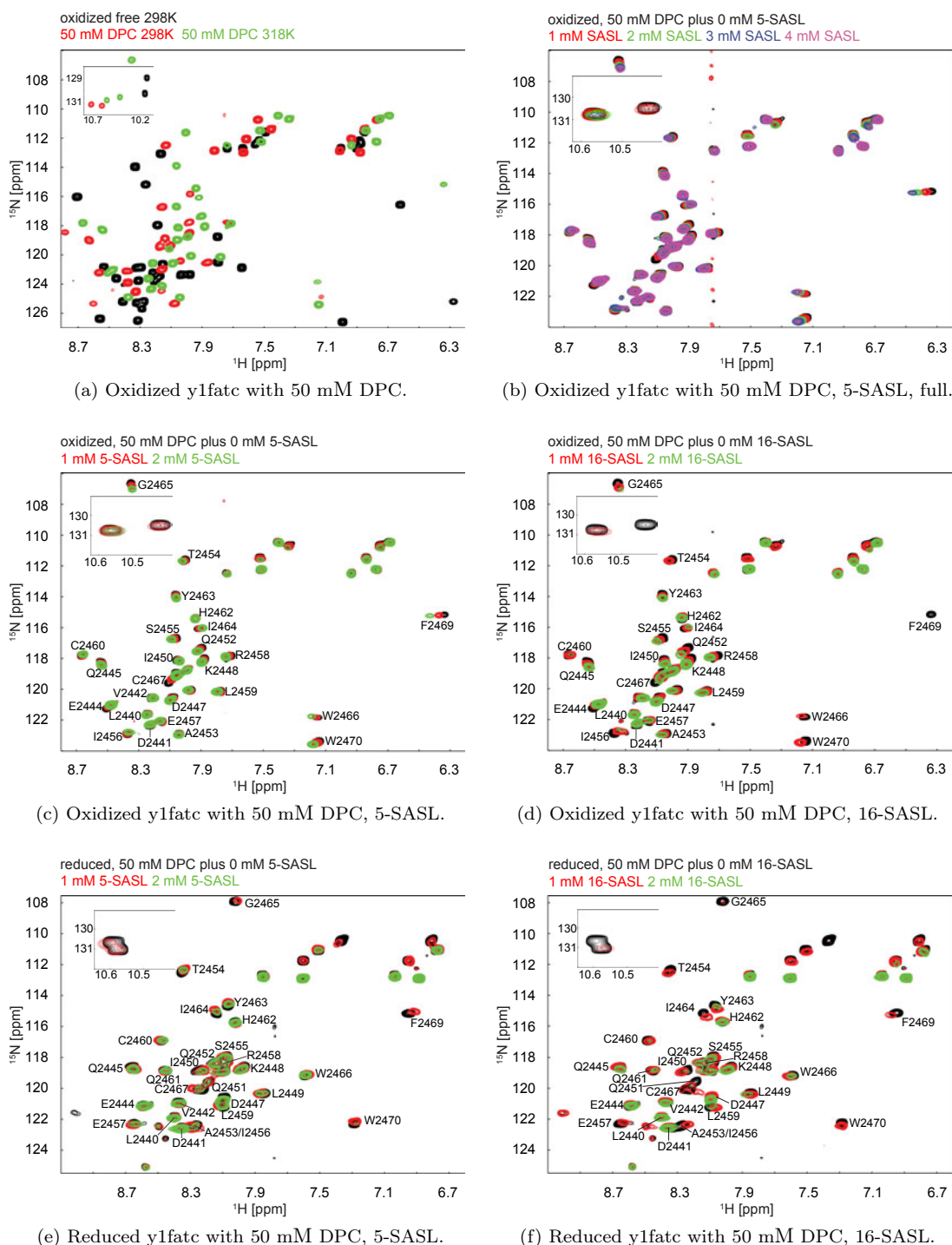
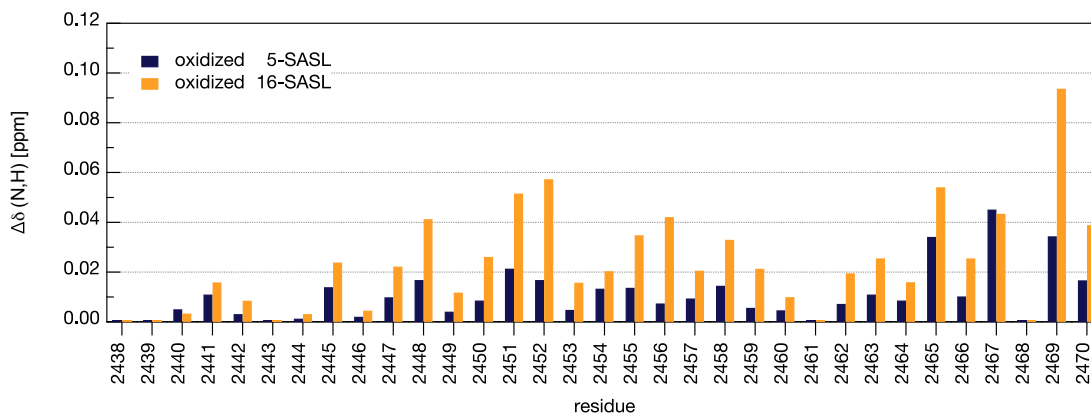
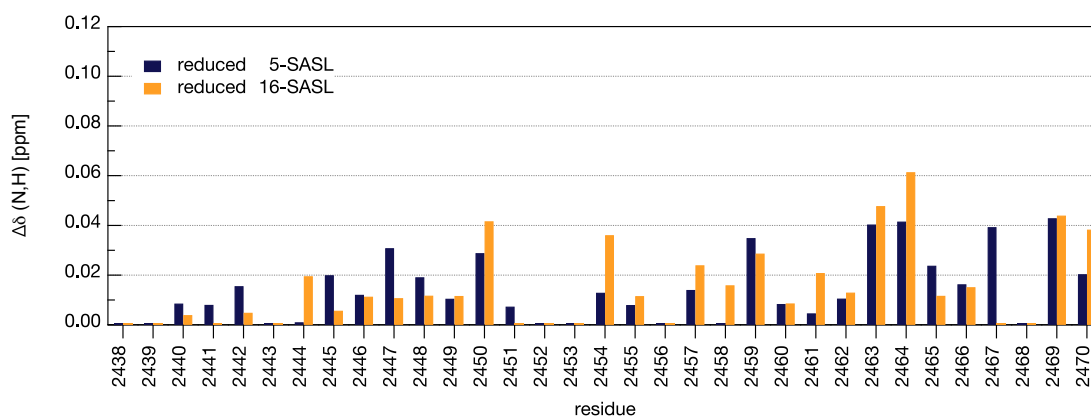


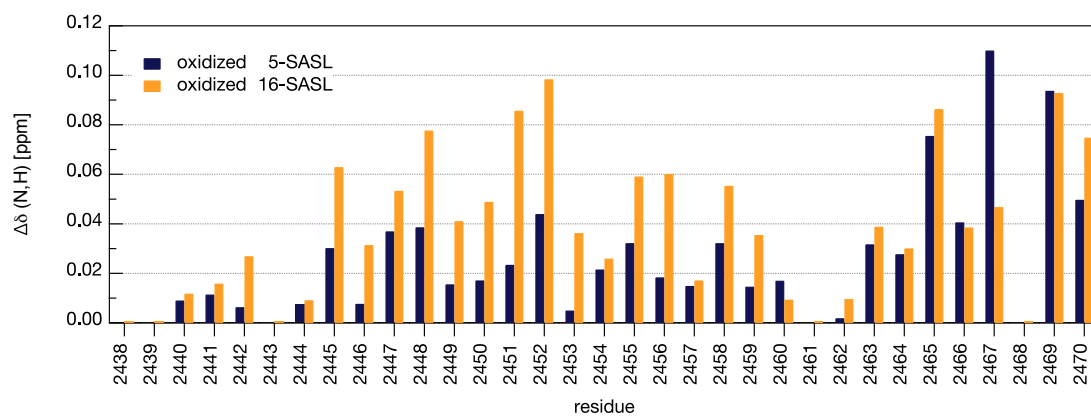
Figure 4.27: Characterization of oxidized and reduced y1fatc using spin labeled DPC micelles. Superposition of the  $^1\text{H}$ - $^{15}\text{N}$  HSQC spectra of oxidized y1fatc with DPC micelles at 298 and 318 K (a). Superposition of the  $^1\text{H}$ - $^{15}\text{N}$  HSQC spectra of oxidized micelle-bound y1fatc in the presence of increasing amounts of 5-SASL, full spectrum (b). Superposition of the  $^1\text{H}$ - $^{15}\text{N}$  HSQC spectra of oxidized micelle-bound y1fatc in the presence of increasing amounts of 5- and 16-SASL, respectively (c-d). Superposition of the  $^1\text{H}$ - $^{15}\text{N}$  HSQC spectra of reduced micelle-bound y1fatc in the presence of increasing amounts of 5- and 16-SASL, respectively (e-f). The color coding and the respective spin label concentrations are given at the top of the spectrum.



(a) Chemical shift changes of oxidized micelle-bound y1fatc, 1 mM.

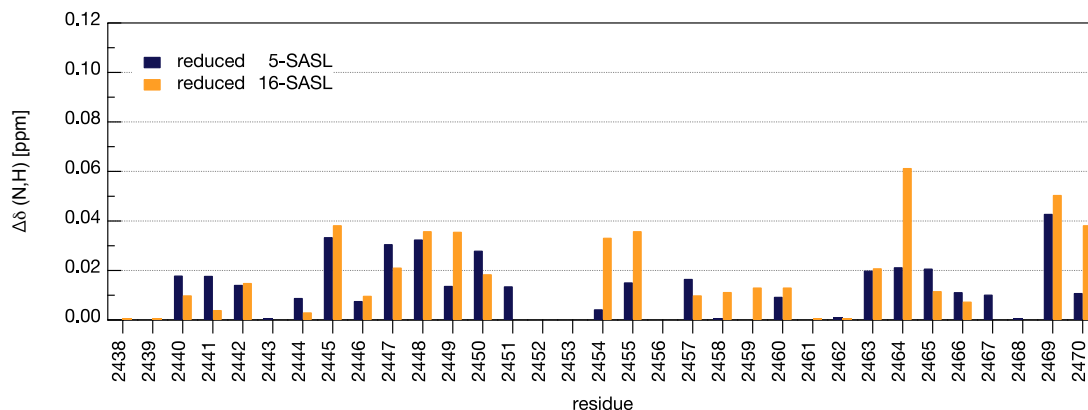


(b) Chemical shift changes of reduced micelle-bound y1fatc, 1 mM.



(c) Chemical shift changes of oxidized micelle-bound y1fatc, 2 mM.

continued on next page



(d) Chemical shift changes of reduced micelle-bound y1fatc, 2 mM.

Figure 4.28: Diagram of the chemical shifts of oxidized and reduced micelle-immersed y1fatc due to the presence of 1 mM or 2 mM 5-doxyl (a, c) and 16-doxyl (b,d) stearic acid.

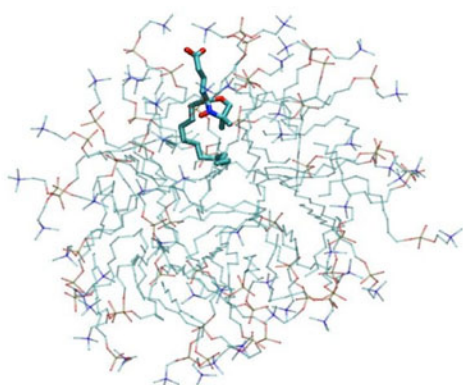
Reduced micelle-bound y1fatc shows strong chemical shifts changes in the presence of 5-SASL (Fig. 4.27e) for the C-terminal region such as F2469, but also rather strong ones for several residues along the  $\alpha$ -helix (Q2445 - I2450). Again the chemical shift changes are stronger in the presence of micelles containing 16-SASL instead of 5-SASL (Fig. 4.27f, 4.28b, 4.28d) and overall smaller as for the oxidized form (Fig. 4.27d). As for the oxidized form, the decrease in signal intensity with either 5- or 16-SASL (data not shown) appears not to be very sensitive to the immersions depth of the different residues of the membrane anchor and is rather uniform.

### 4.3.3 MD simulations of spin labeled micelles

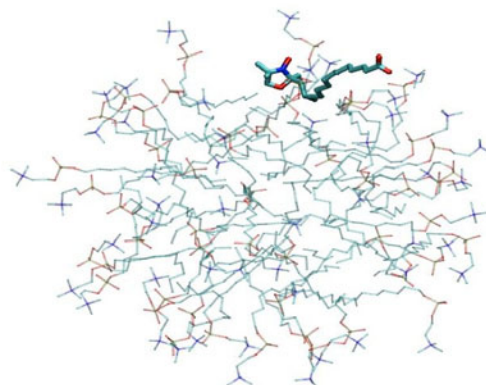
In the literature, NMR data of proteins embedded in 5- or 16-SASL tagged micelles is often interpreted based on the assumption that the doxyl group of 16-SASL is incorporated deeper in the hydrophobic core of the micelle and the one of 5-SASL is expected to reside closer to the micelle solvent interface [206, 139, 207]. If this would be the case, one would expect to observe stronger chemical shift and intensity changes with micelles containing 5-SASL than with such containing 16-SASL for a peripheral membrane-associated protein such as y1fatc. However, oxidized and reduced y1fatc show stronger chemical changes in the presence of 16-SASL compared to 5-SASL tagged micelles. In order to resolve this discrepancy, several MD simulations are run to obtain insights in the conformation of 5- and 16-SASL in DPC micelles as well as about the relative orientation of y1fatc and SASL in DPC micelles. Currently, only the pure DPC micelle consisting of 50 molecules with either one molecule 5- or 16-SASL are analyzed (Fig. 4.29).

Based on these simulations, 5-SASL orients and immerses in DPC micelles as assumed earlier with the carboxyl group (C1) close to the DPC head group, the  $\omega$ -end (C18) embedded in the hydrophobic micelle interior and the doxyl group (C5) is located in between. In contrast to earlier assumptions, the fatty acid chain of micelle-immersed 16-SASL bends such that both, the carboxyl group (C1) and the doxyl group (C16) close to the  $\omega$ -end are rather close to the micelle water interface. Thus, the doxyl group of 16-SASL is even closer to the micelle water interface as the one of 5-SASL. This is consistent with electron spin-echo studies of ionic micelles containing  $x$ -SASL ( $x = 5, 7, 10, 12, 16$ ) that show that the doxyl spin label is the most deepest immersed

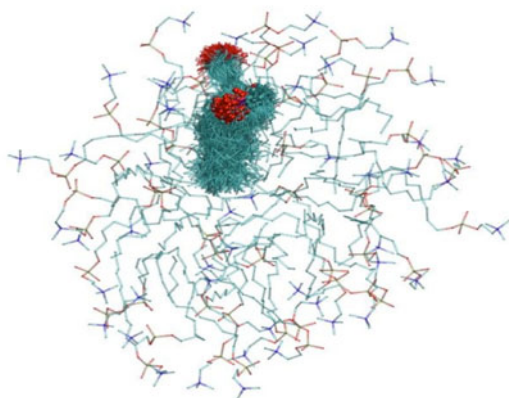
for  $x = 10$  and locates again closer to the surface the more the doxyl group moves towards the  $\omega$ -end ( $x = 12, 16$ ) [208]. This indicates that the energy cost for locating the doxyl group deep in the hydrophobic interior, if it is close to the  $\omega$ -end, is higher than for bending the fatty acid chain. Based on these observations, the stronger spectral changes with micelles containing 16-SASL compared to 5-SASL for  $\gamma$ 1fatc can be explained. The majority of residues of  $\gamma$ 1fatc is expected to be located at the micelle water interface and in the hydrophobic interior region close to the DPC headgroups. Therefore the resonances for most  $\gamma$ 1fatc residues are supposed to show significant shifts in the presence of 16-SASL tagged DPC micelles. However, fewer residues are expected to immerse deeper in the micelle. Thus, spectral changes due to the presence of 5-SASL tagged DPC micelles are expected to be smaller.



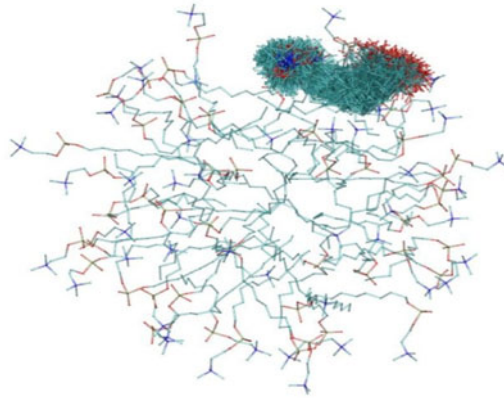
(a) DPC micelle with 5-SASL.



(b) DPC micelle with 16-SASL.



(c) Conformations of DPC micelle with 5-SASL.



(d) Conformations of DPC micelle with 16-SASL.

Figure 4.29: MD simulation of the spin labeled DPC micelle. Structure pictures of simulated DPC micelles (50 molecules) containing either one molecule of 5- or 16-SASL (a,b). Superimposed structures of 5- or 16-SASL from 50 time points of the 500 ns simulation period (c,d).

#### 4.3.4 Oriented CD spectroscopy of bilayer immersed protein

Oriented CD spectroscopy is used for the determination of the orientation of  $\alpha$ -helices embedded in lipid bilayers. First, reference CD measurements of free oxidized and reduced y1fatc show that both populate  $\alpha$ -helical secondary structure, indicated by minima around 205 and 222 nm (Fig. 4.30). However, oxidized y1fatc reveals a significant higher amount of  $\alpha$ -helicity compared to the reduced form (Fig. 4.30, blue and blue dashed spectra), which may be caused by the higher flexibility of the C-terminal end of reduced y1fatc. This is consistent with the structure and dynamic data for free oxidized y1fatc and the observed spectral differences in the  $^1\text{H}$ - $^{15}\text{N}$  HSQC spectra of oxidized and reduced y1fatc [68]. Reconstitution of oxidized and reduced y1fatc in DMPC liposomes with a protein-lipid-ratio (P/L) of 1:50 (Fig. 4.30, orange and orange dashed spectra) results in an increase of  $\alpha$ -helical secondary structure compared to the free state. Using liposomes prepared from a 1:1 mixture of the neutral lipid DMPC and the negatively charged lipid DMPG (P/L of 1:50), the  $\alpha$ -helicity for both redox states increases even further (Fig. 4.30, green and green dashed spectra).

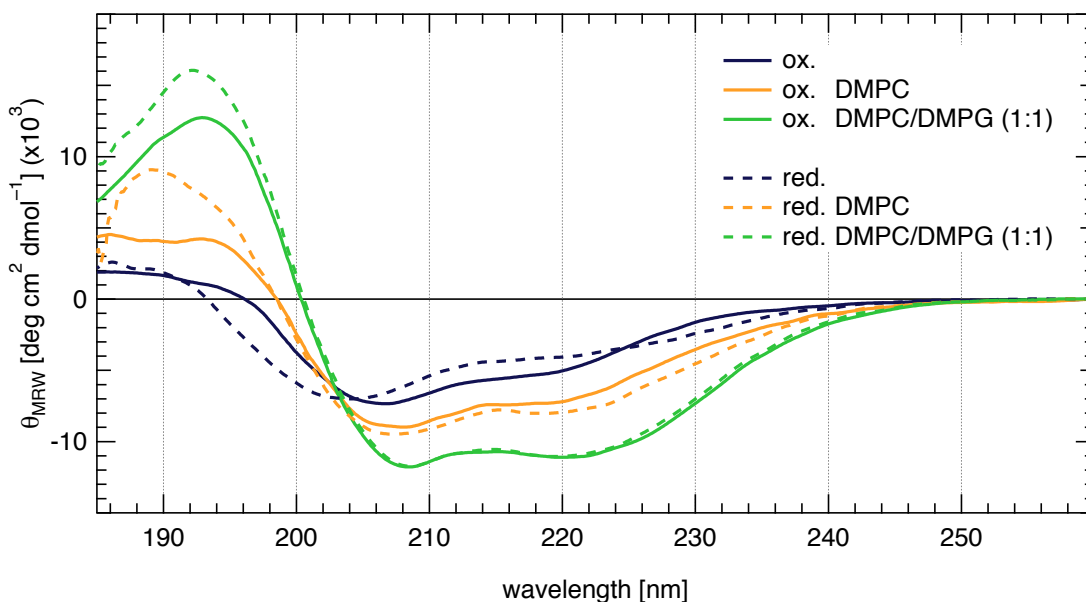


Figure 4.30: CD spectra of oxidized and reduced y1fatc in the absence and presence of liposomes composed of only neutral DMPC or a negatively charged mixture of DMPC/DMPG (1:1). The used liposomes including the ratio and the respective color coding is given in the spectrum.

Based on an estimate of the secondary structure content with the online server dichroweb [143] that employs the CONTIN-LL and CDSSTR algorithms [162, 163, 165, 164], the amount of  $\alpha$ -helical secondary structure in the presence of either DMPC or DMPC/DMPG liposomes is 20 % and 30 %, respectively (see Appendix in Tab. A.6a, A.6b). The  $\alpha$ -helical secondary structure content is lower than estimated for the DPC micelle-immersed oxidized and reduced y1fatc based on the determined NMR structures [69], which was estimated around 57 % and 60 %, respectively. The difference can be explained by several reasons. First, the P/L in these CD measurements was 1:50 and the membrane mimetic concentration for the NMR structure determination was very high (150 - 200 mM DPC) corresponding to a protein/DPC ratio of about 1:300-400. Thus, more protein is expected to be in the membrane mimetic immersed state, in which the  $\alpha$ -helix is stabilized, compared to the free state.



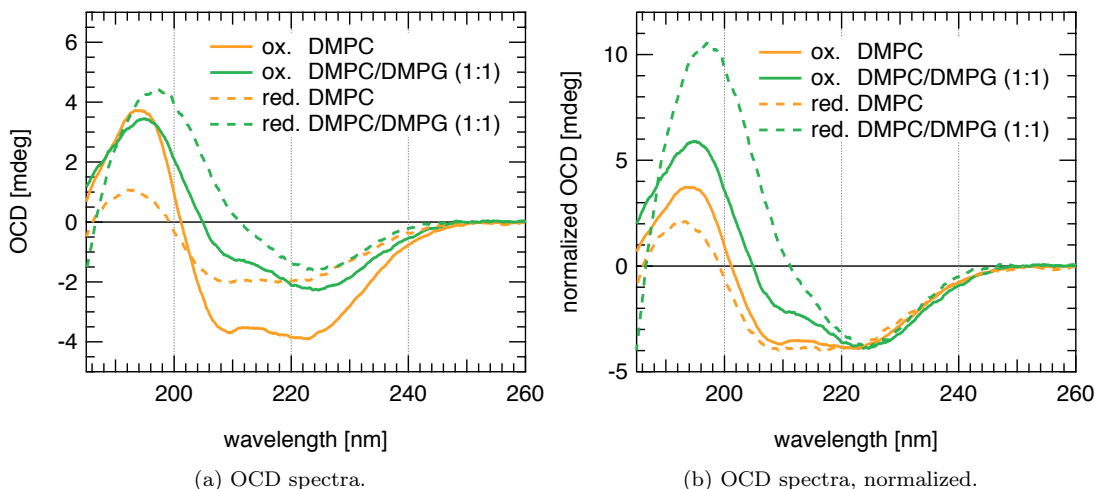


Figure 4.31: OCD spectra of oxidized and reduced y1fatc in the absence and presence of liposomes composed of only neutral DMPC or a negatively charged mixture of DMPC/DMPG (1:1) (a) and normalized to  $\theta$  at 223 nm of oxidized y1fatc DMPC bilayer (b). The used liposomes including the ratio and the respective color coding is given in the spectrum.

Second, y1fatc may have a higher affinity for DPC micelles compared to DMPC and DMPC/DMPG liposomes and/or the micelles may better stabilize the  $\alpha$ -helix in oxidized and reduced y1fatc due to their higher curvature.

CD data of proteins containing a single  $\alpha$ -helix reconstituted in oriented lipid bilayers (OCD data) allows to estimate the orientation of the long axis of the helix with respect to the membrane bilayer [209, 210]. As illustrated in the method section (Chapter 3.3.2 and Fig. 2.16) the theoretical spectrum for a single  $\alpha$ -helix orients either perpendicular (I-spectrum) or parallel (S-spectrum) to the lipid bilayer, respectively. The estimation of the angle between the long axis of the helix and the membrane normal is based on the decomposition of the contributions from the I- and S-spectra. Fig. 4.31 shows the OCD spectra (each time averaged over all measurement angles) of oxidized and reduced y1fatc in oriented bilayers formed by only neutral DMPC or a 1:1 mixture of neutral DMPC and negatively charged DMPG. The OCD spectrum of oxidized y1fatc in pure DMPC bilayers (Fig. 4.31, orange spectrum) shows minima around 209 nm and about 223 nm with similar intensity representing rather similar contributions from the I- and S-spectra, which indicates a tilt angle with respect to the membrane normal roughly between  $30^\circ$  -  $60^\circ$ . The shape of the spectrum of the reduced form in DMPC bilayer (Fig. 4.31, orange dashed spectrum) is rather similar but appears to have a slightly bigger contribution from the I-spectrum (parallel orientation to bilayer), corresponding to a tilt angle of the helix with respect to the membrane normal in the range of about  $35^\circ$  -  $65^\circ$ . However, the overall signal intensity is much lower, presumably because of a lower affinity for DMPC vesicles and thus a smaller amount of protein reconstituted in the oriented bilayers.

The OCD spectra of both redox states in lipid bilayers consisting of DMPC/DMPG look different from those in neutral bilayers composed of only DMPC (Fig. 4.31, green and green dashed spectrum). The minimum at about 209 nm is less deep than the one at about 223 nm indicating a bigger contribution of the I-spectrum and a steeper orientation of the helix of y1fatc with respect to the membrane bilayer. The tilt angle of the helix long axis with respect to the membrane normal is in the range of  $5^\circ$  -  $35^\circ$  for oxidized and  $0^\circ$  -  $30^\circ$  for reduced y1fatc with lower signal intensities for both redox states compared to the neutral DMPC bilayers.



Based on the previously determined NMR experiments of both states in neutral DPC micelles and the corresponding model for membrane immersion, the steeper tilt angle may be due to electrostatic repulsion between the acidic N-terminal region and the negatively charged membrane surface. Combining all data, a refined model for the membrane interactions of oxidized and reduced  $\gamma$ 1fatc in neutral bilayers can be established (Fig. 4.32).

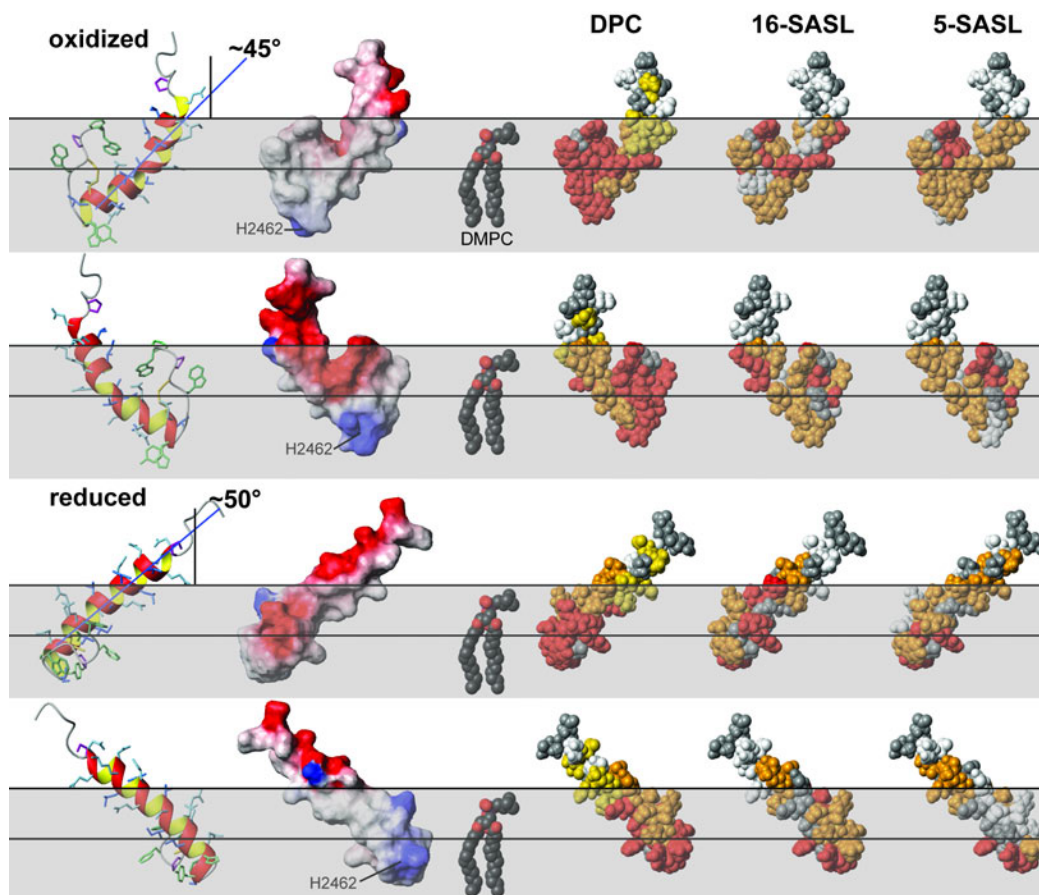


Figure 4.32: Refined model of the membrane immersion of oxidized (upper two panels) and reduced (bottom two panels)  $\gamma$ 1fatc. The membrane region is indicated by the grey shaded area with two horizontal lines marking the head group region. The 1<sup>st</sup> column shows ribbon representations of the determined NMR structures of oxidized and reduced  $\gamma$ 1fatc [69]. The side chains are additionally shown in a neon representation (C – yellow, G – orange, P – magenta, aromatic residues – green, aliphatic – dark blue, polar and charged – light blue). The 2<sup>nd</sup> column shows representations of the surface charge (blue – positive, red – negative). As a reference, the 3<sup>rd</sup> column shows in all panels a CPK representation of a DMPC molecule at the same scale as  $\gamma$ 1fatc. For the 4<sup>th</sup> column the chemical shift changes observed earlier for oxidized  $\gamma$ 1fatc titrated with DPC, are mapped onto the structures of oxidized and reduced  $\gamma$ 1fatc (red – strong, orange – medium, yellow – weak, white no, grey – no data, see [69]). For the 5<sup>th</sup> column the chemical shift changes observed for oxidized and reduced  $\gamma$ 1fatc in the presence of 50 mM DPC and 1 mM 16-SASL are mapped onto the surfaces of the respective structures and for the 6<sup>th</sup> column the chemical shift changes observed for oxidized and reduced  $\gamma$ 1fatc in the presence of 50 mM DPC and 2 or 1 mM 5-SASL, respectively (red – strong, orange – medium, yellow – weak, white – very weak, grey – no data). See appendix for more information.

### 4.3.5 Summary and discussion

TOR has been localized at various cellular membranes and in the nucleus and furthermore the regulation of the localization of TOR is probably mediated by a whole network of interactions involving protein-protein and protein-lipid interactions at membranes. It is supposed that the latter may be mediated by the FRB and the FATC domain [69, 186, 65].

For a better understanding of the role of different residues of the membrane anchor of the FATC domain, several mutants were analyzed regarding their membrane association. All prepared mutants are still able to interact with DPC micelles and DihepPC/DMPC bicelles, even after mutation of seven residues or replacement of G2465, which facilitates the formation of the disulfide bond. Only in the association studies with DMPC liposomes an abrogation is detected for a rather mild mutation of one hydrophobic residue in the C-terminal region (Y2463A). The different affinity of the  $\gamma$ 1fatc mutants to the tested lipids can be explained by the different concentrations of lipids used for the NMR studies. For the DPC micelles, concentrations were in the range of 50 - 150 mM and for bicelles the total lipid concentration was  $\sim$ 270 mM, thus rather high and as a consequence also the available membrane mimetic surface area. In contrast, the concentration of SUVs in the liposome samples was significantly below 30 mM as a result of lipid loss during the preparation procedure. Another reason might be the difference in curvature of the various lipids. While DPC micelles are rather small and spherical particles consisting of  $\sim$ 55 DPC molecules and a molecular weight of 19 kDa [196, 188], bicelles have a molecular weight of  $\sim$ 270 kDa with a rather planar region that is formed by a long chain phospholipid as DMPC, and the rim formed by a short chain lipid such as DihepPC showing a high curvature [197]. Liposomes of the SUV type are also rather spherical, but less curved and are overall much larger compared to bicelles. Based on the presented and earlier data dealing with the membrane association, the wild type FATC domain of TOR appears not to have specific preferences for membrane properties such as the presence of specifically shaped headgroups or the surface charge and curvature or the packing properties of the lipid acyl chain. The binding studies with different mutants suggest that liposomes (of the SUV type) are more suitable in general to find mutants that may also abrogate membrane association in *in vivo* localization studies in cells. Furthermore, the influence of the remaining residues in the membrane anchor in the micelles and bicelles studies is still enough to mediate hydrophobic interactions with micelles. The N-terminal region may have larger contribution to the association than initially expected, which would also be in line with the PRE data showing significant spectral changes for the residues in the N-terminal region of the  $\alpha$ -helix.

An unspecific interaction of peptides and proteins with micelles and bicelles, since highly mutated  $\gamma$ 1fatc proteins show still differences in the spectral appearance with all tested lipids, can be excluded by observations made for proteins with similar molecular weight such as GB1, a peptide corresponding to the loop of Formin C and unpublished data for PknG, which all reveal no interaction with micelles and bicelles [157, 200]. As a consequence, different affinities for different membrane mimetics have to be examined in the context of the current knowledge of the protein function.

The NMR spin studies using micelles containing 5- or 16-doxy stearic acid provide valuable information about the immersion depth and the interactions of  $\gamma$ 1fatc with different regions of the micelle. The studies indicate significant shifts and intensity losses for residues interacting with the micelle. The induced chemical shift changes for oxidized and reduced  $\gamma$ 1fatc are stronger for 16-SASL compared to 5-SASL and are strongest in the C-terminal region. The signal intensity appears not to be very sensitive to the immersion depth of the different residues of the membrane anchor. In the course of these studies it becomes apparent that several factors have to be considered for the interpretation such as the conformation, the location, and the number of the spin labels as well as the dynamic of the whole system. Preliminary results of

MD simulations of only the tagged DPC micelles illustrate the position of the doxyl group in the micelle revealing that in 16-SASL the fatty acid chain is bended such that the doxyl group at C16 is rather close to the micelle water interface and not as formerly assumed rather deep in the hydrophobic interior [206, 139, 207]. Based on this simulation, it can be explained why a peripheral membrane protein as y1fatc shows stronger spectral changes with 16-SASL than expected based on earlier assumptions.

The OCD and CD analysis allows a rough estimation of the angle of the  $\alpha$ -helix of oxidized and reduced y1fatc with respect to the bilayer normal in neutral DMPC ( $\sim 30^\circ - 60^\circ$ ) or negatively charged DMPC/DMPG bilayers ( $\sim 5^\circ - 35^\circ$ ). In negatively charged bilayers the orientation is steeper, which can be explained based on repulsion with the acidic N-terminus of y1fatc. The TOR FATC domain is a peripherally associating protein, which shows a smaller degree of reconstitution in the bilayer compared to a transmembrane protein resulting in a lower signal intensity, S/N ratio, and data quality. Hence a more detailed, quantitative analysis is not possible. The estimate of affinity to DPC micelles by NMR diffusion data has shown that the one of reduced y1fatc is slightly lower compared to that of the oxidized form [69]. Moreover, due to the rather acidic N-terminal region, the affinity for negatively charged membrane mimetics is assumed to be slightly lower than for neutral membrane mimetics, for both, oxidized and reduced y1fatc. In agreement with this, the signal intensity for oxidized y1fatc in neutral bilayer is the highest and for reduced y1fatc in negatively charged bilayers the lowest.

To sum up, using the presented data in combination with the previously determined structures of oxidized and reduced micelle-immersed y1fatc [69], a refined model for the membrane association is established that includes information about the angle of the helical long axis from OCD measurements and the immersion depth from the PRE binding studies. Currently performed MD simulations of DPC micelles containing not only 5- or 16-SASL but also the C-terminal half of the FATC domain that mediates the major interactions with the micelles will give more detailed insights for the analysis of the PRE data.



## Chapter 5

# Conclusion and Outlook

The scope of this work was the investigation of the FATC domains of the known PIKKs, which are composed of rather hydrophobic and aromatic residues, regarding the ability to interact with a membrane mimetic environment. The results presented show that the FATC domains of DNA-PKcs, ATM, SMG-1, TRRAP, and ATR associate to the tested lipids and thereby it appears that a general common property of the FATC domains exists. However, each FATC domain has different preferences for specific membrane properties and thus different binding specificities for cellular membranes or regions. Future detailed interaction studies with differently composed membrane mimetics and different mutant proteins as well as structural studies of the membrane-bound forms for each individual PIKK FATC domain are needed to clarify their specific membrane preferences as well as structural differences in the membrane-associated states.

During the last years the PIKKs have been shown to be part of various signaling pathways and/or regulate different processes. A tight control of their cellular localization by a network of interactions may be one possibility to ensure a specific signaling output in response to the signaling state of the cell. Another aspect that may be considered for future membrane interactions studies, is the effect of reactive oxygen species (ROS) or oxidized lipids on cysteines in the highly conserved region of the FATC domain or about 60 - 80 residues N-terminal of that domain (ATM, SMG-1). It has been shown that ATM has a function in cellular redox signaling [6] and oxidation of C2991 in the less conserved part of the FATC domain region results in the formation of a dimer in which a different accessibility of the FATC domain for interactions with regulators and membrane patches may be present [211]. Also DNA-PKcs, TOR, and SMG-1 have been related to redox influenced cellular processes or states such as the mitochondrial metabolisms and/or hypoxia [104, 212, 213, 214, 31]. Finally, posttranslational modifications may influence the protein and/or membrane interactions of the FATC domain and thereby have to be analyzed, such as for example the acetylation of lysine 3016 in the ATM FATC [108, 215].

Further localization studies in cells will be needed to clarify the cellular localization patterns of PIKKs, especially TRRAP, and how they vary in response to specific signals. In addition, the influence of mutations on the ability to interact with membrane mimetics has to be analyzed as well as the effect of mutations that abrogate these interactions on the cellular localization, cellular stability, or response to specific signals.

Another part of this work was the characterization of the FATC domain of TOR by NMR, CD and OCD, as well as MD simulations to better define the immersion depth and the orientation of the helix in lipid bilayers. Complementary, mutant proteins of TOR FATC were analyzed

for a better understanding of the influence of different residues in the membrane anchor on the interaction with different membrane mimetics. It was shown that for a protein as y1fatc with a broad membrane mimetic binding affinity, only interaction studies employing SUVs at low concentrations are useful to find mutations that may also abrogate membrane interactions *in vivo*. Furthermore, the mutagenesis data reveal that the liposome association of the rather mild FATC single mutant Y2463A or the more harsh double mutant Y2463E/W2466E is abrogated. Therefore they could be useful to be incorporated in full-length yeast TOR1 or TOR from a higher eukaryote for *in vivo* studies to evaluate the influence on the localization pattern of TOR. Y2463 and W2466 are in the bulb-like C-terminal region and appear not to be critical for the loop formation but rather for interactions with lipids based on the structural available data [69, 68]. Based on the NMR data, both are still able to form the disulfide bond between C2470 and C2467. However, to separate the effect of these mutations on the membrane association from other effects on the function, reference experiment such as *in vitro* kinase assays determining the effect on the catalytic activity have to be performed. A recent model of a crystal structure of truncated human TOR in complex with LST8, Y2452 and W2545 (correspond to Y2463 and W2466 in y1fatc) suggests that both residues participate in substrate recognition mediating hydrophobic interactions [74]. This function may only be reduced if only tyrosine is mutated to alanine, whereas replacement of tyrosine and tryptophan by a negatively charged residue will presumably cause a complete abrogation. Moreover, the FATC domain interacts with the kinase domain and with one residue also with LST8, providing a hydrophobic surface region, which might not only be used for substrate binding as suggested but also for membrane interactions that participate in the regulation of TOR localization pattern.

In contrast to previous assumptions, the MD simulations reveals that the nitroxide group of 16-SASL is actually not incorporated in the DPC micelle interior but due to bending of the fatty acid chain rather close to the micelle water interface. The evaluation of NMR and MD simulation data further indicate that not only the number of the spin labels per micelle but also the dynamic reorganization properties of the whole system have to be considered. To conclude, the structural studies about the membrane-binding properties of the TOR FATC domain, combined with the established method of monitoring membrane interactions using GB1 fusion proteins, provide a good reference for future characterization studies of the membrane-binding properties of the other PIKK FATC domains. Coming back to the initial motivation of this work, the data presented give important insights and may support on the open questions regarding the interactions of TOR and the general common properties of the PIKKs.







# Bibliography

- [1] Keith, C. T.; Schreiber, S. L. *Science* **1995**, *270*, 50–51; PMID: 7569949.
- [2] Lempiäinen, H.; Halazonetis, T. D. *EMBO J.* **2009**, *28*, 3067–3073; PMID: 19779456.
- [3] Lovejoy, C. A.; Cortez, D. *DNA repair* **2009**, *8*, 1004–1008; PMID: 19464237.
- [4] Wullschleger, S.; Loewith, R.; Hall, M. N. N. *Cell* **2006**, *124*, 471–484; PMID: 16469695.
- [5] Laplante, M.; Sabatini, D. M. *Cell* **2012**, *149*, 274–293.
- [6] Ditch, S.; Paull, T. T. *Trends Biochem. Sci.* **2012**, *37*, 15–22.
- [7] Shiloh, Y. *Nat. Rev. Cancer* **2003**, *3*, 155–168.
- [8] McMahon, S. B.; Van Buskirk, H. A.; Dugan, K. A.; Copeland, T. D.; Cole, M. D. *Cell* **1998**, *94*, 363–374.
- [9] Herceg, Z.; Wang, Z. *Cell cycle* **2005**, *4*, 383–387; PMID: 15711126.
- [10] Sommer, L. A. M.; Schaad, M.; Dames, S. A. *J. Biol. Chem.* **2013**, *288*, 20046–20063; PMID: 23671275.
- [11] Mordes, D. A.; Glick, G. G.; Zhao, R.; Cortez, D. *Genes Dev.* **2008**, *22*, 1478–1489; PMID: 18519640.
- [12] Bosotti, R.; Isacchi, A.; Sonnhammer, E. L. *Trends Biochem. Sci.* **2000**, *25*, 225–227; PMID: 10782091.
- [13] Andrade, M. A.; Bork, P. *Nature genetics* **1995**, *11*, 115–116; PMID: 7550332.
- [14] Perry, J.; Kleckner, N. *Cell* **2003**, *112*, 151–155; PMID: 12553904.
- [15] Jiang, X.; Sun, Y.; Chen, S.; Roy, K.; Price, B. D. *J. Biol. Chem.* **2006**, *281*, 15741–15746.
- [16] Takahashi, T.; Hara, K.; Inoue, H.; Kawa, Y.; Tokunaga, C.; Hidayat, S.; Yoshino, K.; Kuroda, Y.; Yonezawa, K. *Genes Cells* **2000**, *5*, 765–775; PMID: 10971657.
- [17] Gouet, P.; Robert, X.; Courcelle, E. *Nucleic Acids Res.* **2003**, *31*, 3320–3323.
- [18] Vézina, C.; Kudelski, A.; Sehgal, S. N. *J. Antibiot.* **1975**, *28*, 721–726; PMID: 1102508.
- [19] Martel, R. R.; Klicius, J.; Galet, S. *Can. J. Physiol. Pharmacol.* **1977**, *55*, 48–51; PMID: 843990.
- [20] Singh, K.; Sun, S.; Vézina, C. *J. Antibiot.* **1979**, *32*, 630–645; PMID: 381274.

- [21] Heitman, J.; Movva, N. R.; Hall, M. N. *Science* **1991**, *253*, 905–909; PMID: 1715094.
- [22] Chen, J.; Zheng, X. F.; Brown, E. J.; Schreiber, S. L. *Proc. Natl. Acad. Sci. U. S. A.* **1995**, *92*, 4947–4951; PMID: 7539137.
- [23] Choi, J.; Chen, J.; Schreiber, S. L.; Clardy, J. *Science* **1996**, *273*, 239–242; PMID: 8662507.
- [24] Brown, E. J.; Albers, M. W.; Shin, T. B.; Ichikawa, K.; Keith, C. T.; Lane, W. S.; Schreiber, S. L. *Nature* **1994**, *369*, 756–758; PMID: 8008069.
- [25] Chiu, M. I.; Katz, H.; Berlin, V. *Proc. Natl. Acad. Sci. U. S. A.* **1994**, *91*, 12574–12578; PMID: 7809080 PMCID: PMC45481.
- [26] Sabatini, D. M.; Erdjument-Bromage, H.; Lui, M.; Tempst, P.; Snyder, S. H. *Cell* **1994**, *78*, 35–43; PMID: 7518356.
- [27] Fingar, D. C.; Blenis, J. *Oncogene* **2004**, *23*, 3151–3171; PMID: 15094765.
- [28] Hay, N.; Sonenberg, N. *Genes Dev.* **2004**, *18*, 1926–1945; PMID: 15314020.
- [29] Jacinto, E.; Hall, M. N. *Nat. Rev. Mol. Cell Biol.* **2003**, *4*, 117–126; PMID: 12563289.
- [30] Crespo, J. L.; Hall, M. N. *Microbiol. Mol. Biol. Rev.* **2002**, *66*, 579–591.
- [31] Dazert, E.; Hall, M. N. *Curr. Opin. Cell Biol.* **2011**, *23*, 744–755; PMID: 21963299.
- [32] Blagosklonny, M. V.; Hall, M. N. *Aging* **2009**, *1*, 357–362; PMID: 20157523.
- [33] Yang, Z.; Ming, X.-F. *Obes. Rev.* **2012**, *13 Suppl 2*, 58–68; PMID: 23107260.
- [34] Dann, S. G.; Selvaraj, G., A. and Thomas *Trends Mol. Med.* **2007**, *13*, 252–259; PMID: 17452018.
- [35] Crino, P. B. *Trends Mol. Med.* **2011**, *17*, 734–742; PMID: 21890410.
- [36] Caccamo, A.; Majumder, S.; Richardson, A.; Strong, R.; Oddo, S. *J. Biol. Chem.* **2010**, *285*, 13107–13120; PMID: 20178983.
- [37] Menon, S.; Yecies, J. L.; Zhang, H. H.; Howell, J. J.; Nicholatos, J.; Harputlugil, E.; Bronson, R. T.; Kwiatkowski, D. J.; Manning, B. D. *Sci. Signal* **2012**, *5*, ra24.
- [38] Santini, E.; Heiman, M.; Greengard, P.; Valjent, E.; Fisone, G. *Sci. Signal* **2009**, *2*, ra36; PMID: 19622833.
- [39] Guertin, D. A.; Sabatini, D. M. *Trends Mol. Med.* **2005**, *11*, 353–361; PMID: 16002336.
- [40] Long, X.; Spycher, C.; Han, Z. S.; Rose, A. M.; Müller, F.; Avruch, J. *Curr. Biol.* **2002**, *12*, 1448–1461; PMID: 12225660.
- [41] Oldham, S.; Montagne, J.; Radimerski, T.; Thomas, G.; Hafen, E. *Genes Dev.* **2000**, *14*, 2689–2694; PMID: 11069885.
- [42] Zhang, H.; Stallock, J. P.; Ng, J. C.; Reinhard, C.; Neufeld, T. P. *Genes Dev.* **2000**, *14*, 2712–2724; PMID: 11069888 PMCID: PMC317034.
- [43] Martin, P. M.; Sutherland, A. E. *Dev. Biol.* **2001**, *240*, 182–193.
- [44] Jaworski, J.; Sheng, M. *Mol. Neurobiol.* **2006**, *34*, 205–219; PMID: 17308353.

- [45] Casadio, A.; Martin, K. C.; Giustetto, M.; Zhu, H.; Chen, M.; Bartsch, D.; Bailey, C. H.; Kandel, E. R. *Cell* **1999**, *99*, 221–237; PMID: 10535740.
- [46] Tang, S. J.; Reis, G.; Kang, H.; Gingras, A.; Sonenberg, N.; Schuman, E. M. *Proc. Natl. Acad. Sci. U. S. A.* **2002**, *99*, 467–472; PMID: 11756682.
- [47] Zheng, X.; Sehgal, A. *Curr. Biol.* **2010**, *20*, 1203–1208.
- [48] Kunz, J.; Henriquez, R.; Schneider, U.; Deuter-Reinhard, M.; Movva, N. R.; Hall, M. N. *Cell* **1993**, *73*, 585–596; PMID: 8387896.
- [49] Helliwell, S. B.; Wagner, P.; Kunz, J.; Deuter-Reinhard, M.; Henriquez, R.; Hall, M. N. *Mol. Biol. Cell* **1994**, *5*, 105–118; PMID: 8186460.
- [50] Loewith, R.; Jacinto, E.; Wullschlegel, S.; Lorberg, A.; Crespo, J. L.; Bonenfant, D.; Oppliger, W.; Jenoe, P.; Hall, M. N. *Mol. Cell* **2002**, *10*, 457–468; PMID: 12408816.
- [51] Sturgill, T. W.; Cohen, A.; Diefenbacher, M.; Trautwein, M.; Martin, D. E.; Hall, M. N. *Eukaryotic cell* **2008**, *7*, 1819–1830; PMID: 18723607.
- [52] Loewith, R.; Hall, M. N. *Genetics* **2011**, *189*, 1177–1201; PMID: 22174183.
- [53] Sarbassov, D. D.; Ali, S. M.; Sengupta, S.; Sheen, J.; Hsu, P. P.; Bagley, A. F.; Markhard, A. L.; Sabatini, D. M. *Mol. Cell* **2006**, *22*, 159–168; PMID: 16603397.
- [54] Soulard, A.; Hall, M. N. *Cell* **2007**, *129*, 434.e1–434.e2.
- [55] Berchtold, D.; Walther, T. C. *Mol. Biol. Cell* **2009**, *20*, 1565–1575; PMID: 19144819.
- [56] Drenan, R. M.; Liu, X.; Bertram, P. G.; Zheng, X. F. *J. Biol. Chem.* **2004**, *279*, 772–778; PMID: 14578359.
- [57] Kunz, J.; Schneider, U.; Howald, I.; Schmidt, A.; Hall, M. N. *J. Biol. Chem.* **2000**, *275*, 37011–37020; PMID: 10973982.
- [58] Sancak, Y.; Bar-Peled, L.; Zoncu, R.; Markhard, A. L.; Nada, S.; Sabatini, D. M. *Cell* **2010**, *141*, 290–303; PMID: 20381137.
- [59] Zinzalla, V.; Stracka, D.; Oppliger, W.; Hall, M. N. *Cell* **2011**, *144*, 757–768; PMID: 21376236.
- [60] Zhang, X.; Shu, L.; Hosoi, H.; Murti, K. G.; Houghton, P. J. *J. Biol. Chem.* **2002**, *277*, 28127–28134; PMID: 12000755.
- [61] Partovian, C.; Ju, R.; Zhuang, Z. W.; Martin, K.; Simons, M. *Mol. Cell* **2008**, *32*, 140–149; PMID: 18851840 PMCID: PMC2578831.
- [62] Wedaman, K. P.; Reinke, A.; Anderson, S.; Yates, J.; McCaffery, J. M.; Powers, T. *Mol. Biol. Cell* **2003**, *14*, 1204–1220; PMID: 12631735 PMCID: PMC151591.
- [63] Withers, D. J.; Ouwens, D. M.; Nave, B. T.; van der Zon, G. C.; Alarcon, C. M.; Cardenas, M. E.; Heitman, J.; Maassen, J. A.; Shepherd, P. R. *Biochem. Biophys. Res. Commun.* **1997**, *241*, 704–709; PMID: 9434772.
- [64] Foster, D. A. *Biochim. Biophys. Acta* **2009**, *1791*, 949–955; PMID: 19264150.
- [65] Fang, Y.; Vilella-Bach, M.; Bachmann, R.; Flanigan, A.; Chen, J. *Science* **2001**, *294*, 1942–1945; PMID: 11729323.

- [66] Liang, J.; Choi, J.; Clardy, J. *Acta Crystallogr., Sect. D: Biol. Crystallogr.* **1999**, *55*, 736–744; PMID: 10089303.
- [67] Banaszynski, L. A.; Liu, C. W.; Wandless, T. J. *J. Am. Chem. Soc.* **2005**, *127*, 4715–4721; PMID: 15796538.
- [68] Dames, S. A.; Mulet, J. M.; Rathgeb-Szabo, K.; Hall, M. N.; Grzesiek, S. *J. Biol. Chem.* **2005**, *280*, 20558–20564; PMID: 15772072.
- [69] Dames, S. A. *J. Biol. Chem.* **2010**, *285*, 7766–7775; PMID: 20042596.
- [70] Adami, A.; García-Alvarez, B.; Arias-Palomo, E.; Barford, D.; Llorca, O. *Molecular cell* **2007**, *27*, 509–516; PMID: 17679098.
- [71] Yip, C. K.; Murata, K.; Walz, T.; Sabatini, D. M.; Kang, S. A. *Mol. Cell* **2010**, *38*, 768–774; PMID: 20542007.
- [72] Sturgill, T. W. W.; Hall, M. N. N. *ACS Chem. Biol.* **2009**, *4*, 999–1015; PMID: 19902965.
- [73] Knutson, B. A. *J. Struct. Biol.* **2010**, *170*, 354–363; PMID: 20060908.
- [74] Yang, H.; Rudge, D. G.; Koos, J. D.; Vaidialingam, B.; Yang, H. J.; Pavletich, N. P. *Nature* **2013**, *497*, 217–223; PMID: 23636326.
- [75] Yoshida, S.; Hong, S.; Suzuki, T.; Nada, S.; Mannan, A. M.; Wang, J.; Okada, M.; Guan, K.; Inoki, K. *J. Biol. Chem.* **2011**, *286*, 32651–32660; PMID: 21784859.
- [76] Neklesa, T. K.; Davis, R. W. *Proc. Natl. Acad. Sci. U. S. A.* **2008**, *105*, 15166–15171; PMID: 18812505.
- [77] Sarbassov, D. D.; Ali, S. M.; Sabatini, D. M. *Curr. Opin. Cell Biol.* **2005**, *17*, 596–603; PMID: 16226444.
- [78] Davis, A. J.; So, S.; Chen, D. J. *Cell Cycle* **2010**, *9*, 2529–2536; PMID: 20543558.
- [79] Meek, K.; Gupta, S.; Ramsden, D. A.; Lees-Miller, S. P. *Immunol. Rev.* **2004**, *200*, 132–141.
- [80] Serrano, M. A.; Li, Z.; Dangeti, M.; Musich, P. R.; Patrick, S.; Roginskaya, M.; Cartwright, B.; Zou, Y. *Oncogene* **2012**, 1–11.
- [81] Mansour, W. Y.; Schumacher, S.; Roskopf, R.; Rhein, T.; Schmidt-Petersen, F.; Gatzemeier, F.; Haag, F.; Borgmann, K.; Willers, H.; Dahm-Daphi, J. *Nucleic Acids Res.* **2008**, *36*, 4088–4098; PMID: 18539610.
- [82] Hsu, D.; Gaudet, P.; Hudson, C. J., Jessica J. R. and Pears; Lakin, N. D. *Cell cycle* **2006**, *5*, 702–708; PMID: 16582628.
- [83] Gapud, E. J.; Sleckman, B. P. *Cell Cycle* **2011**, *10*, 1928–1935.
- [84] Ju, J.; Naura, A. S.; Errami, Y.; Zerfaoui, M.; Kim, H.; Kim, J. G.; Elmageed, Z. Y. A.; Abdel-Mageed, A. B.; Giardina, C.; Beg, A. A.; Smulson, M. E.; Boulares, A. H. *J. Biol. Chem.* **2010**, *285*, 41152–41160; PMID: 20966071 PMCID: PMC3003413.
- [85] Kong, X.; Shen, Y.; Jiang, N.; Fei, X.; Mi, J. *Cell. Signalling* **2011**, *23*, 1273–1280; PMID: 21514376.
- [86] Lucero, H.; Gae, D.; Taccioli, G. E. *J. Biol. Chem.* **2003**, *278*, 22136–22143; PMID: 12672807.

- [87] Toulany, M.; Lee, K.-J.; Fattah, K. R.; Lin, Y.-F.; Fehrenbacher, B.; Schaller, M.; Chen, B. P.; Chen, D. J.; Rodemann, H. P. *Mol. Cancer Res.* **2012**, *10*, 945–957.
- [88] Grądzka, I.; Sochanowicz, B.; Brzóska, K.; Wójciuk, G.; Sommer, S.; Wojewódzka, M.; Gasińska, A.; Degen, C.; Jahreis, G.; Szumiel, I. *Biochim. Biophys. Acta* **2013**, *1830*, 2233–2242; PMID: 23116821.
- [89] Rivera-Calzada, A.; Maman, J. D.; Maman, J. P.; Spagnolo, L.; Pearl, L. H.; Llorca, O. *Structure* **2005**, *13*, 243–255; PMID: 15698568.
- [90] Williams, D. R.; Lee, K.; Shi, J.; Chen, D. J.; Stewart, P. L. *Structure* **2008**, *16*, 468–477.
- [91] Dobbs, T. A.; Tainer, J. A.; Lees-Miller, S. P. *DNA repair* **2010**, *9*, 1307–1314; PMID: 21030321 PMID: PMC3045832.
- [92] Sibanda, B. L.; Chirgadze, D. Y.; Blundell, T. L. *Nature* **2010**, *463*, 118–121.
- [93] Spagnolo, L.; Rivera-Calzada, A.; Pearl, L. H.; Llorca, O. *Mol. Cell* **2006**, *22*, 511–519; PMID: 16713581.
- [94] Beamish, H. J.; Jessberger, R.; Riballo, E.; Priestley, A.; Blunt, T.; Kysela, B.; Jeggo, P. A. *Nucleic Acids Res.* **2000**, *28*, 1506–1513.
- [95] Flynn, R. L.; Zou, L. *Trends Biochem. Sci.* **2011**, *36*, 133–140; PMID: 20947357.
- [96] D'Amours, D.; Jackson, S. P. *Nat. Rev. Mol. Cell Biol.* **2002**, *3*, 317–327; PMID: 11988766.
- [97] Krüger, A.; Ralser, M. *Science signaling* **2011**, *4*, pe17; PMID: 21467295.
- [98] Watters, D.; Khanna, K. K.; Beamish, H.; Birrell, G.; Spring, K.; Kedar, P.; Gatei, M.; Stenzel, D.; Hobson, K.; Kozlov, S.; Zhang, N.; Farrell, A.; Ramsay, J.; Gatti, R.; Lavin, M. *Oncogene* **1997**, *14*, 1911–1921; PMID: 9150358.
- [99] Zhang, L.; Tie, Y.; Tian, C.; Xing, G.; Song, Y.; Zhu, Y.; Sun, Z.; He, F. *Cell. Signalling* **2006**, *18*, 1386–1395; PMID: 16325375.
- [100] Brown, E. J.; Baltimore, D. *Genes Dev.* **2003**, *17*, 615–628; PMID: 12629044.
- [101] Oliveira, V.; Romanow, W. J.; Geisen, C.; Otterness, D. M.; Mercurio, F.; Wang, H. G.; Dalton, W. S.; Abraham, R. T. *J. Biol. Chem.* **2008**, *283*, 13174–13184; PMID: 18326048.
- [102] Morita, T.; Yamashita, A.; Kashima, I.; Ogata, K.; Ishiura, S.; Ohno, S. *J. Biol. Chem.* **2007**, *282*, 7799–7808; PMID: 17229728.
- [103] Masse, I.; Molin, L.; Mouchiroud, L.; Vanhems, F., P. and Palladino; Billaud, M.; Solari, F. *PLoS ONE* **2008**, *3*, e3354.
- [104] Chen, R.; Yang, Q.; Chen, Y.; Oliveira, V. A.; Dalton, W. S.; Fearn, C.; Lee, J. *J. Biol. Chem.* **2009**, *284*, 16752–16758; PMID: 19406746.
- [105] Murr, R.; Vaissière, T.; Sawan, C.; Shukla, V.; Herceg, Z. *Oncogene* **2007**, *26*, 5358–5372.
- [106] Sawan, C.; Hernandez-Vargas, H.; Murr, R.; Lopez, F.; Vaissière, T.; Ghantous, A. Y.; Cuenin, C.; Imbert, J.; Wang, Z.; Ren, B.; Herceg, Z. *Stem cells* **2013**, *31*, 979–991; PMID: 23362228.
- [107] Hoke, S. M. T.; Irina Mutiu, A.; Genereaux, J.; Kvas, S.; Buck, M.; Yu, M.; Gloor, G. B.; Brandl, C. J. *Curr. Genet.* **2010**, *56*, 447–465; PMID: 20635087.

- [108] Sun, Y.; Jiang, X.; Chen, S.; Fernandes, N.; Price, B. D. *Proc. Natl. Acad. Sci. U. S. A.* **2005**, *102*, 13182–13187; PMID: 16141325.
- [109] Nakada, D.; Hirano, Y.; Tanaka, Y.; Sugimoto, K. *Mol. Biol. Cell* **2005**, *16*, 5227–5235; PMID: 16148046 PMID: PMC1266421.
- [110] Cavanagh, J.; Fairbrother, W. J.; Palmer, A. G.; Skelton, N. J.; Rance, M. *Protein NMR Spectroscopy, Second Edition: Principles and Practice*, 2nd ed.; Academic Press, 2006.
- [111] Keeler, J. *Understanding NMR Spectroscopy*, 1st ed.; John Wiley & Sons, 2005.
- [112] Evans, J. N. S. *Biomolecular NMR Spectroscopy*, 1st ed.; Oxford University Press, USA, 1995.
- [113] Dyson, H. J.; Palmer III, A. G. In *Comprehensive Biophysics*; Edward H. Egelman, Ed.; Elsevier: Amsterdam, 2012; pp 136–159.
- [114] Palmer, A. G. In *Comprehensive Biophysics*; Edward H. Egelman, Ed.; Elsevier: Amsterdam, 2012; pp 216–244.
- [115] Wishart, D. S.; Sykes, B. D.; Richards, F. M. *Biochemistry* **1992**, *31*, 1647–1651.
- [116] Wishart, D. S.; Bigam, C. G.; Holm, A.; Hodges, R. S.; Sykes, B. D. *J. Biomol. NMR* **1995**, *5*, 67–81.
- [117] Brüschweiler, R. *Curr. Opin. Struct. Biol.* **2003**, *13*, 175–183.
- [118] Bodenhausen, G.; Ruben, D. J. *Chem. Phys. Lett.* **1980**, *69*, 185–189.
- [119] Schanda, P.; Brutscher, B. *J. Am. Chem. Soc.* **2005**, *127*, 8014–8015; PMID: 15926816.
- [120] Jeener, J.; Meier, B. H.; Bachmann, P.; Ernst, R. R. *J. Chem. Phys.* **1979**, *71*, 4546–4553.
- [121] Kay, L. E.; Ikura, M.; Tschudin, R.; Bax, A. *J. Magn. Reson.* **2011**, *213*, 423–441.
- [122] Bax, A.; Clore, G. M.; Gronenborn, A. M. *J. Magn. Reson.* **1990**, *88*, 425–431.
- [123] Olejniczak, E. T.; Xu, R. X.; Fesik, S. W. *J. Biomol. NMR* **1992**, *2*, 655–659.
- [124] Bax, A.; Ikura, M.; Kay, L. E.; Torchia, D. A.; Tschudin, R. *J. Magn. Reson.* **1990**, *86*, 304–318.
- [125] Clore, G. M.; Bax, A.; Driscoll, P. C.; Wingfield, P. T.; Gronenborn, A. M. *Biochemistry* **1990**, *29*, 8172–8184; PMID: 2261471.
- [126] Grzesiek, S.; Anglister, J.; Bax, A. *J. Magn. Reson.* **1993**, *101*, 114–119.
- [127] Price, W. S. *Concepts Magn. Reson.* **1997**, *9*, 299–336.
- [128] Price, W. S. *Concepts Magn. Reson.* **1998**, *10*, 197–237.
- [129] Lucas, L. H.; Larive, C. K. *Concepts Magn. Reson., Part A* **2004**, *20A*, 24–41.
- [130] Stejskal, E. O.; Tanner, J. E. *J. Chem. Phys.* **1965**, *42*, 288–292.
- [131] Tanner, J. E. *J. Chem. Phys.* **1970**, *52*, 2523–2526.
- [132] Orfi, L.; Lin, M.; Larive, C. K. *Anal. Chem.* **1998**, *70*, 1339–1345.

- [133] Begotka, B. A.; Hunsader, J. L.; Oparaeche, C.; Vincent, J. K.; Morris, K. F. *Magn. Reson. Chem.* **2006**, *44*, 586–593; PMID: 16552718.
- [134] Clore, G. M.; Iwahara, J. *Chem. Rev.* **2009**, *109*, 4108–4139; PMID: 19522502.
- [135] Bertini, I.; Banci, L.; Luchinat, C. In *Methods in Enzymology*; Norman J. Oppenheimer and Thomas L. James, Ed.; Academic Press, 1989; Vol. Volume 177, pp 246–263.
- [136] Villafranca, J. J. In *Methods in Enzymology*; Norman J. Oppenheimer and Thomas L. James, Ed.; Academic Press, 1989; Vol. Volume 177, pp 403–413.
- [137] Kutateladze, T. G.; Capelluto, D. G. S.; Ferguson, C. G.; Cheever, M. L.; Kutateladze, A. G.; Prestwich, G. D.; Overduin, M. *J. Biol. Chem.* **2004**, *279*, 3050–3057; PMID: 14578346.
- [138] Andersson, A.; Mäler, L. *FEBS Letters* **2003**, *545*, 139–143.
- [139] Patil, S. M.; Xu, S.; Sheftic, S. R.; Alexandrescu, A. T. *J. Biol. Chem.* **2009**, *284*, 11982–11991; PMID: 19244249.
- [140] Winter, R. *Methoden der Biophysikalischen Chemie*, 2nd ed.; Vieweg+Teubner Verlag, 2011.
- [141] Sreerama, N.; Venyaminov, S. Y.; Woody, R. W. *Anal. Biochem.* **2000**, *287*, 243–251; PMID: 11112270.
- [142] Sreerama, N.; Woody, R. W. *Anal. Biochem.* **2000**, *287*, 252–260; PMID: 11112271.
- [143] 2013. <http://dichroweb.cryst.bbk.ac.uk/html/home.shtml>.
- [144] Greenfield, N.; Fasman, G. D. *Biochemistry* **1969**, *8*, 4108–4116; PMID: 5346390.
- [145] Olah, G. A.; Huang, H. W. *J. Chem. Phys.* **1988**, *89*, 2531–2538.
- [146] Wu, Y.; Huang, H. W.; Olah, G. A. *Biophys. J.* **1990**, *57*, 797–806; PMID: 2344464.
- [147] Moffitt, W. *J. Chem. Phys.* **1956**, *25*, 467–478.
- [148] Moffitt, W.; Fitts, D. D.; Kirkwood, J. G. *Proc. Natl. Acad. Sci. U. S. A.* **1957**, *43*, 723–730; PMID: 16590076 PMCID: PMC528528.
- [149] Chen, F.-Y.; Lee, M.-T.; Huang, H. W. *Biophys. J.* **2002**, *82*, 908–914; PMID: 11806932 PMCID: PMC1301899.
- [150] Bürck, J.; Roth, S.; Wadhvani, P.; Afonin, S.; Kanithasen, N.; Strandberg, E.; Ulrich, A. S. *Biophys. J.* **2008**, *95*, 3872–3881; PMID: 18621832 PMCID: PMC2553147.
- [151] Sambrook, J.; Russell, D. W. *Molecular Cloning: A Laboratory Manual*, 3 Vol., 0003rd ed.; Cold Spring Harbor Laboratory, 2000.
- [152] Huth, J. R.; Bewley, C. A.; Jackson, B. M.; Hinnebusch, A. G.; Clore, G. M. M.; Groenborn, A. M. *Protein Sci.* **1997**, *6*, 2359–2364; PMID: 9385638.
- [153] Stratagene Inc.; *QuickChange® Site-directed mutagenesis*; Agilent; Germany; user manual ed.; 2009.
- [154] Sommer, L. A. M.; Master's thesis; Technische Universität München; 2010.

- [155] Koenig, B. W.; Rogowski, M.; Louis, J. M. *J. Biomol. NMR* **2003**, *26*, 193–202; PMID: 12766417.
- [156] Healthcare, G.; *IgG Sepharose IgG sepharose 6 Fast Flow*; GE Healthcare; Swedden, Germany; user manual ed.; 2008.
- [157] Sommer, L. A. M.; Meier, M. A.; Dames, S. A. *Protein Sci.* **2012**, *21*, 1566–1570.
- [158] Schaad, M.; Master's thesis; Universität Basel; 2005.
- [159] Stafford, R. E.; Fanni, T.; Dennis, E. A. *Biochemistry* **1989**, *28*, 5113–5120; PMID: 2669968.
- [160] Weschayanwivat, P.; Scamehorn, J. F.; Reilly, P. J. *J. Surfactants Deterg.* **2005**, *8*, 65–72.
- [161] Tausk, R. J. M.; Van Esch, J.; Karmiggelt, J.; Voordouw, G.; Overbeek, J. T. G. *Biophys. Chem.* **1974**, *1*, 184–203.
- [162] Provencher, S. W.; Glöckner, J. *Biochemistry* **1981**, *20*, 33–37; PMID: 7470476.
- [163] van Stokkum, I. H.; Spoelder, H. J.; Bloemendal, M.; van Grondelle, R.; Groen, F. C. *Anal. Biochem.* **1990**, *191*, 110–118; PMID: 2077933.
- [164] Lobley, A.; Whitmore, L.; Wallace, B. A. *Bioinformatics* **2002**, *18*, 211–212.
- [165] Whitmore, L.; Wallace, B. A. *Nucleic Acids Res.* **2004**, *32*, W668–W673; PMID: 15215473  
PMCID: PMC441509.
- [166] Delaglio, F.; Grzesiek, S.; Vuister, G. W.; Zhu, G.; Pfeifer, J.; Bax, A. *J. Biomol. NMR* **1995**, *6*, 277–293; PMID: 8520220.
- [167] Johnson, B. A. *Methods Mol. Biol.* **2004**, *278*, 313–352; PMID: 15318002.
- [168] Vuister, G. W.; Bax, A. *J. Am. Chem. Soc.* **1993**, *115*, 7772–7777.
- [169] Schanda, P.; Kupce, E.; Brutscher, B. *J. Biomol. NMR* **2005**, *33*, 199–211; PMID: 16341750.
- [170] Bruker; *Diffusion ordered spectroscopy*; Bruker; Germany; user manual ed.; 2010.
- [171] van der Spoel, D.; Lindahl, E.; Hess, B.; Groenhof, G.; Mark, A. E.; Berendsen, H. J. C. *J. Comput. Chem.* **2005**, *26*, 1701–1718.
- [172] Hess, B.; Kutzner, C.; van der Spoel, D.; Lindahl, . *J. Chem. Theory Comput.* **2008**, *4*, 435–447.
- [173] Berger, O.; Edholm, O.; Jahnig, F. *Biophys. J.* **1997**, *72*, 2002–2013; PMID: 9129804  
PMCID: PMC1184396.
- [174] Schmid, N.; Eichenberger, A. P.; Choutko, A.; Riniker, S.; Winger, M.; Mark, A. E.; Gunsteren, W. F. *Eur. Biophys. J.* **2011**, *40*, 843–856.
- [175] Berendsen, H. J. C.; Postma, J. P. M.; van Gunsteren, W. F.; Hermans, J. *Intermol. Forces* **1981**, 331–342.
- [176] Improta, R.; Matteo, A. d.; Barone, V. *Theor. Chem. Acc.* **2000**, *104*, 273–279.
- [177] Stimson, L.; Dong, L.; Karttunen, M.; Wisniewska, A.; Dutka, M.; Róg, T. *J. Phys. Chem. B* **2007**, *111*, 12447–12453.



- [178] Hess, B.; Bekker, H.; Berendsen, H. J. C.; Fraaije, J. G. E. M. *J. Comput. Chem.* **1997**, *18*, 1463–1472.
- [179] Miyamoto, S.; Kollman, P. A. *J. Comput. Chem.* **1992**, *13*, 952–962.
- [180] Bussi, G.; Donadio, D.; Parrinello, M. *J. Chem. Phys.* **2007**, *126*, 014101; PMID: 17212484.
- [181] Berendsen, H. J. C.; Postma, J. P. M.; van Gunsteren, W. F.; DiNola, A.; Haak, J. R. *J. Chem. Phys.* **1984**, *81*, 3684.
- [182] Darden, T.; York, D.; Pedersen, L. *J. Chem. Phys.* **1993**, *98*, 10089–10092.
- [183] Essmann, U.; Perera, L.; Berkowitz, M. L.; Darden, T.; Lee, H.; Pedersen, L. G. *J. Chem. Phys.* **1995**, *103*, 8577–8593.
- [184] Humphrey, W.; Dalke, A.; Schulten, K. *J. Mol. Graphics* **1996**, *14*, 33–38, 27–28; PMID: 8744570.
- [185] Gronenborn, A. M.; Filpula, D. R.; Essig, N. Z.; Achari, A.; Whitlow, M.; Wingfield, P. T.; Clore, G. M. *Science* **1991**, *253*, 657–661; PMID: 1871600.
- [186] Rodriguez Camargo, D. C.; Link, N. M.; Dames, S. A. *Biochemistry* **2012**, *51*, 4909–4921; PMID: 22620485.
- [187] Warschawski, D. E.; Arnold, A. A.; Beaugrand, M.; Gravel, A.; Chartrand, É.; Marcotte, I. *Biochim. Biophys. Acta* **2011**, *1808*, 1957–1974.
- [188] Tieleman, D. P.; van der Spoel, D.; Berendsen, H. J. C. *J. Phys. Chem. B* **2000**, *104*, 6380–6388.
- [189] Sanders, C. R.; Sönnichsen, F. *Magn. Reson. Chem.* **2006**, *44*, S24–S40.
- [190] Smith, D. B. *Methods Enzymol.* **2000**, *326*, 254–270; PMID: 11036647.
- [191] Sachdev, D.; Chirgwin, J. M. *Methods Enzymol.* **2000**, *326*, 312–321; PMID: 11036650.
- [192] Liew, C. K.; Gamsjaeger, R.; Mansfield, R. E.; Mackay, J. P. *Protein Sci.* **2008**, *17*, 1630–1635; PMID: 18556474 PMCID: PMC252529.
- [193] Wimley, W. C.; White, S. H. *Nat. Struct. Biol.* **1996**, *3*, 842–848; PMID: 8836100.
- [194] Liu, W.; Caffrey, M. *Biochemistry* **2006**, *45*, 11713–11726; PMID: 17002272 PMCID: PMC2568979.
- [195] 2013. [www.avantilipids.com](http://www.avantilipids.com).
- [196] Lazaridis, T.; Mallik, B.; Chen, Y. *J. Phys. Chem. B* **2005**, *109*, 15098–15106; PMID: 16852911.
- [197] Whiles, J. A.; Deems, R.; Vold, R. R.; Dennis, E. A. *Bioorg. Chem.* **2002**, *30*, 431–442; PMID: 12642127.
- [198] Seewald, M. J.; Pichumani, K.; Stowell, C.; Tibbals, B. V.; Regan, L.; Stone, M. J. *Protein science* **2000**, *9*, 1177–1193; PMID: 10892810.
- [199] Walsh, J. D.; Meier, K.; Ishima, R.; Gronenborn, A. M. *Biophysical Journal* **2010**, *99*, 2636–2646; PMID: 20959105 PMCID: PMC2955504.

- [200] Dames, S. A.; Junemann, A.; Sass, H. J.; Schönichen, A.; Stopschinski, B. E.; Grzesiek, S.; Faix, J.; Geyer, M. *J. Biol. Chem.* **2011**, *286*, 36907–36920.
- [201] Farrow, N. A.; Zhang, O.; Forman-Kay, J. D.; Kay, L. E. *Biochemistry* **1997**, *36*, 2390–2402; PMID: 9054544.
- [202] Myers, G. A.; Gacek, D. A.; Peterson, E. M.; Fox, C. B.; Harris, J. M. *J. Am. Chem. Soc.* **2012**, *134*, 19652–19660.
- [203] Sun, H.; Greathouse, D. V.; Andersen, O. S.; Koeppe, R. E. *J. Biol. Chem.* **2008**, *283*, 22233–22243; PMID: 18550546 PMCID: PMC2494914.
- [204] Rehfeld, S. J.; Eatough, D. J.; Plachy, W. Z. *J. Lipid Res.* **1978**, *19*, 841–849; PMID: 213518.
- [205] Nadaud, P.; Helmus, J.; Höfer, N.; Jaroniec, C. *J. Am. Chem. Soc.* **2007**, *129*, 7502–7503.
- [206] Koehler, J.; Meiler, J. *Prog. Nucl. Magn. Reson. Spectrosc.* **2011**, *59*, 360–389; PMID: 22027343 PMCID: PMC3202700.
- [207] Zmoon, J.; Mascioni, A.; Thomas, D. D.; Veglia, G. *Biophys. J.* **2003**, *85*, 2589–2598; PMID: 14507721 PMCID: PMC1303482.
- [208] Szajdzinska-Pietek, E.; Maldonado, R.; Kevan, L.; Berr, S.; Jones, R. R. M. *J. Phys. Chem.* **1985**, *89*, 1547–1550.
- [209] de Jongh, H. H. J.; Goormaghtigh, E.; Killian, J. A. *Biochemistry* **1994**, *33*, 14521–14528.
- [210] de Jongh, H. H. J.; Brasseur, R.; Killian, J. A. *Biochemistry* **1994**, *33*, 14529–14535.
- [211] Guo, Z.; Kozlov, S.; Lavin, M. F.; Person, M. D.; Paull, T. T. *Science* **2010**, *330*, 517–521.
- [212] Wouters, B. G.; Koritzinsky, M. *Nat. Rev. Cancer* **2008**, *8*, 851–864; PMID: 18846101.
- [213] Chen, B. P.; Li, M.; Asaithamby, A. *Cancer Letters* **2012**, *327*, 103–110.
- [214] Pan, Y.; Nishida, Y.; Wang, M.; Verdin, E. *Gerontology* **2012**, *58*, 524–530.
- [215] Sun, Y.; Xu, Y.; Roy, K.; Price, B. D. *Mol. Cell. Biol.* **2007**, *27*, 8502–8509.
- [216] 2013. <http://web.expasy.org/protparam/>.
- [217] Laemmli, U. K. *Nature* **1970**, *227*, 680–685.

This work was created on a Mac using MacOS X (10.8.4 - Leopard), LyX (2.0.5), BibDesk (1.6.1), Adobe CS4 (Photoshop 11.0.1 and Illustrator 14.0.0), IgorPro (6.23) and Zotero (4.08).

# Appendix A

## Appendix

### A.1 Sequences and parameters

Fig. A.1 on the next page shows the vector map and the multiple cloning site of the commercially available vector pET-21(+) (Novagen, Merck, Germany), which was used in the scope of this thesis for expression and cloning purposes.

#### A.1.1 Primer sequences for site-directed mutagenesis

Mutant versions of y1fatc were obtained by site-directed mutagenesis. The primers were designed according the rules described in the manufacture's manual and are listed in Tab. A.1 on page 103 and A.2 on page 104.

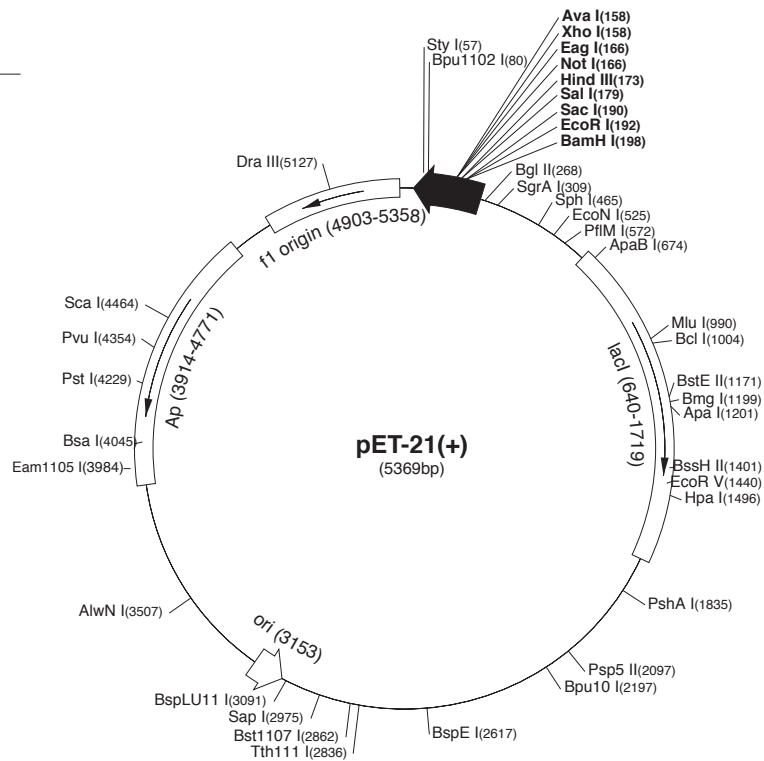
#### A.1.2 Protein sequences

The amino acid sequences of y1fatc wild type and mutants are given in Tab. A.3 on page 105 and these of the FATC domains of DNA-PKcs, ATM, ATR, SMG-1, and TRRAP and the GB1 tag in Tab. A.4 on page 106.

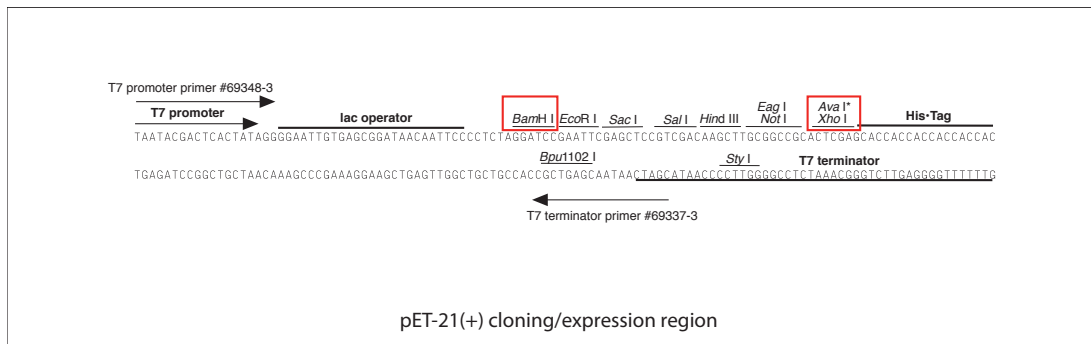
#### A.1.3 Protein parameters

Molar extinction coefficients and molecular weights [216] of y1fatc wild type and mutants are listed in Tab. A.5a on page 107 and these of the FATC domains of DNA-PKcs, ATM, ATR, SMG-1, and TRRAP and the GB1 tag in Tab. A.5b on page 107.

pET-21(+) sequence landmarks	
T7 promoter	237-253
T7 transcription start	236
Multiple cloning sites	
(Bam H I - Xho I)	158-203
His-Tag * coding sequence	140-157
T7 terminator	26-72
lacI coding sequence	640-1719
pBR322 origin	3153
bla coding sequence	3914-4771
f1 origin	4903-5358



(a) Vector map.



(b) Multiple cloning site

Figure A.1: The vector pET-21(+) vector (figure adapted from Novagen). The vector map (a) and the multiple cloning site (b) are depicted. The restriction sites for the endonucleases BamH I and Xho I (highlighted in red) were used for cloning purposes.

Table A.1: Mutant versions of y1fatc and the corresponding primers (I).

mutant Used plasmid	Sequence forward primer (5'→3')	Sequence reverse primer (5'→3')
L2459A wild type	GTT ATG TCA ACA TGC TAT TGG ATG GTG CCC ATT CTG GTA ACT CG	CGA GTT ACC AGA ATG GGC ACC ATC CAA TAG CAT GTT GAC ATA AC
H2462A wild type	GGC ATG TCA ACA TTA TAT TGG ATG GTG CCC ATT CTG GTA ACT CG	CGA GTT ACC AGA ATG GGC ACC ATC CAA TAT AAT GTT GAC ATG CC
Y2463A wild type	GTT ATG TCA AGC TTA TAT TGG ATG GTG CCC ATT CTG GTA ACT CG	CGA GTT ACC AGA ATG GGC ACC ATC CAA TAT AAG CTT GAC ATA AC
F2469A wild type	GTT ATG TCA ACA TTA TAT TGG ATG GTG CCC AGC CTG GTA ACT CG	CGA GTT ACC AGG CTG GGC ACC ATC CAA TAT AAT GTT GAC ATA AC
W2466A wild type	GTT ATG TCA ACA TTA TAT TGG AGC GTG CCC ATT CTG GTA ACT CG	CGA GTT ACC AGA ATG GGC ACC CTC CAA TAT AAT GTT GAC ATA AC
W2466A/W2470A wild type	GGA GCG TGC CCA TTC GCG TAA CTC GAG CAC CAC	GTG GTG CTC GAG TTA CGC GAA TGG GCA GCG TCC
Y2463A/I2464A/W2466A/W2470A	GGT TAT GTC AAC ATG CTG CTG GAG CGT GCC CAT TCG CGT AAC TCG	CGA GTT ACC AGA ATG GGC ACC CTC CAG CAG CAT GTT GAC ATA ACC
W2466A/W2470A		
Y2463E/W2466E	GGT TAT GTC AAC ATG AGA TTG GAG AGT GCC CAT TCT GGT AAC TCG	CGA GTT ACC AGA ATG GGC ACT CTC CAA TCT CAT GTT GAC ATA ACC
W2466A		

Table A.2: Mutant versions of y1fatc and the corresponding primers (II).

mutant Used plasmid	Sequence forward primer (5'→3')	Sequence reverse primer (5'→3')
Y2463D/I2464D/W2466A W2466A	GGT TAT GTC AAC ATG ATG ATG GAG CGT GCC CAT TCT GGT AAC TCG CGA GTT ACC AGA ATG GGC ACG CTC CAT CAT CAT GTT GAC ATA ACC	
Y2463D/I2464D/W2466E/W2470R Y2463D/I2464D/W2466A	GGT TAT GTC AAC ATG ATG ATG GAG AGT GCC CAT TCC GGT AAC TC GAG TTA CCG GAA TGG GCA CTC TCC ATC ATC ATG TTA ACA TAA CC	
H2462R/Y2463D/I2464D/W2466A/F2469D Y2463D/I2464D/W2466A	GGT TAT GTC AAC GTG ATG ATG GAG CGT GCC CAG ACT GGT AAC TC GAG TTA CCA GTC TGG GCA CGC TCC ATC ATC ACG TTG ACA TAA CC	
G2465S/W2466S W2466A	GGT TAT GTC AAC ATT ATA TAA GCT CGT GCC CAT TCT GGT AAC TCG CGA GTT ACC AGA ATG GGC ACG AGC TAA TAT AAT GTT GAC ATA ACC	
H2462R/Y2463D/I2464D/G2465S/W2466S/F2469D H2462R/Y2463D/I2464D/W2466A/F2469D	GGT TAT GTC AAC GTG ATG ATA GCT CGT GCC CAG ACT GGT AAC TC GAG TTA CCA GTC TGG GCA CGA GCT ATC ATC ACG TTG ACA TAA CC	
L2459E/H2462R/Y2463D/I2464D/G2465S/W2466A/F2469D H2462R/Y2463D/I2464D/G2465S/W2466S/F2469D	GCC ACT TCT ATT GAA AGG GAA TGT CAA CGT GAT GAT AGC TCG CGA GCT ATC ATC ACG TTG ACA TTC CCT TTC AAT AGA AGT GGC	
L2459S/H2462R/Y2463D/I2464D/W2466E/F2469D H2462R/Y2463D/I2464D/W2466A/F2469D	CTA TTG AAA GGT CAT GTC AAC GTG ATG ATG GAG AGT GCC CAG AC GTC TGG GCA CTC TCC ATC ATC ACG TTG ACA TGA CCT TTC AAT AG	

Table A.3: Protein sequences of the mutant versions of y1fatc.

mutant	amino acid sequence
yeast TOR1 FATC (wild type)	NELDVPEQVDKLIQQATSIERLCCQHYIGWC <del>PPFW</del>
L2459A	NELDVPEQVDKLIQQATSIERACQHYIGWC <del>PPFW</del>
H2462A	NELDVPEQVDKLIQQATSIERLCCQAYIGWC <del>PPFW</del>
Y2463A	NELDVPEQVDKLIQQATSIERLCCQAIGWC <del>PPFW</del>
F2469A	NELDVPEQVDKLIQQATSIERLCCQHYIGWC <del>PAW</del>
W2466A	NELDVPEQVDKLIQQATSIERLCCQHYIGAC <del>PPFW</del>
W2466A/W2470A	NELDVPEQVDKLIQQATSIERLCCQHYIGAC <del>PPFA</del>
Y2463A/I2464A/W2466A/W2470A	NELDVPEQVDKLIQQATSIERLCCQAAGAC <del>PPFA</del>
Y2463E/W2466E	NELDVPEQVDKLIQQATSIERLCCQHEIGEC <del>PPFW</del>
Y2463D/I2464D/W2466A	NELDVPEQVDKLIQQATSIERLCCQHD <del>DDGACPPFW</del>
Y2463D/I2464D/W2466E/W2470R	NELDVPEQVDKLIQQATSIERLCCQHD <del>DDGECPPFR</del>
H2462R/Y2463D/I2464D/W2466A/F2469D	NELDVPEQVDKLIQQATSIERLCCQR <del>DDGACPDW</del>
G2465S/W2466S	NELDVPEQVDKLIQQATSIERLCCQHYI <del>SSCPFW</del>
H2462R/Y2463D/I2464D/G2465S/W2466S/F2469D	NELDVPEQVDKLIQQATSIERLCCQR <del>DDSSCPDW</del>
L2459E/H2462R/Y2463D/I2464D/G2465S/W2466A/F2469D	NELDVPEQVDKLIQQATSIERECQR <del>DDSA CPDW</del>
L2459S/H2462R/Y2463D/I2464D/W2466E/F2469D	NELDVPEQVDKLIQQATSIERSCQR <del>DDGECPDW</del>

Table A.4: Protein sequences of PIKKs.

protein	amino acid sequence
human DNA-PKcs fusion protein (ent)	MQYKLILNGK TLKGETTTEA VDAATAEKVF KQYANDNGVD GEWTYDDATK TFTVTELVPR GSDDDDDK SGL SEETQVKCLM DQATDPNILG RTWEGWEPWM
human DNA-PKcs fusion protein (xa)	MQYKLILNGK TLKGETTTEA VDAATAEKVF KQYANDNGVD GEWTYDDATK TFTVTELVPR GSIEGR SGLS EETQVKCLMD QATDPNILGR TWEGWEPWM
human DNA-PKcs FATC	SGLSEETQVK CLMDQATDPN ILGRTWEGWE PWM
human ATM fusion protein (ent)	MQYKLILNGK TLKGETTTEA VDAATAEKVF KQYANDNGVD GEWTYDDATK TFTVTELVPR GSDDDDDK TVL SVGGQVLLI QQAIDPKNLS RLFPGWKAWV
human ATM FATC	TVLSVGGQVN LLIQQAIDPK NLSRLFPGWK AWV
human ATR FATC	LPLSIEGHVHYLIQEATDENLLCQMYLIGWTPYM
human SMG-1 FATC	RRMSVAEQVDYVIKEATNLDNLAQLYEGWTAWV
human TRRAP FATC	QFEGGESKVNITLVAAAANSLDNLRCRMDPAWHPWL
gb1	MQYKLILNGK TLKGETTTEA VDAATAEKVF KQYANDNGVD GEWTYDDATK TFTVTE
gb1xa	MQYKLILNGK TLKGETTTEA VDAATAEKVF KQYANDNGVD GEWTYDDATK TFTVTELVPR GSIEGR



Table A.5: Protein parameters.

(a) TOR FATC and mutants.

protein	$\epsilon_{280}$ [ $M^{-1}cm^{-1}$ ]	$M_w$ [Da]
y1fatc (residues 2438 - 2470, UniProt ID )	12615	3960.4
y1fatc-gb1xa	22585	11188.4
L2459A	12615	3918.4
H2462A	12615	3894.4
Y2463A	11125	3868.4
F2469A	12615	3884.4
W2466A	7115	3845.3
W2466A/W2470A	1615	3730.2
Y2463A/I2464A/W2466A/W2470A	125	3596.0
Y2463E/W2466E	5625	3869.3
Y2463E/W2466E-gb1xa	15595	11139.4
Y2463D/I2464D/W2466A	5625	3799.2
Y2463D/I2464D/W2466E/W2470R-gb1xa	10095	11097.2
H2462R/Y2463D/I2464D/W2466A/ F2469D-gb1xa	15595	11056.2
G2465S/W2466S-gb1xa	17085	11161.4
H2462R/Y2463D/I2464D/G2465S/ W2466S/F2469D-gb1xa	15595	11102.2
L2459E/H2462R/Y2463D/I2464D/ G2465S/W2466A/F2469D-gb1xa	15595	11102.2
L2459S/H2462R/Y2463D/I2464D/ W2466E/F2469D-gb1xa	15595	11088.1

(b) PIKKs and GB1 tag.

protein	$\epsilon_{280}$ [ $M^{-1}cm^{-1}$ ]	$M_w$ [Da]
hdnapkfatc (residues 4096 - 4128, UniProt ID P78527)	16500	3809.2
hdnapkfatc-gb1ent	26470	11170.2
hdnapkfatc-gb1xa	26470	11037.2
hatmfatc (residues 3024 - 3056, Uniprot ID13315)	11000	3649.3
hatmfatc-gb1ent	20970	11010.3
hatrfatc (residues 2612 - 2644, UniProt ID Q13535)	9970	3879.4
hsmg1fatc (residues 3629 - 3661, UniProt ID Q96Q15)	13980	3870.3
htrrapfatc (residues 3827 - 3859, UniProt ID Q9Y4A5)	11000	3671.1
gb1xa	9970	7246.0

## A.2 Protocols

### A.2.1 SDS-PAGE

Polyacrylamide gel electrophoresis (PAGE) was performed under denaturing conditions employing sodium dodecyl sulfate (SDS). Polyacrylamide percentages of 15% and 16% (SERVA, precast gels) were used for analysis of samples, respectively. Usually, 15  $\mu\text{L}$  of protein samples were mixed with the 5  $\mu\text{L}$  of 4 $\times$ SDS-loading buffer. Following incubation at 95  $^{\circ}\text{C}$  for 5 min, the samples were chilled at room temperature, and 10  $\mu\text{L}$  each were loaded. Prestained SDS PAGE Protein Marker (Serva, 6.5 - 200 kDa) and Ultra-low Range Molecular Weight Marker (Sigma, 1.06 - 26.6 kDa) were used according to the manufacturer's instructions. Electrophoretic separation of proteins was accomplished in an electrophoresis chamber (Mighty Small II, Hoefer) and by applying a voltage of 220 V. The running period was approximately 1 - 1.5 h. Gels, running buffer, staining and destaining solutions of gels were prepared according to Laemmli [217].

### A.2.2 RP-HPLC

Fig. A.2 illustrates the RP-HPLC protocol used for the purification of y1fatc mutant proteins: The GB1 tag and undigested fusion protein were removed by RP-HPLC using a Phenomenex<sup>®</sup> Jupiter 5 u C4 300 A column connected to an Äkta purifier 900TM system with a UV-900 monitor for UV measurement at 280 nm. After equilibration of the column with 70 % RP-HPLC buffer A and 30 % RP-HPLC buffer B the digested fusion protein sample was applied. Usually, 2 mL of sample were diluted 1:1 with 70 % RP-HPLC buffer A and 30 % RP-HPLC buffer B, 500  $\mu\text{l}$  of 10 % TFA solution were added and then loaded on the column using a 5 mL sample loop. The elution was performed by increasing the ratio of RP-HPLC buffer B from 30 % to 80 % over a period of 60 min. Finally, the remaining protein was removed from the column by washing the column with 100 % RP-HPLC buffer B [154].

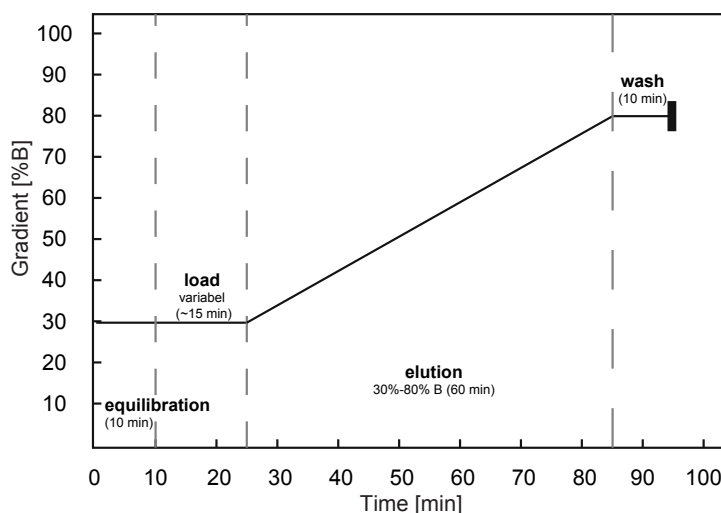


Figure A.2: RP-HPLC protocol.

### A.3 Additional alignments of ATM and ATR FATC

For the FATC domain of ATM and ATR some additional amino acid sequence alignments from different organisms are shown in Fig. A.3 on the following page. Compared to the alignment shown in Fig. 1.4, more variation can be seen if lower eukaryotes and/or plants are included.

### A.4 Secondary structure analysis

Secondary structure analysis was performed using the programs CONTIN (Fig. A.6a on page 111) and CDSSTR (Fig. A.6b on page 111) on the Dichroweb web server [143].

### A.5 Parameter for the membrane immersion model

The detailed parameter for the refined model of the membrane immersion of oxidized and reduced y1fatc (Fig. 4.32 on page 83) for 16-SASL (fifth column) are: The chemical shift changes observed for oxidized y1fatc in the presence of 50 mM DPC and 1 mM 16-SASL are divided in *red*  $\Delta\delta \geq 0.040$  ppm, *orange*  $0.020 \text{ ppm} \leq \Delta\delta < 0.040$  ppm, *white*  $\Delta\delta < 0.015$  ppm and for reduced y1fatc in *red*  $\Delta\delta \geq 0.03$  ppm, *orange*  $0.01 \text{ ppm} \leq \Delta\delta < 0.03$  ppm, *white*  $\Delta\delta < 0.01$  ppm. For both, *grey* corresponds to no data due to spectral overlap.

The detailed parameter for the refined model of the membrane immersion of oxidized and reduced y1fatc (Fig. 4.32 on page 83) for 5-SASL (sixth column) are: The chemical shift changes observed for oxidized y1fatc in the presence of 50 mM DPC and 2 or 1 mM 5-SASL are divided in *red*  $\Delta\delta \geq 0.045$  ppm, *orange*  $0.015 \text{ ppm} \leq \Delta\delta < 0.045$  ppm, *white*  $\Delta\delta < 0.015$  ppm and for reduced y1fatc in *red*  $\Delta\delta \geq 0.03$  ppm, *orange*  $0.01 \text{ ppm} \leq \Delta\delta < 0.03$  ppm, *white*  $\Delta\delta < 0.01$  ppm. For both, *grey* corresponds to no data due to spectral overlap. In the case of the oxidized form in micelles with 5-SASL the chemical shifts changes at 2 mM were used.

Due to the settings of the used program H2462 is also treated as positively charged residue.

	1	10	20	30
Q13315_human	TV	LSVGGQVNL	LIQQAID	PKNLSRFLPGWKAWV
B3VMJ2_dog	TV	LSVGGQVNL	LIQQAAMD	PKNLSRFLPGWKAWV
Q6PQD5_pig	TV	LSVGGQVNF	LIQQAAMD	PKNLSKLFSGWKAWV
Q62388_mouse	TV	LSVGGQVNL	LIQQAAMD	PKNLSRFLPGWKAWV
D4ACL8_rat	TV	LSVGGQVNL	LIQQAAMD	PKNLSRFLPGWKAWV
Q5MPF8_frog	MV	LSVGGQVNH	LIQQAAMD	PKNLSRFLPGWKAWV
Q59IS5_zebrafish	TV	LSVGGQVNL	LIQQAAMD	PKNLSRFLPGWKAWV
H2MBY9_japanesericefish	AV	LSVGGQVNL	LIQQAAMD	PKNLSRFLSGWQAWV
Q9N3Q4_seaurchin	VT	LSVAGQVSL	LIQEARD	PKNLSRLYPWSPL
Q9N3Q4_worm	TA	QSSNLQIRRL	LLREATS	ADNLSRMFCGWM PFL
Q5EAK6_fruitfly	GD	SNVEAQVER	LINEATL	PSNLCMLFPGWDPHL
Q9M3G7_mouseearcress	EM	RSIHGQAQQ	LIQDAID	TDRLSHMFPGWGAWM
B9RB21_castorbean	EL	RSVHGVQVQ	LIQDATD	ADRLCQLFPGWGAWM
P38110_bakersyeast	NG	LSVESVQD	LIQQAAT	PSNLSV IYMGWSPFY
O74630_fissionyeast	ST	LSVEASVGE	LIRIAQD	PSYLA LMF CGW S A F Q

(a) ATM FATC.

	1	10	20	30
Q13535_human	LPLSIEGHV	HVHYLIQEAT	DENLLC	QMYLGWTPYMW
G3QYI4_gorilla	LPLSIEGHV	HVHYLIQEAT	DENLLC	QMYLGWTPYMW
H2PBM9_orangutan	LPLSIEGHV	HVHYLIQEAT	DENLLC	QMYLGWTPYMW
F7HT00_macaque	LPLSIEGHV	HVHYLIQEAT	DENLLC	QMYLGWTPYMW
E2QXA4_dog	LPLSIEGHV	HVHYLIQEAT	DENLLC	QMYLGWTPYMW
F1SKG2_pig	LPLSIEGHV	HVHYLIQEAT	DENLLC	QMYLGWTPYMW
G3TF68_elefant	LPLSIEGHV	HVHYLIQEAT	DENLLC	QMYLGWTPYMW
Q9JJK8_mouse	LPLSIEGHV	HVHYLIQEAT	DENLLC	QMYLGWTPYMW
D3Z822_rat	LPLSIEGHV	HVHYLIQEAT	DENLLC	QMYLGWTPYMW
G1SGC5_rabbit	LPLSIEGHV	HVHYLIQEAT	DANLLC	QMYLGWTPYMW
H0V935_guineapig	LPLSIEGHV	HVHYLIQEAT	DENLLC	QMYLGWTPYMW
F6TZV8_oposum	LPLSIEGHV	HVHYLIQEAT	DENLLC	QMYLGWTPYML
G3WTE5_tasmaniandevil	MVNGMGP	MGTGLFRRA	CEVTMR	LMRQREPLM
F6T1S2_turkey	LPLSIEGHV	HVHYLIQEAT	DENLLC	QMYLGWTPYMW
F1NGW1_chicken	LPLSIEGHV	HVHYLIQEAS	DDNLLC	QMYMGWAPYMW
G1KDD8_chameleon	LPLSIEGHV	HVHYLIQDAT	DETLLC	QMYLGWAPYMW
Q9DE14_frog	LPLSIEGHV	HVHYLIQEAT	DENLLS	QMYLGWAPYMW
F1R6S9_zebrafish	LPLSIEGHV	HVHYLIQEAT	DDNLLC	MMYLGWGPYML
H2M9Q9_japanesericefish	LPLSIEGHV	HVHYLIQEAT	DEKLLC	QMYLGWGPYML
H2UEP9_fugu	LPLSIEGHV	HVHYLIQEAT	DDKLLC	QMYLGWGPYML
Q22258_worm	HPMQVSQ	LASSLIELAT	SEKLS	EMYLGMATL
Q9VXG8_fruitfly	IPLSTEG	QVNF	LINEATK	VDNLASMYIGWGAFL
Q9FKS4_mouseearcress	VPLPVEG	QARR	LIADAV	SL ENL GKMYI WMPWF
A2YH41_riceindian	LPLSVEG	QARR	LIAEAV	SHSNL GKMYV WMAWF
Q5Z987_ricejapanese	LPLSVEG	QARR	LIAEAV	SHSNL GKMYV WMAWF
Q59LR2_candidaalbicans	LPMNIHG	QVDV	LIQEAT	SLE RLS QMYAGWAA YM
P38111_bakersyeast	LVLSVAG	QTE T	LIQEAT	SE DNLS KMYI GLPFW
Q75DB8_ashbyagossypii	LPLSVPG	QVD T	VVOQAS	SD ENL A QMYI GLPFW

(b) ATR FATC.

Figure A.3: Sequence conservation of the FATC domains of ATM (a) and ATR (b) illustrated by alignments of the respective sequences from different organisms including lower eukaryotes and/or plants. All sequence alignments were generated using ESPript 2.2 [17].

Table A.6: Secondary structure analysis by CONTIN and CDSSTR.

(a) CONTIN.													(b) CDSSTR.												
sample	helix1	helix2	strand1	strand2	turns	unordered	total	NRMSD	sum helices	sum strands	sum others	sample	helix1	helix2	strand1	strand2	turns	unordered	total	NRMSD	sum helices	sum strands	sum others		
ox.	0.059	0.105	0.188	0.119	0.134	0.396	1.001	<b>0.162</b> *	0.164	0.307	0.53	ox.	0	0.07	0.23	0.13	0.13	0.43	0.99	0.037	0.07	0.36	0.56		
red.	0.037	0.085	0.203	0.127	0.14	0.408	1	0.072	0.122	0.33	0.548	red.	0	0.006	0.223	0.14	0.12	0.43	0.98	0.036	0.06	0.37	0.55		
ox. DMPC	0.088	0.115	0.258	0.105	0.137	0.396	0.999	0.084	0.203	0.263	0.533	ox. DMPC	0.09	0.12	0.16	0.1	0.14	0.39	1	0.026	0.21	0.26	0.53		
red. DMPC	0.102	0.119	0.158	0.102	0.136	0.383	1	0.085	0.221	0.26	0.519	red. DMPC	0.09	0.12	0.16	0.1	0.14	0.39	1	0.024	0.21	0.26	0.53		
ox. DMPC/DMPG (1:1)	0.159	0.152	0.094	0.075	0.14	0.381	1.001	0.069	0.311	0.169	0.521	ox. DMPC/DMPG (1:1)	0.18	0.16	0.1	0.07	0.14	0.36	1.01	0.014	0.34	0.17	0.5		
red. DMPC/DMPG (1:1)	0.16	0.151	0.114	0.079	0.137	0.36	1.001	0.044	0.311	0.193	0.497	red. DMPC/DMPG (1:1)	0.17	0.15	0.12	0.08	0.13	0.34	0.99	0.013	0.32	0.2	0.47		

\*NRMSD out of range



# Acknowledgements - Danksagung

Herzlicher Dank gilt an dieser Stelle PD Dr. Sonja Dames, die mir die Bearbeitung dieses interessanten Themas im Rahmen meiner Doktorarbeit ermöglicht hat. Insbesondere für die Unterstützung am Beginn, während meiner Diplomarbeit, bin ich sehr dankbar.

Gleichzeitig danke ich Prof. Dr. Michael Sattler und Prof. Dr. Bernd Reif, die unsere Gruppe freundlicherweise in Ihren Räumlichkeiten aufgenommen haben und uns unterstützt haben. Bei Bernd möchte ich mich im Besonderen für die Unterstützung meines Stipendienantrags bedanken.

Frau Dr. Eva Sandmann danke ich stellvertretend für das Frauenbüro der Technischen Universität München für das Promotionsstipendium für die Förderung von Frauen in der Wissenschaft im letzten halben Jahr.

Den Kollaborationspartner vom Karlsruher Institut für Technology (KIT), Herrn Dr. Jochen Bürck und Prof. Anne Ulrich, danke ich für die gute Zusammenarbeit und die OCD Daten, die wir erhalten haben. Herrn Bürck insbesondere für die Zeit, die er sich während unseres Besuchs genommen hat. Für ihren Arbeitseinsatz für die MD Simulationen danke ich Joel Janke, Drew Bennett und Prof. Peter Tieleman von der Universität Calgary, Kanada.

Bei Burghard Cordes (AK Sieber) bedanke ich mich für die Messungen der Masseproben, die er wenn möglich immer schnell dazwischen geschoben hat, und die netten Unterhaltungen.

Den Mitgliedern der Reif und Sattlergruppe, insbesondere Fatiha, Thomas, Gerd, Steffi und Gülden danke ich für die gute Zusammenarbeit und Hilfe. Speziellen Dank an Rainer, der immer geholfen hat, wenn er konnte.

Bei Melanie Meier, Verena Kanoldt und Sarah Hammes möchte ich mich für die nette und produktive Zusammenarbeit während der Bachelorarbeit bzw. des Praktikums bedanken.

Asita, der guten Seele von nebenan, danke ich von Herzen für ihr offenes Ohr, die guten Ratschläge und die interessanten Gespräche, die wir geführt haben. Nicht zu vergessen ihre kulinarischen Mitbringsel, mit denen sie uns verwöhnt hat. Des Weiteren möchte ich mich bedanken bei meinen neuen Laborkollegen Antje, Matthias und Sebastian, die im letzten Jahr zu unserer Gruppe gestossen sind.

Ein herzlicher Dank gilt meinen 'neuen alten' Laborkollegen Katrin und Elke, mit denen ich schöne Stunden in und ausserhalb des Labors hatte. Vielen Dank für Eure Unterstützung, auch in nicht so guten Zeiten.

Bei meinen Eltern, meiner Schwester und meinen Freunden bedanke ich mich für die Unterstützung und den Rückhalt in den letzten Jahren.

Und Florian, ich bin sehr froh, dass wir uns über den Weg gelaufen sind.





# Curriculum vitae

Lisa A. M. Sommer

Falkenstrasse 33, 81541 München

born: October 9<sup>th</sup> 1982 in München, Germany

nationality: German

mobile: +49.171.6737028

email: lisa.sommer@tum.de

## Education

since 03/2010 **PhD candidate**

Technische Universität München - Department Chemistry

Chair of Biomolekular NMR Spectroscopy

Group of PD Dr. Sonja A. Dames

*“Structural characterization of the membrane mimetic interactions of the FATC domains of the protein kinase ‘Target of rapamycin’ and other related kinases”*

Member of the TUM Graduate School

04 - 09/2013 TUM Diversity Scholarship

11/2010 **Diploma, Pharmacy**

Martin-Luther-Universität Halle-Wittenberg

Prof. Dr. W. Sippl and PD Dr. Sonja A. Dames

*“Detailed characterization of the association of TOR FATC domain with membrane-mimetic micelles”*

12/2007 **Pharmaceutical license (Approbation)**

Regierung von Oberbayern, München

10/2002-10/2006 **State examination, Pharmacy**

Ludwig-Maximilians-Universität München

06/2002 **A-levels (Abitur)**

Wittelsbacher Gymnasium, München

## Professional experience and training

- 09-11/2009 **Internship**  
University of Copenhagen, Denmark - Department of Pharmacy  
Pharmaceutical Technology and Engineering, Prof. Jukka Rantanen  
*"Simulation of the freeze-drying process by XRPD"*
- 09/2008-08/2009 **Pharmacist, full-time**
- 11/2006-10/2007 **Internship to obtain approbation**  
Rennerische Apotheke, München  
Roche Diagnostic GmbH, Penzberg, Trouble-Shooting
- 09/2008-08/2009 **Internship**  
Dt. Herzentrum, München,  
Experimentelle und Molekulare Kinderkardiologie  
Regulation of the plasminogen activator inhibitor-1 (PAI-1)

## Conferences

- 08/2012 **Int. Conference on Magnetic Resonance in Biological Systems**  
ICMRBS - Lyon, France  
Poster: A comparison of the Association of the FATC Domains of TOR  
DNA-PKcs with Membrane-mimetic Systems
- 08/2011 **European Magnetic Resonance Meeting**  
Euromar - Frankfurt a. M., Germany  
Poster: A comparison of the Association of the FATC Domains of TOR  
with Membrane-mimetic Systems
- 07/2011 **European Molecular Biology Organization**  
EMBO Kurs - Munich, Germany

# Publications

Sommer, L.A.M.; Bennett, D.; Janke, J.; Bürck, J.; Ulrich, A.S.; Tielemann, P.; Dames, S.A.; Lipid, environment, and residue dependent differences in the peripheral membrane-association of the FATC domain of the kinase 'target of rapamycin' by NMR, oriented CD spectroscopy and MD simulations. (submitted)

Sommer, L.A.M.; Schaad, M.; Dames, S. A.; NMR- and CD-Monitored Lipid-Binding Studies Suggest a General Role for the FATC Domain as Membrane Anchor of Phosphatidyl-Inositol-3 Kinase-Related Kinases (PIKKs) (2013) *Journal of Biological Chemistry*, 288, 20046-20063. doi:10.1074/jbc.M113.467233 (\*)

Sommer, L.A.M.; Meier, M.A.; Dames, S.A.; A fast and simple method for probing the interaction of peptides and proteins with lipids and membrane-mimetics using GB1 fusion proteins and NMR spectroscopy (2012) *Protein Science*, 21, 1566-1570. doi:10.1002/pro.2127 (\*)

Some ideas and figures have appeared previously in the marked (\*) publications. Reference [157] is reprinted with permission from Protein Science (Copyright 2012); reference [10] with permission from Journal of Biological Chemistry (Copyright 2013).



# Declaration

Hiermit bestätige ich, dass die der Fakultät für Chemie der Technischen Universität München zur Promotionsprüfung vorgelegte Arbeit mit dem Titel: "Structural characterization of the membrane mimetic interactions of the FATC domains of the protein kinase 'Target of rapamycin' and related kinases" im Lehrstuhl für Biomolekulare NMR Spektroskopie unter Anleitung und Betreuung durch PD Dr. Sonja Dames ohne sonstige Hilfe erstellt und bei der Abfassung nur die gemäss Paragraph 6 Abs. 6 angegebenen Hilfsmittel benutzt worden sind. Die Dissertation ist in keinem anderen Prüfungsverfahren als Prüfungsleistung vorgelegt.

München, 30.08.2013



Lisa A. M. Sommer